Coding of Synthetic Aperture Radar Data

Sujit Bhattacharya

A thesis submitted for the degree of Doctor of Philosophy.

The University of Edinburgh.

August 2009.

Abstract

Synthetic Aperture Radar (SAR) is a dedicated high-resolution sensor with imaging capability in all weather and day-night conditions and has been employed in several earth and interplanetary observation applications. A significant characteristic of this system is the generation of a large amount of data that involves major problems related to on-board data storage and downlink transmission. The near future SAR satellite missions planned would be pushing downlink data bandwidths to prohibitive levels, which dictate efficient on-board compression of raw data. Due to the limitation of the on-board resources in the satellite, it is desirable to have a computationally efficient encoder.

In this thesis, we address the compression of the complex-valued SAR raw data in the compressed sensing (CS) framework, in which the encoder is simple whereas the decoder is computational expensive. CS is an emerging technique for signal measurement and reconstruction that takes advantage of the fact that many signals are sparse under some basis or frame. The measurement of the signal in the CS framework is obtained by taking a small number of projections of the signal onto an incoherent basis. For the SAR raw data compression here we have considered a simple encoder, with a 2D-FFT followed by a random sampler. The reconstruction of the sparse coefficients of the signal from these projections is then based on the sparsity induced optimization techniques like Orthogonal Matching Pursuit (OMP) and iterative reconstruction methods.
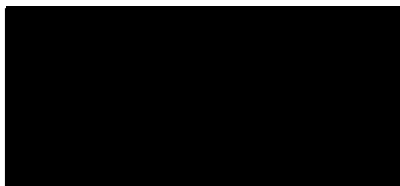
We demonstrate empirically that the CS framework for compression of the complex-valued SAR raw data is effective for the cases when the SAR image is sparse in the spatial domain. We also address the limitation of this framework while dealing with

actual satellite images due to lack of good sparsifying transforms for the complex-valued data.

In this thesis, we present a new algorithm based on regularized iterative algorithm for finding sparse solution for the complex-valued data in which the regularization parameter is adaptively computed in each iteration. The effectiveness of the new algorithm is compared with existing methods like basis pursuit (BP), orthogonal matching pursuit (OMP), etc with both real-valued and complex-valued data set.

Declaration of Originality

I hereby declare that the research recorded in this thesis and the thesis itself was composed and originated entirely by myself in the Institute for Digital Communications, Joint Research Institute for Signal and Image Processing, School of Engineering and Electronics at the University of Edinburgh.

Sujit Bhattacharya

August 2009.

Acknowledgements

Contents

List of Figures

ix

x

List of Tables

Acronyms and Abbreviations

ADC	Analog-to-Digital Conversion
AGC	Automatic Gain Control
ASAR	Advanced Synthetic Aperture Radar
BAQ	Block Adaptive Quantization
BP	Basis Pursuit
BPDN	Basis Pursuit with Denoising
CG	Conjugate Gradient
CoSaMP	Compressive Sampling Matching Pursuit
CS	Compressed Sensing
CWT	Complex Wavelet Transform
DCT	Discrete Cosine Transform
DEM	Digital Elevation Models
DT-CWT	Discrete Time Complex Wavelet Transform
DWT	Discrete Wavelet Transform
EM	Expectation Maximization
FFT	Fast Fourier Transform
FIR	Finite Impulse Response
GIS	Geographical Information System
i.i.d.	Identical Independent Distribution
ISLR	Integrated Sidelobe Ratio
LARS	Least Angle Regression Selection
LASSO	Least Absolute Shrinkage and Selector Operator
LFM	Linear Frequency Modulation
LP	Linear Program
MP	Matching Pursuit
MRI	Magnetic Resonance Imaging

MSE	Mean Square Error
MSTAR	Moving and Stationary Target Acquisition and Recognition
OMP	Orthogonal Matching Pursuit
POCS	Projection onto Convex Sets
PRF	Pulse Repetition Frequency
PRI	Pulse Repetition Interval
PSF	Point Spread Function
PSLR	Peak Sidelobe Ratio
PSNR	Peak Signal-to-Noise Ratio
QCLP	Quadratically Constrained Linear Program
QP	Quadratic Program
RAR	Real Aperture Radar
RIP	Restricted Isometric Property
ROMP	Regularized Orthogonal Matching Pursuit
SAR	Synthetic Aperture Radar
SNR	Signal-to-Noise Ratio
SOCP	Second Order Cone Program
StOMP	Stagewise Orthogonal Matching Pursuit
TCQ	Trellis Coded Quantization
TCVQ	Trellis Coder Vector Quantization
TV	Total Variance
UUP	Uniform Uncertainty Principle
VQ	Vector Quantization

Nomenclature

$\ll$	Much lesser
$\bullet^T$	Transpose of a matrix
$\in$	Belongs to
$\simeq$	Almost equal
$\otimes$	Convolution
α	Chirp rate
$\mathbf{A}$	Measurement matrix
$\mathbf{A}^\dagger$	Pseudo-inverse of matrix $\mathbf{A}$
c	Velocity of light
$\mathbb{C}$	Complex field
δ_{ra}	Range resolution
δ_{az}	Azimuth resolution
δ_R	Isometric constant
$\delta^{(n)}$	Standard descent step
$\mathbf{e}$	Noise vector
ε_{min}	Minimum of discrepancy function
f_c	Carrier frequency
$\mathfrak{I}(\bullet)$	Fourier transform
f_s	Sampling frequency
f_{max}	Maximum frequency content
$f(\mathbf{x})$	Discrepancy function
$\mathbf{G}_0$	Wavelet synthesis lowpass filter
$\mathbf{G}_1$	Wavelet synthesis highpass filter
$\mathcal{H}$	Hilbert space

$\mathbf{H}_0$	Wavelet analysis lowpass filter
$\mathbf{H}_1$	Wavelet analysis highpass filter
$\mathbf{I}$	Identity matrix
$\mathbf{1}(\cdot)$	Indicator function
k_u	Slow-time Doppler domain
$\mathbf{K}$	Matrix consisting of holographic basis
$\mathbf{K}^*$	Adjoint of matrix $\mathbf{K}$
M	Size of measurement signal
$\mu_\mathbf{A}$	Mutual coherence of matrix $\mathbf{A}$
N	Length of the signal
$\mathcal{N}(\mathbf{A})$	Null space of $\mathbf{A}$
$O(\cdot)$	Complexity order
$p(t)$	Transmitted LFM pulse
$\mathbb{P}_R$	l_2-projection operator
R	Size of sparse signal
$\mathbb{R}$	Real field
$\mathbf{r}$	Residual vector
$\mathbb{S}_\tau(\cdot)$	Vector soft-thresholding operation
S_r	Component-wise shrinkage
σ_1	Largest singular value
τ	Pulse width
T	Pulse repetition interval
t	Fast-time domain
u	Slow-time domain
v	Speed of the platform
ω	Fast-time frequency domain
$\mathbf{W}$	Dictionary consisting of orthogonal basis
X_c	Range distance to centre of the target

$\mathbf{x}^{\dagger}$ Minimum norm solution

$\mathbf{y}$ Measurement vector

$\mathbf{z}$ Sparse vector

Chapter 1

1. Introduction

This dissertation presents a new approach to the problem of synthetic aperture radar (SAR) raw data compression. SAR is an active sensor that has been extensively used for a variety of remote sensing applications. The purpose of this chapter is to: i) introduce the problem addressed and the motivation, ii) summarize the SAR technology and within this context discuss the needs for raw data compression and iii) provide a concise description of the approach taken in this work by highlighting the main contributions and an outline of the subsequent chapters.

1.1 Synthetic Aperture Radar

The optical and infrared sensing technologies have been used for several decades for remote sensing of the earth's surface. These passive sensors rely on the energy reflected or radiated from the earth's surface and thus depend upon the sun as a source of illumination. Microwave radar imaging has emerged as an alternative approach to remote earth observation, which generates reflectivity maps of an illuminated area through transmission and reception of electromagnetic energy. The use of microwave energy allows for the observation of the earth properties unique to the microwave region and not detectable with visible and infrared systems. Among other types of microwave sensor, special attention has been paid to synthetic aperture radar (SAR) because of its high spatial resolution and various modes of operations.

SAR sensors are active sensors with their own illumination source and are typically mounted on aircrafts and satellites. Being an active sensor, it can gather imagery equally well during the day and night. SAR sensors operate in the microwave region between 0.3 - 30 GHz of the electromagnetic spectrum with typical wavelengths between 1 cm and a meter with various polarizations. The SAR sensor is independent of the solar illumina-

tion and is generally unaffected by the cloud cover. Thus, SAR can operate even in the presence of clouds, fog, haze and rain with its own source of radiation, which are generally the limiting factor in the case of optical remote sensing. This weather independence combined with the day and night operation capabilities make SAR an operational monitoring sensor for the earth and other planetary surfaces of Venus and Saturn, a task which cannot be achieved with optical sensors. These capabilities have made the SAR a natural choice for military surveillance and also for the inter-planetary imaging missions like Magellan, Cassine etc [1]. Earth planetary SAR applications include geographical information system (GIS), terrain mapping, crop estimation, geology, oceanography etc. Interferometric SAR campaigns are also conducted for generation of the digital elevation models (DEM) [2]. The SAR has a wide range of possible applications as various parameters like power, frequency, phase, polarization, incidence angle, spatial resolution and swath suited for various environments, can be controlled.

The earth orbital SAR satellite started with the SEASAT in 1978 followed by SIR-A/B/C, ERS-1/2, ALMAZ, RADARSAT-I, ENVISAT –I, TERRASAR, etc. The future Earth orbital satellites include RADARSAT-II, ENVISAT-II, etc. The interplanetary SAR missions include imaging Venus and Saturn by Magellan and Cassine [1].

SAR sensors are typically mounted on a moving platform such as aircraft or satellite, which travels along a particular direction transmitting and receiving microwave pulses towards the ground, as illustrated in Figure 1.1. In SAR, the radar platform moves along the flight path usually with a constant velocity in a direction oblique to the target to be imaged as shown in Figure 1.1. The airborne SAR images have to be corrected for deviations from their nominal path, using inertial sensors and autofocus. SAR produces 2-dimensional (range and cross-range) terrain reflectivity images by emitting sequence of closely spaced radio frequency pulses and by sampling the echoes scattered from the ground targets. The spatial resolution in the range direction is dependent upon the bandwidth of the transmitted waveform and is usually achieved by transmitting a wide-band linear frequency modulated (LFM) waveform. In the direction orthogonal to the

radar beam (also called cross range, azimuth, or along-track in broadband operation) the resolution is greatly enhanced by coherently integrating the return echoes, described later in chapter 2. The improved azimuth resolution for swath SAR thus obtained by processing the return, unlike real aperture radars (RAR), is independent of the range and proportional to the real antenna aperture [3]. This is described in details in Section 2.1 of chapter 2.
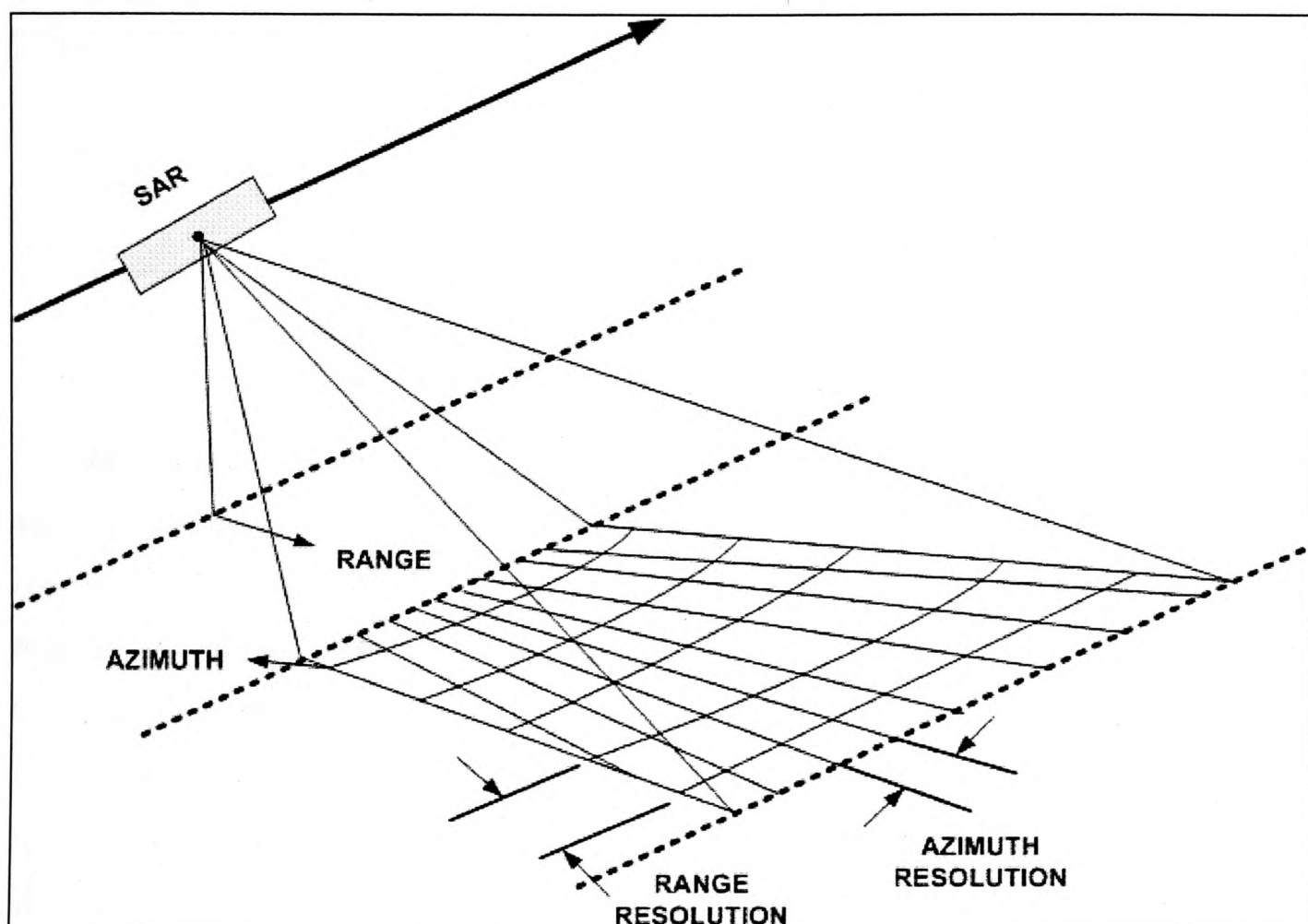
Figure 1.1 Illustration of the SAR data collection.

1.2 SAR Data Acquisition

The SAR image generation process consists of three distinctive stages : i) sensing the target area using the imaging radar, ii) sampling and compression of the scattered SAR signal for downlink to the ground, and iii) processing of the reconstructed SAR signal into image also known as *focusing*. A simplified block diagram of a typical SAR system is shown in Figure 1.2. The SAR system comprises of a pulsed transmitter, an antenna

and a phase-coherent receiver. The transmitter transmits a wideband signal like a linear frequency modulated (LFM) at a regular interval, known as pulse repetition interval (PRI), in order to illuminate the terrain strip of interest. The PRI of SAR is constrained within bounds established by the geometry and signal ambiguity limits.
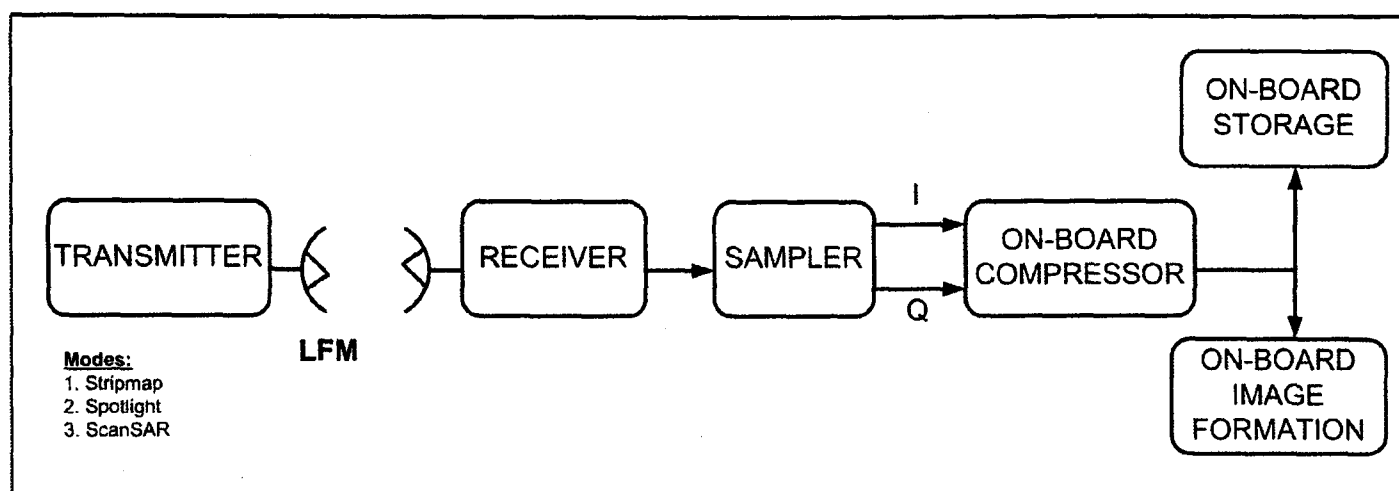
Figure 1.2 A simplified SAR on-board system.

Returned signals from the terrain strip (swath) are received via a coherent receiver and then are demodulated into I and Q for analog-to-digital (A/D) conversion. These received echoes are sampled into in-phase (I) and quadrature (Q) component to preserve both phase and magnitude of the return signal. These digitized complex data are referred to as raw SAR data. In satellite system, these raw data undergo data compression before being directly transmitted to the ground segment via a dedicated transmission link when in view with the ground segment or are stored on-board for later transmission to the ground.

The amount of data generated by the SAR system is proportional to the pulse repetition frequency (PRF), the sampling frequency, swath and the number of bits allocated to each sample. The limits on the PRF arise to avoid along track phase ambiguity whereas the sampling frequency is dependent upon the bandwidth of the transmitted waveform which in turn is dependent upon the range resolution. The classical methods of SAR raw data compression thus relied on reducing the no. of bits allocated to the data samples.

1.3 The Need for SAR Raw Data Compression

The various modes of SAR like stripmap, scanSAR, spotlight, etc. [1] coupled with the high resolution and wide swath requirements result in a huge amount of data for processing to generate high resolution images. The amount of data generated by these SAR systems will easily exceed the on-board storage and downlink bandwidth of the satellite. The data rate of the past satellites like ERS-1, Envisat and Radarsat is in order of hundred Mbit/s and incorporated Block Adaptive Quantizer (BAQ) [4] to achieve compression factors from 2 to 8. The raw data rate will increase in future with increasing requirements on the resolution and wider swath. Thus, an efficient on-board SAR raw data compressor has become imperative for the future SAR satellite systems. Conversely the data compressor will provide a larger capacity for higher data rates to support higher resolution, wider coverage, multi-polarization and multi-frequency operations.

The research proposal focuses on the compression the SAR raw data for on-board storage and transmission from the satellite to the ground. The proposed work is motivated by interest in compression algorithms and their efficient hardware implementation which when included in the design of future satellite missions will provide a sufficient data reduction without degrading the quality of the final images. Some of the performance measures of the quality of the final images are described in Section 2.6 of Chapter 2. However, the compression of raw SAR data poses several challenges due to its noise like characteristics and high entropy [1].

1.4 Raw SAR Data Characteristics

The radar return from a SAR instrument is the result of the super-position of the responses of many small scatterers within the antenna beam footprint. Each scatterer within the view of antenna provides a contribution whose amplitude and phase are statistically independent of each other and of other scatterers. The phase of the scatterers are uniformly distributed in the angle between $-\pi$ to $+\pi$. The raw SAR Data can be viewed as a complex random process, who's real and imaginary parts are Gaussian, with

zero mean and same variance, and uncorrelated according to the Central Limit Theorem. The distribution of the real and imaginary samples (5-bits) for the case of Advance SAR payload (ASAR) of ERS-1 is shown is Figure 1.3. The amplitude distributions for both the components are found to be Gaussian with zero mean and same variance.
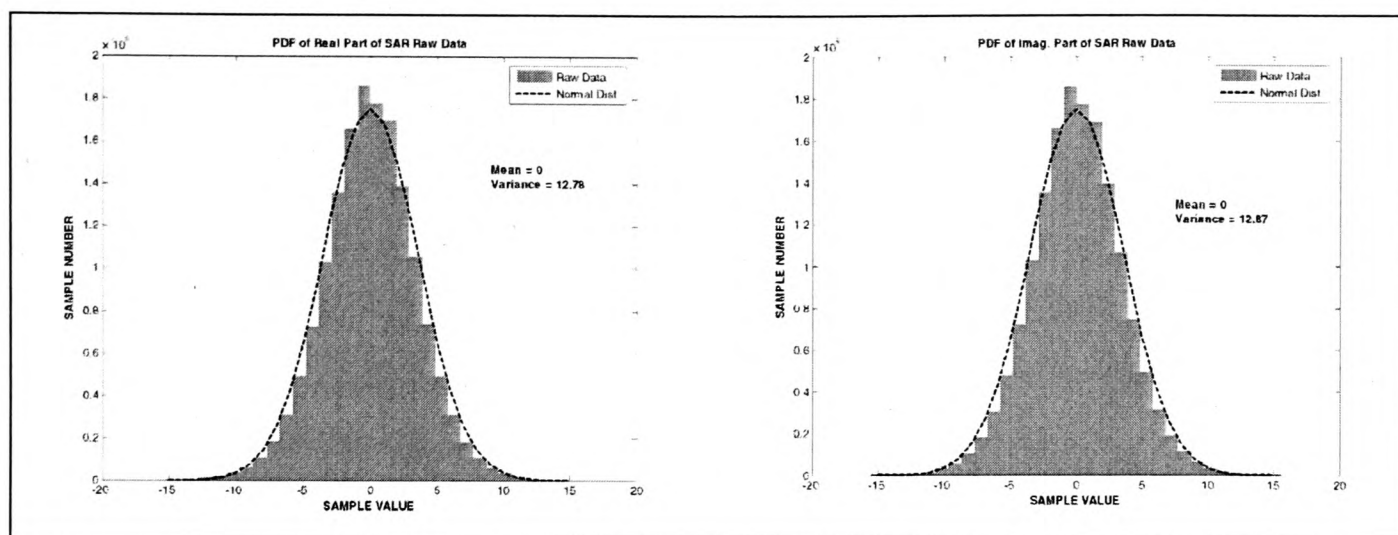
Figure 1.3 Amplitude Distribution of 5-bits Raw ASAR (ERS-1) Data (a) Real, (b) Imaginary.

In general, an analysis of raw SAR data from various airborne and satellite system indicates that the entropy is very high and is around $H_0 \approx 6 - 7$ bits/sample with a high dynamic range of 40 dB [1]. This sets the upper limit of the quantizer to 8-bits. The reason for such large dynamic range of the return signals is the presence of corner shapes that are very common in man-made buildings and vehicles. The returns from such corner shaped objects are much stronger than the natural background areas. It is also observed that the raw SAR data exhibits a very poor correlation in the range and the azimuth directions. Another reason for uncorrelated returns from pulse to pulse is because of random returns from multiple scatterers present in the beamwidth of the antenna.

The data compression of SAR images also poses various challenges due to high entropy of the SAR image and the relevant information is contained in both the low frequency and high frequency part of the spectrum [5]. Another important characteristic of the processed SAR display images is the presence of noise known as *speckle noise* which arises due to presence of multiple scatterers within a resolution cell [1]. This results in a lower pixel correlation than general images.

6

Previous studies which exploit the correlation among adjacent samples have shown to have poor rate distortion performance. Researchers have tried various quantization like block adaptive quantization (BAQ) [4], vector quantization (VQ) [6], Trellis-coded quantization (TCQ) and of its vectorial version, referred to as Trellis-coded vector quantization (TCVQ) for raw data encoding to achieve interesting performance improvement [7]. The survey of the several compression algorithms for the raw SAR data can be found in [8]. The most popular technique that has been used in spaceborne SAR is the BAQ. The BAQ acts like an automatic gain control (AGC) in the digital domain. The incoming data is divided into consecutive disjoint blocks and variance of each block is calculated. The quantization step size for the block is then proportional to the estimated variance. The blocked quantized data along with the variance i.e. the scale factor is stored for each block for transmission.

1.5 Contributions

The research objective is to design a low-complexity encoding scheme at low rates that could be easily implemented on-board a satellite. Previous methods relied on reducing the number of bits allocated to the sampled data. This thesis proposes a new framework for compressing the complex-valued SAR raw data by sampling the signal below the *Nyquist rate*, using the ideas from compressive or compressed sensing (CS). CS is an emerging technique for signal measurement in which the signal is sampled much below the *Nyquist rate* with the reconstruction algorithms taking advantage of the fact that many signals are sparse under some basis or frame. The measurement of the signal in the CS framework is obtained by taking a small number of projections of the signal onto an incoherent basis usually random sampling of the data. In this study of SAR raw data compression, we have considered a simple encoder with a 2D-FFT followed by a random sampler. The reconstruction of the sparse coefficients of the signal from these projections is then based on the sparsity induced optimization techniques which is much complex as compared to the encoder. These features of low complexity encoder with high complexity decoder of the CS framework make it an appropriate framework for on-board SAR raw data compression. In this thesis, we thus have proposed a new approach

of compressing the SAR raw data by reducing the number of samples by random sampling the Fourier transformed data. In one of the experiments, we have used the complex wavelet transform (CWT) as a frame by decomposing both the negative and positive part of the spectrum of the input data.

In this thesis, we have demonstrated empirically that the CS framework for compression of complex-valued SAR raw data is effective for the cases when the SAR image is sparse in the spatial domain. We also address the limitation of this framework while dealing with actual satellite images due to lack of good sparsifying transforms for the complex-valued data. The sparsity of the actual complex-valued SAR raw data in magnitude-phase domain, real-imaginary domain and by converting it to real-valued by shifting the frequency spectrum to all positive frequencies were tested and found to be ineffective to compress the data in CS framework. We believe that though this framework is not effective for full SAR image reconstruction due to lack of a good sparsifying transform but it would be effectively used for applications like detection, classification and partial image reconstruction.

We also present a new algorithm based on regularized iterative algorithm for finding sparse solution for the complex-valued data in which the regularization parameter is adaptively computed in each iteration. The effectiveness of the new algorithm is compared with existing methods like basis pursuit (BP) and orthogonal matching pursuit (OMP) with both real and complex data set.

1.6 Thesis Outline

This dissertation is organized as follows. In chapter 2, we review the principles of SAR and provide the necessary background information on SAR. The chapter also describes the signal processing steps involved in generating SAR images from the data collected by the SAR sensor. It also mentions the sources for the raw SAR data and the performance metric to evaluate the performance of SAR raw data compression. In chapter 3, we introduce the theory of compressive or compressed sensing (CS). We describe the theory

of sparse approximation on which the compressed sensing framework is based. It is shown that the signal recovery in the compressed sensing framework can be formulated as solving the inverse problem with *sparsity* constraints. We also present several examples to show the recovery of signal from undersampled data in CS framework. In chapter 4, we provide a brief overview of the inverse problems and associated regularization methods to get their solutions. This chapter also describes a new iterative algorithm to get a sparse solution to the inverse problems along with several examples of real and complex-valued data. In chapter 5, we describe a framework for compressing the SAR raw data by sampling the signal below the *Nyquist rate* using the ideas from compressed sensing. The chapter discussed the regularization based SAR image reconstruction from sub-sampled complex-valued raw data. We provide results both with simulated SAR raw data and actual satellite data and measure the reconstruction quality. Finally, in chapter 6 we summaries the results that we have obtained and also suggest some future research directions as a continuation of the work presented here.

Chapter 2

2. Principles of Synthetic Aperture Radar (SAR)

In this chapter, we provide the necessary background information on SAR that will be useful for the rest of the dissertation. We describe here the SAR geometry, the principles of SAR operation and also the signal processing steps involved in generating SAR images from the data collected by the SAR sensor. We also briefly describe the sources for the raw SAR data and the performance metric to evaluate the performance of SAR raw data compression.

There are three distinct modes of SAR imaging: stripmap-mode SAR, spotlight-mode SAR and scan-mode SAR. In the stripmap mode, the radar antenna remains fixed with respect to the platform, illuminating a sequence of ground patches that form a strip parallel to the flight path. In the spotlight-mode SAR, the antenna is steered mechanically or electronically to continuously illuminate the same patch of terrain during its flight duration [9, 10]. The main advantage of the spotlight SAR imaging is increased resolution. Scan-mode effectively increases the swath with degraded azimuth resolution by allowing the look direction and illuminated ground patch both to vary during the flight duration. In this thesis, we focus on the stripmap-mode SAR which is widely used to generate large swath images.

2.1 Stripmap-mode SAR Geometry

The imaging geometry of the stripmap SAR is shown in Figure 2.1, in which the antenna is directed towards the ground at a fixed angle of elevation and normal to the flight path [1]. The co-ordinate along the line of flight of the radar is termed as *azimuth* and the co-

11

ordinate perpendicular to the azimuth is called *range*. The radar which is mounted on the moving platform transmits pulses at a regular interval known as pulse-repetition-interval (PRI) and the backscattered signal is measured in order to reconstruct the continuous area illuminated also known as *swath*.

To obtain a high resolution along the range direction with the limited peak power available on-board, long linear frequency-modulated (LFM) pulses are transmitted. Pulse compression is used to achieve wide bandwidth pulses with high duty ratio and limited peak power. The range resolution which is inversely proportional to the bandwidth (BW) of the transmitted waveform is given by the formula:

$$\delta_{ra} = \frac{c\tau_c}{2} = \frac{c}{2BW} \tag{2.1}$$

where τ_c is the compressed pulse width. The wideband LFM return pulses are compressed through a matched filter to give high resolution in the range direction.

The real-aperture-radar (RAR) azimuth footprint is as shown in Figure 2.2. The azimuth resolution of RAR is inversely proportional to the size of the aperture is given by

$$\delta_{az} = \frac{\lambda R}{L} = \frac{cR}{f_c L} \tag{2.2}$$
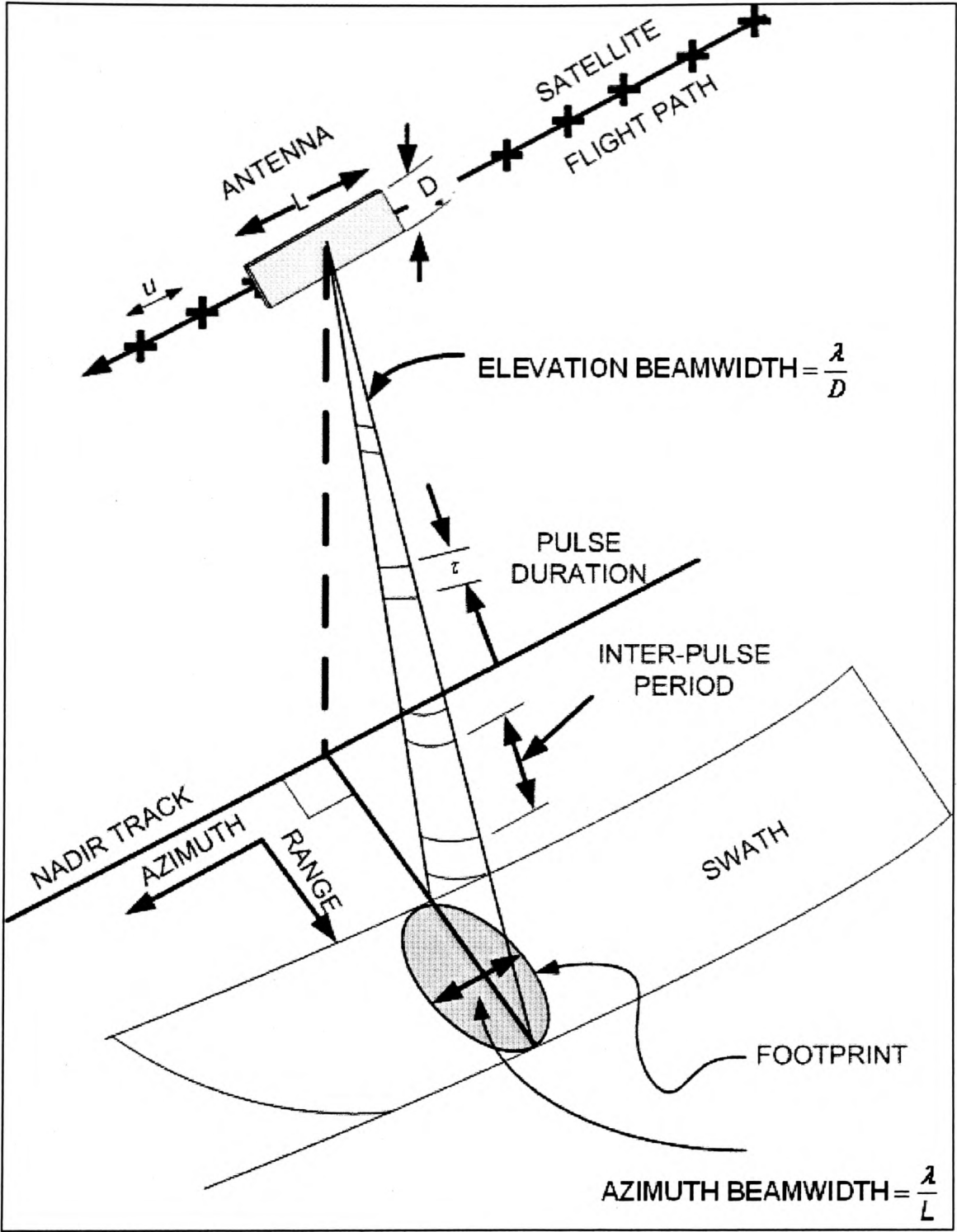
Figure 2.1 Geometry of stripmap SAR [1].

where f_c is the carrier frequency of transmission. From the above equation, we see that

high resolution in the azimuth direction requires large antenna and short object distances.
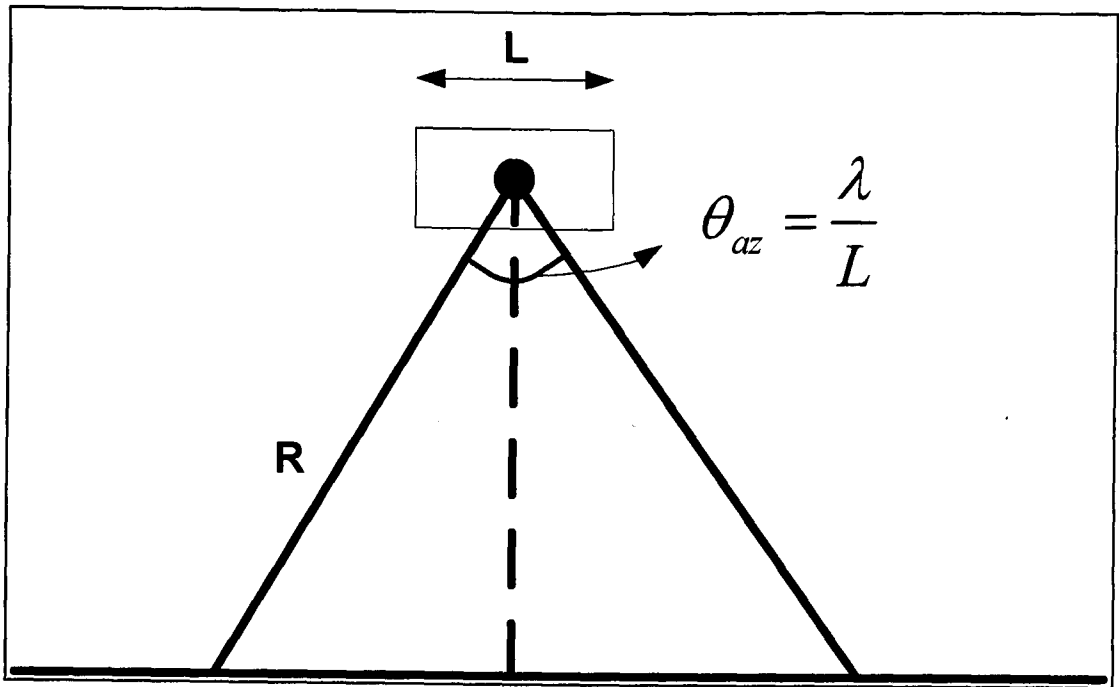
Figure 2.2 Real aperture radar azimuth footprint.

To demonstrate the requirement of small pulse duration for high range resolution and a large antenna size for high azimuth resolution, let us consider radar operating with the following requirements:

Parameter	Value
Slant Range, R	10 km
Carrier frequency, f_c	10 GHz
Range resolution, δ_{ra}	1 m
Azimuth resolution δ_{az}	1 m

$$\delta_{ra} = \frac{c}{2BW} \implies BW = 150 \text{ MHz} \implies \tau = 6.7 \text{ ns}$$

$$\delta_{az} = \frac{\lambda R}{L} = \frac{cR}{f_c L} \implies L = 300 \text{ m}$$

14

The above example shows that fundamental problem of the classical real aperture radar imaging systems which require an impractically long antenna for acceptable azimuth resolution.

Synthetic aperture radar solves this problem by transmitting multiple pulses of large bandwidth from a number of observation points and then focusing the received signal coherently to obtain a high resolution 2-D image. SAR transmits a pulse with wide bandwidth such as LFM or *chirps*. The transmitter in such radar varies the frequency of the pulse linearly over a particular frequency range, which determines the bandwidth. The chirp length and the chirp rate are based on various radar hardware capabilities such as RF pulse power, PRF, ADC sampling rate, etc and also on the range resolution requirement [1]. The transmitted LFM is mathematically expressed as

$$p(t) = \exp\left\{ j2\pi\left(f_c t + \frac{\alpha}{2}t^2 \right) \right\} \operatorname{rect}\left(\frac{t}{\tau} \right)$$

(2.3)

where α is the chirp rate in Hz/sec, τ is the pulse duration in sec.

On the other hand, to improve the azimuth resolution, the SAR makes use of the motion of the platform to simulate an array of antennae and synthesize a long aperture. This technique, as shown in Figure 2.3, is based on the fact that a scatterer is observed by various locations (marked with black dots) along the azimuth direction. The aperture synthesized through this mechanism has a size of M whereas the real aperture is of the size L.
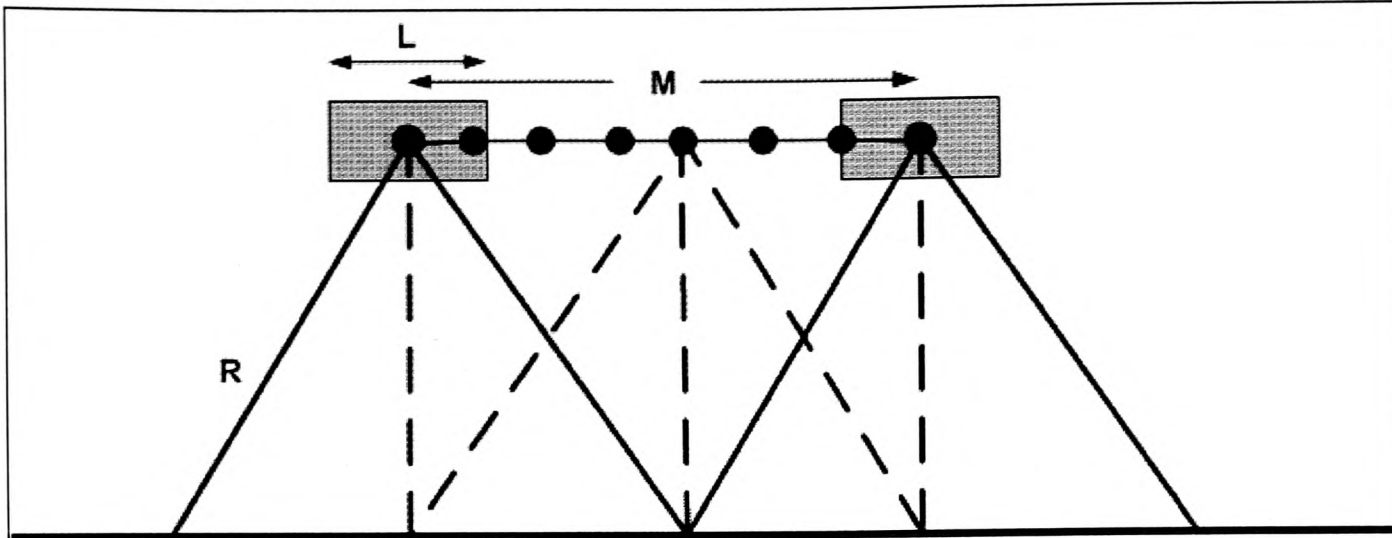
Figure 2.3 Synthetic array formed due to moving platform.

The maximum synthesized aperture is given by

$$M = \frac{\lambda R}{L} \tag{2.4}$$

and the azimuth resolution for the full synthesized aperture is

$$\delta_{az} = \frac{\lambda R}{2M} = \frac{L}{2} \tag{2.5}$$

which is independent of the range and frequency of the radar and improves with smaller antenna aperture. The factor of 'two' is the result of the synthetic aperture, The phase difference between elements of the synthetic aperture result from a two-way path difference and are therefore, two times larger than in the case of a real antenna [1].

In the raw SAR data, the signal return of a scatterer is spread in both range and azimuth directions. The transmission of long pulses causes the contributions coming from a scatterer to spread along the range direction. Moreover, in the azimuth direction the return from the scatterer is spread by the duration it is illuminated by the beam, or the synthetic aperture. As a scatterer passes through the antenna beam, the range to the target changes. On the scale of the transmitted wavelength, this range variation causes a phase variation in the received signal as a function of the azimuth. High resolution in the azimuth direction can be obtained by processing the coherent phase history of the

16

received signal over the radar illumination or integration time. The range variation to a scatterer can result in a variation in the range delay to the target that is larger than the range sampling spacing which is also know as range migration and is shown in Figure 2.4.
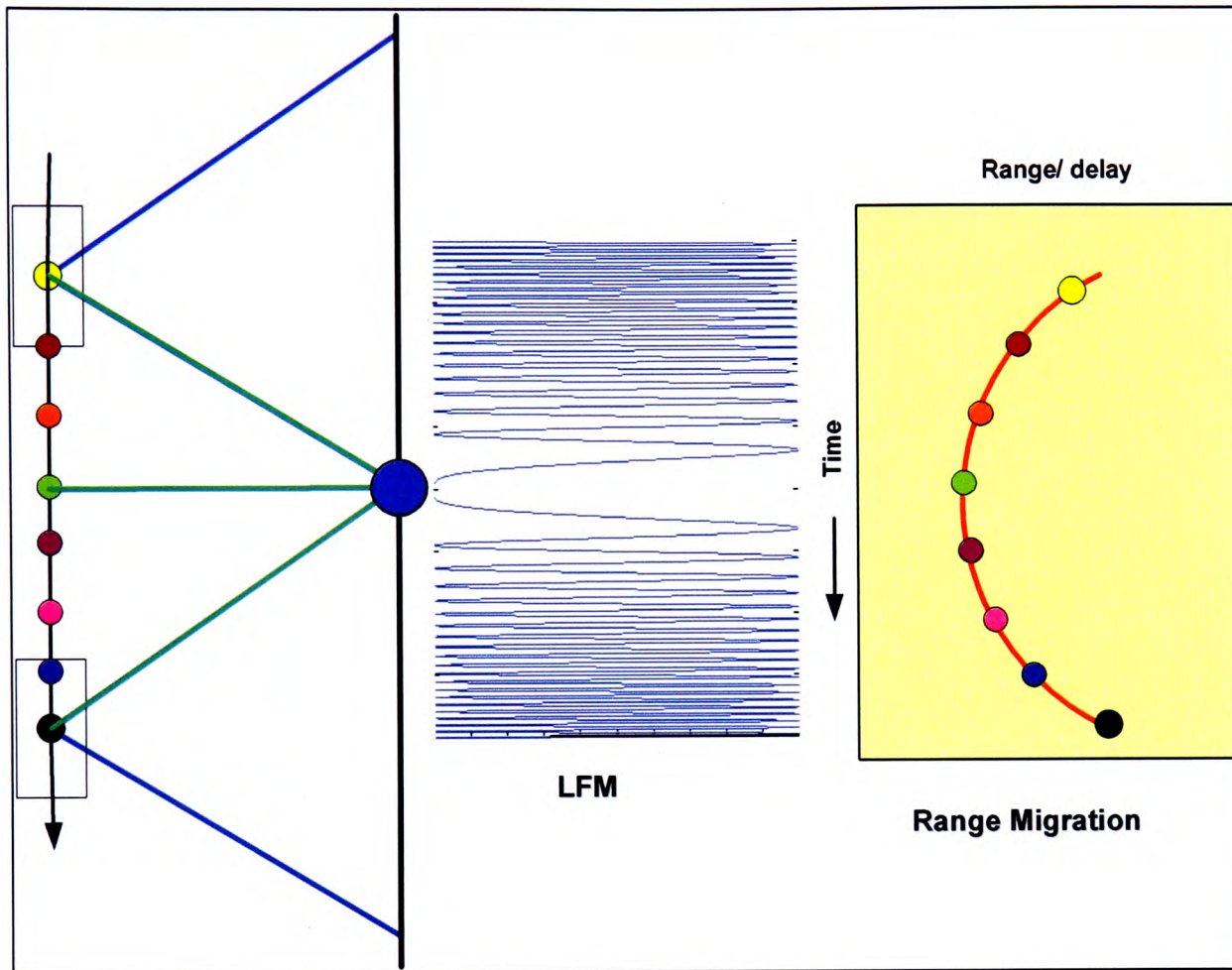
Figure 2.4 Return of a scatterer to a moving platform.

2.2   SAR Stripmap Imaging Model

In the stripmap mode the radar maps the surface with the antenna pointing downward such that the boresight (centre) of the mainlobe of the real aperture radiation pattern is perpendicular of the flight path. The simplified model for the SAR stripmap mode is to consider the stationary imaging surface to consist of several point reflectors with reflectivity σ_n and located at the location $\left(x_n, y_n\right)$ as shown in the Figure 2.5; with x-axis denoting the range and y-axis denoting the azimuth direction with the scene centre at $\left(X_c, Y_c\right)$ [11]. It is also to be noted that the centre of the synthesized aperture M is at the

17
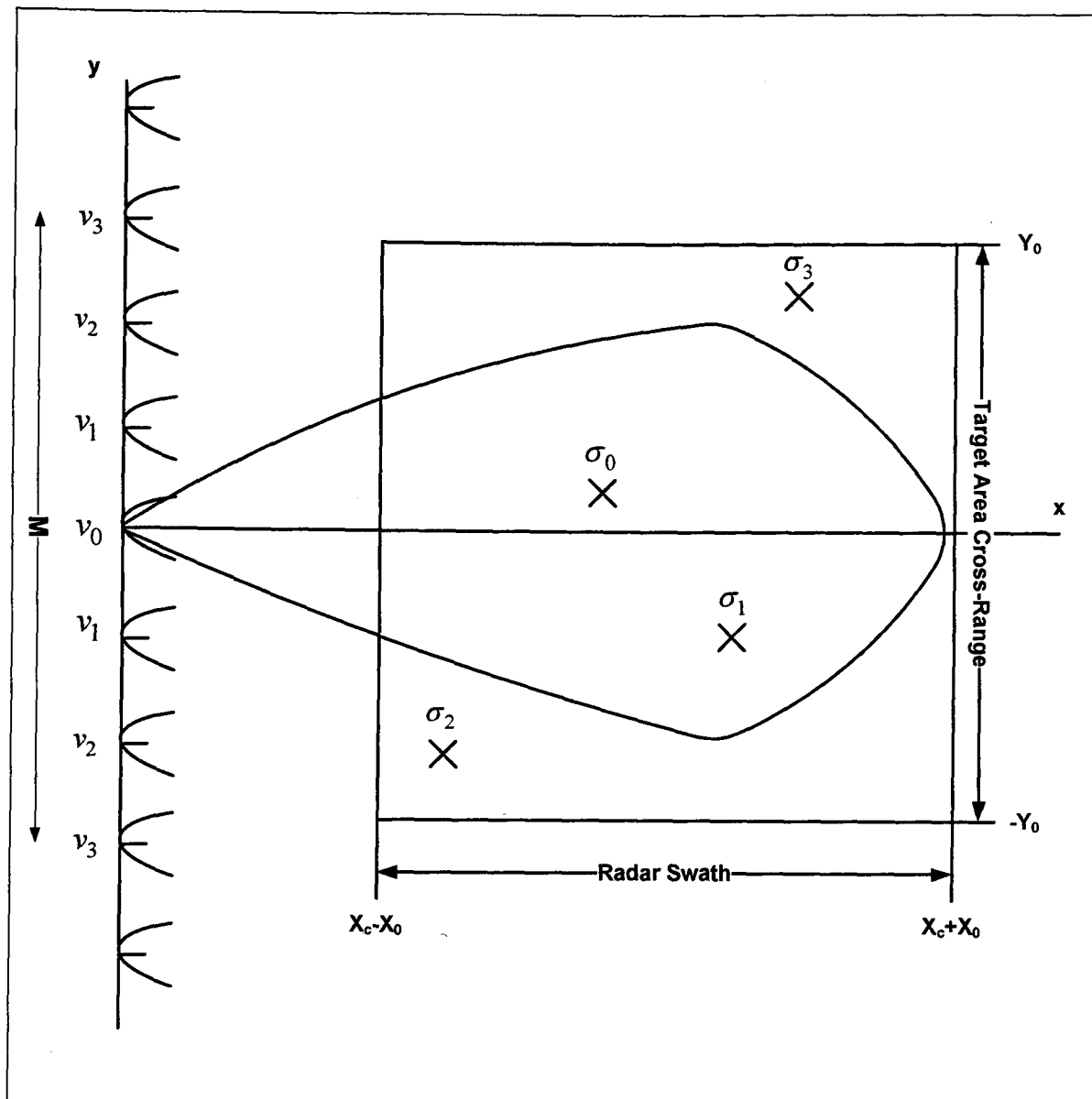
Figure 2.5 Geometry of SAR stripmap imaging model.

middle of the imaging surface. The radar located at (o, u_n) in the spatial domain transmits wide bandwidth signal $p(t)$ of duration τ at regular interval T. Synthetic aperture system models are generally developed based on the "*start-stop*" approximation i.e. the platform is considered stationary during the transmission of a pulse and the reception of the echoes from this pulse; then the platform moves to the next location (o, u_n), and the process repeats. This approximation is justified as the speed of light is considerably higher than the speed at with which the platform moves. The use of the start-stop approximation for spaceborne SAR imaging is described in [12]. The sensor trajectory is assumed to be in a prescribed path and the radar's radiation pattern omni-directional.

A point target at location $\left(x_n, y_n\right)$ is defined as an isolated point reflector with unit-impulse reflectivity, $\sigma_n = \delta\left(x - x_n, y - y_n\right)$. The target function of such point targets within an imaging surface is given by:

$$ff(x,y) = \sum_n \sigma_n \delta(x - x_n, y - y_n) \tag{2.6}$$

for which the 2D-Fourier transform is given by

$$FF(k_x, k_y) = \sum_n \sigma_n \exp(-jk_x x_n - jk_y y_n) \tag{2.7}$$

Considering the roundtrip time delay for the n-th target as $2R_n/c$, where $R_n = \sqrt{(x_n^2 + (y_n - u)^2}$, the measured echoed signal for the scatterers for a transmitted pulse of $p(t)$ is given by:

$$ss(t,u) = \sum_n \sigma_n p\left(t - \frac{2R_n}{c}\right) \tag{2.8}$$

with t denoting the *fast-time* along the range direction and u denoting the *slow-time* along the azimuth direction. The variation of the amplitude function, which is related to the wave divergence, is absorbed in σ_n [13].

With the above system model, the point target returns for several scatterers were generated using the parameters tabulated in Table 2-1 and is as shown in Figure 2.6 [11]. LFM waveform is considered as a transmitted waveform for the simulation.

Parameters	Values
Speed of the platform, v	77.73 m/sec
PRF	200Hz
Range distance to centre of the target, X_c	500m
Size of footprint in range direction, X_0	400m
Range resolution, δ_{ra}	1.5m
Azimuth resolution, δ_{az}	6m
Carrier frequency, f_c	100MHz
Pulse width, τ	0.15 μs

Table 2-1 Parameters for simulation of point targets
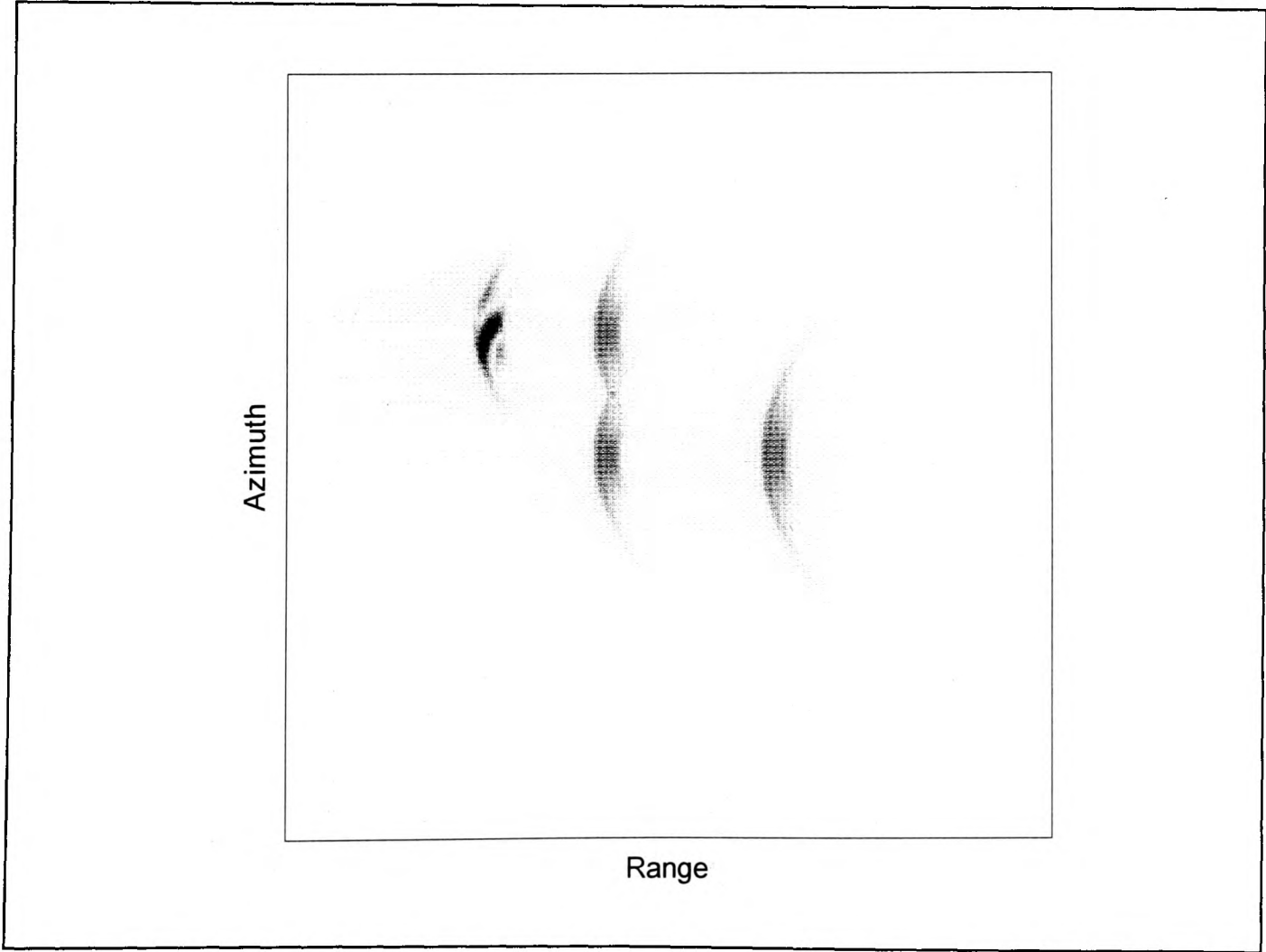
Figure 2.6 Return signal of point targets.

2.3 SAR Signal Processing and Image Formation

The return echoes, as shown in Figure 2.6, are dispersed both in the range direction and the azimuth direction. As mentioned earlier, the dispersion along the range direction is due to the wideband LFM signal transmitted of duration τ, whereas the dispersion along the azimuth direction is due to the movement of the platform relative to the point targets. The range curvature is due to the variation of the range of the point target as the platform moves along the azimuth direction.

The processing steps required to get the desired target function from the return signal is shown in Figure 2.7, and is explained below.
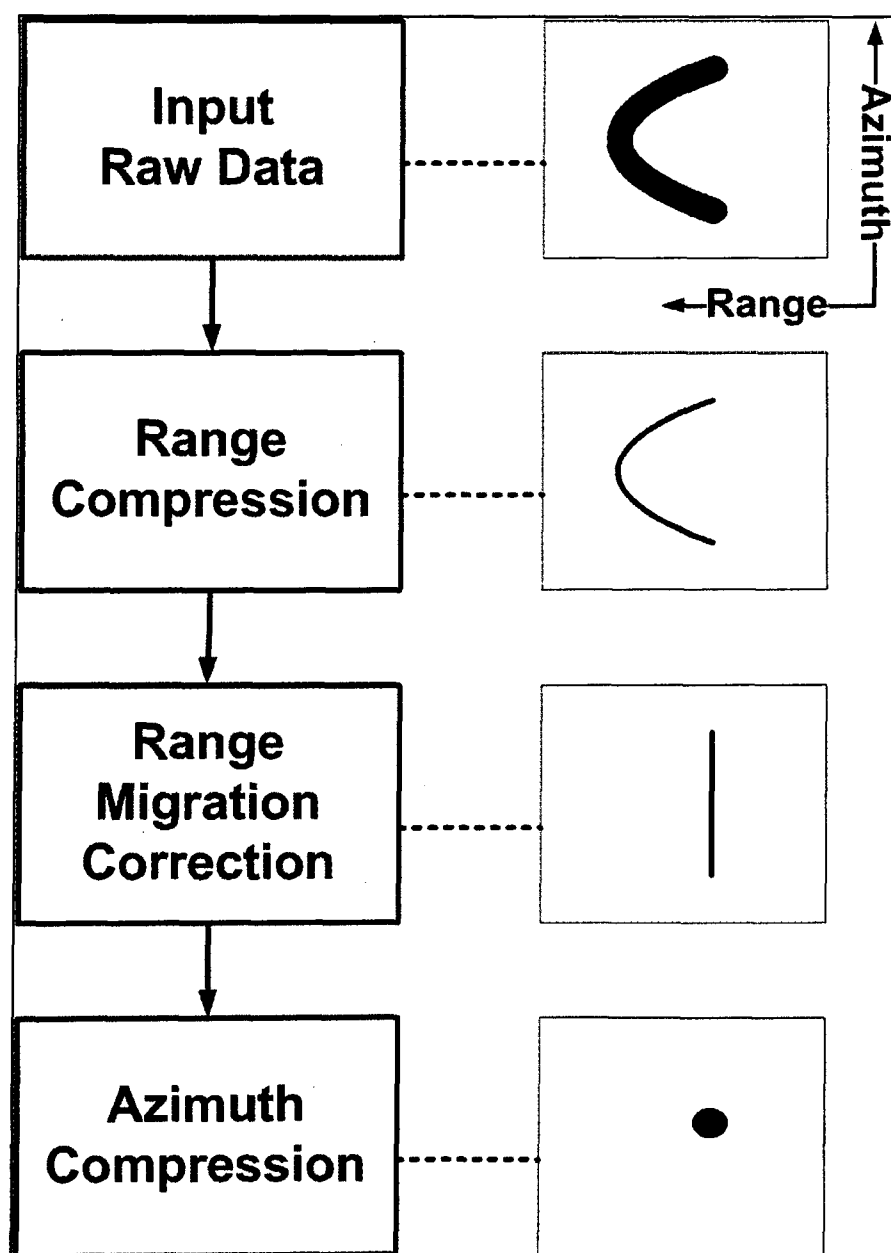
Figure 2.7 Basic processing steps for stripmap SAR.

2.3.1 Range Compression

The large-bandwidth dispersion-energy return in range direction is processed so as to compress the energy into a much narrower pulse. The range resolution is then determined by the compressed pulse, as if it had been the transmitted waveform. The most commonly used method for the pulse compression is the matched filtering with the time-reversed complex conjugate of the signal and the deramp-FFT method [14], which is a form of matched filter implemented differently. It is well known that the optimal filter, in the sense of obtaining the maximum peak-signal-to-noise ratio in the presence of white noise, is the matched filter [1]. The deramp-FFT is used generally in the case when the swath-width return duration is smaller compared to the transmitted waveform τ.

2.3.1.1 Matched Filtering Method

The transmitted LFM pulse of duration τ is given by:

$$p(t) = A\exp\left[-j\left(\omega_c t + \pi\alpha t^2\right)\right]rect\left(\frac{\tau}{T}\right)$$

$$(2.9)$$

where ω_c = carrier frequency , α = Chirp rate

The measured echo for the transmitted waveform $p(t)$ is

$$ss(t,u) = \sum_n \sigma_n p\left(t - \frac{2x_n}{c}\right)$$

$$(2.10)$$

where x_n is equal to the distance of the target from transmitter.

The matched filter output is given by

$$ssm(t,u) = ss(t,u) \otimes p^*(t)$$

$$(2.11)$$

where $\otimes$ denotes convolution. The matched filter is the time-reversed complex conjugate of the signal [11].

The matched filter output of three targets simulated with the parameters: $X_c = 2\text{km}, f_c = 1\text{GHz}, BW = 200\text{MHz}, \tau = 10\mu\text{s}$, is shown in Figure 2.8. The swath-width return duration in this case is $0.67\mu\text{s}$.
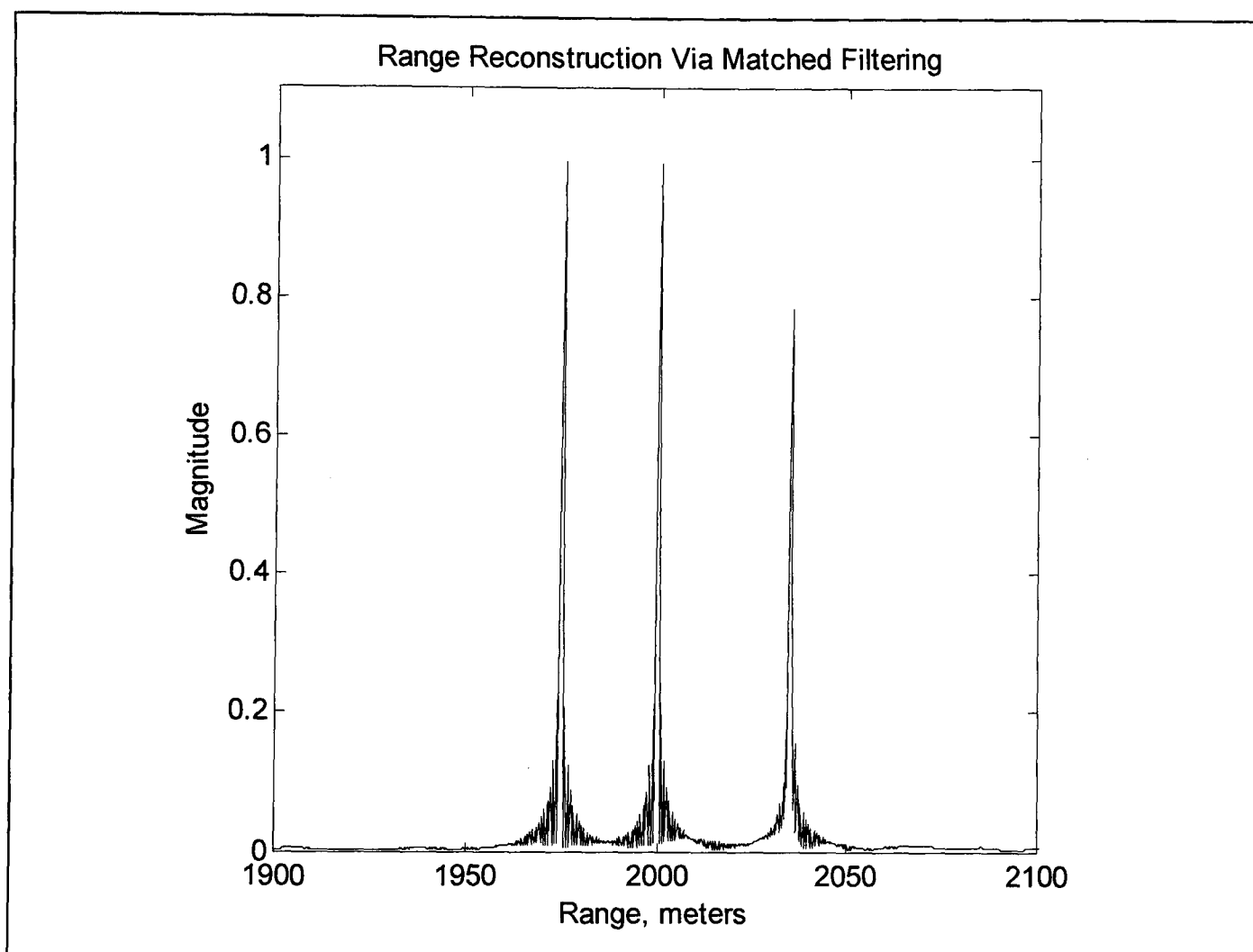
Figure 2.8 Matched filter output of three point targets.

2.3.1.2 Deramp-FFT Method

In this method the received echo signal is demodulated by the reference transmitted signal to directly acquire the Fourier transform of the reflectivity [14]. An estimate of the

surface reflectivity is typically found from the output of the demodulator by Fourier transform.

The demodulated output is given by:

$$scb(t,u) = ss^*(t,u) \times p(t) \tag{2.12}$$

and the range compressed output is found by using the Fourier transform

$$fscb(\omega,u) = \mathfrak{I}\left(scb(t,u)\right) \tag{2.13}$$

The deramp-FFT output of simulated three point targets of variable magnitude with the following parameters: $X_c = 2\text{km}, f_c = 1\text{GHz}, BW = 200\text{MHz}, \tau = 0.1\mu\text{s}$, is shown in Figure 2.9. The swath-width return duration in this case is $0.67\mu\text{s}$.
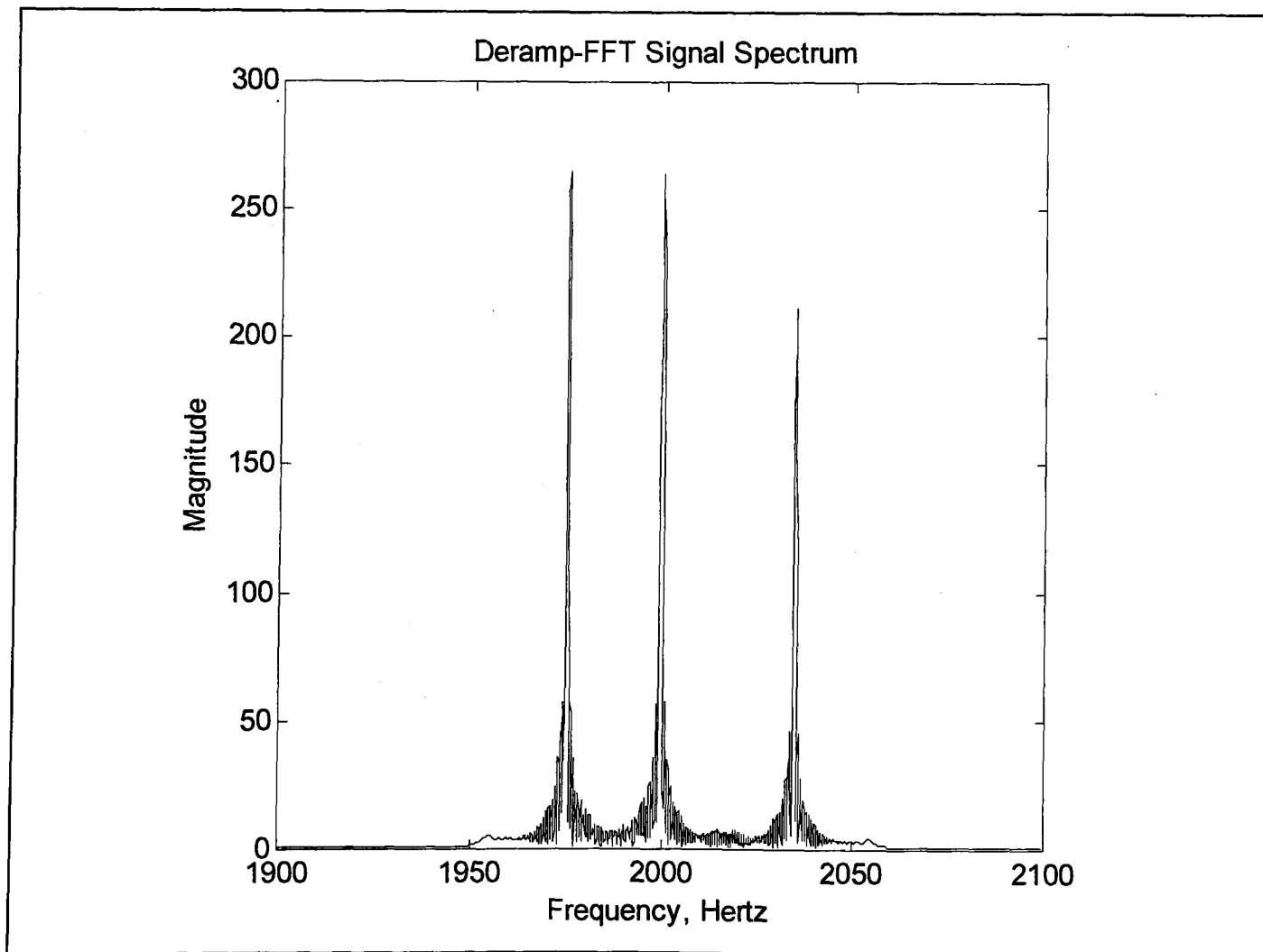
Figure 2.9 Deramp-FFT output of three point targets.

2.3.2 Range Migration Correction and Azimuth Compression

The radar return signal is spread in the azimuth direction as the platform moves past the point targets on the surface. The change in the range due to the movement of the platform causes a phase variation in the received echo signal. High resolution in the azimuth direction can be obtained by processing the coherent phase history of the received signal over the radar illumination or integration time. The range variation to point target can result in a variation in the range delay to the target that is larger than the range sample spacing, resulting in *range migration*. This range migration of the signal energy over several range bins must be corrected before azimuth compression is applied.

There are several algorithms which corrects this range migration along with the azimuth compression. The most accurate and inefficient of these algorithms being a point-by-point, brute force correlation of the recorded data with the appropriate point spread function for the point under consideration. This is known as *exact* reconstruction algorithm. The exact reconstruction algorithm is made more efficient by several approximations. An excellent survey of the existing SAR processing algorithms depending upon the type of approximation is presented in [15]. The paper [14] compares the performance of various algorithm viz. Range Doppler, SPECAN, Chirp Scaling, Polar Format, wavenumber, etc. Two of the most well known algorithms are the *range-Doppler* and the *wavenumber* reconstruction algorithms [16]. The range-Doppler algorithm which is based on *Fresnel approximation* [17], performs this correction very efficiently in the range-time, azimuth-frequency domain. The wavenumber approximation, often termed as *Omega-k* algorithm, achieves the exact reconstruction [13]. In this thesis, we have used the *Omega-k* algorithm which is described in the next section with an example.

2.3.3 Omega-k Processing

The Fourier transform of the returned echo signal, as given in (2.8), with respect to the fast-time t is [11]

$$Ss(\omega,u) = P(\omega)\sum_n \sigma_n \exp\left[-j2k\sqrt{x_n^2 + (y_n - u)^2}\right]$$

(2.14)

where $k = \dfrac{\omega}{c}$ is the wavenumber.

Using the principle of the stationary phase [1], [11], the Fourier transform of (2.14) with respect to the slow-time u is found to be:

$$SS(\omega,k_u) = P(\omega)\sum_n \sigma_n \exp\left(-j\sqrt{4k^2 - k_u^2}\, x_n - jk_u y_n\right)$$
$$= P(\omega)\sum_n \sigma_n \exp\left(-jk_x x_n - jk_y y_n\right)$$

(2.15)

where

$$k_x(\omega,k_u) = \sqrt{4k^2 - k_u^2}$$
$$k_y(\omega,k_u) = k_u$$

(2.16)

The variable ω is the fast-time frequency domain. The variable k_u corresponds to the spatial frequency domain of the synthetic aperture domain u. The spatial frequency variable k_u is also referred to as the slow-time frequency or slow-time Doppler domain.

From (2.15) and (2.7) we have,

$$SS(\omega,k_u) = P(\omega)FF\left(k_x,k_y\right)$$

(2.17)

The fast-time matched filtered *inversion* for the (ω,k_u) domain SAR model is

$$FF\left(k_x,k_y\right) = P^*(\omega)SS\left(\omega,k_u\right)$$

(2.18)

For the target with the scene centre $\left(X_c,Y_c\right)$ the reference function for the inversion is generated for the target at the scene centre i.e.

$$FF\left(k_x, k_y\right) = SS_o^*(\omega, k_u)SS\left(\omega, k_u\right) \qquad (2.19)$$

where

$$SS_0(\omega, k_u) = P(\omega)\exp\left(-j\sqrt{4k^2 - k_u^2}X_c - jk_uY_c\right) \qquad (2.20)$$

The reconstruction based on the above formulation is shown in Figure 2.10.
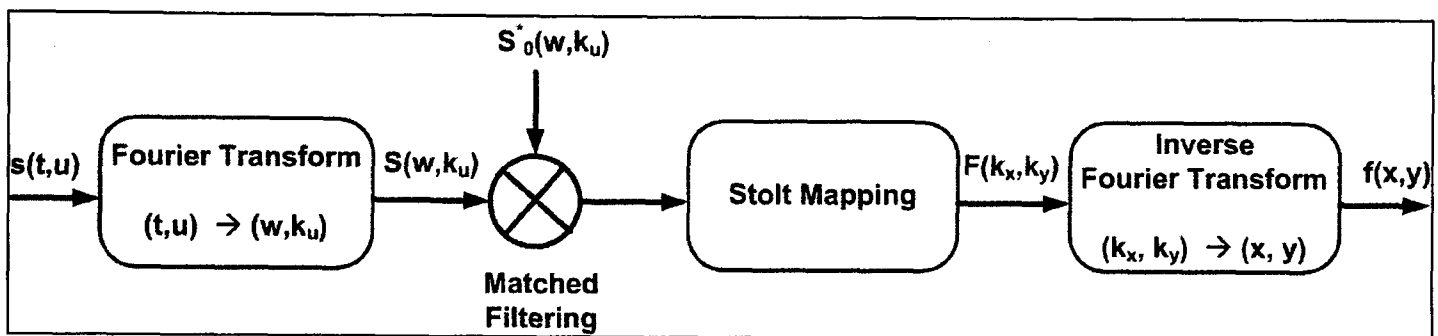
Figure 2.10 Reconstruction of target function through *Omega-k* algorithm.

After the 2D Fourier transform on the received data, the matched filtering with the reference signal is performed. The matched signal output is the Fourier domain response in the polar co-ordinate. The polar format data is converted to the rectangular format through "*Stolt mapping*" as indicated in (2.16). The *Omega-k* algorithm first focuses all the data by using the exact transfer function tuned to the centre$\left(X_c, Y_c\right)$. The Stolt mapping takes care of the space-variance, i.e. eliminates aberration for all points other than the centre point.

2.4 Example of Stripmap SAR Processing

We take the example of reconstruction of the stripmap mode return signal simulated for five targets as shown in Figure 2.6. The matched filtered output of the return signal in the range direction is shown in Figure 2.11. The stripmap SAR reconstruction through *Omega-k* algorithm is shown in Figure 2.12 and the zoomed point targets is shown in Figure 2.13. The point target response due to the *Omega-k* algorithm is shown in Figure 2.14.
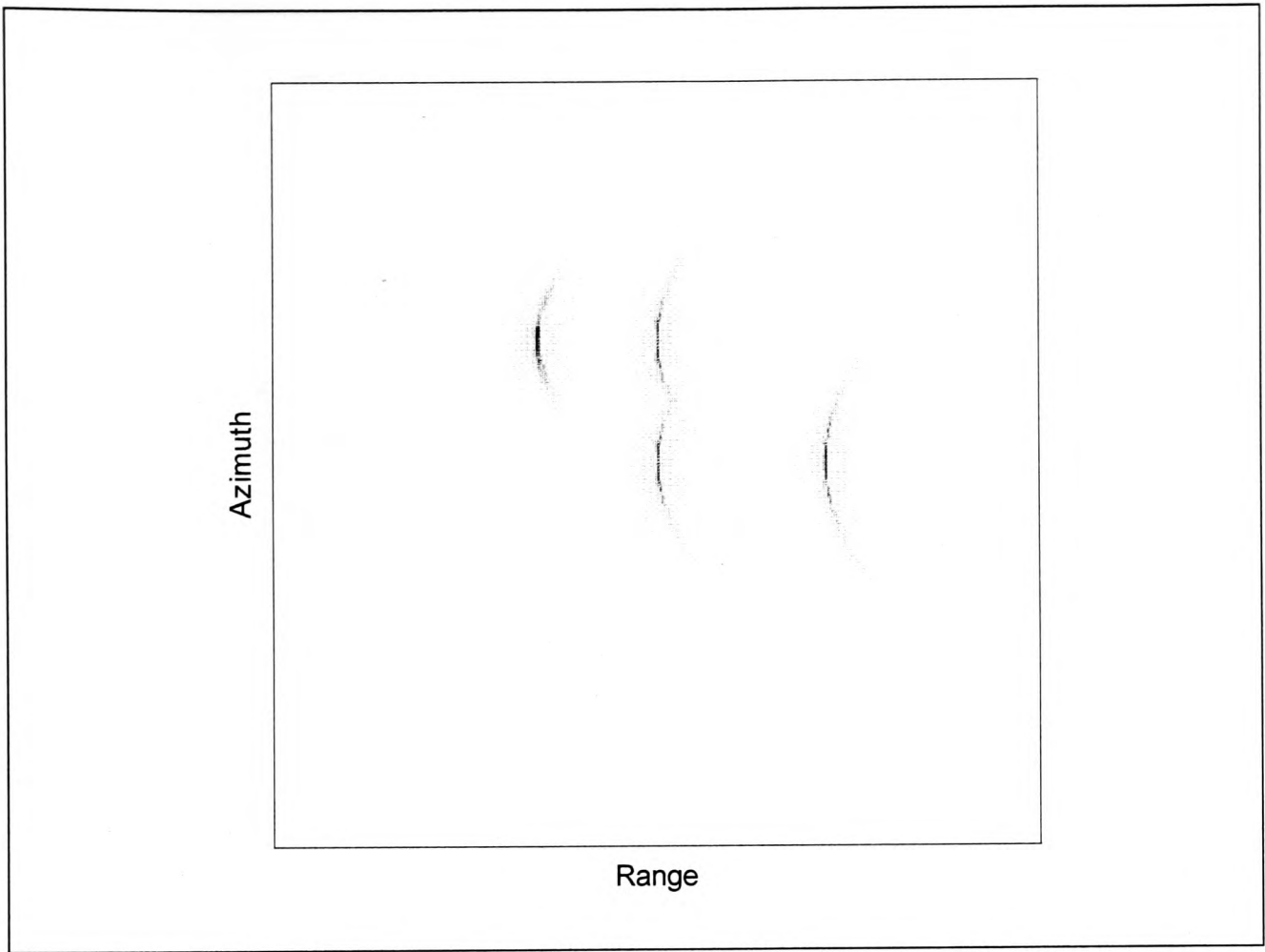
Figure 2.11 Matched filtered output in range direction.
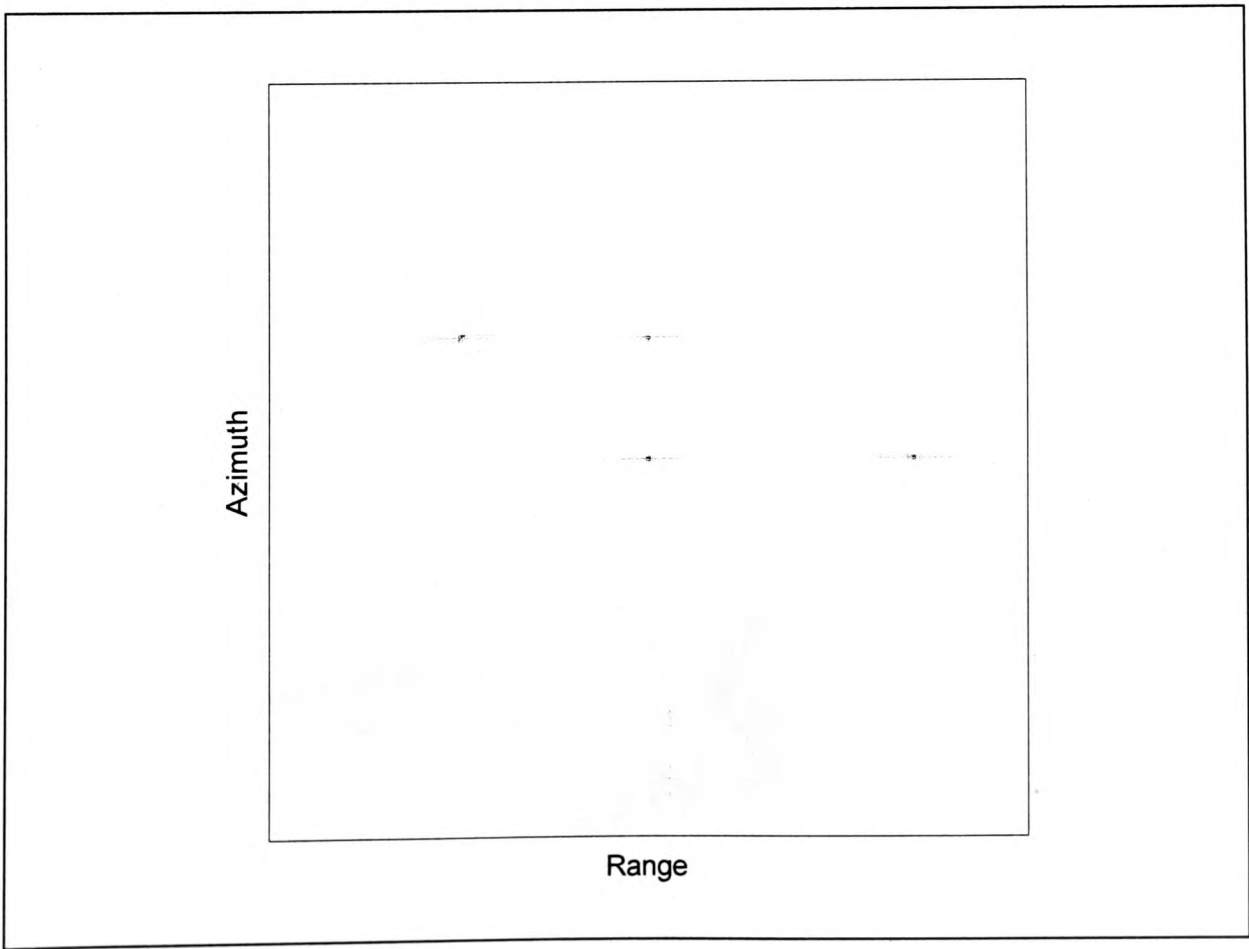
Figure 2.12 Stripmap reconstruction through *Omega-k* algorithm (five targets).

28
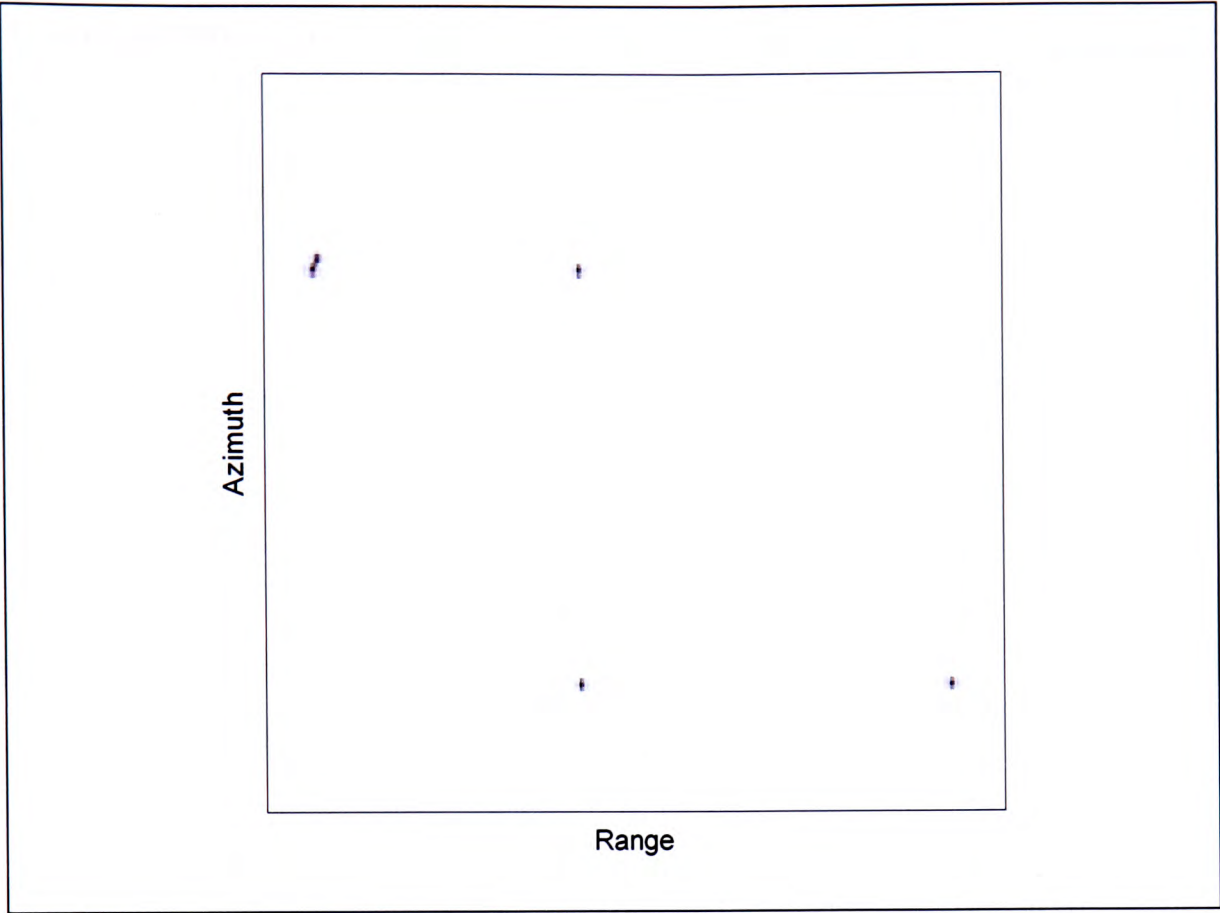
Figure 2.13 Zoomed version of Figure 2.12 showing five point targets.
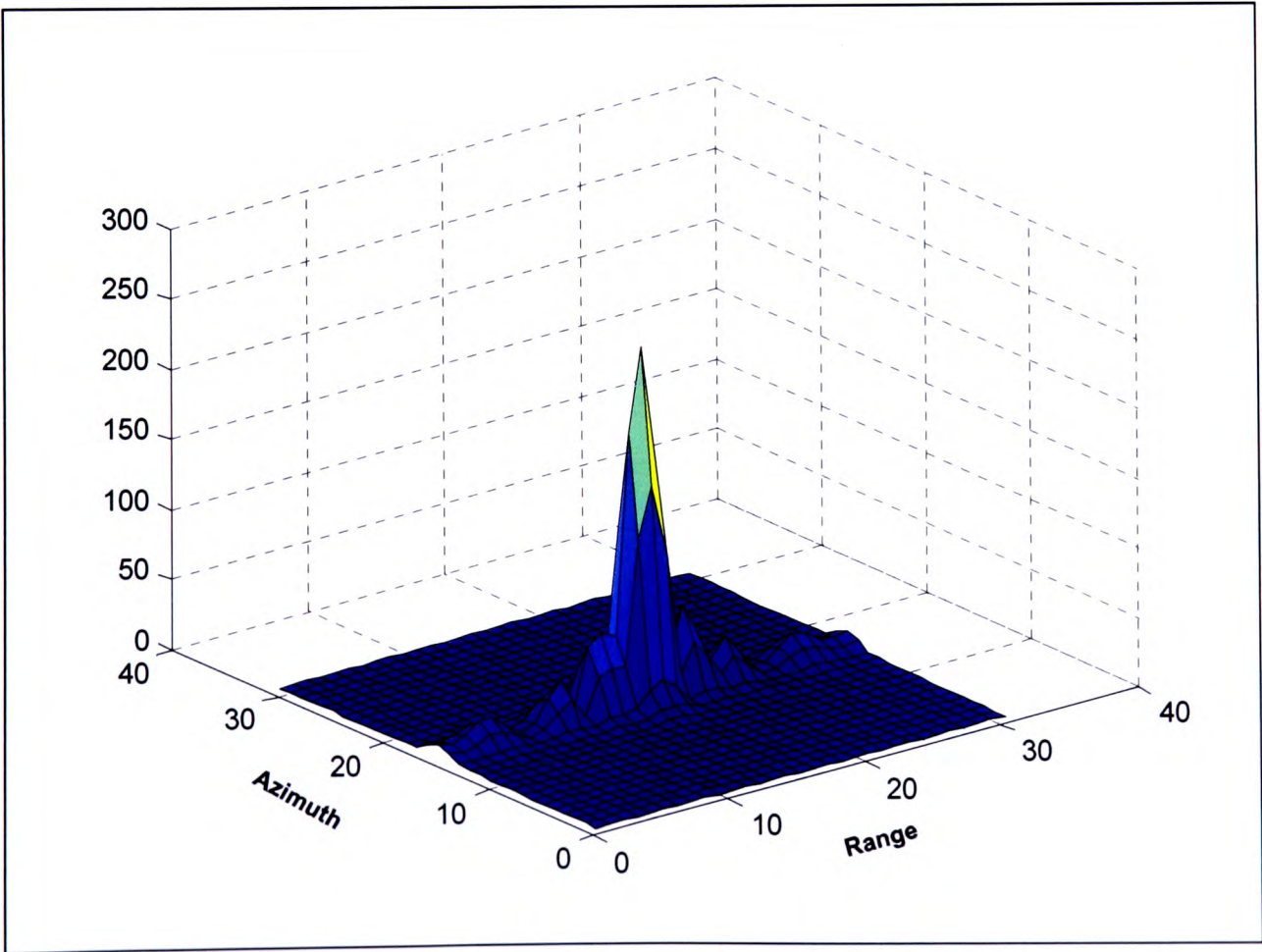
Figure 2.14 Point target impulse response.

2.5 Generation of Test Data

The various methods for generation of the test data as required for the analysis of the imaging algorithm and also to test the performance of the SAR raw data compressing system are:

1. **Point target simulator**: A point target simulator is used to generate the point target response of several scatterers within the footprint of the antenna beam-width through (2.8). The position of the scatterers is uniformly distributed over the desired footprint and their amplitude distribution is Gaussian. The option of having multiple scatterers within a resolution cell to get the effect of the *speckle* noise is also available.

2. **Actual satellite data**: The actual satellite raw SAR data is acquired from various web repositories. These SAR data is obtained from various SAR sensors on various remote sensing satellites taken over several terrains. The point target simulator can also be used along with the satellite data to get additional point targets on the final image.

3. **Inverse SAR processing**: The SAR raw data is generated from the SAR complex image or SAR magnitude image through inverse SAR processing [18]. The block diagram of generating the complex raw data from the complex image through inverse *Omega-k* algorithm is shown in Figure 2.15. In case of SAR magnitude data the phase distribution is assumed to be uniformly distributed with the values between $-\pi$ to π.
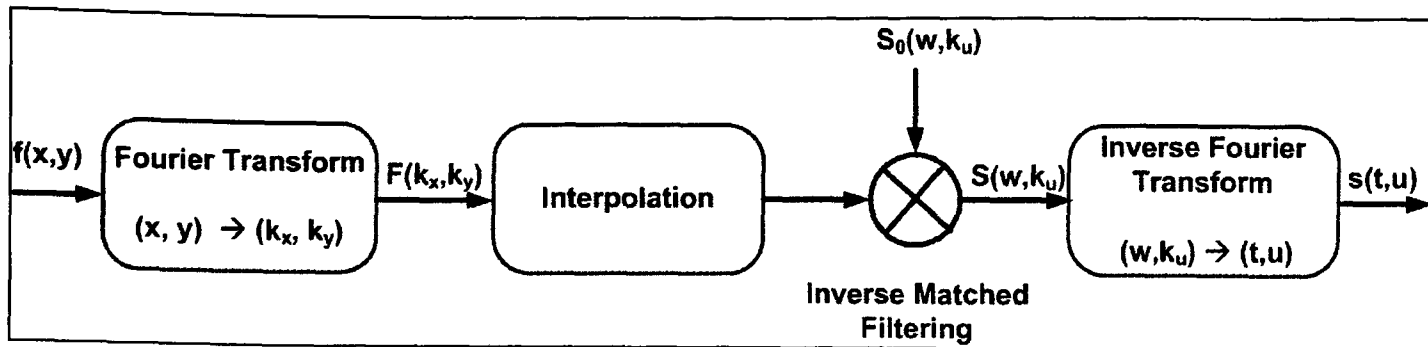
Figure 2.15 Inverse Omega-k algorithm, to generate raw data from complex SAR image.

2.6 Performance Measurement and Metric

The compression accuracy of the proposed algorithm will be measured by a number of qualitative and quantitative parameters. One of the important measures is the ratio of number of bits required to represent the original data to number of bits required to represent the compressed data which is known as *compression ratio*.

The following parameters are used to evaluate the performance of the compression system

1. **Signal-to-Noise Ratio (SNR) :**

$$SNR = 10\log\left[\frac{\sum_{m=0}^{M-1}\sum_{n=0}^{N-1}s_{m,n}^2}{\sum_{m=0}^{M-1}\sum_{n=0}^{N-1}\left(s_{m,n} - u_{m,n}\right)^2}\right]$$

with $s_{m,n}$ = Original Data

$u_{m,n}$ = Reconstructed Data, $M \times N$ = size of the image

2. **Integrated Sidelobe Ratio (ISLR):** The point spread function (PSF) of a point target from the terrain is shown in Figure 2.16 which consists of a narrow, strong peak at the location of the scatterer called mainlobe, surrounded by smaller peaks called sidelobes. The ratio of the power in the sidelobes (shaded region in the Figure 2.16) to the total power is the ISLR.
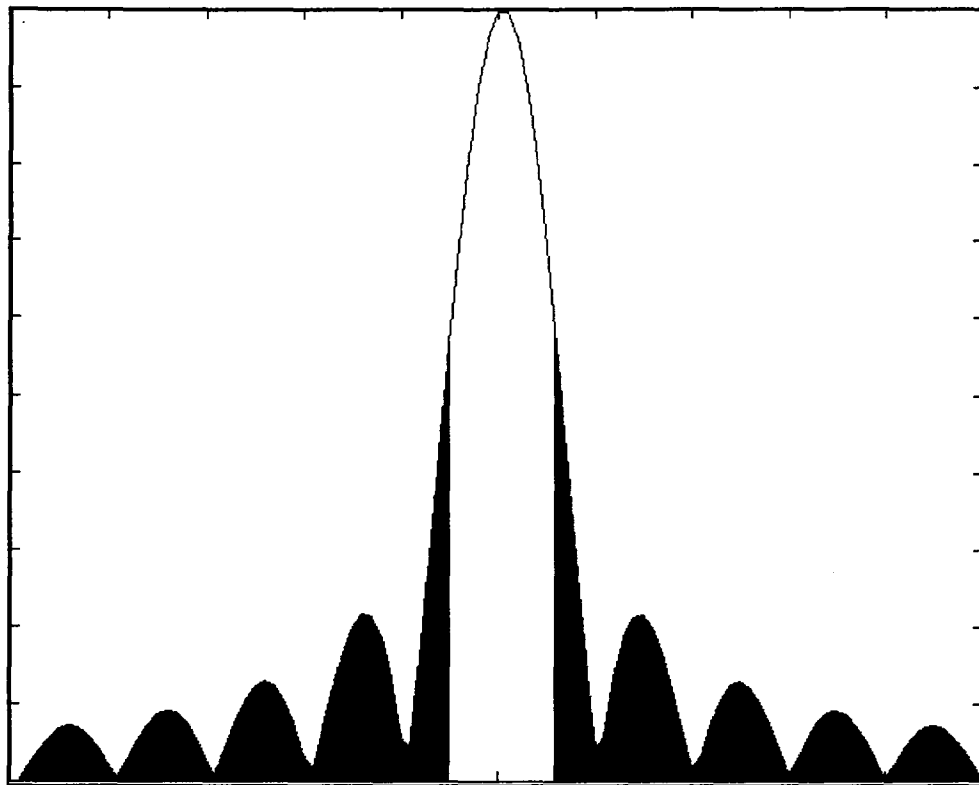
Figure 2.16 Point spread function (PSF) of a point target.

3. **Peak sidelobe ratio (PSLR):** The ratio of the power in the mainlobe (unshaded region of Figure 2.16) to the total power is the PSLR.

4. **Range and Azimuth Resolution:** The measure of the spread of the PSF along the range and azimuth directions gives the range and azimuth resolution respectively.

2.7 Conclusions

In this chapter, we have briefly described the principles of synthetic aperture radar imaging. We have described the *Omega-k* algorithm used to process the SAR data in stripmap-mode of operation, which is the framework used in this thesis for the compression of SAR raw data. The sources and methods to generate SAR raw data are mentioned. The various performances metric to be used to evaluate the performance of the compressed data are also described.

Chapter 3

3. Theory of Compressed Sensing

In this chapter, we describe an emerging technique for sampling signals based on their information content rather than their bandwidth. It is known as compressive or compressed sensing (CS). Modern radar and various other measuring systems generate a huge amount of data and the size of the data generated is rapidly growing. However, the number of salient features required to reconstruct the object is usually much smaller than the size of the measured data. The compressibility of many signals arises due to their sparse representation i.e. fewer non-zero coefficients, in some orthogonal basis or frame. In the field of computational and harmonic analysis sparsity plays a fundamental role in (i) compression based on transform coding, (ii) estimating signals in the presence of noise by the methods of shrinkage and soft thresholding and (iii) reconstruction of signal through the solution of inverse problems.

In traditional data acquisition methods, the data is measured by sampling the signal at the *Nyquist rate* determined by the bandwidth. The sampled data is then compressed before storage and transmission. This results in an inefficient compression system in which the data is first captured at a very high rate followed by massive computation to get sparse representation like Fourier transform or Wavelet transform etc., before retaining fewer coefficients. Moreover, the present acquisition methods have several technological limitations arising due to faster sampling rate, large dynamic range and higher energy consumption.

In compressed sensing (CS) the measurements are acquired at a reduced rate so that no additional compression is necessary. However, the penalty is that more sophisticated recovery procedures become necessary to reconstruct the signal. CS is basically *"sparsity based"* sampling based on the proof that sparse or compressible signals can be

accurately reconstructed from minimally redundant set of randomly sampled data under very general conditions [19, 20].

SAR images have been shown to be compressible in wavelet and complex wavelet basis [5, 21, 22]. This compressibility of SAR images along with the simplicity of the encoder in the CS framework form the basis of investigating the performance of the SAR raw data compression in this framework. In this chapter, we describe the CS framework including the measurement schemes and conditions by which compressible signals can be compressively sampled and reconstructed.

3.1 Transform Based Compression

The block diagram of the traditional compression paradigm based on transform coding is shown in Figure 3.1.
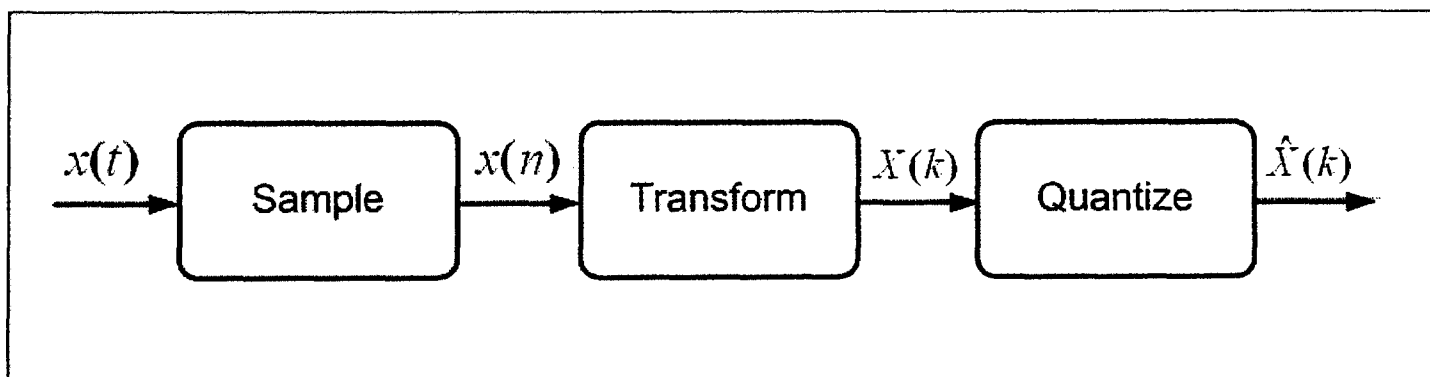
Figure 3.1 Block diagram of transform base compression.

The steps involved in traditional transform based compression are:

Sampling: In traditional signal acquisition system, any signal $x(t)$ is modeled as bandlimited signal. The sampling for such signal are then based on the *Shannon* sampling theorem which states that in order to reconstruct a bandlimited signal, it must be sampled at a rate $f_s \geq 2f_{max}$, where f_s is the sampling rate and f_{max} is the maximum

frequency content of the signal $x(t)$. The sampling rate at twice the maximum frequency present in a lowpass signal is usually called the *Nyquist* rate. The sampling in this case is uniform and the reconstruction of original signal, $x(t)$, from the sampled signal, $x(n)$, is then achieved by linear $\sin(x)/x$ interpolation. The data is usually acquired for a fixed interval of time, resulting in N samples of $x(n)$.

Transform: The next step is to apply a suitable transform to the sampled data for compaction of energy i.e. to have significant energies in fewer coefficients. In many natural and man made signals such as audio, video, image, geophysical data, SAR images, etc. it is observed that there exists a transform where the coefficients $X(k)$ with significant energies are fewer. It is to be noted that one obtains exactly N coefficients of $X(k)$ for '*critically-sampled*' transforms and possibly more for redundant transforms when using frames.

Sparse signals are those signals whose transformed non-zero coefficients are fewer and much less in number than the original size of the signal. Mathematically, a signal is R-sparse if only R coefficients of $X(k)$ are non-zero, with $R \ll N$. Whereas, for compressible signals we have just a few large coefficients and many small coefficients. Compressible signals are well approximated by R- sparse representation. The example for the most commonly used transform in case of JPEG 2000 is wavelet transform whereas JPEG uses local DCT to compress signals.

Quantization: The next step is to apply a quantization process to the transform coefficients $X(k)$, such that we are left with a sparse representation consisting of approximations to only R of the coefficients. The compression is thus obtained by retaining R-sparse coefficients (both value and its location) out of the N sampled signal. The Figure 3.2(a), shows an example of a synthetic data, *Cusp,* of size $N = 1024$, which has a sparse representation in the *Daubechies-8* wavelet domain [23] as shown in

Figure 3.2(b). The decay of the ordered wavelet coefficients is shown in Figure 3.2(c), where the black vertical solid line represents the maximum number of wavelet coefficients retained for reconstruction. The reconstruction of the signal with only $R = 171$ significant wavelet coefficients (i.e. those coefficients with values greater than 10^{-6}) is shown in Figure 3.2(d) with the SNR of the reconstructed signal as 132.86 dB.

The major drawback for the classical transform based coding is that we have to acquire N samples when only $R \ll N$ coefficients are retained. The encoder first computes N coefficients and then only the locations and the values of R largest coefficients are encoded. The only major advantage of this method is that the reconstruction of the signal is linear and consists of performing inverse transformation on these R-encoded coefficients.

A natural question which arises by observing the inefficiency of sampling at higher rate and then compressing is that why to acquire data at such high rates and then discard most of it. Is there a possibility of compression of the data right at the acquisition stage? The answer to this is the new technique of sampling as given by compressed sensing (CS) in which the sampling is related to the information rather than the bandwidth of the signal. It improves the conventional compression method by providing mathematical tools that when coupled with specific acquisition methods reduces the acquired dataset sizes, without reducing the resolution or quality of the compressed signal.
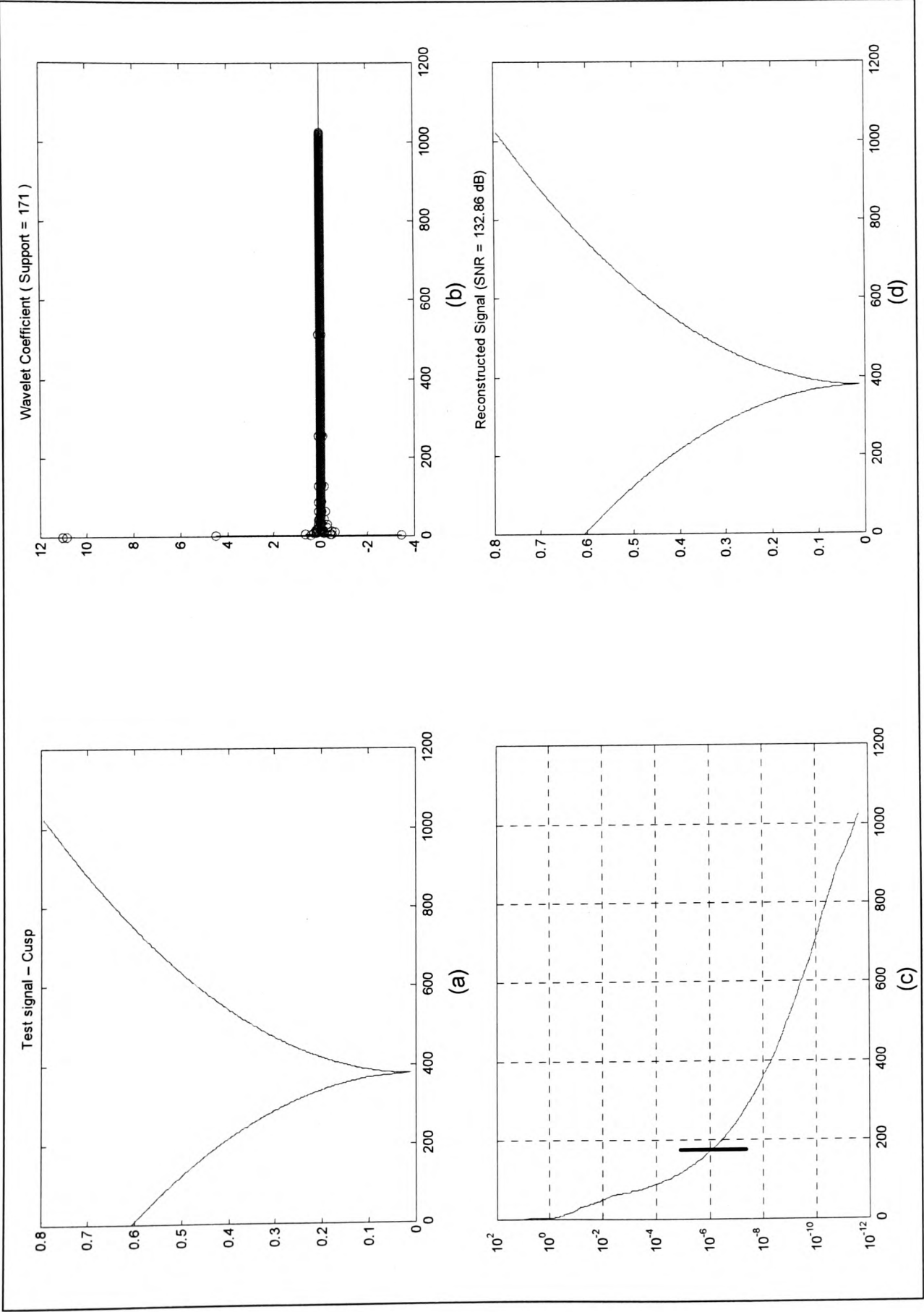
Figure 3.2 (a) Test signal – *Cusp*, (b) *Daubechies*-8 wavelet coefficients, (c) the log plot of ordered wavelet coefficients, (d) reconstructed signal with 171 wavelet coefficients.

3.2 Compressed Sensing Formulation

It is shown in [19], that a signal which is sparse in time/ spatial domain can be reconstructed from incomplete frequency samples by solving a convex optimisation problem. The size of data depends upon the sparsity of the signal and is much less that what is required by the Shannon sampling theorem. Also, it is shown in [20] that a signal which is sparse in frequency domain can be acquired by random sampling in the time domain. These initial papers laid a foundation to the compressed sensing framework where it was demonstrated that it is indeed possible to reconstruct sparse signals encoded by a small number of random linear projections. Since then, there has been widespread applications of CS in imaging [24, 25], bio-sensing [26], radar [27], astronomy [28], rapid MR imaging [29], missing data recovery [30] etc.

The new model for signals adapted in CS is based on sparse approximation and, what is termed, the incoherence of the measurement modality. Hence, we describe the sparse approximation theory background and incoherence before describing the compressed sensing framework.

3.2.1 Sparse Approximation Theory

We describe here the discrete version of the CS in which the signal is represented as a vector $x \in \mathbb{R}^N$ with N typically very large. Let $\left\{w_i \in \mathbb{R}^N\right\}_{i=1}^{N}$ form an orthogonal basis for $\mathbb{R}^N$ with $w_i \perp w_j$. In such as case, $\mathbf{W} = \left\{w_1, \ldots, w_N\right\} \in \mathbb{R}^{N \times N}$ denotes a dictionary consisting of N real valued vectors w_i, with $\mathbf{WW}^T = \mathbf{I}$ where $\mathbf{W}^T$ is the transpose of $\mathbf{W}$.

The signal $x \in \mathbb{R}^N$ is transformed by this dictionary, W, into a vectors of coefficients z, formed by inner products between x and vectors from W. Mathematically, by the orthonormality of W, we have $x = \sum_{i=1}^{N} w_i z_i = Wz$ with $z_i = \langle x_i, w_i \rangle$.

Let x^k be the representation of x with k coefficients under W. The error of representation x^k is then defined as a sum squared difference between x^k and x i.e. $\|x^k - x\|^2$. The optimal k representation of x under W is to take the k coefficients with the largest $|w_i|$'s and is denoted as x_{opt}^k. Thus, the error in representing the signal x in the compressed form using k coefficients from W is then given by $\|x_{opt}^k - x\|^2 = \sum_{i=k+1}^{N} w_i^2$. The various models for the signals which are well represented by k terms are

1. *k-support* : In this case, signals have most of the coefficients exactly zero i.e. k non-zero coefficients under W, where $k \ll N$. Hence, the error is $\|x_{opt}^k - x\|^2 = 0$.

2. *p-compressible*: In this case, the coefficients of the signal when sorted by magnitude have a power-law like decay i.e. $|w_i| = O(i^{-1/p})$, for some $p \in (0,1)$ and for all i. In such cases, the error $\|x_{opt}^k - x\|^2 \leq C_p k^{1-2/p}$ for some constant C_p.

3. *α-exponentially decaying:* In this case, the coefficients decay faster than any polynomial. That is, for some α and all i, $|w_i| = O(2^{-\alpha i})$.

4. *General* : For all other cases, where x is arbitrary, there is no assumptions on the error $\|x_{opt}^k - x\|^2$.

The *k-support* signals, where most of the coefficients are required to be exactly zero, are modeled as *strong sparsity*. Whereas, the *p-compressible* and *α-exponentially*

decaying signals, where most of the coefficients are very small but need not be exactly zero, are modeled as *weak sparsity*. For real data, it is rare for transform coefficients to be exactly zero; hence in most practical cases *weak sparsity* is the better model. However, the theory of CS is better explained with *strong sparsity* model and then extended for the *weak sparsity* model.

3.2.2 Incoherence

The incoherence is an extension of duality of the time and frequency, which states that a signal compact in time domain is spread out in the frequency domain and vice versa. This idea is carried over for the CS sampling which implies that the objects having a sparse representation in **W** are to be captured through sampling waveforms which have an extremely dense representation in **W**.

Mathematically, suppose we have pair (Φ, Ψ) of orthonormal bases of $\mathbb{R}^N$. The coherence between these two bases is then defined as

$$\mu(\Phi, \Psi) = \sqrt{N} \max_{1 \le k, j \le N} \left| \left\langle \varphi_k, \psi_j \right\rangle \right| \tag{3.1}$$

The coherence measures the largest correlation between any two elements of Φ and Ψ i.e. how the two bases look alike. The coherence is large when Φ and Ψ contain correlated elements. Otherwise, it is small. If the two bases are normalized, then the mutual incoherence always obeys $\sqrt{N} \le \mu(\Phi, \Psi) \le 1$ [31]. For example, if Φ is the canonical or spike basis and Ψ is the Fourier basis, then this time-frequency pair obeys $\mu(\Phi, \Psi) = 1$, showing that they have *maximal incoherence*.

The next section describes the compressed sensing framework where the sparse/ compressible signal is measured by simply correlating with a small number of fixed waveforms that are *incoherent* with the sparsifying basis and also *non-adaptive* to the

input signal. It also describes the numerical optimization techniques to reconstruct the full-length signal from the small amount of collected data.

3.3 Compressed Sensing Framework

Before discussing the framework, we need to generalize the notion of sampling a signal. In most practical cases, the information about a signal $x(t)$ is obtained by linear functionals recording the values

$$y_k = \langle x, \varphi_k \rangle, \quad k = 1, 2, ..., M \tag{3.2}$$

This means, we simply calculate the inner product of the object we wish to acquire with the sensing waveform $\varphi_k(t)$.

The choice of the sensing waveform $\varphi_k(t)$ allows us to choose in which domain the information about the signal is gathered. For examples, (i) if the sensing waveform are indicator functions of pixels, then y is the image data typically collected from standard digital cameras, (ii) if the sensing waveform are sinusoidal at different frequencies, we are collecting Fourier coefficients as in the case of magnetic resonance imaging (MRI) and (iii) if the sensing waveform are delta ridges, we are observing line integrals as in the case of tomography. Since the measurements y_k are in some sense coded versions of the original object rather than direct observations, we often refer to such system as *coded signal acquisition system*. In such system, the best way to minimize the number of measurements M to reconstruct $x(t)$ faithfully is to match the sensing waveform to the structure of signal. That is, we try to make the measurements in the same domain in which the signal is sparse by keeping only M significant coefficients as measurement. As these M significant coefficients are different for different input signal, we cannot have a fixed sensing waveform. Surprisingly, the theory of CS suggests that it is indeed possible to take fewer measurements with the sensing functions which are incoherent with the sparsifying functions. In other words, the sensing function should be completely

unstructured and look more like random noise than any feature we would expect to see in the object.

Although the CS theory is developed for the continuous time/ space signals, we restrict our discussion to finite dimensional discrete signal $\mathbf{x} \in \mathbb{R}^N$, where N is the dimension of signal $\mathbf{x}$. Let $\mathbf{A}$ denote the $M \times N$ sensing matrix with the vectors $\varphi_1^*, \varphi_2^*, \ldots, \varphi_M^*$ as rows, where a^* is the complex transpose of a. The measurements are then expressed as $\mathbf{y} = \mathbf{A}\mathbf{x}$, where $\mathbf{y} \in \mathbb{R}^M$. The sparse representation of the input signal $\mathbf{x} \in \mathbb{R}^N$ is obtained by expanding in an orthonormal basis (such as wavelet basis) $\mathbf{W} = \{w_1, w_2, \ldots, w_N\}$ as follows:

$$\mathbf{x} = \sum_{i=1}^{N} z_i w_i \tag{3.3}$$

where $\mathbf{z}$ is the coefficient sequence of $\mathbf{x}$, $z_i = \langle \mathbf{x}, w_i \rangle$. It is convenient to express $\mathbf{x}$ as $\mathbf{x} = \mathbf{W}\mathbf{z}$, where $\mathbf{W} \in \mathbb{R}^{N \times N}$ with $w_1, \ldots, w_N$ as columns. When the input signal $\mathbf{x}$ is R-sparse under the sparsifying transform $\mathbf{W}$, we have $\|\mathbf{z}\|_0 \leq R \ll N$. Such signals are known as R-*sparse* signal w.r.t. the dictionary $\mathbf{W}$. Note that the l^0-norm, $\|\mathbf{z}\|_0 = \#\{i : z_i \neq 0\}$, simply counts the number of non-zeros in $\mathbf{z}$. The set of positions of non-zeros coefficients in $\mathbf{z}$ is called the *sparsity pattern* and we define the *sparsity ratio* as $\alpha = R/N$.

The CS framework consisting of the encoder, decoder and the sparsifying process is shown in Figure 3.3 and described below.
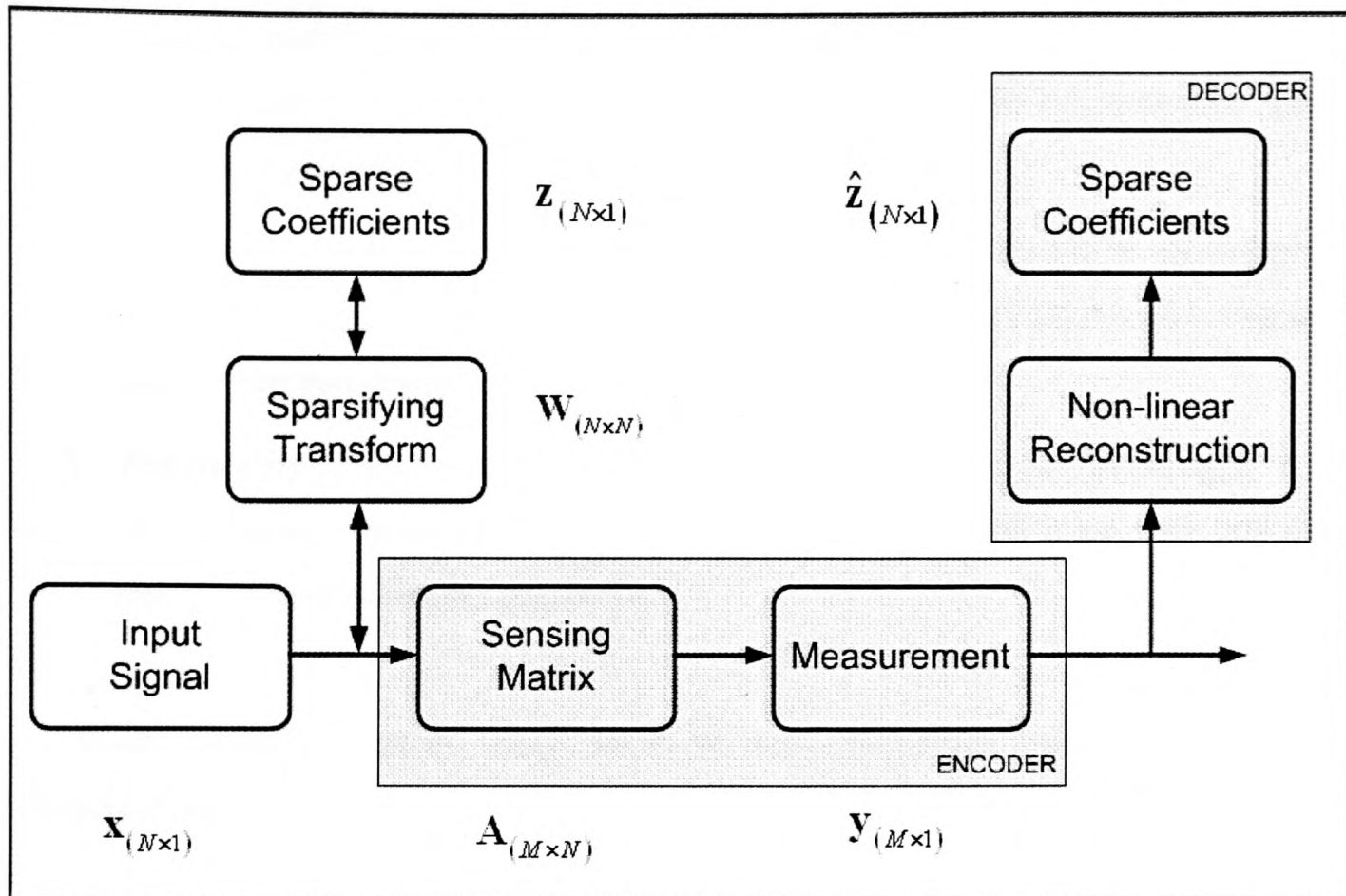
Figure 3.3 The compressed sensing framework – showing the encoder, decoder and the sparsifying process.

3.3.1 Encoder

The encoding process consists of obtaining M measurement $\mathbf{y}$ from linear projection onto a sensing matrix $\mathbf{A}$. The sensing and sparsifying matrices must be incoherent and also the sensing matrix should be non-adaptive to the input signal. A key assumption in the theory of CS is that the sampling process determined by matrix $\mathbf{A}$ and the sparsity transform $\mathbf{W}$ are incoherent. This means that if a signal has a sparse representation in one, then it must have a dense representation in the other and vice versa; but a signal cannot have a sparse representation in both. This also implies that the vectors w_i cannot sparsely represent the vectors φ_i and vice versa. The desirable properties of the sensing operator include:

1. **Optimal performance**: This dictates the requirement of minimum number of compressed measurement to get an acceptable SNR of the reconstructed signal depending upon the application.

2. **Universality**: This implies that the measurement operator should be non-adaptive to the input signal i.e. independent of the input signal and incoherent to various sparsifying transforms.

3. **Practicality**: This means that the sensing operator should be fast enough to be implemented in practice, easy to implement in hardware and sometimes desirable that it possess streaming capabilities.

Various sensing matrices, which satisfy the above properties, have been reported in CS related papers [32-34]. The major types of sensing matrices are:

1. *Uniform spherical ensemble.* The columns of $\mathbf{A}$ are independent and identically distributed (i.i.d.) random uniform on the sphere $\mathbf{S}^{N-1}$. Generate normalised entry from $\mathcal{N}(0,1)$. Then with high probability, the coherence between $\mathbf{A}$ and most of $\mathbf{W}$ is about $\sqrt{2\log N}$.

2. *Random signs ensemble*: Independently select each entry of $\mathbf{A}$ to be $\pm 1/\sqrt{N}$ with equal probability (Bernoulli, normalized). These are also largely incoherent with any fixed basis $\mathbf{W}$.

3. *Partial Fourier ensemble*: Select at random M rows out of $N \times N$ Fourier matrix, getting $M \times N$ partial Fourier matrix. The spikes and sinusoids are not only maximally incoherent in one dimension but in any dimension.

4. *Partial Hadamard ensemble*: Select at random M rows out of $N \times N$ Hadamard matrix, getting $M \times N$ partial Hadamard matrix.

5. *Noiselets*: Defined in [35] it comes with very fast algorithms and takes $O(N)$ time to run. Moreover, the noiselets matrix does not need to be stored to be ap-

plied to a vector. They are maximally incoherent with spikes and incoherent with the Fourier basis.

One of the important problems in encoding the signal is the designing of a stable sensing matrix $\mathbf{A}$ such that the salient features in any R-sparse or compressible signal is not damaged by dimensionality reduction from $\mathbf{x} \in \mathbb{R}^N$ to $\mathbf{y} \in \mathbb{R}^M$. The construction of the sensing/ measurement matrix has been studied in [36], which suggests that the linear projections that mix the signal can be designed such that the average *mutual coherence* of the effective dictionary becomes favourable. For a dictionary $\mathbf{A}$, its *mutual coherence* is defined as the maximum of the off-diagonal elements of the normalized inner products between different columns in $\mathbf{A}$ (when columns of $\mathbf{A}$ are normalized to l_2-norm). Put formally,

$$\mu_\mathbf{A} = \max_{1 \le k, j \le N; k \ne j} \left| \left\langle \varphi_k, \varphi_j \right\rangle \right| \tag{3.4}$$

It has been shown in [20, 37] that $\hat{\mathbf{x}}$ can be recovered from the observation $\mathbf{y} = \mathbf{Ax}$ by solving the linear program $\hat{\mathbf{x}} = \arg\min \|\mathbf{x}\|_1$, if $\|\hat{\mathbf{x}}\|_0 < \frac{1}{2}\left(1 + \frac{1}{\mu_\mathbf{A}}\right)$ with $\mu_\mathbf{A} > 0$.

3.3.2 Decoder

The acquisition of the input signal $\mathbf{x}$ is represented as a linear transformation by the sensing matrix $\mathbf{A}$ yielding a measurement sample vector $\mathbf{y} = \mathbf{Ax}$. When the input signal $\mathbf{x}$ is R- sparse with respect to the sparsifying basis $\mathbf{W}$, we can write the measurement vector in terms of its sparse coefficients $\mathbf{z}$ as

$$\begin{aligned} \mathbf{y} &= \mathbf{Ax} \\ &= \mathbf{AWz} = \mathbf{Kz} \end{aligned} \tag{3.5}$$

where $\mathbf{K} = \mathbf{AW}$ is a *holographic* basis.

A decoder must recover $x \in \mathbb{R}^N$ from the measurement samples $y \in \mathbb{R}^M$ knowing A and W, but not necessarily the *sparsity pattern* of the unknown signal z. When the no. of measurements M is equal to size of the input signal N, decoding simply entails solving a linear system of equations i.e. $\hat{x} = A^{-1}y$. When $M < N$, the linear system $y = Ax$ is under-determined and permits infinitely many solutions. This is because if $Ax = y$ then $A(x + s) = y$ for any vector s in the null-space $\mathcal{N}(A)$ of A. In the absence of any other information, no solution to (3.5) is to be preferred over any other. If we know that the measurement y is from a highly sparse signal with very few non-zero coefficients, then a reasonably decoding model is to look for the sparest signal among all those that produce the measurement y.

Since, z is R- sparse, it must belong to one of the $\binom{N}{R}$ subspaces of $\mathbb{R}^N$. For all

As with $M \geq R + 1$, the recovery of the signal's sparsity pattern and values is possible by an exhaustive search through the subspaces to determine which subspace x belongs to. This exhaustive search is unfortunately not tractable for reasonable sizes of problems since the number of spaces to search $\binom{N}{R}$, can be enormous. Mathematically, searching for the sparsest set of coefficients $\hat{z}$ in the basis K that matches the sensed values y, as given in (3.5), leads to the following l_0-optimization problem

$$\hat{z} = \arg\min_z \|z\|_0 \text{ subject to } y = Kz \tag{3.6}$$

The objective function enforces the sparsity whereas the constraint enforces data consistency.

As stated previously that the problem of recovery of $z \in \mathbb{R}^N$ from the measurement samples $y \in \mathbb{R}^M$, where $M < N$, is ill-posed without the sparseness assumption. With

sparseness assumption, the l_0-optimization problem is well-posed but computationally intractable. Although, the l_2-optimization problem for such under-determined system of equations

$$\hat{\mathbf{z}} = \arg\min_{\mathbf{z}} \|\mathbf{z}\|_2 \quad \text{subject to } \mathbf{y} = \mathbf{Kz} \tag{3.7}$$

has a convenient closed form solution $\hat{\mathbf{z}} = \mathbf{K}^T \left(\mathbf{KK}^T \right)^{-1} \mathbf{y}$, but never finds a R-sparse solution, returning instead a non-sparse $\hat{\mathbf{z}}$ with many non-zero elements.

The two most common approaches to solve the sparse l_0 approximation problem are convex relaxation methods and greedy methods. The convex relaxation replaces the combinatorial sparse l_0 approximation problems with a related convex program l_1 -- known as *basis pursuit* (BP) [38] and it can be solved using linear programming techniques whose computational complexities are polynomial in N [39]. Most of the existing work on CS [19, 20] has concentrated on optimization based on l_1 minimisation which is recast either as linear program (LP) or as a second order cone program (SOCPs) and can be attacked with variety of methods, such as the classical simplex method or more recent interior point methods that yield polynomial time algorithms. The l_1 approach seeks a sparse coefficient $\hat{\mathbf{x}}$ by solving the linear program [38]:

$$\hat{\mathbf{z}} = \arg\min_{\mathbf{z}} \|\mathbf{z}\|_1 \quad \text{subject to } \mathbf{y} = \mathbf{Kz} \tag{3.8}$$

where $\|\mathbf{z}\|_1 = \sum_N |z_i|$.

Greedy reconstruction algorithms, on the other hand, build a sparse approximation iteratively by selecting the basis most strongly correlated with the residual part of the signal and use it to update the current approximation. The two most prevalent greedy techniques are the matching pursuit (MP) and orthogonal matching pursuit (OMP) [40, 41]. These techniques are adapted in CS framework in [20, 32, 42].

Before describing the robustness of the recovery of undersampled signal and the details of the reconstruction algorithms, we present a geometric intuition for why l_1 is better than l_2 for finding the sparse solution to (3.5) in Figure 3.4. Part (a) shows the l_1 ball in $\mathbb{R}^2$ of certain radius r, which contains all $\mathbf{x} \in \mathbb{R}^2$ such that $|x_1| + |x_2| \leq r$. It is to be noted that the l_1 ball is anisotropic i.e. it is "pointy" along the axes whereas the standard Euclidean l_2 ball, which is spherical and thus completely isotropic. Part (b) shows the recovery obtained through l_1-optimization (3.8), which correctly finds the sparse solution $\hat{\mathbf{x}}_{l_1}$. The action of (3.8), for finding the sparse solution, can be imagined as increasing the radius of a small l_1-ball gradually until it bumps into space $\mathbf{H} = \{\mathbf{x} : \mathbf{A}\mathbf{x} = \mathbf{y}\}$. The first intersection point is the sparse solution, $\hat{\mathbf{x}}_{l_1}$, and is unique due to anisotropy of the l_1-ball and the flatness of the space $\mathbf{H}$. Part (c) shows the intersection of the l_2-ball, which is spherical and perfect isotropic, with $\mathbf{H}$. The point of first intersection point, $\hat{\mathbf{x}}_{l_2}$, of $\mathbf{H}$ and the expanding l_2-ball does not have to be sparse at all.
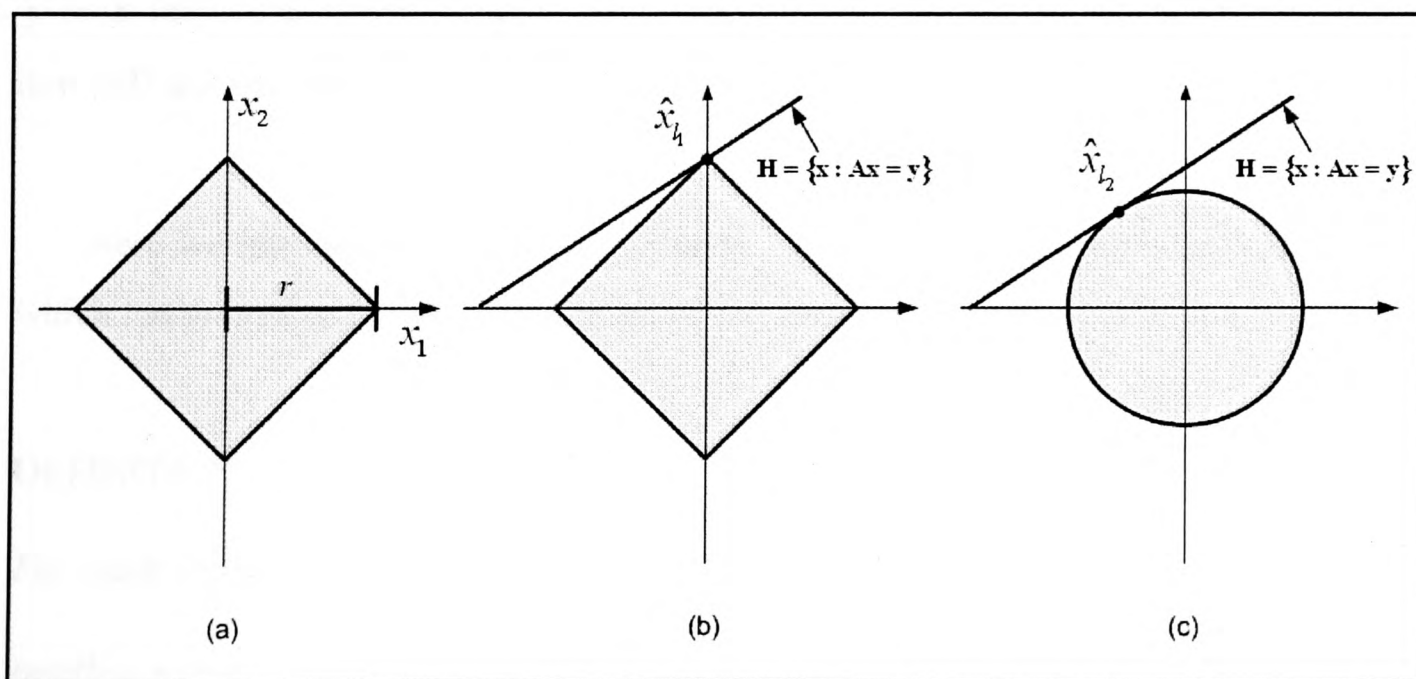
Figure 3.4 Geometry of l_1 recovery. (a) l_1 ball of radius r, containing all $\mathbf{x} \in \mathbb{R}^2$ such that $|x_1| + |x_2| \leq r$, (b) recovery of sparse solution $\hat{\mathbf{x}}_{l_1}$ through l_1-optimization (3.8), (c) minimizing the l_2 norm of x through (3.7) gives $\hat{\mathbf{x}}_{l_2}$, which in general will not be sparse at all.

3.4 Robust Signal Recovery

It is imperative that the CS framework should be able to deal with both nearly sparse signal i.e. compressible signal and also noise. As mentioned earlier, most of the practical signals are not exactly sparse but approximately sparse. We will see later in this section that it is possible to obtain accurate reconstruction of such compressible signals from highly undersampled measurements. Also, in any practical application measured data is invariably corrupted with noise. The CS framework is shown to work for such cases as well, where small perturbations in data cause small perturbations in the reconstruction.

This section deals with the recovery the compressible signals $z \in \mathbb{R}^N$ from the measurement data $y \in \mathbb{R}^M$ corrupted with noise e i.e.

$$y = Kz + e \tag{3.9}$$

where $K \in \mathbb{R}^{M \times N}$ is the holographic matrix. Adaptations to deal with additive noise in y or z include basis pursuit with denoising (BPDN) [38], complexity-based regularization [33] and the Dantzig selector [43].

Here we introduce an important property called *restricted isometry property* (RIP) which has proved to be very useful to study the general robustness of CS [44, 45]

DEFINITION 1.

For each integer $R = 1, 2, ...$, define the isometry constant δ_R of a matrix K as the smallest number such that

$$\left(1 - \delta_R\right)\|z\|^2 \le \|Kz\|^2 \le \left(1 + \delta_R\right)\|z\|^2 \tag{3.10}$$

holds for all R-sparse vectors z.

A matrix $\mathbf{K}$ is said to have RIP of order R if δ_R is not too close to one. When $\delta_R < 1$, these inequalities imply that each collection of R columns from $\mathbf{K}$ is non-singular, which is the minimum requirement for acquiring $R/2$-sparse signals. The RIP property ensures that the matrix $\mathbf{K}$ approximately preserves the Euclidean length of R-sparse signals, which means that R-sparse vectors cannot be in the null space of $\mathbf{K}$. The RIP ensures that the matrix $\mathbf{K}$ does not map any non-zero R-sparse signal $\mathbf{z}$ to zero measurement data i.e. $\mathbf{y} = \mathbf{Kz} = 0$ and also does not map two distinct R-sparse signals say $\mathbf{z}$ and $\mathbf{z}'$ to the same compressed data i.e. $\mathbf{y} = \mathbf{Kz} = \mathbf{Kz}'$. The RIP is so named because it describes matrices that impose a near-isometry i.e. approximate length preservation on a restricted set of subspace i.e. the subspace of R-sparse vectors. The RIP is sometimes also referred to as uniform uncertainty principles (UUP) [32, 44].

The general signal recovery for the noiseless case from undersampled data is then based on the following theorems.

THEOREM 1 (Noiseless recovery) [37]

Assume that $\delta_{2R} < \sqrt{2} - 1$. Then the solution $\hat{\mathbf{z}}$ to (3.8) obeys

$$\begin{aligned}
\|\hat{\mathbf{z}} - \mathbf{z}\|_2 &\leq C_0 \|\mathbf{z} - \mathbf{z}_R\|_1 / \sqrt{R} \quad \text{and} \\
\|\hat{\mathbf{z}} - \mathbf{z}\|_1 &\leq C_0 \|\hat{\mathbf{z}} - \mathbf{z}_R\|_1
\end{aligned} \tag{3.11}$$

for some constant C_0, where $\mathbf{z}_R$ is the vector $\mathbf{z}$ with all but the largest R components set to 0.

The above theorem shows that if the solution to (3.8) contains a R-sparse vector, and if $\mathbf{K}$ has RIP of order $2R$ with $\delta_{2R} < \sqrt{2} - 1$, then that R-sparse vector is unique

51

and is the unique l_1 minimizer of (3.8) i.e. the convex relaxation is exact. In general when $\delta_{2R} \ll 1$ the sampling operator very nearly maintains the l_2 distance between each pair of R- sparse signals. In consequence, it is possible to invert the sampling process stably.

The above theorem is extended for the noisy measurement case as given by (3.9). One of the reconstruction algorithms for this case is the l_1 minimization with relaxed constraints

$$\hat{z} = \arg\min_z \|z\|_1 \text{ subject to } \|Kz - y\| \le \varepsilon \qquad (3.12)$$

where ε bounds the amount of noise in the data. The above formulation (3.12) is a *quadratically constrained linear program* (QCLP) and is often referred to as basis pursuit denoising (BPDN) [38], which is a convex problem. Another ways to express the l_1 minimization with relaxed constraints is

$$\hat{z} = \arg\min_z \|Kz - y\|^2 \text{ subject to } \|z\|_1 \le t \qquad (3.13)$$

The above formulation (3.13) is a quadratic program (QP) and is often referred to as *least absolute shrinkage and selector operator* (LASSO) [38, 46], which is also a convex problem and can be solved efficiently.

THEOREM 2 (Noisy recovery) [37]

Assume that $\delta_{2R} < \sqrt{2} - 1$. Then the solution $\hat{z}$ to (3.12) obeys

$$\|\hat{z} - z\|_2 \le C_0 \|z - z_R\|_1 / \sqrt{R} + C_1 \varepsilon \qquad (3.14)$$

for some constant C_0 *and* C_1.

The theorem suggests that the reconstruction error is bounded by the sum of two terms. The first term corresponds to the noiseless case while the second term is just proportional to the noise term. Also, the constants C_0 and C_1 are typically small e.g. for $\delta_{2R} = 0.25$, we have $C_0 \leq 5.5$ and $C_1 \leq 6$ [45].

The last two theorems establish that CS framework is robust and can handle both compressible signals and noisy measurements when the sensing matrices obey the RIP conditions. The most widely used matrices that satisfy the RIP conditions are the ones whose rows are formed from the realization of Gaussian noise or a sequence of Bernoulli random variables taking values ±1 with equal probability. It has been shown in [20, 32, 42, 44, 47] that taking random measurements is in some sense an optimal strategy for acquiring sparse/ compressible signals, where M measurements can recover signals with sparsity $R \cong M/\log(N/M)$. Similar bounds have been obtained using greedy [42] and complexity-based [33] recovery algorithms in place of l_1 minimization.

3.5 Recovery Techniques for CS

In this section we review the existing techniques and algorithms to recover signal from the undersampled data. The recovery methods in general are classified as 1) l_1 minimization, 2) iterative thresholding and 3) greedy methods.

3.5.1 l_1 - Minimization Methods

The constrained l_1-minimization problem, as given in (3.8), can formulated as unconstrained l_1-minimization problem as

$$\hat{z} = \arg\min_{z} \frac{1}{2} \| y - Kz \|^2 + \tau \| z \|_1 \qquad (3.15)$$

where $\tau \in \mathbb{R}^+$.

This unconstrained l_1-minimization approach consists in minimizing an objective function which includes a quadratic (squared l_2) error term combined with sparseness inducing l_1-regularization term. Basis pursuit (BP), least absolute shrinkage and selection operator (LASSO), wavelet-based deconvolution, gradient, homotopy methods, projection algorithm [48], etc. are known examples of this approach.

Basis pursuit (BP) and basis pursuit denoising (BPDN) [38] solve the convex representation as given in (3.15) and approximation problem as given in (3.12) by using interior-point methods. The wavelet based deconvolution involves the recovery of the piece-wise smooth functions from a noisy observation, by solving a convex relaxation problem using the appropriate wavelet basis and a value of the τ parameter related to the variance of the noise [47]. Homotopy algorithms [49-51] trace all solutions of basis pursuit for all non-negative values of the scalar parameters in the various formulations τ as in (3.15), ε as in (3.12) and t in (3.13). These homotopy methods perform pivoting operations involving sub-matrices of K or $K^T K$ at certain critical values of the corresponding parameter (τ in (3.15), ε in (3.12) and t (3.13)). The least angle regression (LARS) [49] can be adapted to solve the LASSO formulation as in (3.13).

The gradient projection is applied to a quadratic programming formulation of (3.15) in which the search path from each iterate is obtained by projecting the negative gradient direction onto the feasible set [48].

It is also possible to use intermediate quasi-norms i.e. $0 < p < 1$ by the following regularisation [52-54]

$$\hat{\mathbf{z}} = \arg\min_z \frac{1}{2}\|\mathbf{y} - \mathbf{Kz}\|^2 + \tau\|\mathbf{z}\|_p^p \qquad (3.16)$$

These norms do not lead to convex cost functions and therefore the global optimum is difficult to calculate. It is to be noted that the minimum value of norm for which the above cost function is convex is $p = 1$.

3.5.2 Iterative Thresholding

Iterative thresholding algorithms have been proposed recently to solve this problem in [55-61]. A similar algorithm to solve the l_0 optimization problem had been previously proposed in [62] and more recently in [63]. All of these methods address particular instances of a more general class of iterative algorithms based on expectation- maximization (EM) technique [64, 65] . A good overview of the iterative thresholding methods can be found in [66] with the convergence results in [67]. More details of the iterative thresholding algorithms and its use in the CS framework is described in the Chapter 4 of this thesis.

3.5.3 Greedy Methods

It is shown that the iterative greedy algorithms such as matching pursuit (MP) [40, 68] and orthogonal matching pursuit (OMP) [68] can be used for recovery problem at the expense of slightly more measurements as compared to BP. MP provides a low-complexity alternative to BP and has been proven to achieve an accurate decomposition of the signal but requires an unbounded number of iterations for convergence. OMP converges in a fixed number of iterations but requires the additional orthogonalisation at each step. Various variations of the matching pursuit for the compressed sensing applications includes regularized orthogonal matching pursuit (ROMP) [69, 70], subspace pursuit [71], stagewise orthogonal matching pursuit (StOMP) [72], tree matching pursuit [73-75] and compressive sampling matching pursuit (CoSaMP) [76].

We have used the orthogonal matching pursuit (OMP) in Section 3.6 of this chapter to demonstrate the CS in action and also used it for recovery of complex-valued SAR sparse signals in the CS framework as it was easily adapted for the complex-valued signal. OMP converges in a fixed number of iterations and is faster than the BP method though it requires slightly more measurements.

OMP is an iterative greedy algorithm which attempts to identify the most significant element of the dictionary by guaranteeing that the residue is orthogonal to all previously chosen atom. The pseudo-code of OMP is shown in Table 3-1.

1. $t = 1$, set residual vector $\mathbf{r}_t = \mathbf{y}$, index set $\mathbf{I}_t = \phi$

2. Find index λ_t, that yields the maximum correlation with the residue

$$\lambda_t = \arg \min_{1 \le i \le n} \left| \langle \mathbf{r}_t, a_i \rangle \right|$$

3. Augment $\mathbf{I}_t = \mathbf{I}_t \bigcup \lambda_t$

4. Form new signal estimate by solving the least square equation

$$\mathbf{z}_t = \arg \min_{\mathbf{c}} \left\| \mathbf{y} - \mathbf{K}_{\mathbf{I}_t} \mathbf{c} \right\|$$

5. Set the new residual $\mathbf{r}_t = \mathbf{y} - \mathbf{K}_{\mathbf{I}_t} \mathbf{z}_t$

6. $t = t + 1$ and stop when $\left\| \mathbf{r}_t \right\| \le \varepsilon$ or $t > P$

Table 3-1 Pseudo-code of Orthogonal Matching Pursuit.

The convergence criteria is when the residue has reached a minimum fixed value of ε or the loop has reached a pre-defined no. of iterations P. The least square solution in the step 4 is obtained by using the conjugate gradient (CG) method [77].

3.6 Compressed Sensing in Action

We now present several examples to show the recovery of signal from undersampled data.

Example 1:

We start with a 1D example by constructing a true sparse signal of length $N = 1024$ with a fixed number $R = 20$, located in random positions in the time domain, all of equal amplitude and random signs as shown in Figure 3.5(a). The signal is sparse in time-domain. We form the measurement matrix $\mathbf{A}$ of size 128×1024 by randomly selecting the entries from a Gaussian distribution with zero mean and unit variance and then orthogonalizing the rows. Figure 3.5(b) shows the measurements signal of size $M = 128$. Note that the sparsifying basis $\mathbf{W}$ in this example is an identity matrix i.e. $\mathbf{W} = \mathbf{I}$. Figure 3.5(c) shows the l_2 reconstruction which is not sparse at all. This corresponds to the minimum energy solution which is vector in $\{\mathbf{x} : \mathbf{Ax} = \mathbf{y}\}$ that is closest to the origin. Figure 3.5(d) displays the recovered signal from the incomplete measurements using the OMP reconstruction method. The reconstructed signal is almost same as the original signal with the mean square error (MSE) equal to 6.6033×10^{-16}.

Example 2:

We take the case of the compressible signal by considering a test signal, *Doppler*, from *Donoho-Johnstone* [78] collection of synthetic test signals. The test signal, *Doppler*, of length $N = 1024$ is shown in Figure 3.6(a). This signal is compressible in *Daubechies-8* (D8) wavelet basis which is shown in Figure 3.6(b). The measurement matrix $\mathbf{A}$ of size 380×1024 is formed by randomly selecting the entries from a Gaussian distribution with zero mean and unit variance followed by orthogonalization. This results in the measurement signal of size $M = 380$. Figure 3.6(c) shows the recovery with the l_2 minimization. The recovery of 304 wavelet coefficients based on OMP is shown in Figure 3.6(d) with the mean square error (MSE) equal to 1.89×10^{-6}.

Example 3

In this example, we consider a 2D example of 256×256 *Shepp-Logan* phantom as shown in Figure 3.7(a), which is a dummy image of MRI scan of human brain. The 2D *Haar* wavelet transform is shown in Figure 3.7(b) and the ordered wavelet coefficients is

shown in Figure 3.7(c). The compressibility of the test signal in the *Haar* wavelet domain is evident from these figures. The MRI measurement is usually carried out in the *Fourier* domain as shown in Figure 3.7(d). We under sample this 2D *Fourier* plane taking $M = 5481$ samples through the sampling pattern (radial lines) as shown in Figure 3.8(a). The measurement signal is shown in Figure 3.8(b). The minimum norm l_2 solution is shown in Figure 3.8(c) and the recovered phantom with 3800 wavelet coefficients is shown in Figure 3.8(d).
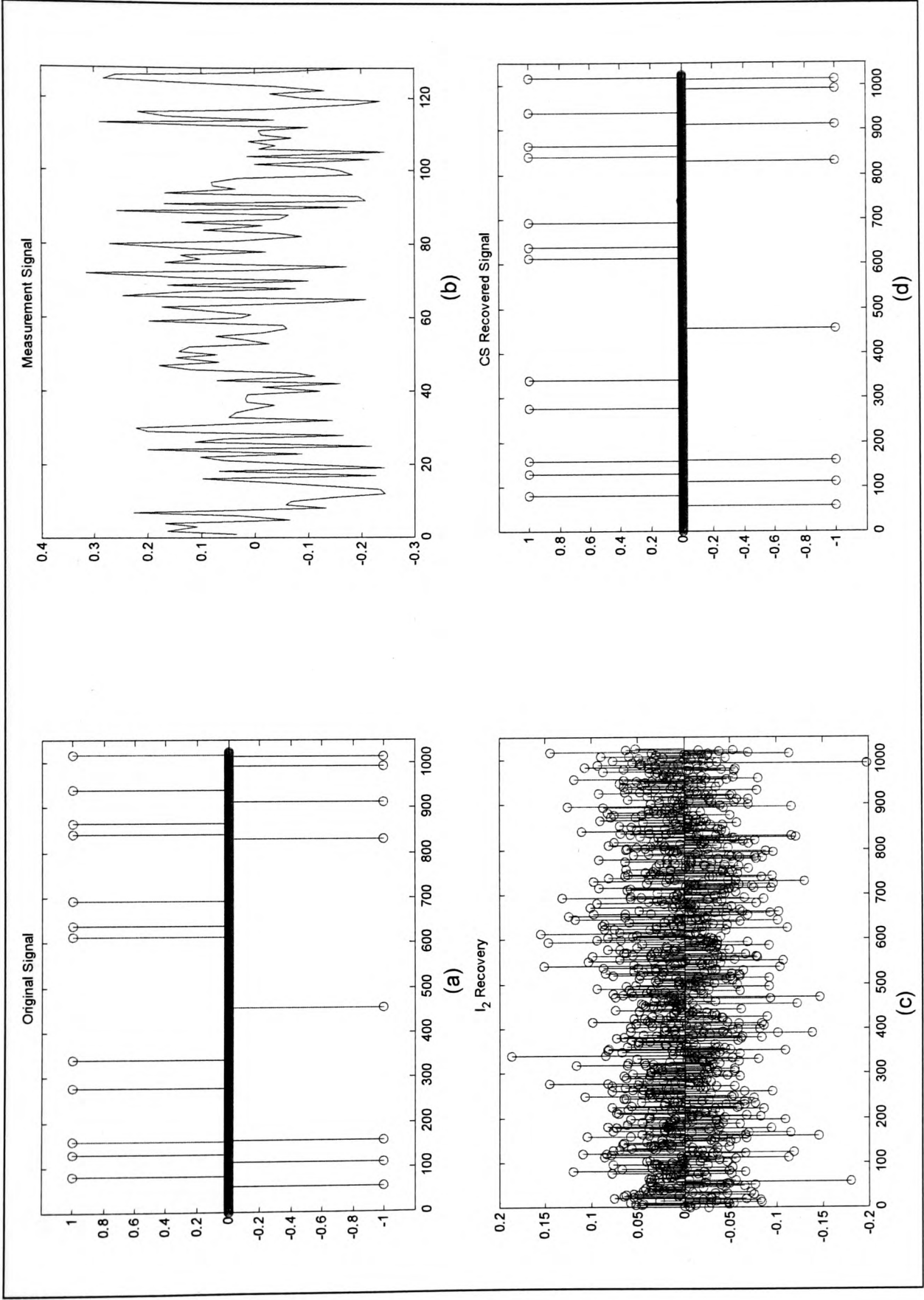
Figure 3.5 (a) Original sparse signal of size $N = 1024$, (b) Measurement signal of size $M = 128$, (c) the l_2 recovery, (d) reconstructed signal with 171 wavelet coefficients through OMP.

59
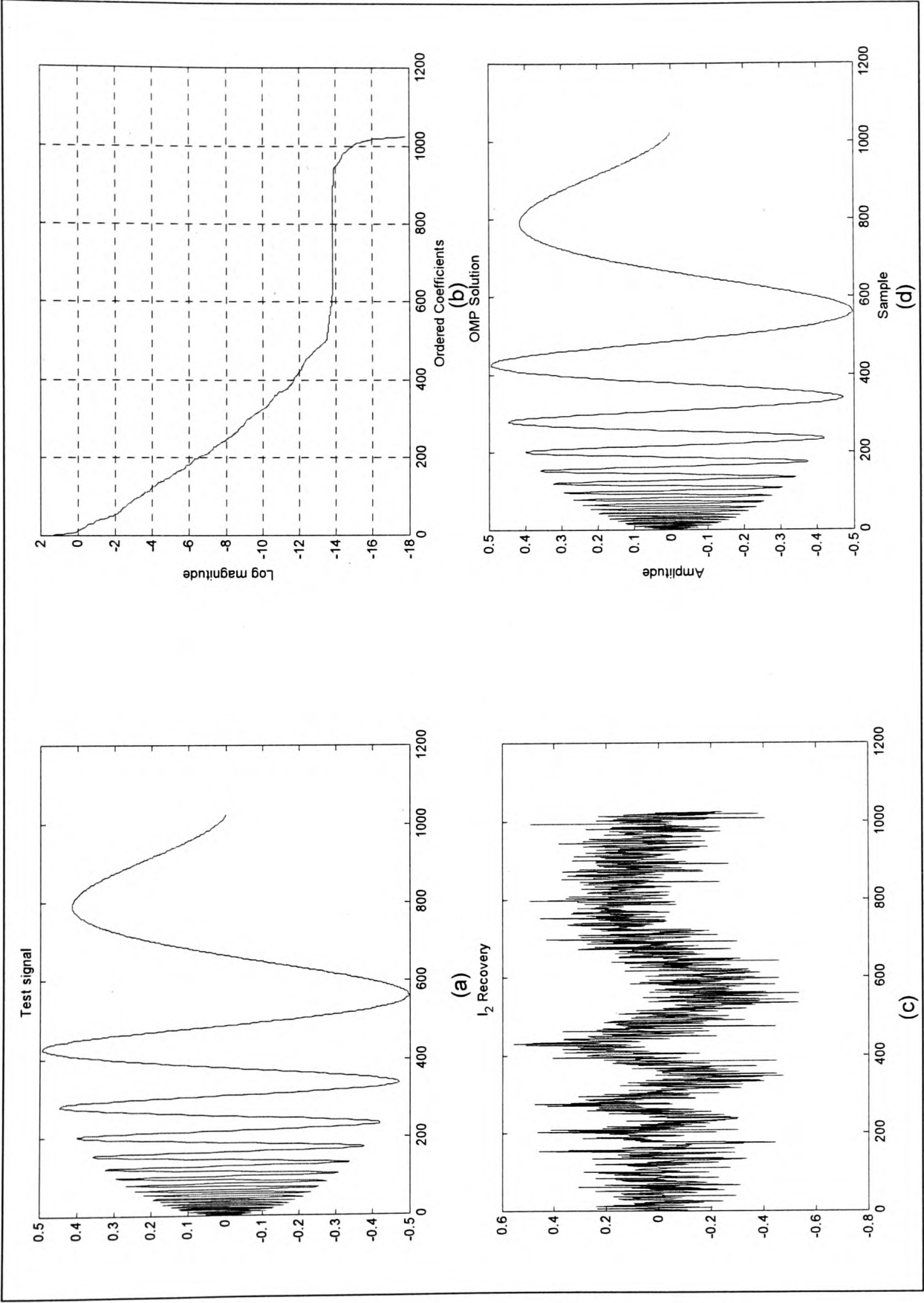
Figure 3.6 (a) Test signal, Doppler, of size $N = 1024$, (b) the log plot of sorted wavelet coefficients, (c) the l_2 recovery, (d) reconstructed signal with 304 wavelet coefficients with MSE of 1.89×10^{-6}.

60
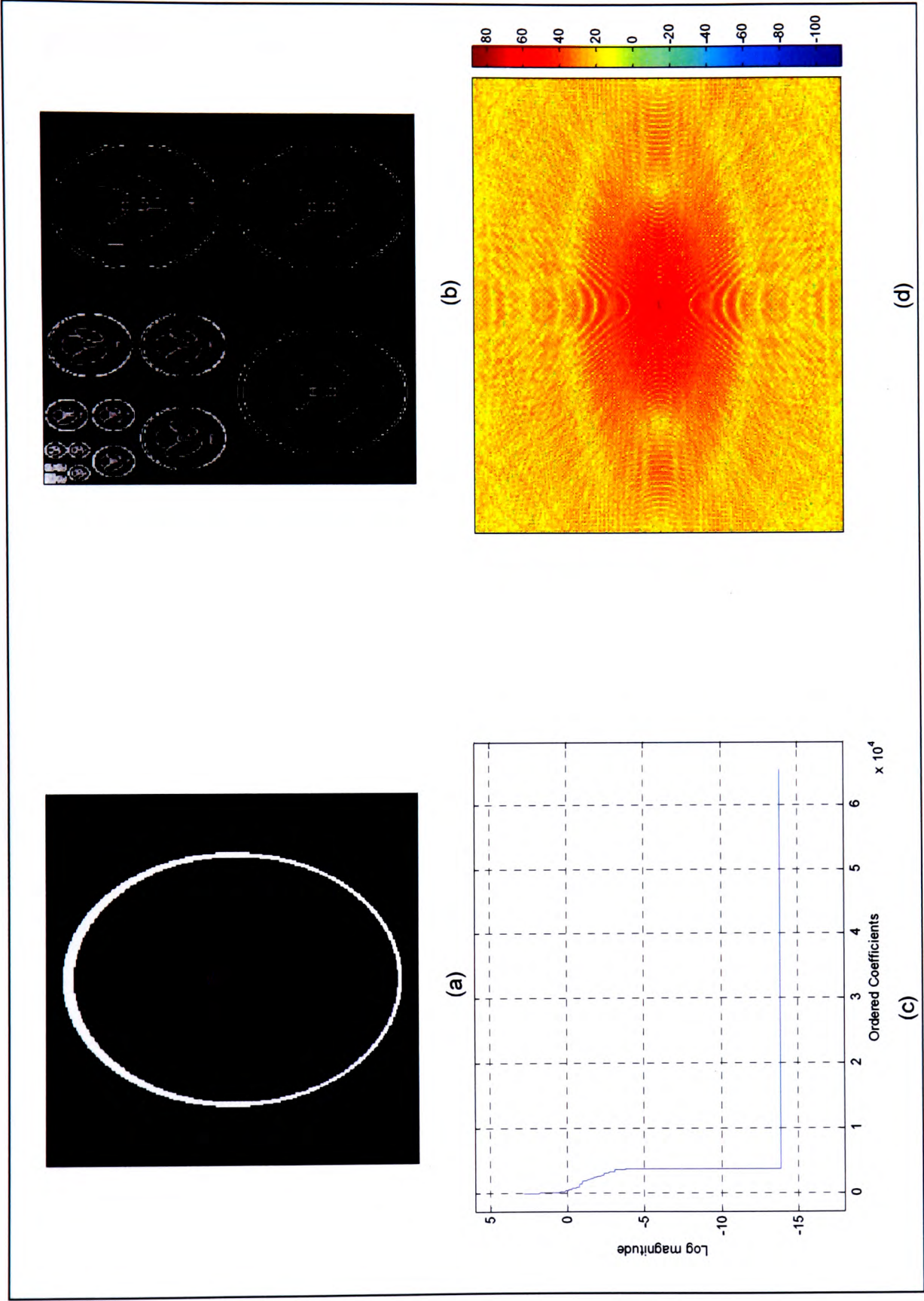
Figure 3.7 (a) Shepp-Logan image of size $N = 256 \times 256$**, (b)2D Haar wavelet transform (c) plot of ordered wavelet coefficients, (d) 2D Fourier domain, where the measurement is usually carried out.**

61
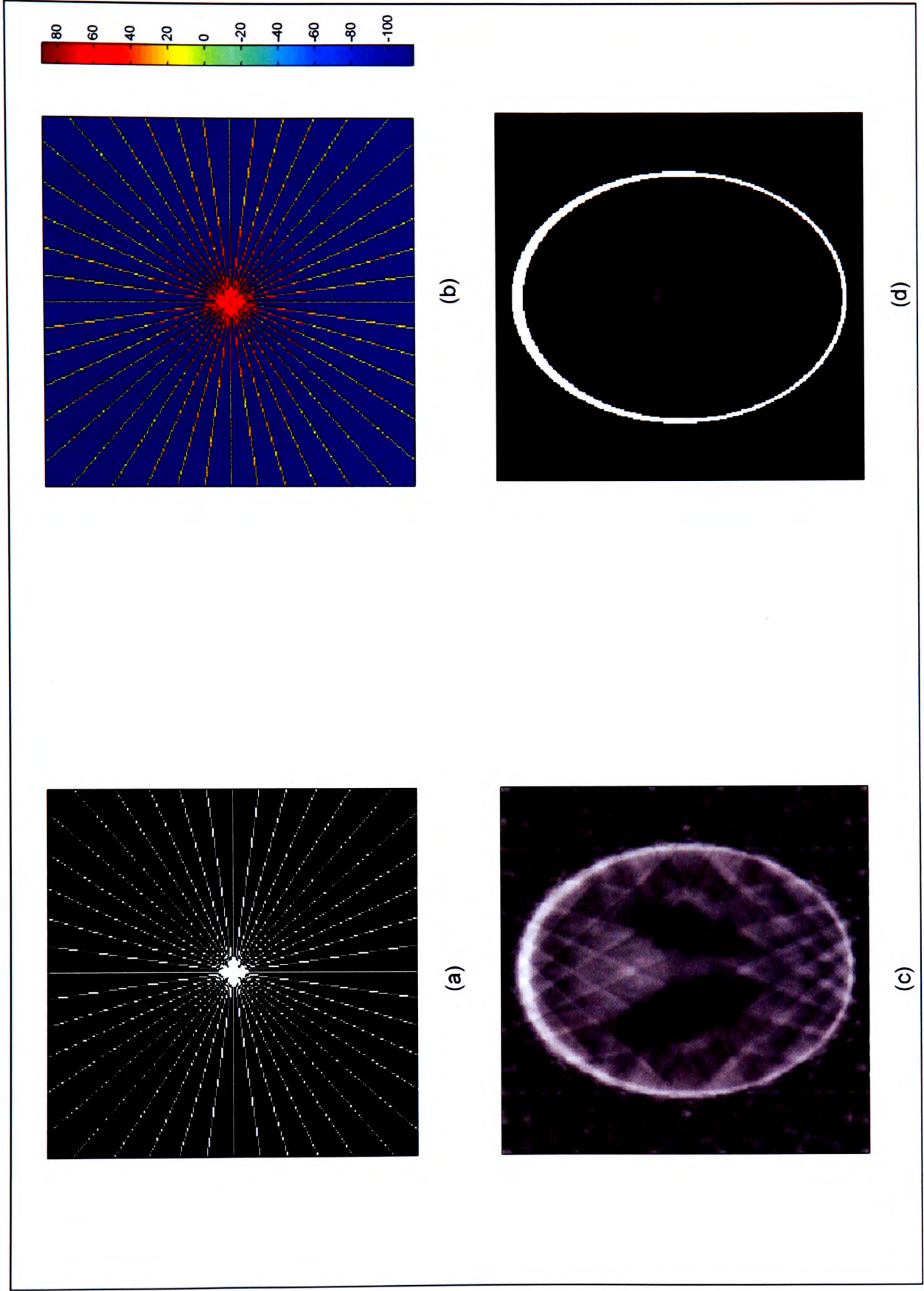
Figure 3.8 (a) **Radial sampling pattern, (b) Measurement signal of size** $M = 5481$, (c) **the minimum norm** l_2 **recovery, (d) reconstructed phantom with 3800 wavelet coefficients.**

62

3.7 Conclusions

In this chapter we presented an emerging paradigm to recovery sparse signals from highly undersampled signals. We have reviewed the conventional sampling and transform based compression. The disadvantages of higher sampling rate followed by high computation required in conventional compression are taken care in the compressed sensing framework. The major components in this framework are the encoder, the measurement process and the decoder. A compressible signal is captured (encoded) from a small number of random linear projections onto a measurement basis. The measurement process is *non-adaptive*. The essential properties like mutual coherence and restricted isometric properties of the measurement matrices are discussed. The randomized measurement ensemble drawn from Gaussian i.i.d. or Bernoulli's distribution succeeds for all signals, with high probability over the random choices in its construction. We have seen that the reconstruction problem in compressed sensing is essentially the classical linear inverse problem with the number of variables N much greater than the number of observations M. The signal can be reconstructed (decoded) through a non-linear decoding scheme that uses the sparsity as *a-priori* information.

This framework where the encoder is simple and the decoder is computationally extensive is ideally suitable for on-board compression of SAR raw data due to the limited computational resources on a satellite. Before discussing the compression of SAR raw data and its performance in the compressed sensing framework in chapter 5, we present in Chapter 4 a new iterative algorithm to recover the sparse solution of a linear inverse problem.

Chapter 4

4. Inverse Problems and Regularization Methods

In this chapter, we provide a brief overview of the inverse problems and associated regularization methods to get their solutions. In Chapter 3, it is shown that the signal recovery in the Compressed Sensing framework can be formulated as solving the inverse problem with *sparsity* constraints. The major contribution of this chapter is the development of new iterative algorithm to get a sparse solution to the inverse problems. Often, it has been proposed to use regularization of ill-posed linear inverse problems via l_1-penalization when the solution is sparse. The regularization parameter controls the trade off between fidelity to the data and smoothness of the solution and hence the choice of the regularization parameter is crucial and is either manually set or estimated. The proposed algorithm, which is based on iterative soft-thresholding, adaptively estimates the regularization parameter in each iteration. The new algorithm is tested with several real and complex data and is compared with standard algorithms like Basis Pursuit (BP) and Orthogonal Matching Pursuit (OMP).

4.1 Inverse Problems and Mathematical Formulation

One of the most important problems in signal processing has been the recovery or the restoration of the signal from its degraded version. Such problems are described as *inverse problems*, where one makes indirect observations of a quantity of interest. Examples of inverse problems are deconvolution i.e. recovery of the input to a linear time-invariant system from its output, restoration of signal from its projection, recovery of inputs from a time variant system, recovery of signal from incomplete measurements (*Compressed Sensing*), signal denoising, overcomplete representation of signals and

extrapolation of data from a given length of data. In all such cases, an appropriate mathematical representation is the *Fredholm equation of first kind* [79],

$$y = Ax \qquad (4.1)$$

where x is the unknown input signal, y is the known measurement and A is the known distortion operator or transformation. Mathematically, $x \in \mathcal{H}_1$, $y \in \mathcal{H}_2$ and $A : \mathcal{H}_1 \to \mathcal{H}_2$ a compact operator with $\mathcal{H}_1, \mathcal{H}_2$ as separable Hilbert spaces of finite or infinite dimensions. The problem of signal reconstruction is to recover x given y and A. The direct solution to (4.1) by computing $x = A^{-1}y$ often leads to catastrophic results due to inappropriate computation of inverse operator or due to error in the measurement y.

In practical cases, the measurement y is often corrupted by noise e, i.e.:

$$y = Ax + e \qquad (4.2)$$

In such cases, we find an estimate of x as $\hat{x}$ from the measurement y by minimizing the *discrepancy function* $f(\hat{x})$ [55],

$$f(\hat{x}) = \|A\hat{x} - y\|^2 \qquad (4.3)$$

where $\|\cdot\|$ denotes the regular Euclidean norm. Any solution of this variational problem is called a *least-squares solution*.

The above equation has a unique minimizer, given by $\hat{x} = (A^*A)^{-1}A^*y$, where A^* is the adjoint operator, when the operator A has a trivial null space i.e. $\mathcal{N}(A) = \{x \in \mathcal{H}_1 : Ax = 0\} = \{0\}$. If the null space of A, $\mathcal{N}(A) \neq \{0\}$, we find the *generalized solution* of the inverse problem that is the least squares one with minimum

norm i.e. $x^\dagger = \arg\min\{\|x\| : x \text{ minimizes } f(x)\}$. The *generalized inverse* operator of A, $A^\dagger$, may be unbounded for *ill-posed* problems or may have a very large norm for *ill-conditioned* problems. In order to get a numerically stable solutions and a meaningful approximation of the true solution, a *regularization* technique is required which take advantage of the prior knowledge of the solution x. The classical regularization methods include (1) the *Tikhonov* regularization, (2) regularization by singular value truncation and (3) regularization by truncated iterative methods [79]. Here, we discuss the *Tikhonov* regularisation and also show that the regularization by truncated iterative method is a particular case of *generalized Tikhonov* regularization.

4.1.1 Tikhonov Regularization

The *Tikhonov* regularization tries to find a solution by balancing the fidelity of the data with the smoothness of the solution. Mathematically, the fidelity of the data is expressed as the norm of the residual $r = A\hat{x} - y$ and the smoothness of the solution is expressed as the norm of the approximate solution $\|\hat{x}\|^2$. The *Tikhonov* regularized solution $x_\mu \in \mathcal{H}_1$ is the minimizer of the functional

$$F_\mu(\hat{x}) = \|A\hat{x} - y\|^2 + \lambda\|\hat{x}\|^2 \tag{4.4}$$

The parameter $\lambda > 0$ is called the regularization parameter which balances the fidelity of the data and the smoothness of the solution, which is generally known *a priori*. The first part of the above equation is the fidelity term and the second term is the penalty term. Perfect fidelity to the data is achieved if $\lambda = 0$, whereas perfect fidelity to the priors is achieved if $\lambda = \infty$. Figure 4.1 shows the *Tikhonov* solution to lie at the intersection of ellipse corresponding to the minimum of the discrepancy, ε_{min}, and surface of the l_2 ball of the solution size E. The l_2-ball of radius E for $x \in \mathbb{R}^2$ is formed by points on $\sqrt{x_1^2 + x_2^2} = E$. It is shown in [79], that if $A : \mathcal{H}_1 \to \mathcal{H}_2$ be a compact operator, the *Tikhonov* regularised solution exists, is unique, and is given by the formula

$$\mathbf{x}_\mu = \left(\mathbf{A}^*\mathbf{A} + \mu\mathbf{I}\right)^{-1}\mathbf{A}^*\mathbf{y} \tag{4.5}$$

which also corresponds to the solution of the regularized normal equations

$$\mathbf{A}^*\mathbf{Ax} + \mu\mathbf{x} = \mathbf{A}^*\mathbf{y} \tag{4.6}$$

The above set of normal equations (4.6) is obtained by taking the gradient of (4.4) with respect to $\mathbf{x}$, and setting it equal to zero.
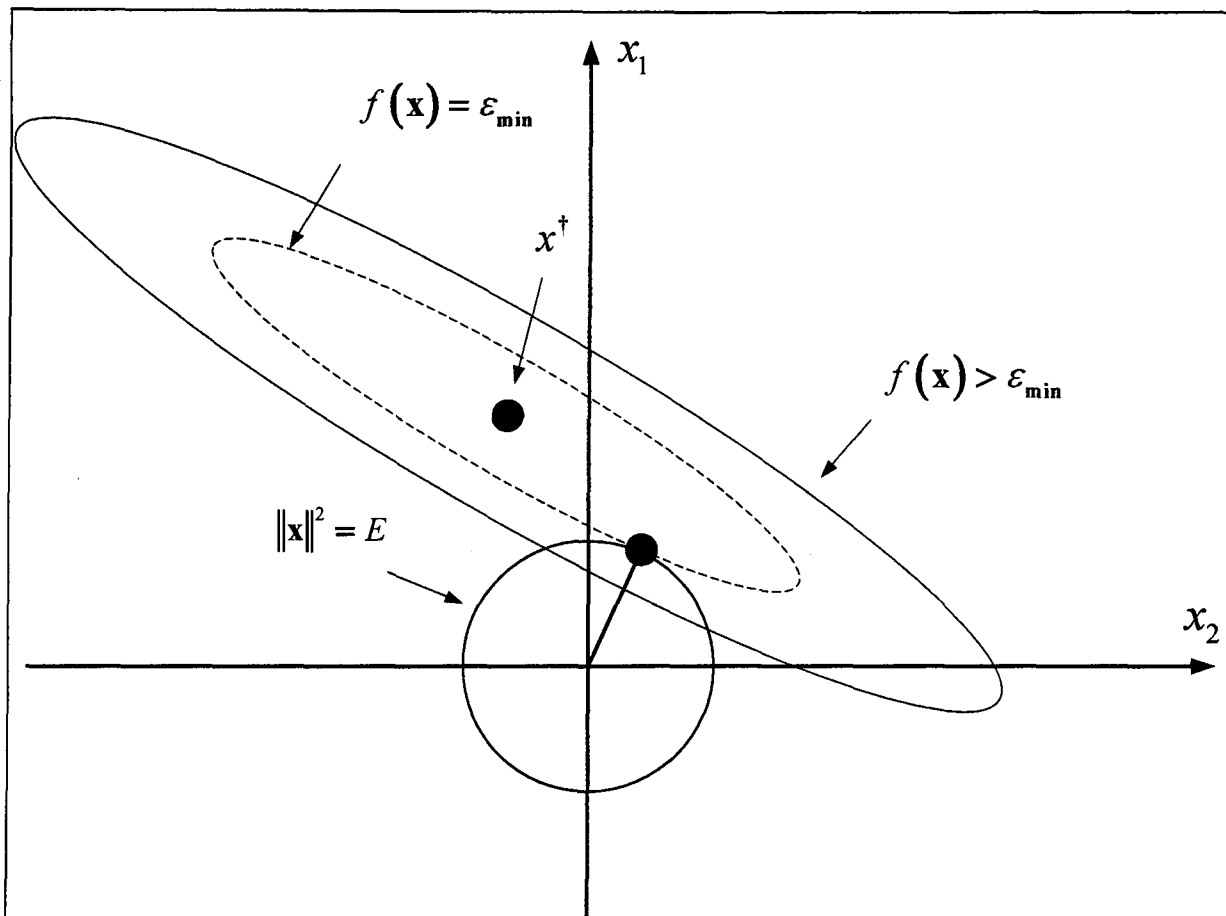
Figure 4.1 **Example for** $\mathbf{x} \in \mathbb{R}^2$ **i.e.** $\mathbf{x} = (x_1, x_2)$ **showing the solution of the** *Tikhonov* **regularization, where** $\mathbf{x}^\dagger$ **is the solution to** $\min \|\mathbf{Ax} - \mathbf{y}\|^2$.

4.1.2 Non-Quadratic Regularization

The optimality condition (4.6) is a linear function of $\mathbf{x}$, as the *Tikhonov* cost function (4.4) is a quadratic function of $\mathbf{x}$. This results in the linear processing of data $\mathbf{x}$ for

signal recovery. But the major drawback of minimizing the discrepancy function with a penalty on the l_2-norm is that it does not encourage sparsity and the resulting solution typically have non-zero values associated with all coefficients. It is shown in [80], that better results are obtained if non-linear methods are used. The *Tikhonov* regularization can be generalized by replacing a linear operator $\mathbf{A}$ by a non-linear one and also with a different choice of the penalty term. The *generalized Tikhonov* regularization deals with finding a solution which minimizes a functional of type

$$F_\mu(\hat{\mathbf{x}}) = \left\| \mathbf{A}\hat{\mathbf{x}} - \mathbf{y} \right\|^2 + \mu G(\hat{\mathbf{x}}) \tag{4.7}$$

where $G : \mathcal{H}_1 \to \mathbb{R}$ is a non-negative functional. To get a smooth solution, often the highly oscillating components, which are most sensitive to noise, are penalized. The formulation of (4.7) includes well known regularization approaches such as maximum entropy and total variation methods [81].

Amongst several methods of non-quadratic regularization, we focus on the problems where the signal representation and linear inverse problems are expressed as underdetermined system of equations that uses an over-complete dictionary and the solution can be represented by a *sparse* expansion. This is related to the compression of the signal in the compressed sensing framework as described in chapter 3. The solution to such underdetermined problems is not unique. The non-uniqueness of the underdetermined system is commonly addressed by using the *sparseness* as a criteria to select from among the (many) possible representations. *Sparseness* constraint refers to the requirement that the vector or solution being sought or optimized must have a small number of large coefficients with respect to an orthogonal basis or frame. The sparsity promoting feature of the solution to the underdetermined system of equations has been explored extensively in various signal processing applications including image, audio, video compression and recently in the framework of *compressed sensing* (CS) [19, 20]. In CS,

a non-adaptive, low dimensional linear projector is used to acquire an efficient representation of a sparse or compressible signal directly using just a few measurements.

4.2 Sparse Representation Problem

Let us consider a $M \times N$ measurement matrix $\mathbf{A}$ with $M \ll N$ and $\text{rank}(\mathbf{A}) = M$. Then, for an observation $\mathbf{y} \in \mathbb{C}^M$ the system of equations, $\mathbf{y} = \mathbf{A}\mathbf{x}$, has infinite solutions in $\mathbf{x} \in \mathbb{C}^N$. Any solution for this underdetermined system of equations can be expressed as

$$\hat{\mathbf{x}} = \mathbf{x}_{LS} + \mathbf{v} \tag{4.8}$$

where $\mathbf{x}_{LS}$ is the minimum norm solution (i.e. solution which has the smallest l_2 norm defined as $\|\mathbf{x}\|_2^2 = \sum_{i=1}^N x_i^2$) and is given by $\mathbf{x}_{LS} = \mathbf{A}^\dagger \mathbf{y}$, where $\mathbf{A}^\dagger$ denotes the *Moore-Penrose* pseudo-inverse of $\mathbf{A}$. The vector $\mathbf{v}$ is any vector that lies in the null space of $\mathbf{A}$, $\mathcal{N}(\mathbf{A})$. In this case of underdetermined system of equations, the null space is non-trivial. The least square solution, $\mathbf{x}_{LS}$, has many non-zero coefficients and hence not sparse. Another drawback of the least square solution is their lack of robustness i.e. their strong sensitivity to the errors in a data set. To overcome these drawbacks various algorithms to find the sparse solution to the problem have been undertaken as described below.

Suppose that the solution $\mathbf{x}$ has the sparsity index R in the orthogonal basis or frame $\mathbf{W} = \{\varphi_i\}_{i=1}^N$ i.e. $\|\mathbf{W}\mathbf{x}\|_0 = \|\mathbf{z}\|_0 = \#\{i : |z_i| \neq 0\} = R$, where the function $\#\{i : |z_i| \neq 0\}$ is simply the number of non-zero terms in the candidate vector $\mathbf{z}$. When $\mathbf{z}$ is sparse we have $R \ll N$. The overall sparse representation problem is as shown in Figure 4.2.
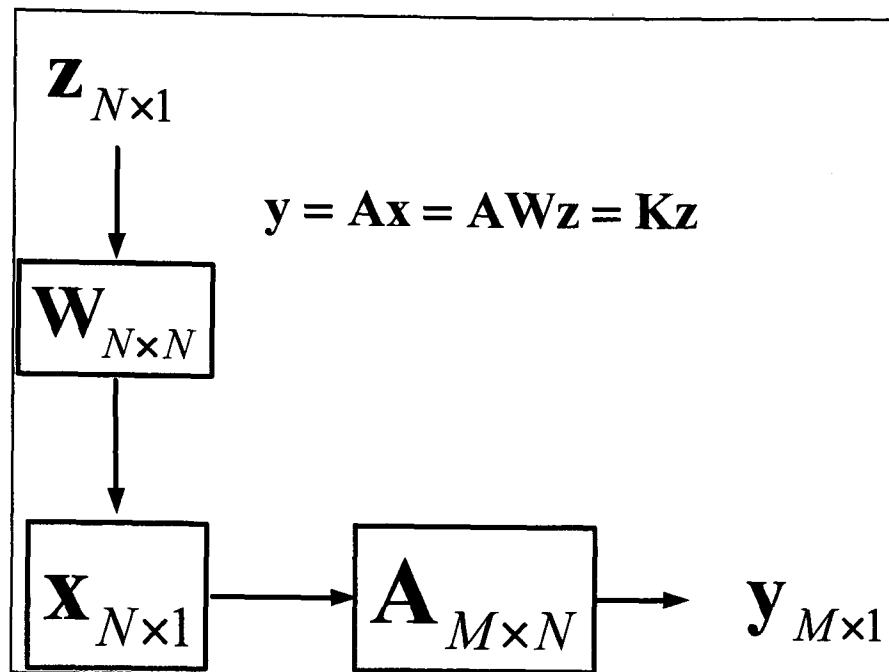
Figure 4.2 Overall Sparse representation problem.

The sparse recovery of the signal z is made possible by solving the combinatorial optimization problem

$$z_{0u} = \arg \min \|z\|_0 \quad \text{s.t. } y = Kz \tag{4.9}$$

where $K = AW^*$ is the *holographic* basis.

The l_0-norm term leads to non-smooth and non-convex problem which is NP-hard to solve and several alternate methods to find a solution like greedy algorithms [40], gradient descent, linear programming [38] and global optimization were devised.

In the case of CS framework, the above non-convex combinatorial problem is relaxed by minimizing the l_1- norm. Under suitable conditions, minimization of the l_1-norm is equivalent to minimization of l_0- norm [44]. The CS theory shows that when the matrix K has the *restricted isometric property* (RIP) [44], then it is possible to recover R sparse coefficients from measurement of size $M = O\left(C \log M/R\right)$, where C is a positive constant. When the RIP holds, the signal z can be recovered exactly in the

71

absence of any noise from $\mathbf{y}$ by solving the l_1 minimization or *Basis Pursuit* (BP) problem [38],

$$\mathbf{z}_{1u} = \arg\min \|\mathbf{z}\|_1 \quad \text{s.t. } \mathbf{y} = \mathbf{Kz} \tag{4.10}$$

where $\|\mathbf{z}\|_1 = \sum_{i=1}^{N} |z_i|$ is the l_1- norm.

However, if there is noise in the measurement y, the sparse solution is obtained through the *Basis Pursuit Denoising* (BPDN) problem [38]

$$\mathbf{z}_{1c} = \arg\min\left\{ \frac{1}{2}\|\mathbf{Kz} - \mathbf{y}\|^2 + \tau\|\mathbf{z}\|_1 \right\} \tag{4.11}$$

where $\tau \in \mathbb{R}^+$. It is to be noted that the above equation is an unconstrained convex optimization problem in terms of $\mathbf{z}$ but non-differentiable when $z_i = 0$ for any z_i and thus there exists no closed form solution for the global minimum in the same way that we have in case of *Tikhonov* regularization (l_2 penalty). This drawback has led to the introduction of techniques which use equivalent unconstrained formulation as least absolute shrinkage and selector operator (*LASSO*) problem [46]

$$\mathbf{z}_{1L} = \arg\min \|\mathbf{Kz} - \mathbf{y}\|^2 \quad \text{s.t. } \|\mathbf{z}\|_1 < t \tag{4.12}$$

which is equivalent to (4.11) under appropriate constants τ and $t \in \mathbb{R}^+$. In all these cases, the l_1 term encourages small components of $\mathbf{z}$ to become exactly zero, thus promoting sparse solutions.

4.3 Iterative Soft-Thresholding Algorithms

Several authors have proposed an iterative soft-threshold algorithm to approximate the sparse solution $\bar{z}(\tau)$ [57, 65, 82] for equation (4.11). The connection between a minimum l_1-norm penalty and soft shrinkage was also pointed out in [83]. More precisely, $\bar{z}(\tau)$ is the limit of sequences $z^{(n)}$ defined recursively by gradient based solution as

$$z^{(n+1)} = \mathbb{S}_\tau \left[z^{(n)} + K^* \left(y - K z^{(n)} \right) \right]$$

(4.13)

starting from an arbitrary $z^{(0)}$, where $*$ denotes *Hermitian* transpose and $\mathbb{S}_\tau$ is the vector soft-thresholding operation defined by component-wise shrinkage, S_τ, of each element of the vector as

$$S_\tau(g) = sign(g)(|g| - \tau)_+ = \begin{cases} g - \tau & g > \tau \\ 0 & |g| \le \tau \\ g + \tau & g < -\tau \end{cases}$$

(4.14)

where the scalar $g \in \mathbb{R}$, $(\cdot)_+$ denotes the positive part operator defined as $(g)_+ = \max(g, 0)$, and $sign(\cdot)$ is the sign function defined as $sign(g) = 1$ if $g > 0$, and $sign(g) = -1$ if $g < 0$. The convergence of this algorithm is proved in [55]. The above iteration with fixed τ is often called as the *iterative soft-thresholding algorithm* or the *thresholded Landweber iteration* [84]. The *Landweber* method is an example of the so-called gradient methods, i.e. of the methods where, at each step, the new approximation is obtained by modifying the old one in the direction of the gradient of the discrepancy function $f(x)$ as defined in (4.3) [85]. The convergence of the above recursion (4.13) to a fixed point occurs for K with norm strictly bounded by 1 and with trivial null space. We can always assume without the loss of generality that $\|K\| < 1$, which is the largest singular value of K; if necessary, this can be achieved by a suitable re-scaling of K and y.

The soft thresholding in (4.14) is defined for the complex signal $g \in \mathbb{C}^N$, also known as complex thresholding operator, as $S_\tau(re^{i\theta}) = S_\tau(r)e^{i\theta}$ [55]. The soft-thresholding operation is as shown in Figure 4.3.
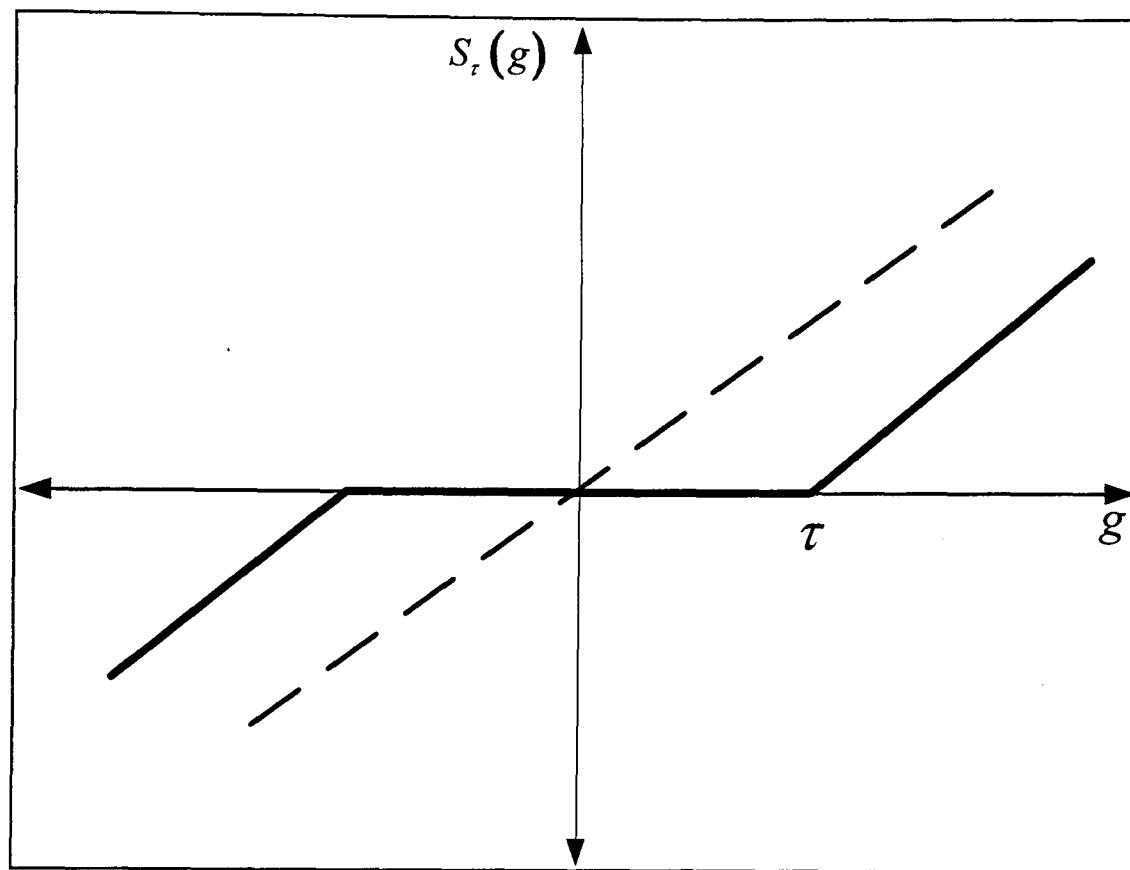
Figure 4.3 Soft-thresholding operation.

The non-linear thresholding of the *Landweber iteration* $z^{(n+1)} = z^{(n)} + K^*\left(y - Kz^{(n)}\right)$, which is a gradient descent algorithm with a fixed step size, converges quite slowly [84]. This algorithm would converge faster, if the solution in each iteration is restricted to the l_1-ball $B_R := \left\{ z \mid \|z\|_1 \le R \right\}$, with $R := \|\bar{z}(\tau)\|$ where

$\bar{z}(\tau) = \lim_{n \to \infty} z^{(n)}$. This could be achieved by projecting the *Landweber* iterates $z^{(n)}$ on the l_1-ball B_R. We thus obtain the following algorithm, which is also known as *projected Landweber iteration*,

$$z^{(n+1)} = \mathbb{P}_R\left[z^{(n)} + K^*\left(y - Kz^{(n)}\right)\right] \qquad (4.15)$$

where $\mathbb{P}_R$ is an non-expansive l_2-projection operator in the sense that $\|\mathbb{P}_R \mathbf{u} - \mathbb{P}_R \mathbf{v}\| \le \|\mathbf{u} - \mathbf{v}\|$ for all $\mathbf{u}, \mathbf{v} \in \mathbb{C}^N$.

The following lemma shows that the l_2-projection $\mathbb{P}_R(\mathbf{a})$ can be obtained by a suitable thresholding of $\mathbf{a}$.

Lemma 1 [84] : *If* $\|\mathbf{a}\|_1 > R$, *then the l_2-projection of* $\mathbf{a}$ *on the l_1-ball with radius R is given by* $\mathbb{P}_R(\mathbf{a}) = \mathbb{S}_\tau(\mathbf{a})$ *where* τ *(depending on* $\mathbf{a}$ *and R) is chosen such that* $\left\| \mathbb{S}_\tau(\mathbf{a}) \right\|_1 = R$. *If* $\|\mathbf{a}\|_1 \le R$ *then* $\mathbb{P}_R(\mathbf{a}) = \mathbb{S}_0(\mathbf{a}) = \mathbf{a}$.

Thus, the orthogonal projection $\mathbb{P}_R$ onto the l_1-norm ball is re-interpreted as the problem of finding a suitable soft-threshold value, τ. The projection on the l_1-ball can then be computed by the following steps:

1. Sort the absolute values $\mathbf{b}$, of the components of $\mathbf{a}$, which results in the rearranged sequence (b_j) with $b_j \ge b_{j+1} \ge 0$ for all j, where $b_j = |a_j|$.

2. Perform a search to find k such that

$$\left\| \mathbb{S}_{b_k}(\mathbf{b}) \right\| \le R \le \left\| \mathbb{S}_{b_{k+1}}(\mathbf{b}) \right\|_1 \text{ where } \left\| \mathbb{S}_{b_k}(\mathbf{b}) \right\|_1 = \sum_{j=1}^{k-1}(b_j - b_k)$$

3. Set $v = \left(R - \left\| \mathbb{S}_{b_k}(\mathbf{b}) \right\|_1 \right) / k$ and $\tau = a_k^* + v$, where the scalar $k \in \mathbb{R}$.

4. Complete the projection by soft-thresholding $\mathbf{a}$ as $\mathbb{S}_\tau(\mathbf{a})$.

The *projected Landweber iteration* in (4.15) can now be expressed as

$$\mathbf{z}^{(n+1)} = \mathbb{S}_{\tau}\left[\mathbf{z}^{(n)} + \mathbf{K}^{*}\left(\mathbf{y} - \mathbf{K}\mathbf{z}^{(n)}\right)\right] \qquad (4.16)$$

where the thresholding parameter τ depends upon the radius of the l_1-ball on which the iterate is projected. The above procedure is the *projected Landweber*, which we are contrasting with the earlier *thresholded Landweber* where the thresholding parameter, τ, is fixed in all iteration.

Similar method of projection onto convex sets is used for getting the sparse solution of the inverse problems and is discussed below.

4.4 Projection on Convex Sets

It is shown in [57] that, if in addition to the measurement values $\mathbf{y}$, if we are also given the l_1-norm of the true solution, α, we can recover the sparse solution by projecting on two convex sets $\mathbf{H} = \{\mathbf{z} \mid \mathbf{y} = \mathbf{K}\mathbf{z}\}$ and $\mathbf{B}_R := \{\mathbf{z} \mid \|\mathbf{z}\|_1 \le \alpha\}$ i.e. by iterating the solution as

Projection onto $\mathbf{H}$:

$$\beta = \mathbf{z}^{(n)} + \mathbf{K}^{*}\left(\mathbf{K}\mathbf{K}^{*}\right)^{-1}\left(\mathbf{y} - \mathbf{K}\mathbf{z}^{(n)}\right) \qquad (4.17)$$

It is to be noted that when $\mathbf{K}$ is orthogonal we have $\beta = \mathbf{z}^{(n)} + \mathbf{K}^{*}\left(\mathbf{y} - \mathbf{K}\mathbf{z}^{(n)}\right)$.

Projection onto $\mathbf{B}_R$:

$$z^{(n+1)} = \mathbf{S}_{\tau}(\beta) \qquad (4.18)$$

where $S_\tau(\beta)$ is defined in (4.14). The threshold τ is determined by sorting the coefficients by magnitude and perform a linear search such that $\left\| z^{(n+1)} \right\|_1 \leq \alpha$, as described in the *projected Landweber* algorithm. It is shown in [85] that for projections onto convex sets (POCS) based algorithms, every known *a-priori* property about the solution can be formulated as a corresponding convex set in a Hilbert space $\mathbf{H}$. Given n closed convex set $C_i, i = 1,2,.....,n$ with $C_0 = \bigcap_{j=1}^{n} C_i \neq 0$, the iteration $\mathbf{z}_{k+1} = P_n P_{n-1} .... P_1 \mathbf{x}_k$, $k = 0,1,2.....,$ where P_i is the corresponding projection operators defined by $\left\| \mathbf{z} - P_i \mathbf{z} \right\| = \min_{g \in C_i} \left\| \mathbf{z} - \mathbf{h} \right\|$ and $\mathbf{h}$ is the projection of $\mathbf{z}$ onto C_i, will converge to a point in C_0 for any initial $\mathbf{z}_0$. The projection on two convex sets is illustrated in Figure 4.4.
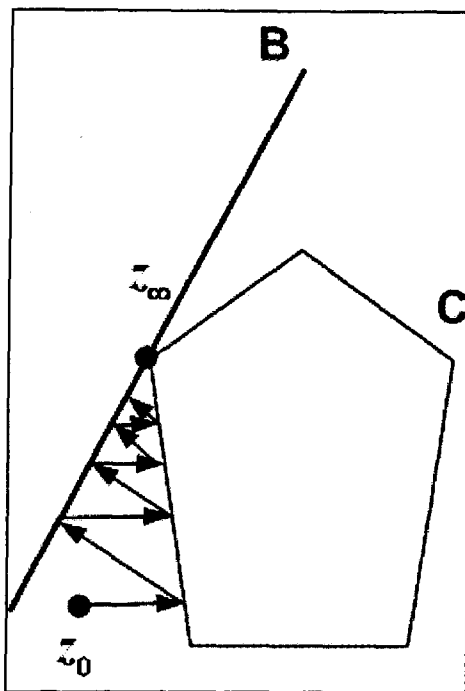
Figure 4.4 Alternating projection between two convex sets with non-empty intersection results in convergence to a fixed point $\mathbf{z}_\infty \in B \cap C$ from the initial point $\mathbf{z}_0$.

The success of the above method relies on the fact that the l_1-norm of the true solution, α, is known beforehand. In contrast, the alternative of using one of the many algorithms which solve the unconstrained problem of the form (4.11) requires the determination of the regularization parameter. This could be quite challenging as this

parameter is often either assigned manually or determined iteratively using computational expensive estimation techniques such as *generalized cross validation* [85].

Here an algorithm is proposed that solves the BPDN problem (4.11) and does not require any priori knowledge of the l_1-norm of the true solution, α, or the regularization parameter, τ, but instead projects the solution onto a sequence of convex set of increasing l_1-norm.

4.5 Proposed Algorithm L1_Adapt

The proposed algorithm works by projecting the solution onto two convex set as in equations (4.17) and (4.18). The value of l_1 norm $\alpha^{(n)}$ for determining the threshold τ in equation (4.18) is gradually increased in each iteration. The pseudo-code of the proposed algorithm L1_Adapt is shown in Table 4-1.

Initialise

$L = 1, \mathbf{z}^{(1)} = 0, \varepsilon_1 = 1e^{-5}, \varepsilon_2 = 1e^{-6}, \alpha^{(0)} = 0, n = 1$

1. $\boldsymbol{\beta} = \mathbf{z}^{(n)} + \mathbf{K}^* \left(\mathbf{y} - \mathbf{K}\mathbf{z}^{(n)} \right)$

2. $\mathbf{a} = \text{sort}(|\boldsymbol{\beta}|)$ such that $a_i > a_{i+1}, \forall i$

3. $\alpha^{(n)} = \sum_{j=1}^{L} a_j$

4. If $\alpha^{(n)} - \alpha^{(n-1)} < \varepsilon_1 \cdot \alpha^{(n)}$, then $L = L + 1$

5. Find k such that

$\left\| \mathbb{S}_{a_k}(\mathbf{a}) \right\|_1 \le \alpha^{(n)} \le \left\| \mathbb{S}_{a_{k+1}}(\mathbf{a}) \right\|_1$

where $\left\| \mathbb{S}_{a_k}(\mathbf{a}) \right\|_1 = \sum_{j=1}^{k-1} \left(a_j - a_k \right)$

6. $v = \left(\alpha^{(n)} - \left\| \mathbb{S}_{a_k}(\mathbf{a}) \right\|_1 \right) / k, \quad \tau = a_k + v$

7. $\mathbf{z}^{(n+1)} = \mathbb{S}_{\tau}(\boldsymbol{\beta})$

8. If $\left\| \mathbf{y} - \mathbf{K}\mathbf{z}^{(n+1)} \right\|^2 > \varepsilon_2, n = n + 1$, go to step 1

Table 4-1 Pseudo-code of L1_Adapt.

The description of the algorithm L1_Adapt is as follows:

1. **Initialisation:** The algorithm begins with the initialization of the iteration no. n, the index L for computation of l_1-norm, the initial guess $z^{(1)} = 0$, the convergence factor ε_1 for incrementing the index L and the convergence factor ε_2 for the algorithm to terminate.

2. **Gradient Descent Step:** This step computes the gradient of the function and finds a new value by moving in the opposite direction of the computed gradient as $\beta = z^{(n)} + K^* \left(y - K z^{(n)} \right)$.

3. **Computation of l_1-norm:** The value of the l_1-norm to which the inner iteration has to converge is computed by first sorting the coefficients in the descending order and then computing the l_1-norm as $\alpha^{(n)} = \sum_{j=1}^{L} a_j$. The Figure 4.5 illustrates the computation of the l_1-norm.
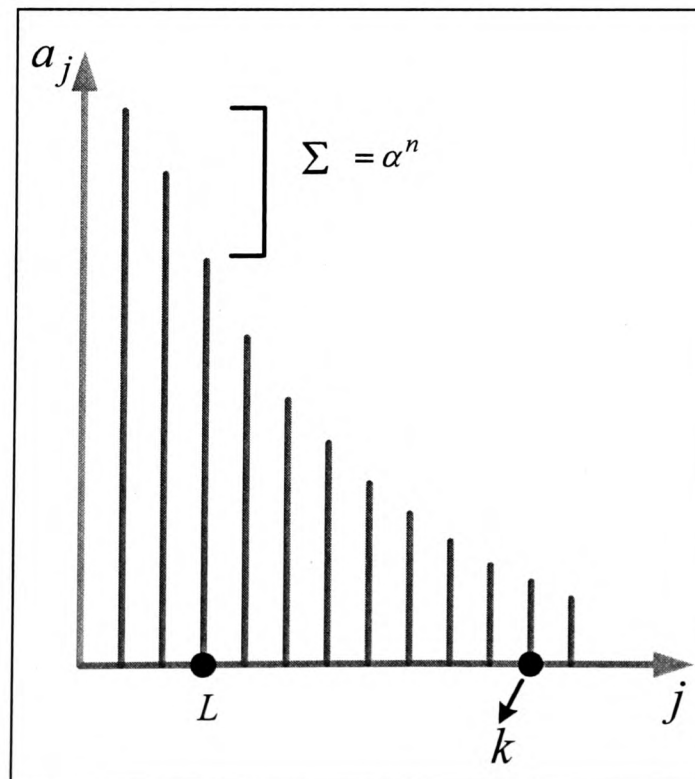
Figure 4.5 Plot of l_1-norm and its associated parameters.

79

4. The index, L, for estimating the $\alpha^{(n)}$ value in step 3. of the pseudo-code is increased stepwise whenever the solution has converged to the previous reference of l_1-norm. It is to be noted that because of the shrinkage, the number of terms, k, used to form a norm of size $\alpha^{(n)}$ after thresholding will always be greater than or equal to the number L before thresholding.

5. **Computation of Soft-thresholding value:** The step 5 and 6 computes the value τ, which is used for soft-thresholding. A search is performed to find the index k such that $\left\| \mathbb{S}_{a_k}(\mathbf{a}) \right\|_1 \leq \alpha^{(n)} \leq \left\| \mathbb{S}_{a_{k+1}}(\mathbf{a}) \right\|_1$ where $\left\| \mathbb{S}_{a_k}(\mathbf{a}) \right\|_1 = \sum_{j=1}^{k-1}(a_j - a_k)$. Then we set $v = \left(\alpha^{(n)} - \left\| \mathbb{S}_{a_k}(\mathbf{a}) \right\|_1 \right) \big/ k$ and compute $\tau = a_k^* + v$.

6. **Projection onto l_1-ball:** The projection onto the l_1-ball is computed via the soft-thresholding as $z^{(n+1)} = \mathbb{S}_\tau(\boldsymbol{\beta})$ as per (4.14) with the value τ as computed in the earlier step.

The algorithm iterates till the l_2-norm of the residue $\mathbf{y} - \mathbf{Kz}^{(n)}$ is below the threshold ε_2. Generally, ε_2 is the estimated noise level.

The pictorial representation of the algorithm, L1_Adapt, is as shown in Figure 4.6. The 2D problem, illustrated in this figure, is to obtain the point constrained to lie on a given straight line $\mathbf{y} = \mathbf{Kx}$, which is closest to the l_1-ball. This algorithm solves the problem by "expanding" the l_1 norm until it touches the hyperplane $\mathbf{y} = \mathbf{Kx}$. The proposed algorithm converges to a solution which has a minimum l_1 norm.

$$\left\| x^{(n+p)} \right\|_1 = \alpha^{(n+p)}$$

$$\alpha^{(n)} < \alpha^{(n+1)} ... < \alpha^{(n+p)}$$

$$\left\| x^{(n)} \right\|_1 = \alpha^{(n)}$$

$$\left\| x^{(n+1)} \right\|_1 = \alpha^{(n+1)}$$
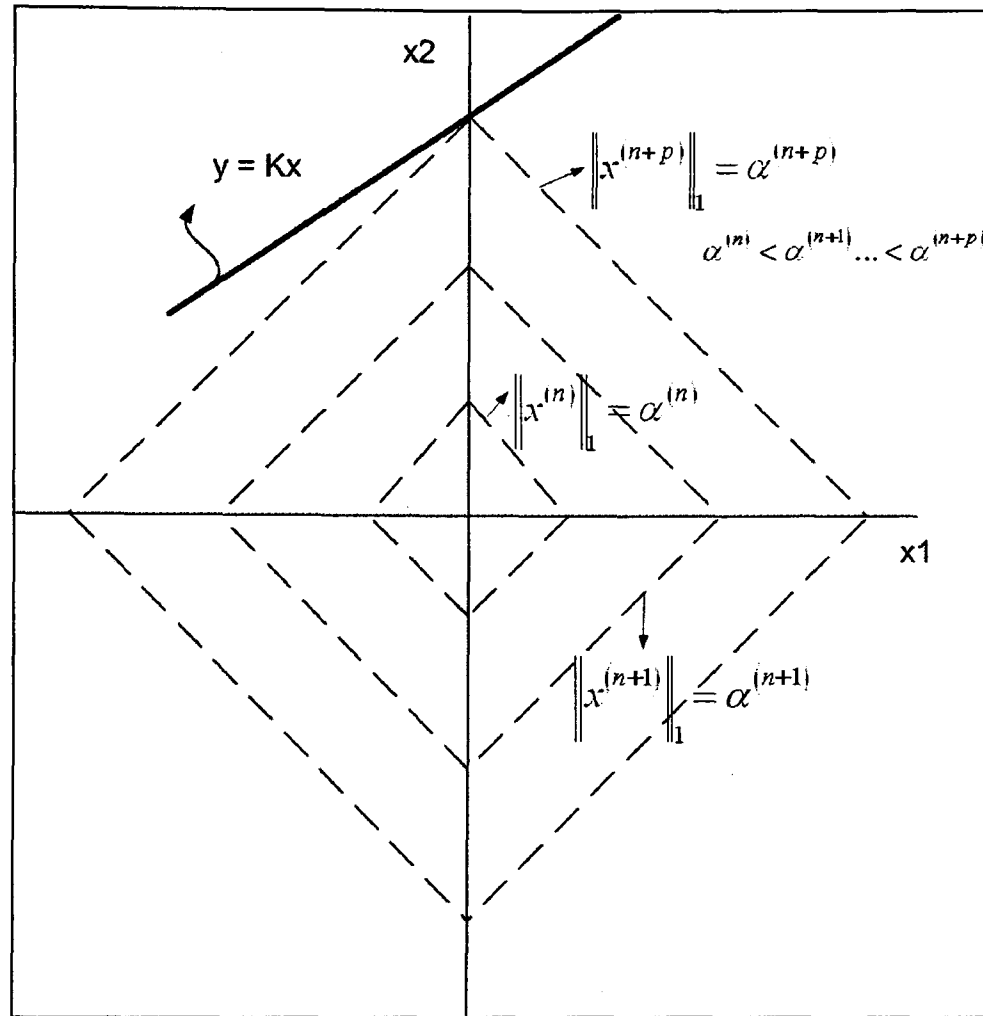
Figure 4.6 Minimization of l_1 **norm under a linear constraint.**

The convergence of L1_Adapt is accelerated by introducing a standard descent step in (4.16) as

$$\mathbf{z}^{(n+1)} = \mathbb{S}_\tau \left[\mathbf{z}^{(n)} + \delta^{(n)} \mathbf{K}^* \left(\mathbf{y} - \mathbf{Kz}^{(n)} \right) \right] \qquad (4.19)$$

where $\delta^{(n)} = \dfrac{\|\mathbf{r}\|^2}{\|\mathbf{K}^*\mathbf{r}\|^2}$, with $\mathbf{r} = \mathbf{y} - \mathbf{Kz}^{(n)}$ and $\delta^{(n)}$ is the standard descent step as calcu-

lated in steepest descent algorithm. The pseudo-code of this algorithm L1_Adapt_SD is shown in Table 4-2.

Initialise

$$L = 1, \mathbf{z}^{(1)} = 0, \varepsilon_1 = 1e^{-5}, \varepsilon_2 = 1e^{-6}, \alpha^{(0)} = 0, n = 1$$

1. $\mathbf{r} = \mathbf{y} - \mathbf{K}\mathbf{z}^{(n)}$

2. $\delta^{(n)} = \dfrac{\|\mathbf{r}\|^2}{\|\mathbf{K}^*\mathbf{r}\|^2}$

3. $\boldsymbol{\beta} = \mathbf{z}^{(n)} + \delta^{(n)}\mathbf{K}^*\mathbf{r}$

4. $\mathbf{a} = \text{sort}(|\boldsymbol{\beta}|)$ such that $a_i > a_{i+1}, \forall i$

5. $\alpha^{(n)} = \displaystyle\sum_{j=1}^{L} a_j$

6. If $\alpha^{(n)} - \alpha^{(n-1)} < \varepsilon_1 \cdot \alpha^{(n)}$, then $L = L + 1$

7. Find k such that

$$\left\| \mathbb{S}_{a_k}(\mathbf{a}) \right\|_1 \le \alpha^{(n)} \le \left\| \mathbb{S}_{a_{k+1}}(\mathbf{a}) \right\|_1$$

where $\left\| \mathbb{S}_{a_k}(\mathbf{a}) \right\|_1 = \displaystyle\sum_{j=1}^{k-1}\left(a_j - a_k\right)$

8. $v = \left(\alpha^{(n)} - \left\| \mathbb{S}_{a_k}(\mathbf{a}) \right\|_1\right)\Big/ k$, $\tau = a_k + v$

9. $\mathbf{z}^{(n+1)} = \mathbb{S}_\tau(\boldsymbol{\beta})$

10. If $\left\| \mathbf{y} - \mathbf{K}\mathbf{z}^{(n+1)} \right\|^2 > \varepsilon_2, n = n + 1$, go to step 1

Table 4-2 Pseudo-code of L1_Adapt_SD.

The convergence of such algorithm with the step size $\delta^{(n)} \ge 1$ is proved in [84]. It is also shown in [85] that the convergence of (4.19) is assured, if and only if $0 < \delta^{(n)} < \dfrac{2}{\sigma_1^2}$ where σ_1 is the largest singular value and $\sigma_1^2 = \|\mathbf{K}^*\mathbf{K}\|$. The block diagram of the proposed algorithm L1_Adapt_SD is as shown in Figure 4.7.
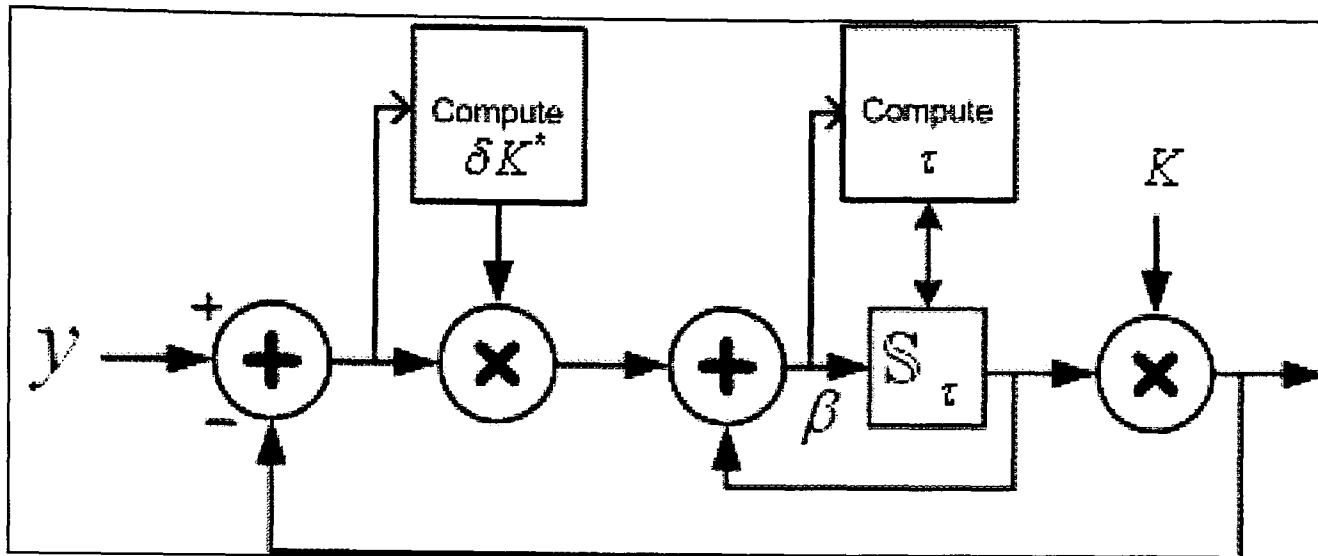
Figure 4.7 Block Diagram of L1_Adapt.

The paths, in the $\|\mathbf{x}\|_1$ vs $\|\mathbf{Kx} - \mathbf{y}\|^2$ plane, followed by the L1_Adapt_SD with the descent step and the *projected Landweber iterations* are shown in the Figure 4.8. It is seen in the Figure 4.8 that the L1_Adapt_SD with the descent step, $\delta^{(n)}$, soon catches up with the *projected Landweber iterations* and also converges faster than the *projected Landweber iterations* as shown in Figure 4.9. The graph is obtained by running an experiment with a sparse signal of length 128 samples with 20 as the sparsity index. The measurement signal of length 50 samples was obtained with a measurement matrix of Gaussian i.i.d.

The proposed algorithms, L1_Adapt and L1_Adapt_SD, work for both real and complex vectors and are more flexible as compared to the BP algorithm solved through interior-point methods as it is possible to include a-priori knowledge about the original signal expressed in form of deterministic constraints. Examples of the deterministic constraints include non-negativity or restricted bounded range of signal intensity values and finite support by defining particular region in the signal. This algorithm is also tailored for the matrices that are formed by rows taken from orthonormal matrices corresponding to fast transforms so that $\mathbf{Kx}$ and $\mathbf{K}^*\mathbf{x}$ can be computed by fast transforms.
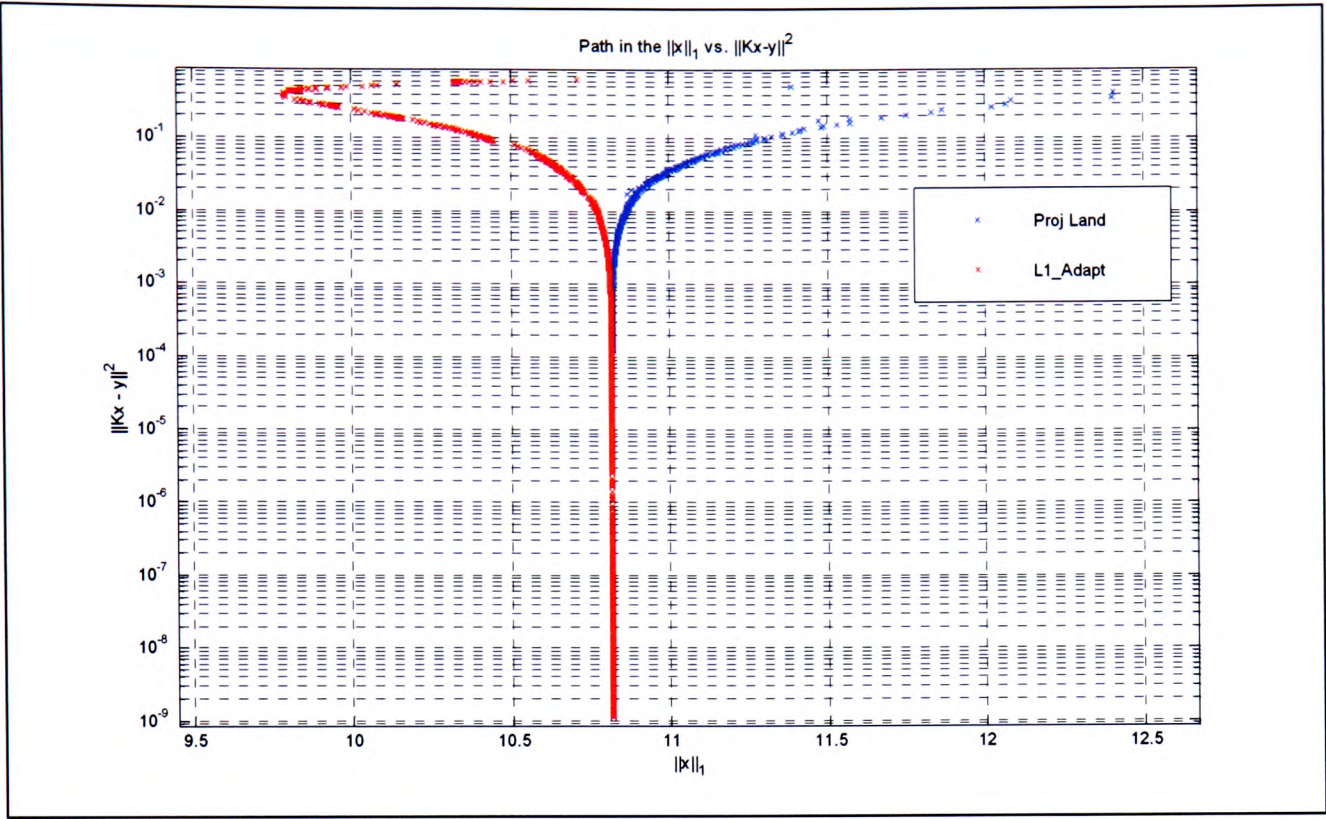
Figure 4.8 Path in the $\|x\|_1$ vs $\|Kx-y\|^2$ plane.
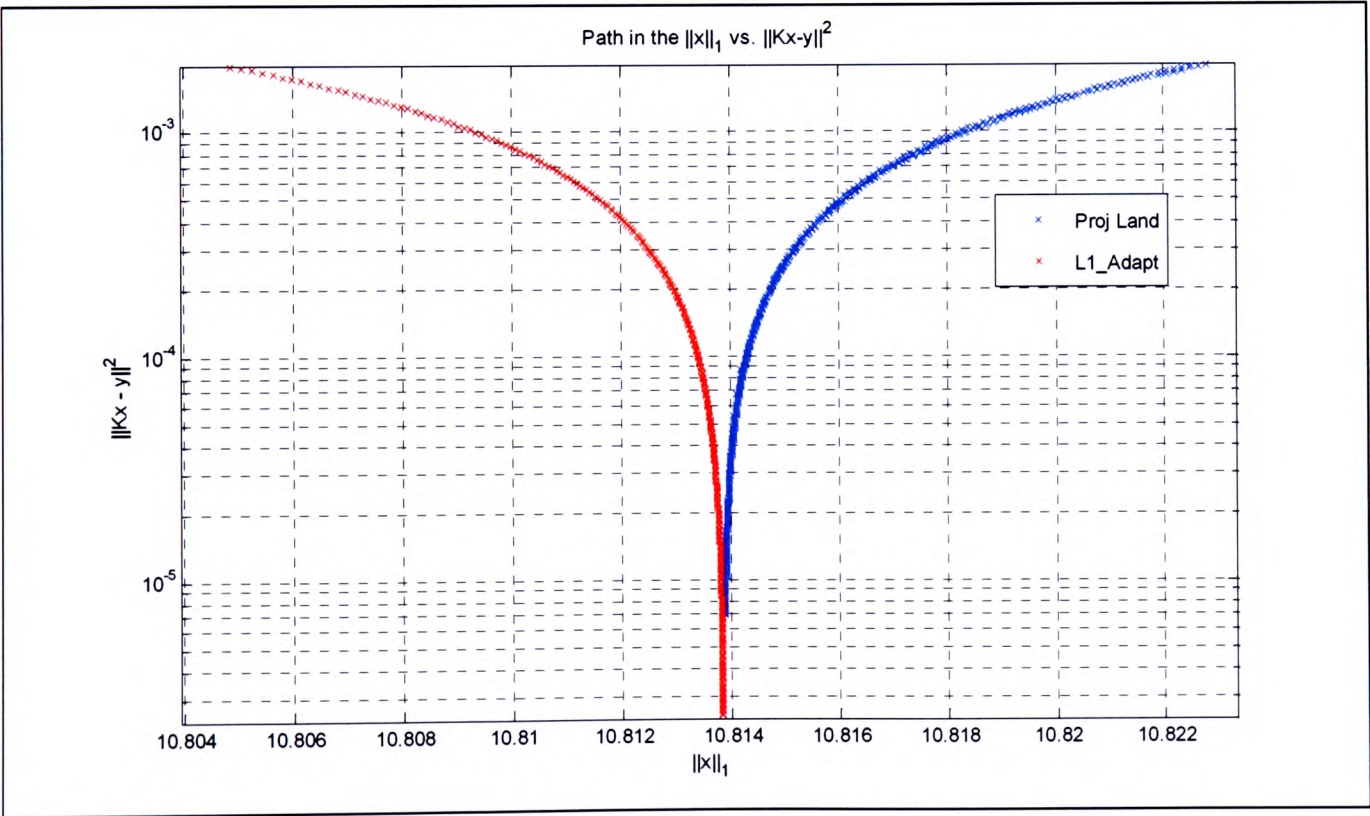
Figure 4.9 Zoomed portion of Figure 4.8.

Iterative algorithms offer interesting advantages like the possibility of developing adaptive procedures, easier ways to include constraints e.g. positivity, monitoring of the solution process and also the parameters determining the solution can be updated as the iteration progresses. The various extensions of proposed algorithm are discussed in subsequent section.

4.6 Results of L1_Adapt

The L1_Adapt algorithm is tested with four 1D examples with $N = 1024$ from *Donoho-Johnstone* [78] collection of synthetic test signals namely, '*Cusp*', '*Heavisine*' and '*Doppler*'. The other two test cases are '*Piecewise Polynomial*' and '*Piecewise Regular*', as shown in Figure 4.10. These test signals are compressible in the wavelet domain and are imitation of spatially variable functions arising in imaging, spectroscopy and other scientific signal processing applications.
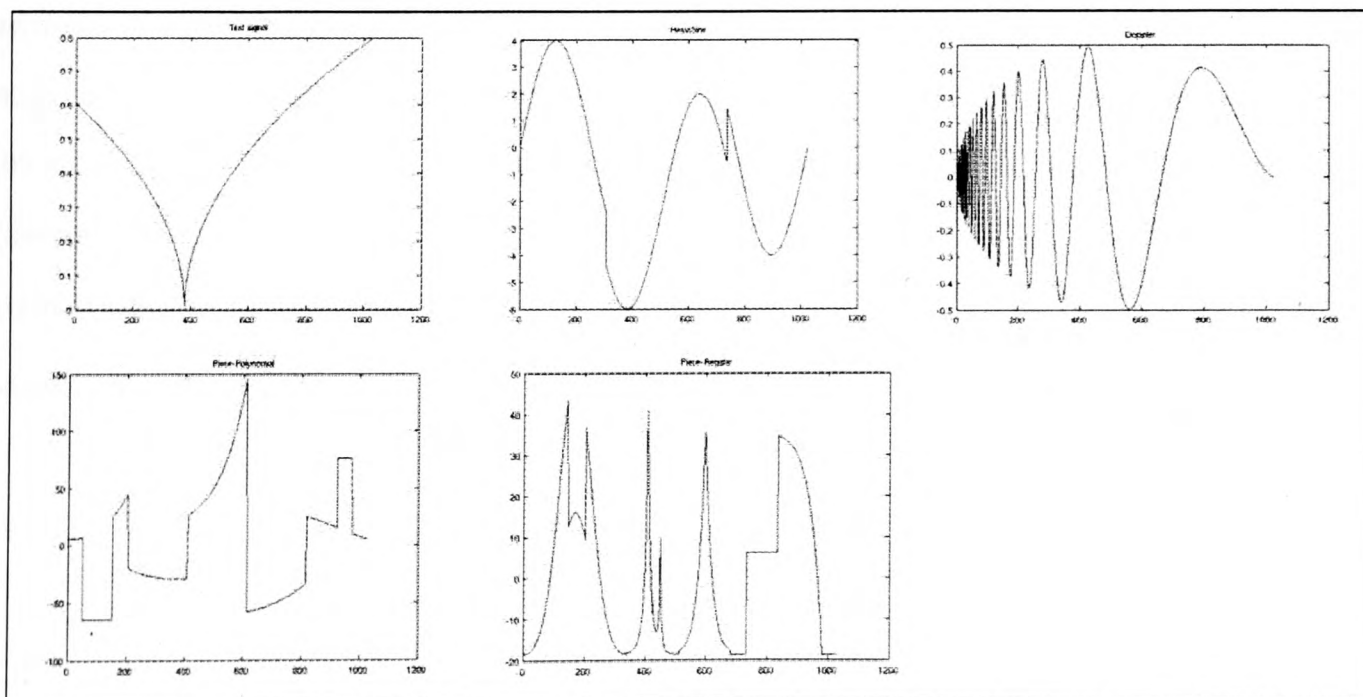
Figure 4.10 Test signals: *Cusp, Hevisine, Doppler, Piece_Polynomial, Piece_Regular.*

An experiment was performed with the measurement matrix A obtained by sampling a matrix with Gaussian i.i.d. entries which are then orthonormalized. The sparsifying transform used here is Daubechies-8 (D8) wavelet of level 1. The results for several values of M (the size of measurement vector) in comparison with SolveBP [86] for 100 runs of each experiment and are shown in Table 4-3. The mean and standard deviation of SNR and l_1-norm are tabulated as Std_SNR and Std_L1 respectively in Table 2. In the first row of each table we have the mean value of the SNR obtained by running the experiment 100 times both for the L1_Adapt and BP algorithm. The second row in each table consists of the mean value of the l_1-norm to which these both algorithms have converged to. The third and the fourth rows of each table capture the standard deviation of the SNR and l_1-norm respectively of 100 runs of the experiment for L1_Adapt algorithm. These extensive numerical results suggest that the L1_Adapt algorithm converges to the minimum l_1-norm as the *SolveBP* converges to.

In another experiment, the test signal *Cusp* of length 1024 with the sparsity of around 171 in the Daubechies-8 (D8)-wavelet basis is captured through the measurement matrix A . The signal measurement length of 250 samples is captured through a measurement matrix consisting of Gaussian i.i.d. As mentioned earlier, L1_Adapt has the flavour of decreasing soft-thresholding value, τ with increasing iteration no. and corresponding increase in l_1-norm of the solution which is shown in Figure 4.11 for the same test signal *Cusp*.

Measurement Length $M = 100$

	Cusp		Heavisine		Doppler		Piece_Poly		Piece_Regular	
	L1-Adapt	BP	L1-Adapt	BP	L1-Adapt	BP	L1-Adapt	BP	L1-Adapt	BP
SNR	24.52	24.57	16.92	16.84	4.77	4.86	3.55	3.65	4.48	4.60
L1	35.18	35.19	308.21	308.35	36.41	36.45	6431	6439	2238	2240
Std_SNR	2.93		3.47		1.84		1.60		2.04	
Std_L1	0.09		1.43		0.49		88.62		30.17	

Measurement Length $M = 200$

	Cusp		Heavisine		Doppler		Piece_Poly		Piece_Regular	
	L1-Adapt	BP	L1-Adapt	BP	L1-Adapt	BP	L1-Adapt	BP	L1-Adapt	BP
SNR	42.52	42.31	31.67	31.63	12.72	12.81	9.28	9.36	11.32	11.38
L1	36.48	36.49	327.81	327.82	46.58	46.59	8518	8522	2874	2875
Std_SNR	4.31		2.81		1.83		1.34		1.31	
Std_L1	0.01		0.20		0.15		35.97		10.06	

Measurement Length $M = 300$

	Cusp		Heavisine		Doppler		Piece_Poly		Piece_Regular	
	L1-Adapt	BP	L1-Adapt	BP	L1-Adapt	BP	L1-Adapt	BP	L1-Adapt	BP
SNR	79.80	78.35	58.74	58.60	22.16	22.22	15.20	15.27	19.11	19.18
L1	36.58	36.58	330.33	330.33	49.69	49.69	9550	9551	3144	3145
Std_SNR	18.16		3.47		1.58		1.17		1.46	
Std_L1	0.00		0.01		0.04		15.45		3.31	

Table 4-3 Results of L1_Adapt and SolveBP for various measurement size M
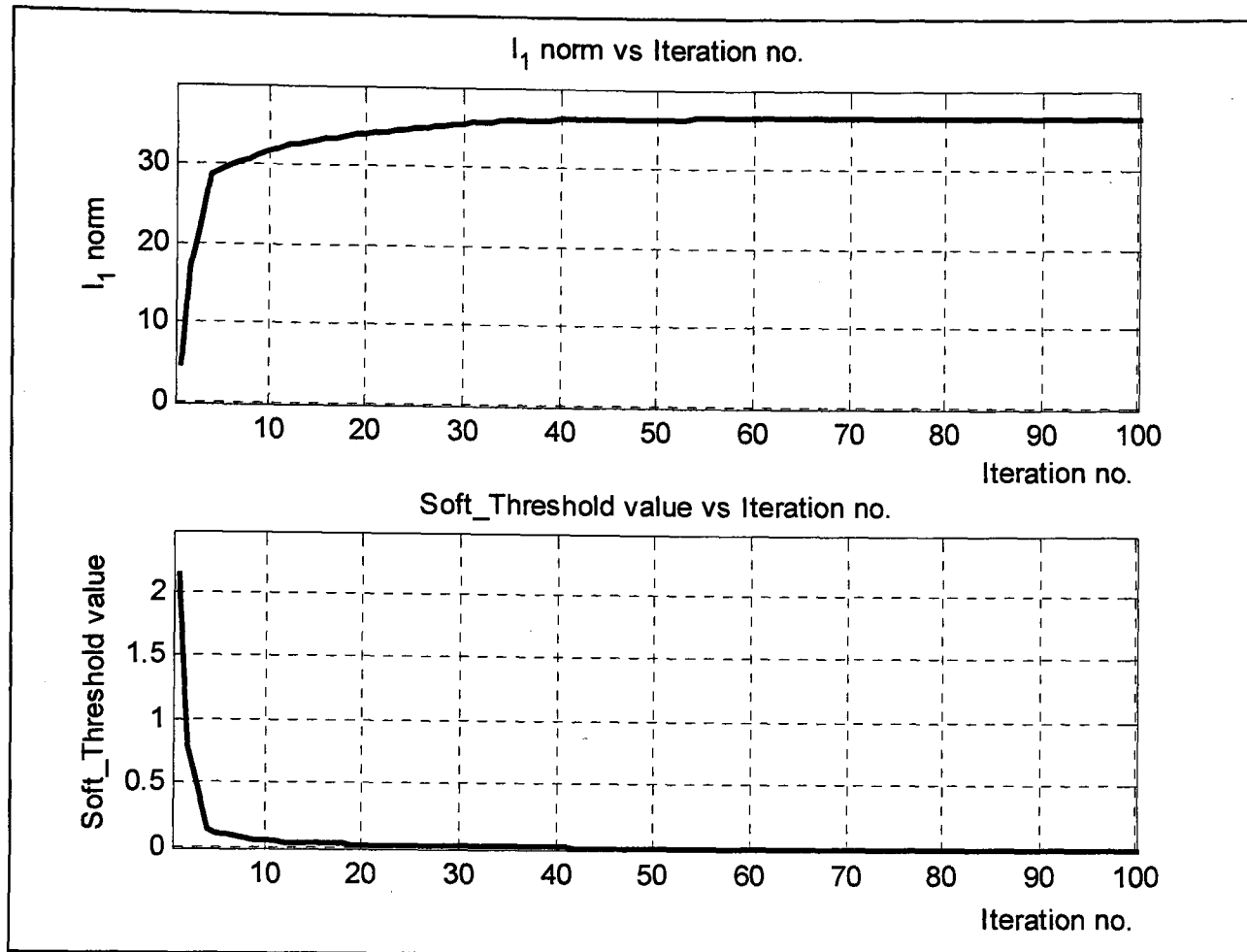
Figure 4.11 Showing increasing l_1-norm of solution and the decrease in the Soft threshold value, τ, for the first 100 iterations (Test case : *Cusp*)

The test signal and its recovery result are shown in Figure 4.12. The test signal *Cusp* of length 1024 is shown in Figure 4.12(a). The D8 wavelet transformed coefficients with sparsity index of 171 coefficients are shown in Figure 4.12(b). The measurement signal of length 256 obtained by using a measurement matrix of Gaussian i.i.d. is shown in Figure 4.12(c). The L1_Adapt algorithm recovers the sparse solution from these 256 measurement signal with a SNR of 110.24 dB as shown in Figure 4.12(d).

The algorithm is also tested with complex wavelet transform (CWT) as a frame, where the signal is sparse. More details of the use of CWT as a frame is described in chapter 5. The sparse signal of length $M = 256$ is synthetically created with the sparsity index of 46. The size of the transformed data is 544. There is an increase of the size of the data by more than 2:1 when CWT is used as a frame. The *SolveBP* is not used in this

case as $\mathbf{K}$ and $\mathbf{K}^*$ are not matrices but functions and also $\mathbf{y} \in \mathbb{C}^M, \mathbf{x} \in \mathbb{C}^N$. Instead, the L1_Adapt algorithm is compared with OMP method and the results are shown in Figure 4.13. The sparse signal of size 256 with the sparsity index of 46 is shown in Figure 4.13(a). The l_2-norm recovery is shown in Figure 4.13 (b), which does not correspond to the desired sparse solution. The OMP recovery is shown in Figure 4.13(c), which also fails to recover the desired sparse solution giving a SNR of only 10.18 dB. The result of the L1_Adapt is shown in Figure 4.13(d), which shows the recovery of the desired sparse solution with a SNR of 81.46 dB. This shows that L1_Adapt works well for some cases where the OMP fails to get the sparse solution or the minimum l_1-norm solution.

4.7 Some Further Extensions of L1_Adapt

4.7.1 Hard-Thresholding

The hard-thresholding could be used instead of soft thresholding defined in (4.14) as

$$\mathrm{H}_\tau(g) = sign(g)(1(|g| > \tau)) = \begin{cases} g & g > \tau \\ 0 & |g| \le \tau \\ -g & g < -\tau \end{cases} \tag{4.20}$$

to get sparse solution in some cases.

It has been observed that the L1_Adapt_SD converges faster, if we use the hard thresholding (4.20) initially when the difference in the computed l_1-norm in successive iterations is greater than a threshold $\xi = 0.01$ and subsequently use the soft-thresholding (4.14) when the difference in computed l_1-norm in successive iterations is below a threshold $\xi = 0.01$. We call this as Hard+Soft thresholding. An experiment is conducted with 128 length signal with 20 random values located at random locations. The measurement matrix is Gaussian i.i.d. The signal measurement length is 70.
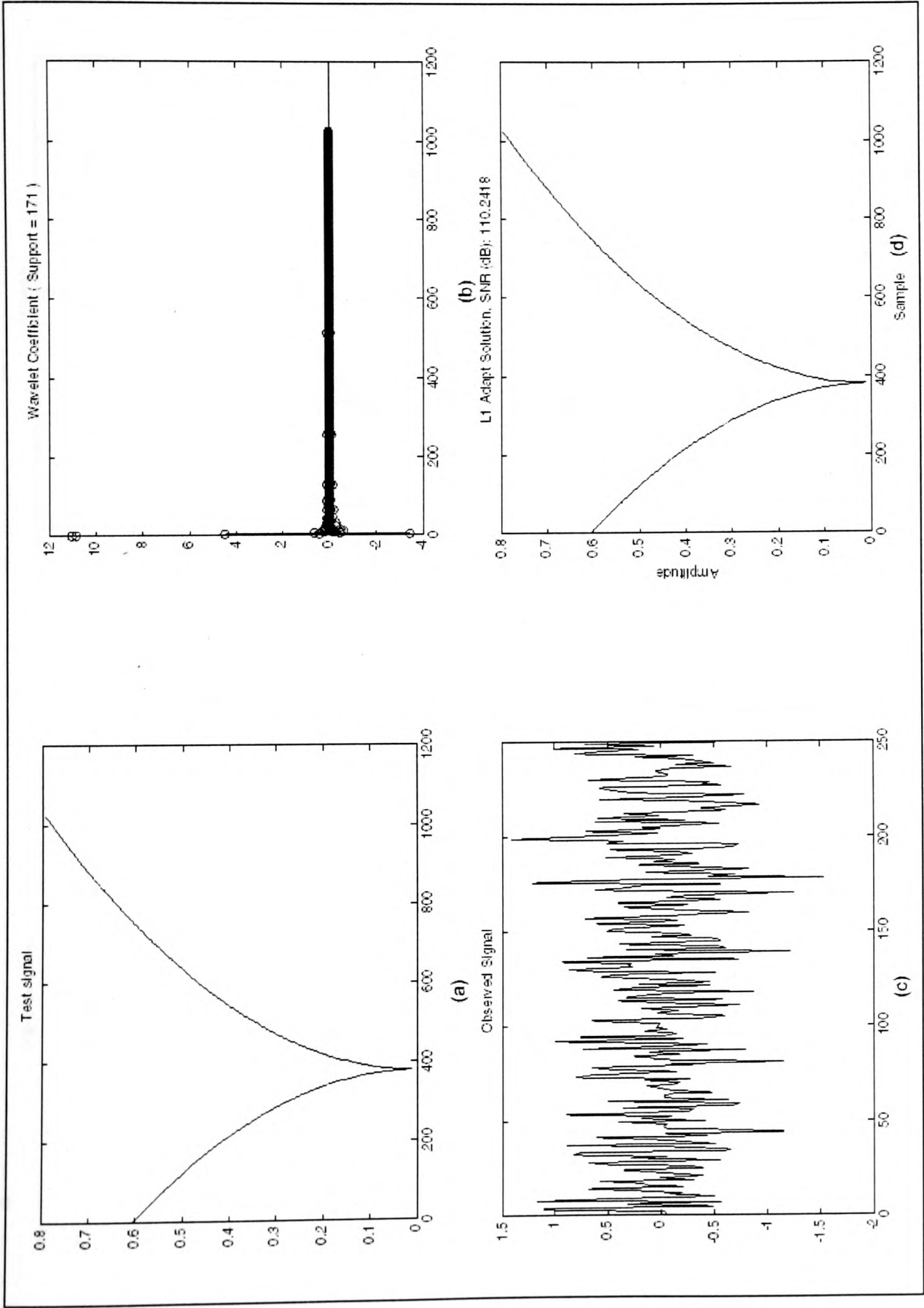
Figure 4.12 (a) *Cusp* **Signal of length 1024, (b) D8 wavelet coefficients (Sparsity = 171), (c) the measurement signal of length 250 and (d) the L1_Adapt reconstructed signal with SNR = 110.24 dB.**
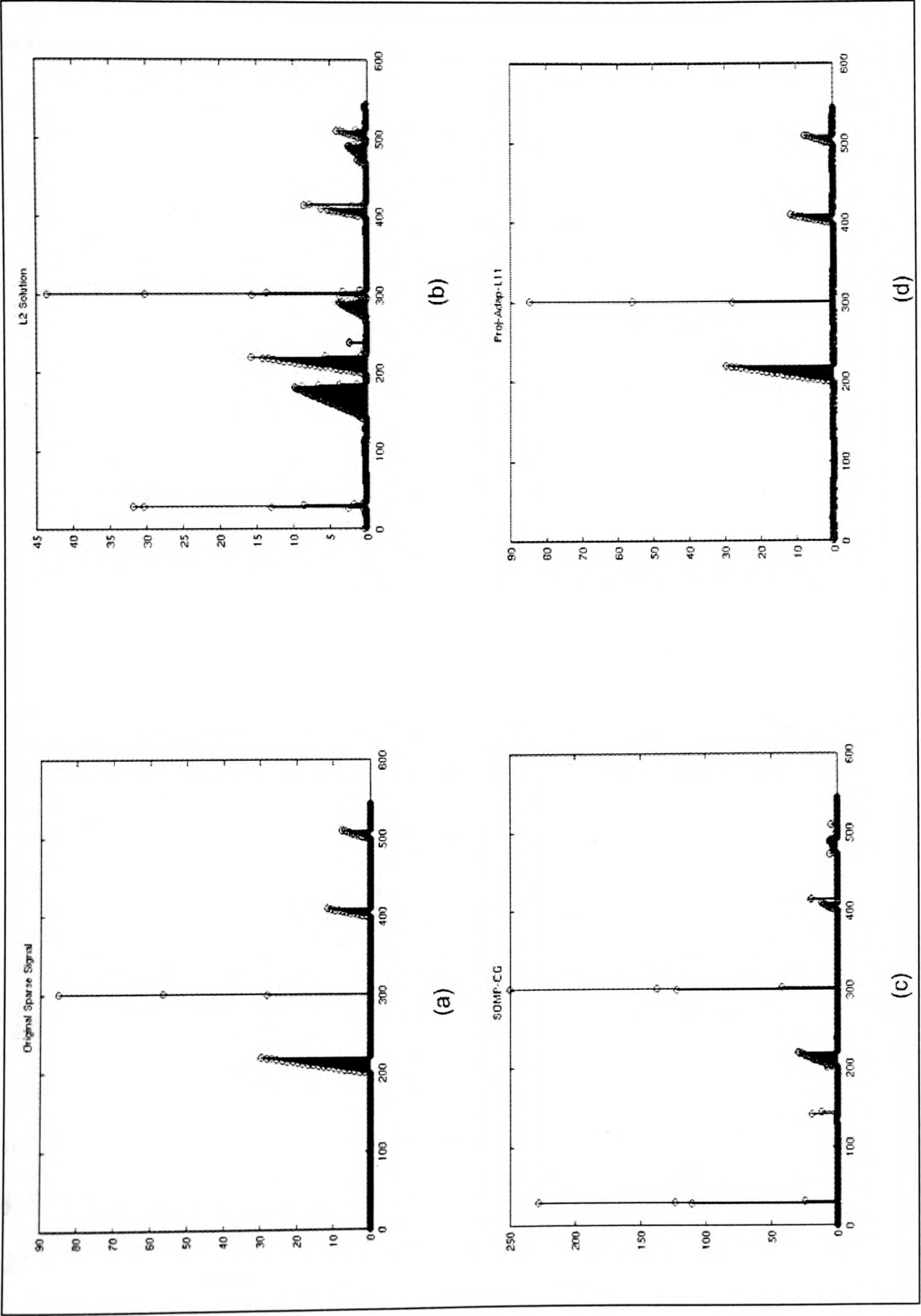
Figure 4.13 Results with CWT (a) Original Sparse Signal, (b) l_2-norm solution, (c) OMP solution (SNR = 10.18 dB), (d) L1_Adapt solution (SNR = 81.46 dB).

The sparse solution is computed with Hard+Soft thresholding and soft thresholding and the plot of l_1-norm vs the iteration no. is as shown in Figure 4.14. The L1_Adapt_SD takes 2520 iterations to compute the sparse solution whereas the Hard+Soft thresholding scheme takes only 551 iterations to converge.
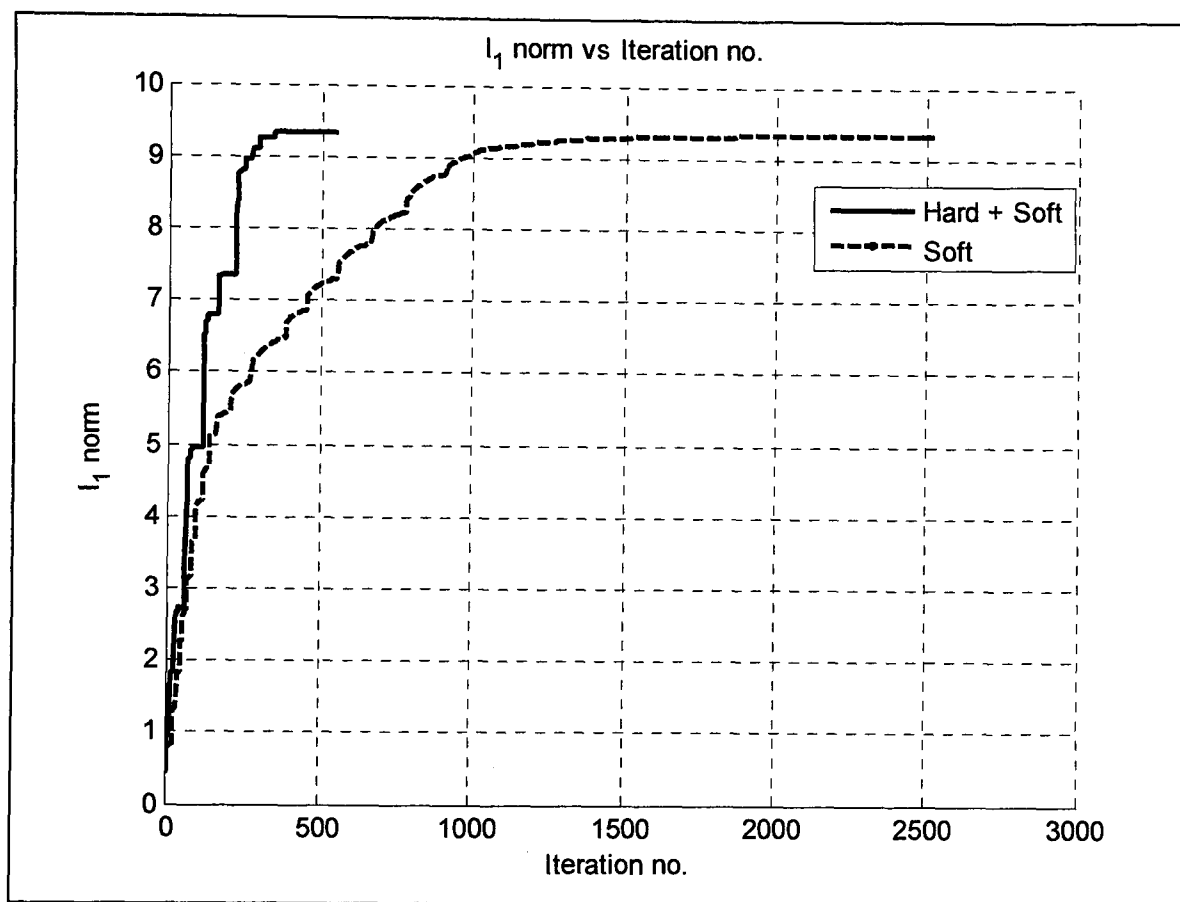
Figure 4.14 Plot of l_1-norm vs iteration no. for the Hard+Soft and Soft Thresholding.

4.7.2 Positivity Constraint

An additional constraint of positivity can be included in cases where the solutions have all positive coefficients. The positivity constraint is accounted for in L1_Adapt by projecting at each iteration the solution of the previous update equation on the cone generated by the vectors having positive entries as $\mathbf{z}^{(n)} \leftarrow \mathbb{P}_C\left(\mathbf{z}^{(n)}\right)$ where the projector $\mathbb{P}_C$ for vector is defined by component-wise projection, P_c, of each element of the vector as

92

$$P_C\left(z_i\right) = \begin{cases} z_i & \text{if } z_i > 0 \\ 0 & \text{otherwise} \end{cases} \tag{4.21}$$

We performed an experiment by simulating a test signal with all positive values of amplitude 1 at random positions of size $N = 1024$ as shown in Figure 4.15(a). The measurement signal of length $M = 100$ is obtained through a Gaussian i.i.d. matrix. The signal recovery with OMP is shown in Figure 4.15 (b) with an SNR of -2.04 dB and the recovery through L1_Adapt is shown in Figure 4.15(c) with an SNR of 4.79 dB. The L1_Adapt with an additional constraint of positivity resulted in a very good recovery of the original sparse signal with an SNR of 95.70 dB. A good recovery of the signal for this experiment with L1_Adapt and OMP were obtained for measurement length of 128 samples. Thus, the recovery of the signal in this case was observed to be successful with much less measurement data as compared to when no such additional constraint was included. This demonstrates the improvement that can be achieved by including all the *a-priori* information that we have for the solutions.

4.7.3 TV Regularization

In [87], it is shown that wavelet soft shrinkage on a single scale with *Haar* wavelets and threshold parameter τ is equivalent to TV regularization of two-pixels pair with regularization parameter $\tau/2$. An experiment was performed with a test signal of length 1024 and sparse in Haar wavelet transform domain, as shown in Figure 4.16(a). The sparse Haar coefficient with support of 65 is shown in Figure 4.16(b). The measurement signal of size of 300 is obtained by Gaussian i.i.d. matrix. The signal recovery with total variation (TV) method [57, 88] is shown in Figure 4.16(c) with an SNR of 14.48 dB and the recovery through L1_Adapt is shown in Figure 4.16(d) with an SNR of 95.70 dB. The L1_Adapt in this case gives much result than the equivalent TV method.
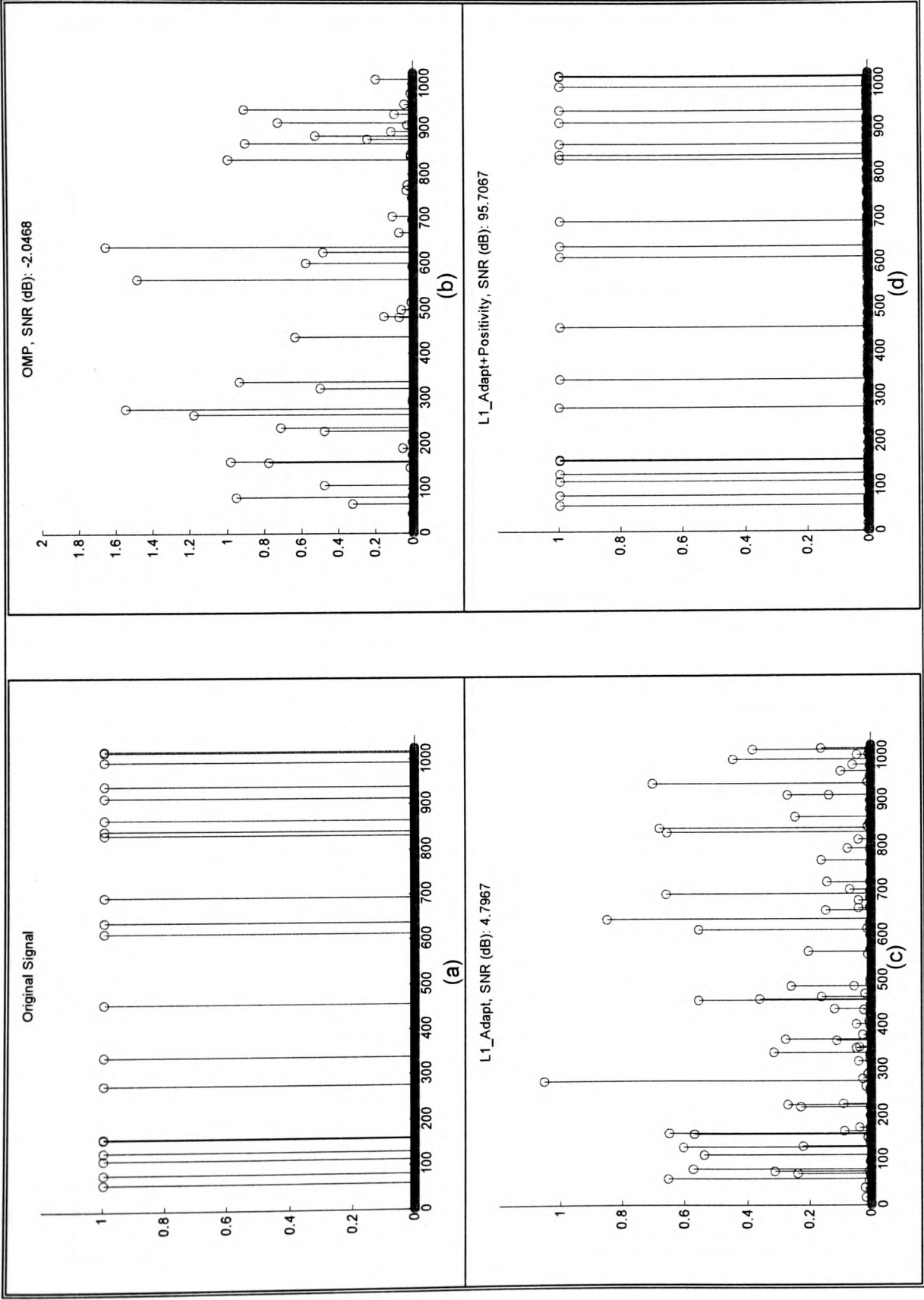
Figure 4.15 Results with 100 points measurements (a) Original Sparse Signal, (b) OMP solution (SNR = -2.04 dB), (c) L1_Adapt solution (SNR = 4.79 dB), (d) L1_Adapt + Positivity solution (SNR = 95.70 dB).

94
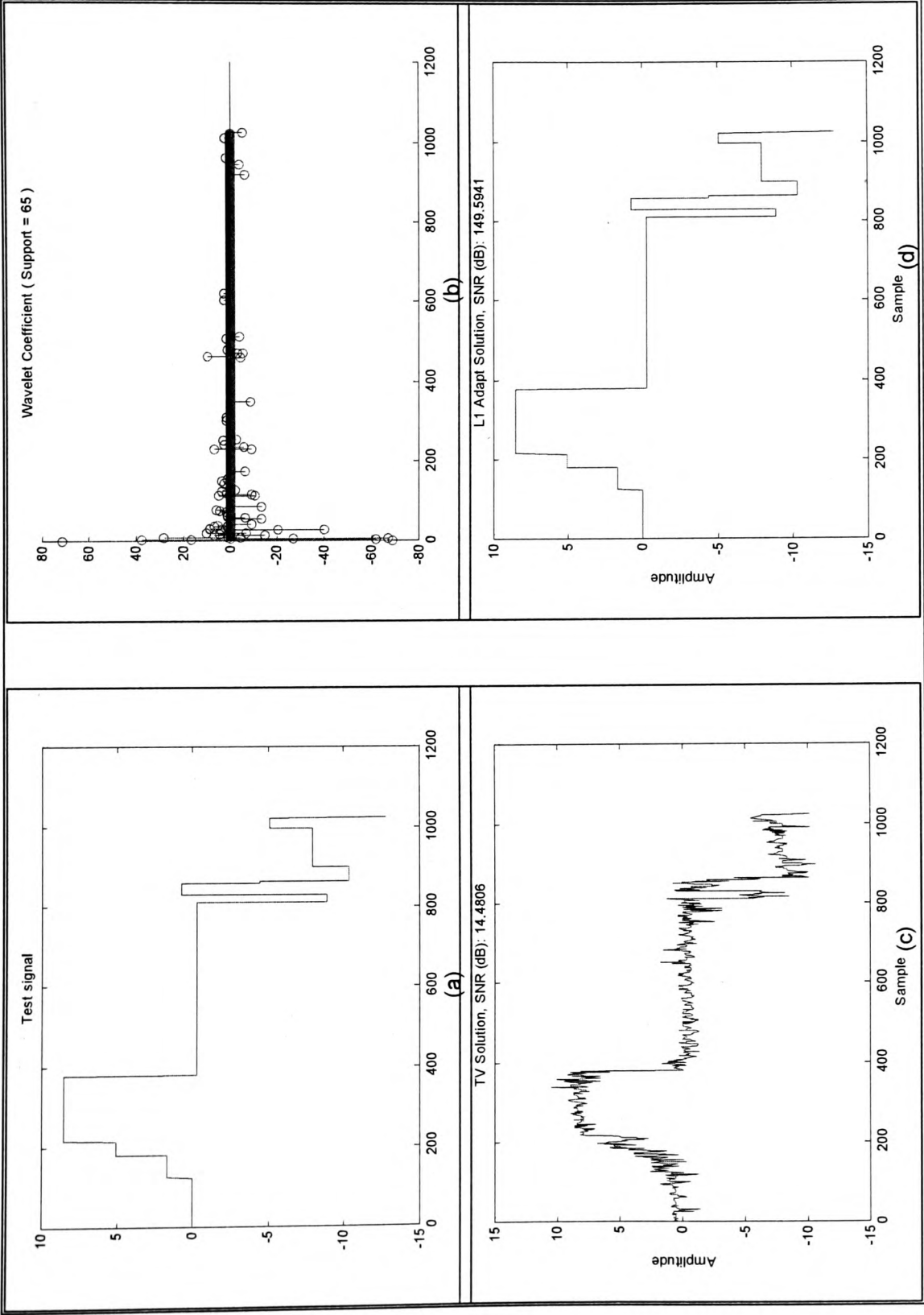
Figure 4.16 Results with 300 points measurements (a) Original test signal, (b) Sparse Wavelet coefficients (Support = 65), (c) TV solution (SNR = 14.48 dB), (d) L1_Adapt (SNR = 149.59 dB).

The L1_Adapt algorithm, in fact, could be used to find a solution $\hat{x}$ as a minimizer of a more general convex objective function $f : \mathbb{C}^m \rightarrow \mathbb{R}$ given by and defined in [60]

$$f(\mathbf{x}) = \frac{1}{2} \| \mathbf{y} - \mathbf{K}\mathbf{x} \|^2 + \tau \Phi(\mathbf{x}) \tag{4.22}$$

where $\Phi : \mathbb{C}^n \rightarrow \mathbb{R}$ is a function defined as:

1. Weighted l_p norm

The weighted l_p norms, for $p \geq 1$, are defined as

$$\Phi_{l_p^w} = \| \mathbf{x} \|_{p,w} = \left(\sum_i w_i |x_i|^p \right)^{1/p} \tag{4.23}$$

where $w_i \geq 0$.

For the case when $p = 1$, the projection onto to the convex set B_R is given as

$$\mathbf{z}^{(n+1)} = \mathbb{S}_\tau(\boldsymbol{\beta}) \tag{4.24}$$

where $S_\tau(z_i) = \text{sign}(z_i)(|z_i| - \tau w_i)^+$.

It is shown in [89] that sparse recovery of the algorithm which consists of solving a sequence of weighted l_1-minimization problems, where the weights used for the next iteration are computed from the value of the current solution, outperforms l_1 minimization algorithms. In such case,

$$w_i^{n+1} = \frac{1}{|x_i^n| + \varepsilon} \tag{4.25}$$

where $\varepsilon > 0$.

2. p^{th} Power of a Weighted l_p Norm

This class of regularizes, is defined as

$$\Phi^p_{l^w_p} = \|\mathbf{x}\|^p_{p,w} = \sum_i w_i |x_i|^p \tag{4.26}$$

The denoising operator for various p is discussed in [60] and given below

a) For $p = 1$, the denoising operator is as described in (4.14).

b) For $p > 1$, the denoising operator or the *shrinkage* function is given as

$$\hat{x}_i = S_{\tau w_i, p}(\beta_i) \tag{4.27}$$

where $S_{\lambda,p} = F^{-1}_{\lambda,p}$ is the inverse function of

$$F_{\lambda,p}(\mathbf{x}) = \mathbf{x} + \lambda p \, \text{sign}(\mathbf{x}) |\mathbf{x}|^{p-1} \tag{4.28}$$

Generalized Landweber Iterations:

The algorithms discussed in the above sections can be considered as a special case of Generalized Landweber iterations which are summarized as below.

If $\mathbf{z}^{(n+1)} = \mathbb{S}_\tau \left[\mathbf{z}^{(n)} + \mathbf{M}^* \alpha^{(n)} \mathbf{r}^{(n)} \right]$, $\mathbf{r}^{(n)} = \left(\mathbf{y} - \mathbf{K}\mathbf{z}^{(n)} \right)$ then we have

1. *Thresholded Landweber* : $\tau = $ constant, $\alpha^{(n)} = I$

2. *Projected Landweber* : $\tau = \mu \left(R, \mathbf{z}^{(n)} \right)$, $\alpha^{(n)} = I$

3. *Projected Steepest Descent*: $\tau = \mu \left(R, \mathbf{z}^{(n)} \right)$, $\alpha^{(n)} = \dfrac{\left\| \mathbf{r}^{(n)} \right\|^2}{\left\| \mathbf{M}\mathbf{r}^{(n)} \right\|^2}$

4. *Projections on Convex Sets* : $\tau = \mu\left(R, \mathbf{z}^{(n)}\right)$, $\alpha^{(n)} = \left(\mathbf{MM}^*\right)^{-1}$

5. *L1_Adapt* : $\tau =$ compute, $\alpha^{(n)} = I$

6. *L1_Adapt_SD:* $\tau =$ compute, $\alpha^{(n)} = \dfrac{\left\|\mathbf{r}^{(n)}\right\|^2}{\left\|\mathbf{Mr}^{(n)}\right\|^2}$

It is also possible to include the l_2-norm of the solution in the unconstrained optimization formulation of (4.11) as $\mathbf{z}_{1c} = \operatorname{argmin}\left\{\dfrac{1}{2}\|\mathbf{Kz} - \mathbf{y}\|^2 + \zeta\|\mathbf{Lz}\|^2 + \tau\|\mathbf{z}\|_{l_1}\right\}$ and solving through the iterative algorithm $\mathbf{z}^{(n+1)} = \mathbb{S}_\tau\left(\left(1 - \zeta\mathbf{L}^*\mathbf{L}\right)\mathbf{z}^{(n)} + \mathbf{K}^*\left(\mathbf{y} - \mathbf{Kz}^{(n)}\right)\right)$.

4.8 Conclusions

An iterative algorithm for the computing sparse solutions (or sparse approximate solutions) to linear inverse problems is presented, in which no prior knowledge about the regularization parameter is required. The required regularization parameter is computed at each iteration step. The algorithm starts with $\mathbf{z}^{(0)} = 0$ and slowly increases the l_1-norm of the successive approximations. The various advantages of the iterative methods over the standard l_1-norm minimization algorithms and various possible extensions are also discussed. We emphasize that our algorithm does not require any linear system solvers or matrix factorizations and requires only vector operations and matrix-vector multiplications. The algorithm can also take full advantage of fast transforms like fast Fourier transform (FFT), discrete wavelet transform (DWT), etc. The algorithm is tested with various test signals both real and complex and is shown to converge to the min l_1-norm solution as that of BP algorithm. Few mechanisms to increase the speed of convergence of the algorithm are also presented. This new algorithm is used as a reconstruction algorithm to compress SAR raw data in the compressed sensing framework, as discussed in the chapter 5.

Chapter 5

5. Compressed Sensing Framework for SAR Raw Data Compression

In this chapter, we describe a framework for compressing the SAR raw data by sampling the signal below the *Nyquist rate* using the ideas from *Compressed Sensing*. The major contribution of this chapter is a regularization based SAR image reconstruction from sub-sampled complex-valued raw data. Due to the low computational resources available onboard satellite, the idea is to use a simple encoder, with a 2D FFT and a random sampling. Decoding is then based on the *iterative algorithm*, as described in Chapter 4, or uses greedy algorithms such as *orthogonal matching pursuit* (OMP). Unlike standard image processing problem, SAR involves data processing with complex-valued and random-phase coefficients corresponding to scatterers on the ground, as seen in Chapter 2. This complex-valued and random-phase characteristic of the SAR images makes the extension and application of real-valued regularization methods challenging. Moreover, *speckle* noise is formed during the processing of the radar returns into a SAR image which in turn severely degrades the compression/ decompression results. In one of our experiments described here we have modified the complex wavelet transform (CWT), generally applied to the real data for shift invariance, for the complex-valued data to use it as a *sparsifying* transform. We provide results both with simulated SAR raw data and actual satellite data and measure the reconstruction quality with metrics such as PSLR and ISLR, as described in Chapter 2.

5.1 SAR Raw Data Collection and its Characteristics

The SAR system being a linear system, it is natural to characterize its performance through its impulse response. In a SAR system, the impulse response is obtained by measuring the system response to a single, isolated scatterer on the ground, such as

100

corner reflector. The most important parameters that can be measured from the point target are 1) the impulse response width that defines the SAR resolution and 2) the peak sidelobe ratio (PSLR) and the integrated sidelobe ratio (ISLR) which is related to the image contrast. The PSLR is defined as the ratio of the peak intensity of the most prominent sidelobe to the peak intensity of the mainlobe. The ISLR is the ratio of the power in the mainlobe to the total power in all the sidelobes.

The radar return for SAR system can be modeled as the superposition of several small scatterers within the antenna beam footprint. The contribution from each of these scatterers on the ground is independent and their amplitude and phase are also statistically independent. The radar return signal is due to the convolution of the transmitted signal with the individual point scatterers within the antenna beam footprint. The radar return thus received by the SAR receiver is then converted to complex I and Q channels. It is shown in Chapter 2 that the real and imaginary parts of the complex radar return are uncorrelated, have zero mean with Gaussian distribution and with variable variance (power). The magnitude of these complex-valued return has a *Rayleigh* distribution with its phase being uniformly distributed between $-\pi$ to π.

The raw data used in this study is from a SAR point target simulator, actual satellite data and raw data generated through inverse SAR processing of SAR magnitude data. The details for generating SAR raw data through the above processes are described in Chapter 2. The SAR image formation from the raw data is shown in Figure 5.1 which involves the transformation of complex raw data, via the Fourier transform and geometric projections, to produce a complex-valued image. A detected SAR image is formed through non-linear transformation consisting of the sum of squares of I and Q components. It is to be noted that complex SAR image preserves both the phase and the magnitude information of the returned signal whereas the SAR detected image is produced that corresponds to the point-by-point magnitude of the complex data from which all phase information has been removed.
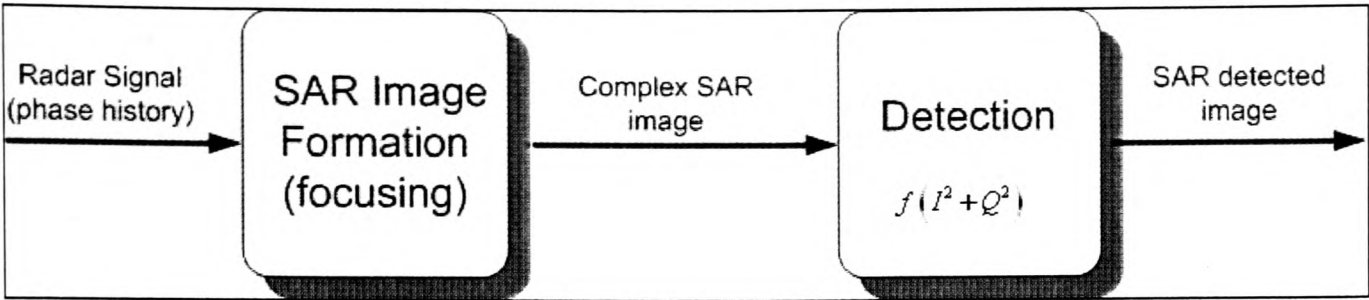
Figure 5.1 Block diagram of SAR image formation.

5.2 Compressed Sensing Framework Description

The compressed sensing (CS) framework for compressing the SAR raw data is shown in the Figure 5.2. The three essential ingredients required to carry out compression in the CS framework are: 1) the incoherent projection of the signal to get the measurement data, 2) the implicit sparsity of the SAR images and 3) the non-linear reconstruction algorithm. By implicit sparsity of SAR images, we mean that the underlying object to recover happens to have a sparse representation in a known and fixed mathematical transform domain e.g. wavelets, Fourier domain, spatial finite differences, etc. In Figure 5.2, the top path shows the random sampling and the sparse reconstruction to get the reconstructed image where the lower path shows the conventional $\omega - k$ SAR processing.
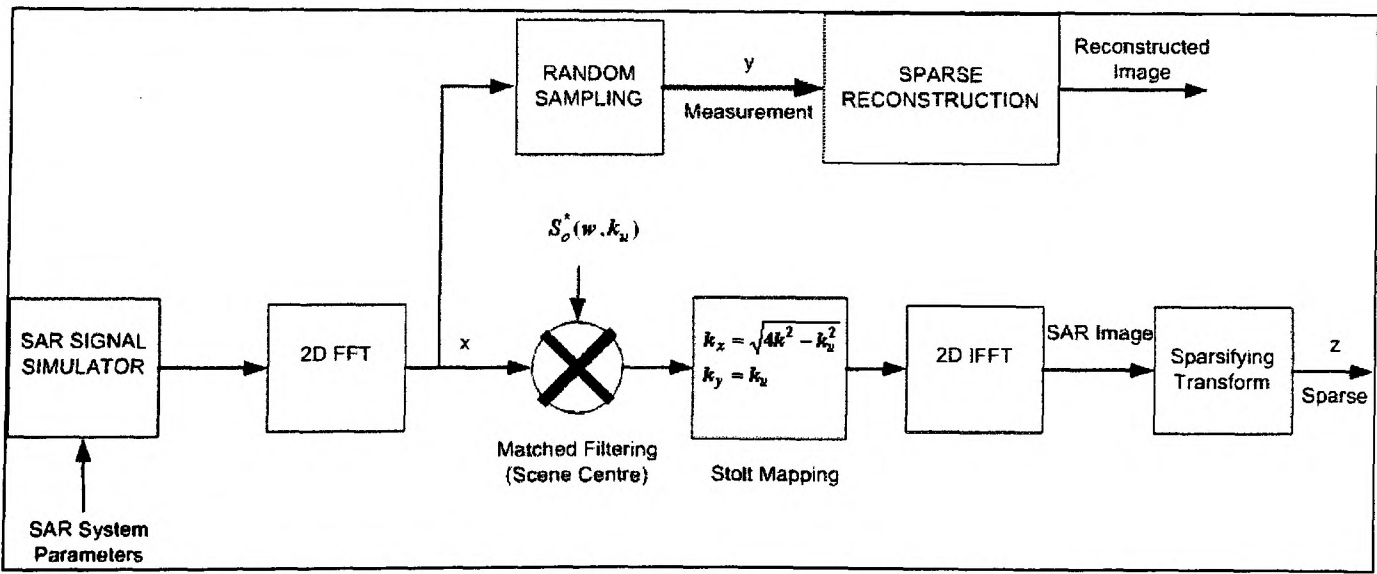
Figure 5.2 Compressed sensing framework to compress SAR raw data.

5.3 SAR Signal Simulator

To study the feasibility of using CS for SAR raw data compression, we used five point targets simulated through the SAR simulator, as shown in Figure 5.3(a), with ideal point target response in Figure 5.3(b). The important parameters used for the simulation of the point targets are as given in Table 1.1 of Chapter 2. The point targets generation is based on the $\omega - k$ algorithm. The raw data can also be generated from the actual satellite SAR complex image or the SAR magnitude image (with random phase) by inversing the $\omega - k$ algorithm [18].

5.4 SAR Processing

The SAR image formation methods can be broadly classified into two classes: methods based on Fourier transform and backprojection (time domain) methods. The most common Fourier transform based methods are the range-Doppler [90], polar format [9], $\omega - k$ [91, 92] and chirp-scaling algorithms [93]. These algorithms either require interpolation in the frequency domain or an approximation to the interpolation (as in the case of Chirp-Scaling algorithm) to compensate for the range migration effects. On the other hand, the backprojection algorithm [10, 94] eliminates the requirement for the interpolation associated with the Fourier based methods, at the expense of substantially greater processing time. In backprojection method, we select a pixel to integrate over the aperture to compute its value and then move on to the next pixel. Though, there are fast back projection methods which go in some way to re-dress the balance.

The method adapted here to process the SAR images is the $\omega - k$ algorithm which can handle large swath and large squint angles. The processing of SAR raw data as shown in Figure 5.2, involves computation of a 2D FFT, matched filtering with the scene centre reference function, converting the polar format data to the rectangular format through *Stolt* mapping and finally a 2D IFFT to get the SAR complex image [11]. The detected image is formed by a non-linear operation i.e. a squared magnitude operation on this complex image.

103

Range
(a)

Range
(b)
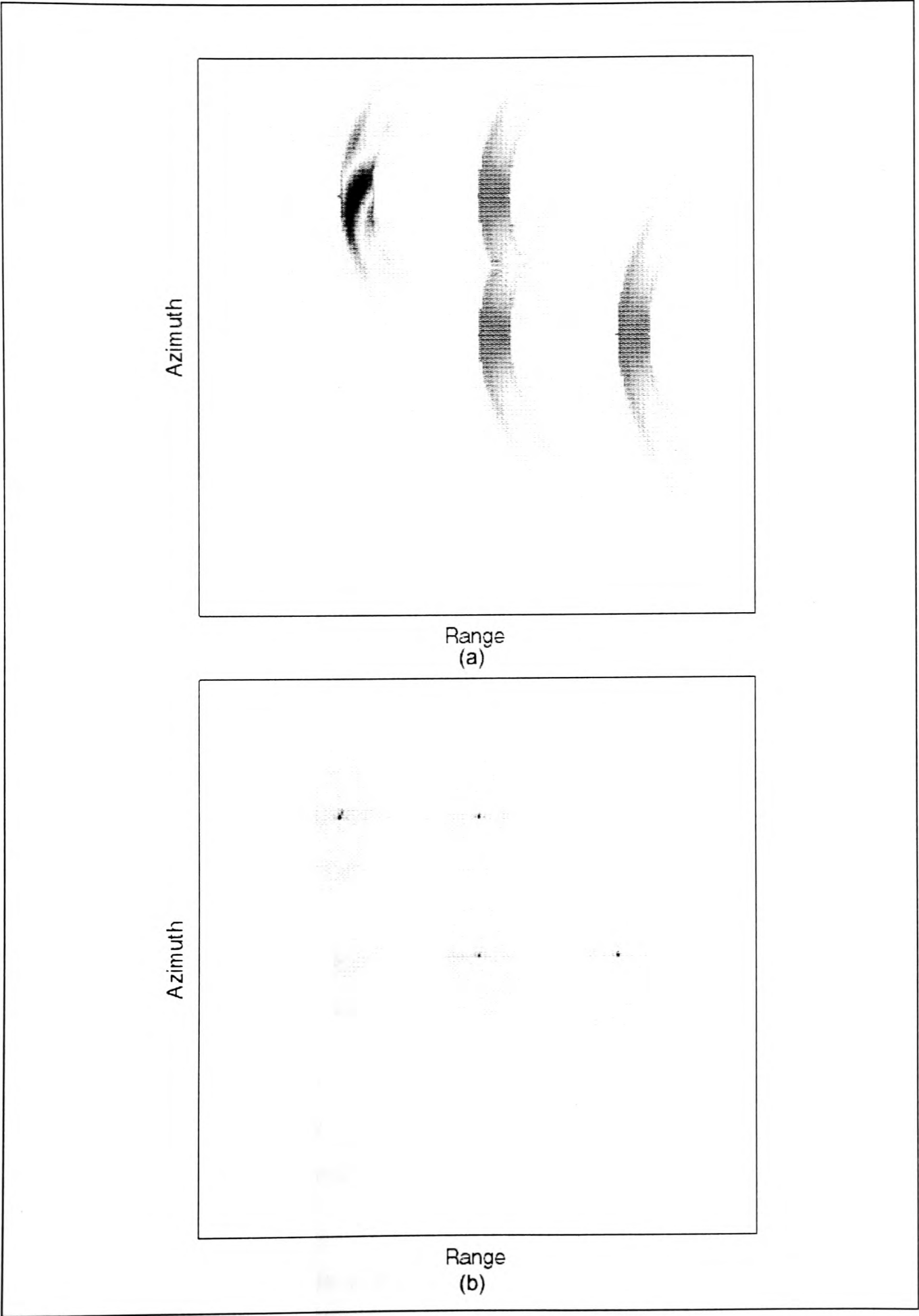
Figure 5.3(a) SAR simulated signal, (b) Point targets.

5.5 Incoherent Sampling

We have considerable freedom to design incoherent sampling trajectories as required for CS. Enhanced performance is reported in [19, 95, 96] by sampling along the radial lines in the k-space and sampling along the spiral trajectories for magnetic resonance images (MRI). As we can see from the $\omega - k$ plot in Figure 5.4(b) of the actual SAR image in Figure 5.4(a), there is no specific concentration of coefficients which would enable us to design any specific sampling strategies like spiral or radial to get high performances. In such cases, it is best to have random sampling of the data in k-space, which is often termed as Cartesian sampling. In the original CS papers [19, 20], sampling a completely random subset of k-space was also chosen to guarantee a very high degree of incoherence, which is an essential ingredient for CS. It is also important to note that the Cartesian sampling is the most common approach as an implementation of such under-sampling scheme is simple and requires minor modification to the data acquisition system.

5.6 Sparsifying Transform

One of the major ingredients for the successful compression of the signal in a CS framework is the sparse representation of the underlying object. The approaches considered here to provide a sparse representation of the complex-valued SAR data are

a) sparse representation of the magnitude and phase separately,

b) sparse representation of the real and imaginary separately and

c) sparse representation by shifting the frequency spectrum to all positive frequencies, so that the real part of the complex data carries both phase and magnitude information of the original complex image [5].

In the case of reconstruction of the point targets, we consider the identity transform, so that the transform domain is the image domain itself. For this case, the *sparsity* specifies that there are few pixels with non-zero values. Actual satellite SAR images are

not sparse in the pixel representation but they do exhibit transform sparsity. Discrete wavelet transform (DWT) based methods have been used to compress the complex valued SAR raw data [5, 21, 22, 97, 98]. Their success is shown to be the fact that wavelet transforms of such images tends to be sparse i.e. few coefficients have significant values. We have used both the DWT and complex wavelet transform (CWT) as sparsifying transform for the actual satellite SAR complex images in Section 5.9 and 5.10 respectively and have shown that the performances of these transforms are not sufficient to provide a substantial compression for the suggested framework.

Conventional compression of detected (amplitude or magnitude) SAR images has been studied in [21] and it is found that in many cases the detected SAR images have compression ratios much better than the complex images. However, such sparsifying transforms with the detected images could only be used in the CS framework by using non-linear reconstruction algorithms like the half-quadratic regularization [99], which is a topic for further study. The following objective function was used in [99] for feature enhanced imaging for SAR,

$$J(\mathbf{z}) = \left\| \mathbf{y} - \mathbf{Kz} \right\|^2 + \lambda_1^2 \left\| \mathbf{z} \right\|_k^k + \lambda_2^2 \left\| \mathbf{D} |\mathbf{z}| \right\|_k^k \tag{5.1}$$

where $\left\| \bullet \right\|_k$ denotes the l_k-norm, $\mathbf{D}$ is the discrete approximation to the 2D derivative operator (gradient), $|\mathbf{z}|$ denotes the vector of magnitudes of the complex-valued vector $\mathbf{z}$, and λ_1, λ_2 are scalar parameters. The second and the third terms in (5.1) are aimed at enhancing point-based and region-based features respectively. The iterative algorithm and the greedy algorithm used here for the linear case are not appropriate for and hence do not perform well for such non-linear measurement model.

(a)

(b)
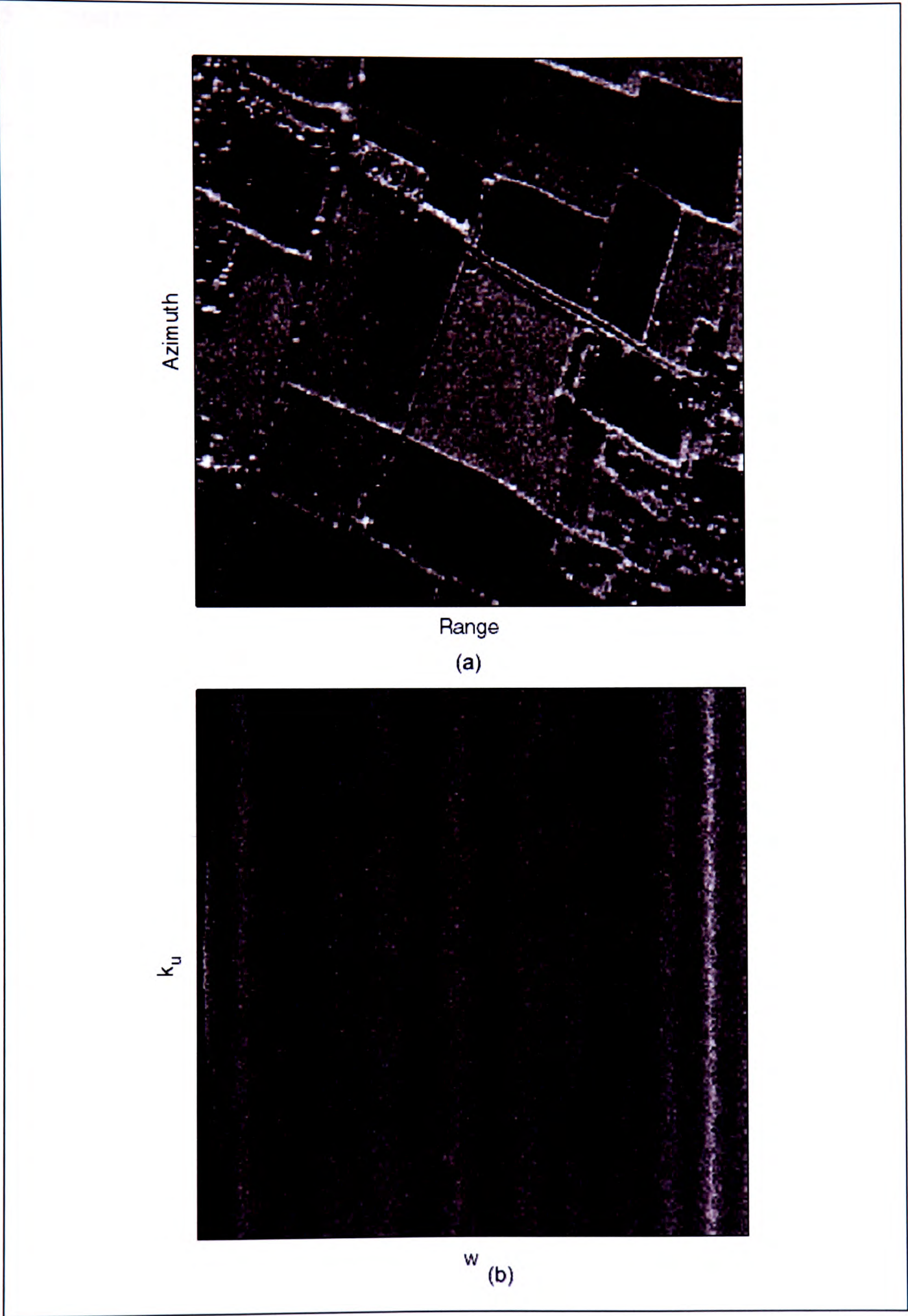
Figure 5.4(a) Original SAR image, (b) $\omega - k$ **plot.**

5.7 Sparse Reconstruction

Let us consider signal $\mathbf{x} \in \mathbb{C}^N$, which has a sparse representations over a fixed orthogonal transform, $\mathbf{W} \in \mathbb{C}^{N \times N}$. Thus, we can describe the signal as $\mathbf{x} = \mathbf{W}^* \mathbf{z}$ with $\|\mathbf{z}\|_0 \leq R \ll N$. Such a signal is known as $R - Sparse$ signal with respect to the dictionary $\mathbf{W}$.

As discussed in chapter 2, in the CS framework to measure (encode) $\mathbf{x}$ we compute the measurement vector $\mathbf{y} \in \mathbb{C}^M$ using a linear projector $\mathbf{A} \in \mathbb{C}^{M \times N}$, with $R < M \ll N$ via $\mathbf{y} = \mathbf{A}\mathbf{x}$. We refer to $\mathbf{A}$ as the measurement matrix whose rows are the measurement vectors.

The measurement signal $\mathbf{y} \in \mathbb{C}^M$ is written is terms of $\mathbf{z} \in \mathbb{C}^N$ as

$$\begin{aligned} \mathbf{y} = \mathbf{A}\mathbf{x} &= \mathbf{A}\mathbf{W}^*\mathbf{z} \\ &= \mathbf{K}\mathbf{z} \end{aligned}$$

(5.2)

where $\mathbf{K} = \mathbf{A}\mathbf{W}^*$ is the *holographic* basis.

The original signal $\mathbf{x}$ can be reconstructed from $\mathbf{y}$ by exploiting the sparsity of its representation i.e. by searching for all possible $\hat{\mathbf{z}}$ satisfying $\mathbf{y} = \mathbf{K}\hat{\mathbf{z}}$ that is the sparsest. Mathematically, $\hat{\mathbf{x}}$ can be found by first solving the linear inverse problem through l_0-optimization $\hat{\mathbf{z}} = \arg\min\|\mathbf{z}\|_0$ s.t. $\mathbf{y} = \mathbf{K}\mathbf{z}$ and then computing $\hat{\mathbf{x}} = \mathbf{W}^*\hat{\mathbf{z}}$. The objective function enforces the sparsity whereas the constraint enforces data consistency. The l_0-optimisation is a combinatorial problem and is NP-hard to solve. The two methods which are used here for the reconstruction are the *orthogonal matching pursuit* (OMP) and the *iterative* algorithm, L1_Adapt_SD (described in Chapter 4), which is based on the l_1-optimisation

$$\hat{\mathbf{z}} = \arg\min \|\mathbf{z}\|_1 \quad \text{s.t. } \mathbf{y} = \mathbf{Kz} \tag{5.3}$$

On the other hand, the greedy reconstruction algorithms build a sparse approximation iteratively by selecting the basis most strongly correlated with the residual part of the signal and use it to update the current approximation. The two most prevalent greedy techniques are the *matching pursuit* (MP) and *orthogonal matching pursuit* (OMP) [41]. These techniques are adapted in CS framework in [32, 68]. It is also to be noted that the reconstruction algorithms based on iterative and greedy methods make use of the fast transforms used in the $\omega - k$ algorithm to speed up the computation as opposed to the matrix inversions required in other methods like *basis pursuit* (BP) and its variants.

For the block diagram in Figure 5.2, if the matched filter is denoted by M_t, the *Stolt* mapping by S_t, the 2D FFT (IFFT) by $\mathcal{F}$ ($\mathcal{F}^*$), sparsifying transform as $\mathbf{W}$ and the random sampling as $\mathbf{A}$, we then have the following optimization problem to solve

$$\min\left(\|\mathbf{z}\|_1\right) \quad \text{s.t. } \mathbf{y} = \mathbf{Ax}$$
$$\text{where } \mathbf{z} = \mathbf{W}\mathcal{F}^* S_t M_t x \tag{5.4}$$

5.8 SAR Raw Data Compression of Point Targets

To study the feasibility of using CS for SAR raw data compression, we used five point targets simulated through the SAR simulator as shown in Figure 5.3(a) with ideal point target response in Figure 5.3(b). The 2D FFT of the complex raw data was performed to obtain the k-space data, as shown in Figure 5.5(a). The k-space data thus obtained was sampled randomly. The size of the randomly sampled measurement data is 4200 for the image size of 256 x 256, which is the size of the image to be reconstructed. We then recover 200 samples of the sparse image corresponding to the five targets. The Figure 5.6 depicts the compression of point targets in CS framework. It shows the spatial image domain, the full k-space, the transform domain and an undersampled k-space along

with the operators. The reconstruction algorithm is based on OMP with the least square estimation performed through the conjugate gradient (CG) method, as described in Chapter 3. The reconstruction process involves computation of (forward and inverse) matched filtering, *Stolt* mapping and 2D FFT. The point targets image is sparse in the magnitude domain of the image itself and doesn't require any additional *sparsifying* transform. The reconstructed image for the point target simulation is shown in Figure 5.5(b) and was evaluated in terms of the *peak side lobe ratio* (PSLR) and *integrated side lobe ratio* (ISLR). The PSLR and the ISLR of the point targets simulation for 256 x 256 size complex SAR processed image and the image generated with 4200 measurement samples and 200 coefficients are tabulated in Table 5-1. The plots of the point targets response along the range direction for the original image and the CS reconstructed image is shown in Figure 5.7 and Figure 5.8 respectively.

	PSLR (dB)	ISLR (dB)
Original Image	-11.21	-1.75
CS Image	-10.97	-4.96

Table 5-1 PSLR and ISLR of the original and reconstructed CS image.

There is no degradation in PSLR and the improvement in the ISLR is due to the recovery of only 200 coefficients which resulted in the reduction of the sidelobes power. We could also see from the Figure 5.7 and Figure 5.8 that there is no degradation in the resolution (mainlobe width) of the point targets. We have similar results with the reconstruction algorithm based on the iterative algorithm, L1_Adapt_SD, described in Chapter 4.

This experiment shows that it is indeed possible to compress the SAR raw data by a significant factor (in this case 15.6:1) when the SAR magnitude image is sufficiently sparse without any degradation in the resolution, PSLR and ISLR.

(a)

(b)
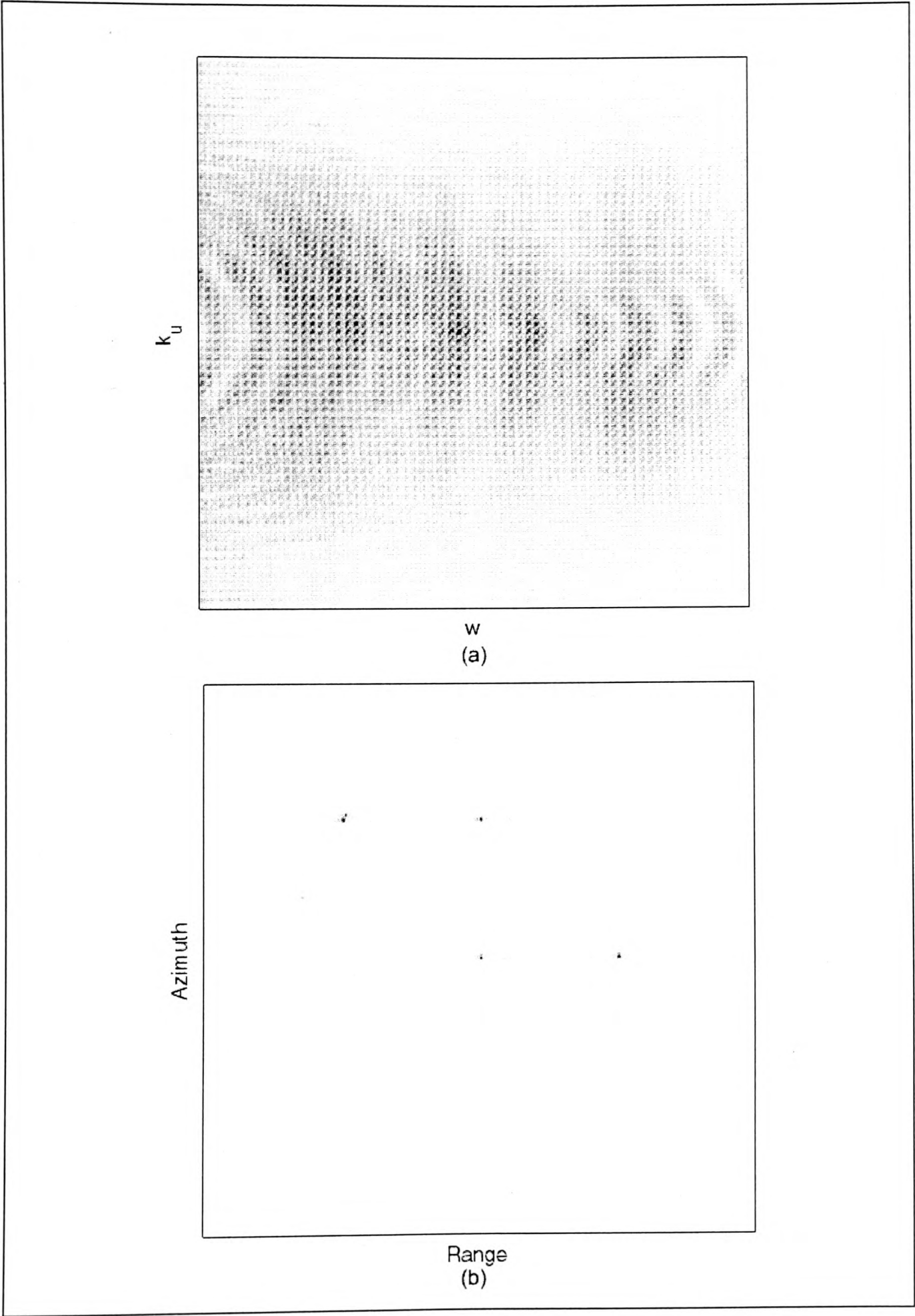
Figure 5.5(a) k-space **Signal (b) Reconstructed image (200 pts) showing amplitude in linear scale.**
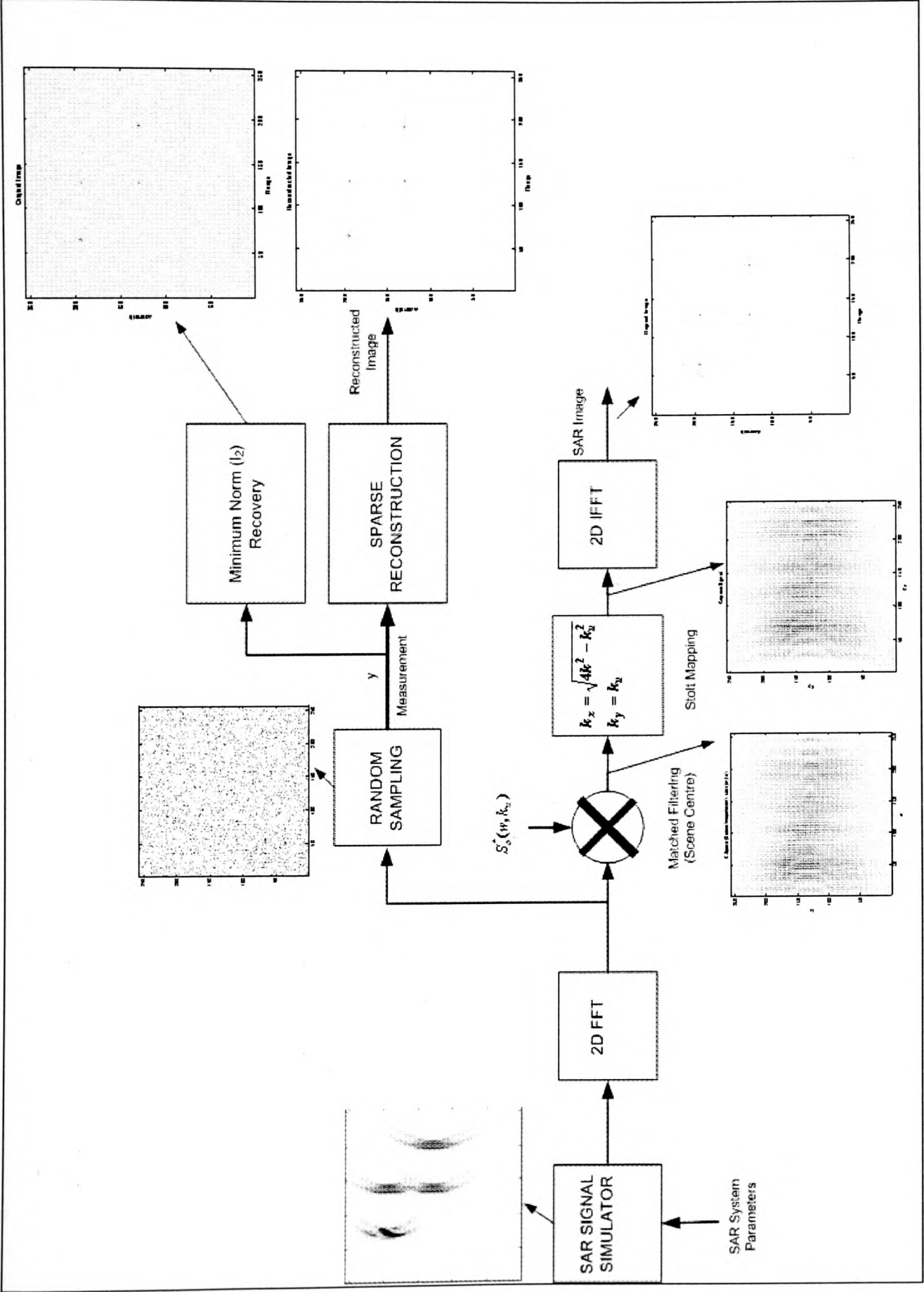
Figure 5.6 Point targets compression in CS framework.
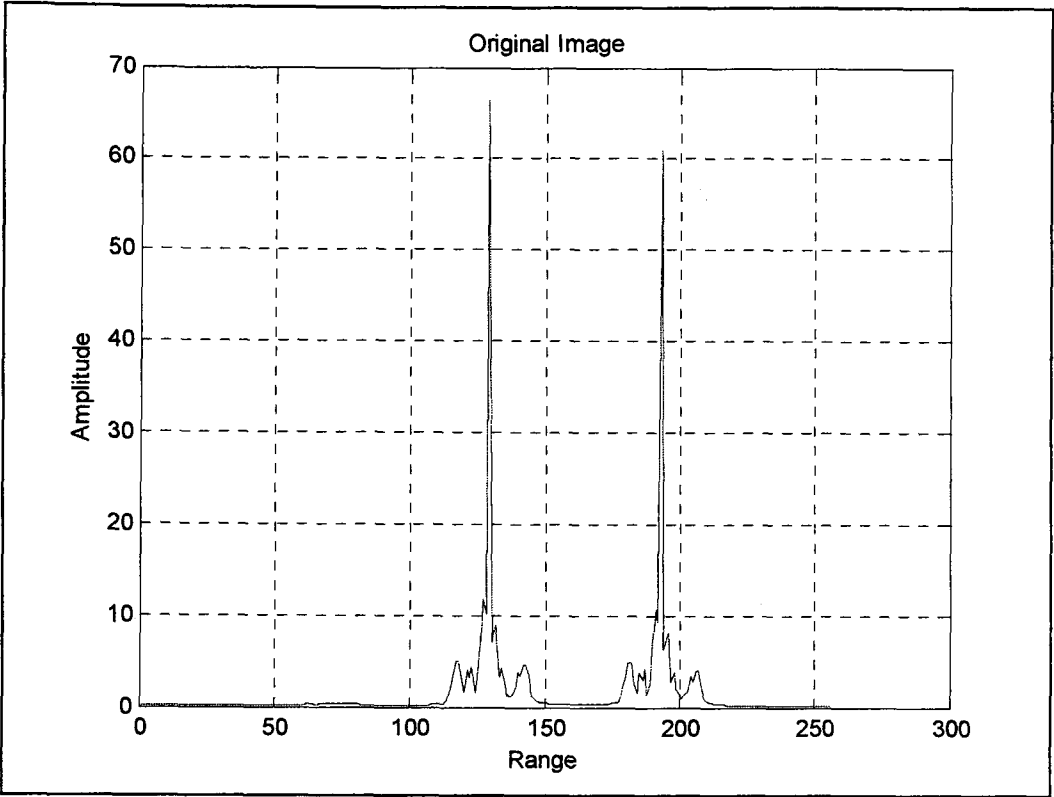
Figure 5.7 The point targets response along the range direction of the simulated image in linear amplitude scale.
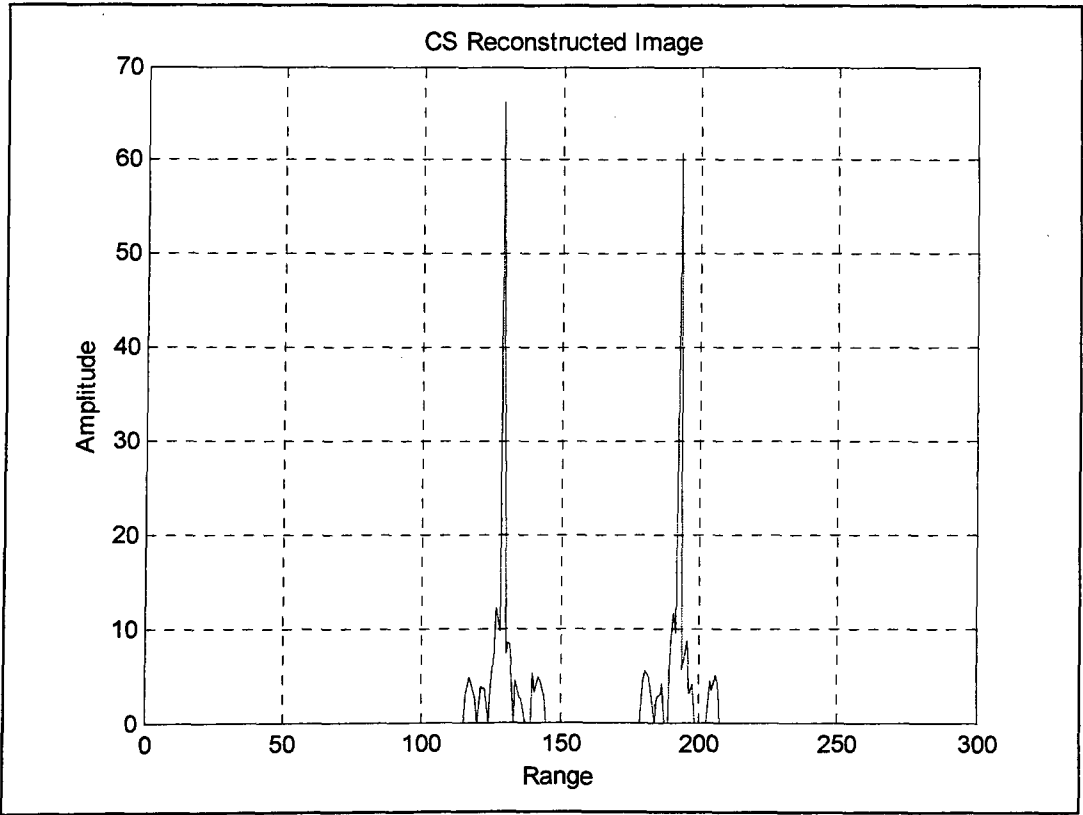
Figure 5.8 The point targets response along the range direction of the CS reconstructed image in linear scale.

113

5.9 SAR Raw Data Compression with DWT as Sparsifying Transform

The compression of the complex SAR data by using real wavelets was reported in [5] where the complex image data is converted to a real data format using Fourier transform. The signal is converted to a discrete "*analytic*" signal by shifting the frequency spectrum by half of the bandwidth to positive frequencies [100]. The inverse Fourier transform of this analytic signal can now be represented by its real part without loss of any information, since the real and imaginary part of the signal are mutual *Hilbert* transforms. But in many practical scenarios, the acquired data does not satisfy the *Hermitian* assumptions required to form the analytic signal and one must instead handle the data in its complex form. For such cases, we have used the real wavelets on the complex signal. The particular advantage of these techniques is that several wavelet bases used in conventional image compression could be used as a sparsifying transform.

5.9.1 Discrete Wavelet Transform (DWT)

The one-level decomposition of an image using a 2-D separable DWT is illustrated in Figure 5.9. The analysis filters $\mathbf{H_0}, \mathbf{H_1}$ and synthesis filters $\mathbf{G_0}, \mathbf{G_1}$ are L-tap *perfect reconstruction quadrature mirror filters* (PR-QMFs) [101] satisfying the following conditions

$$\mathbf{G_0} = \mathbf{H_1}(-z), \qquad \mathbf{G_1} = -\mathbf{H_0}(-z),$$

$$\mathbf{H_1}(z) = -z^{1-L}\mathbf{H_0}(-z^{-1}),$$

and

$$\left|\mathbf{H_0}(e^{i\omega})\right|^2 + \left|\mathbf{H_1}(e^{i\omega})\right|^2 = 1, \quad \forall \omega$$

These analysis and synthesis filters are combined with downsampling by a factor of 2 in both horizontal (row-wise) and vertical (column-wise) directions to compute an approximate image $\mathbf{X}_{LL}$ and three detailed images namely horizontal sub-image $\mathbf{X}_{LH}$, vertical sub-image $\mathbf{X}_{HL}$ and diagonal sub-image $\mathbf{X}_{HH}$ at each level. The indices "L" and "H" refer to low and high frequency sub-band components. The decomposition first

starts row-wise filtering with the lowpass filter $\mathbf{H}_0$ to produce the lowpass component and with the highpass filter $\mathbf{H}_1$ to produce a highpass component. These filtered components are then downsampled by a factor of two without any loss of information. The aliasing which takes place due to this downsampling is eliminated by the perfect reconstruction (PR) properties of these filters. The row-wise filtered components are then filtered column-wise to generate four sub-images namely, $\mathbf{X}_{LL}, \mathbf{X}_{LH}, \mathbf{X}_{HL}, \mathbf{X}_{HH}$. The reconstruction of the decomposed is performed by the dual of the system in Figure 5.9 and is shown in Figure 5.10. The coding performance of wavelets with its multi-resolution capabilities for images is described in [101].
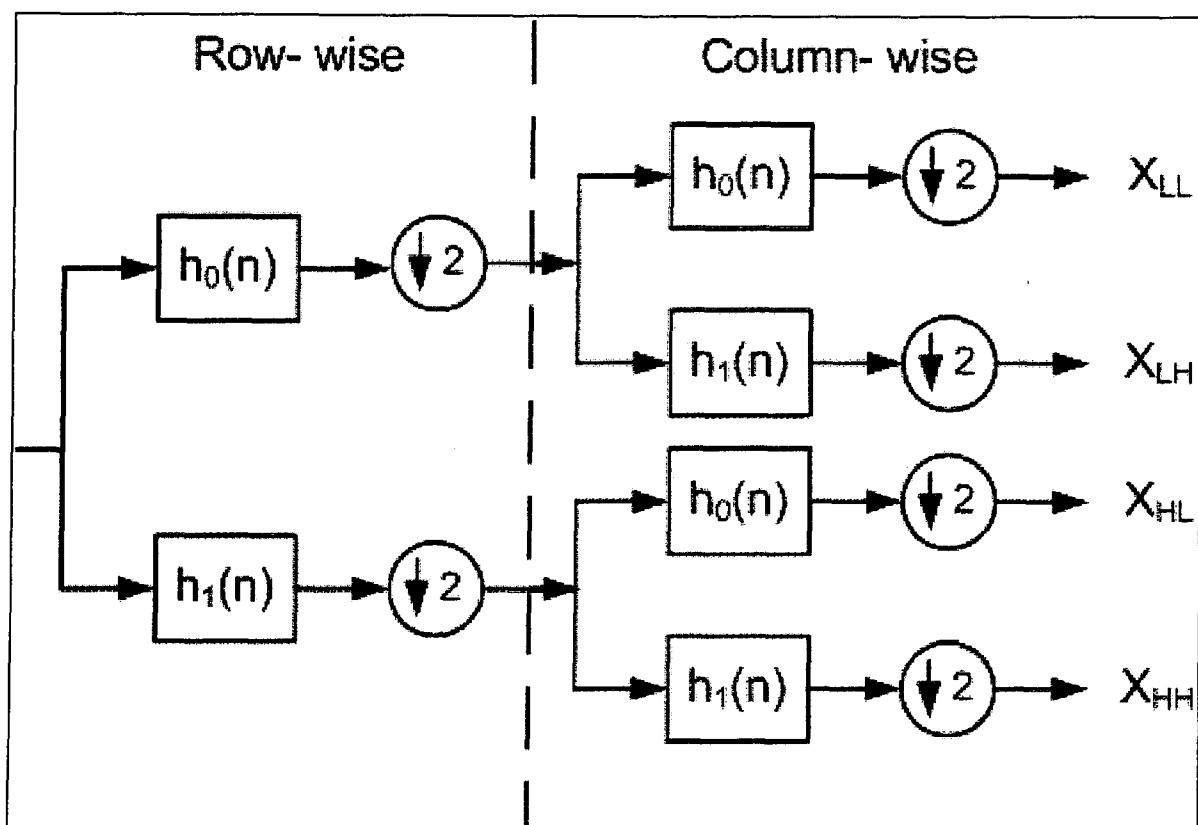
Figure 5.9 One level of forward DWT.
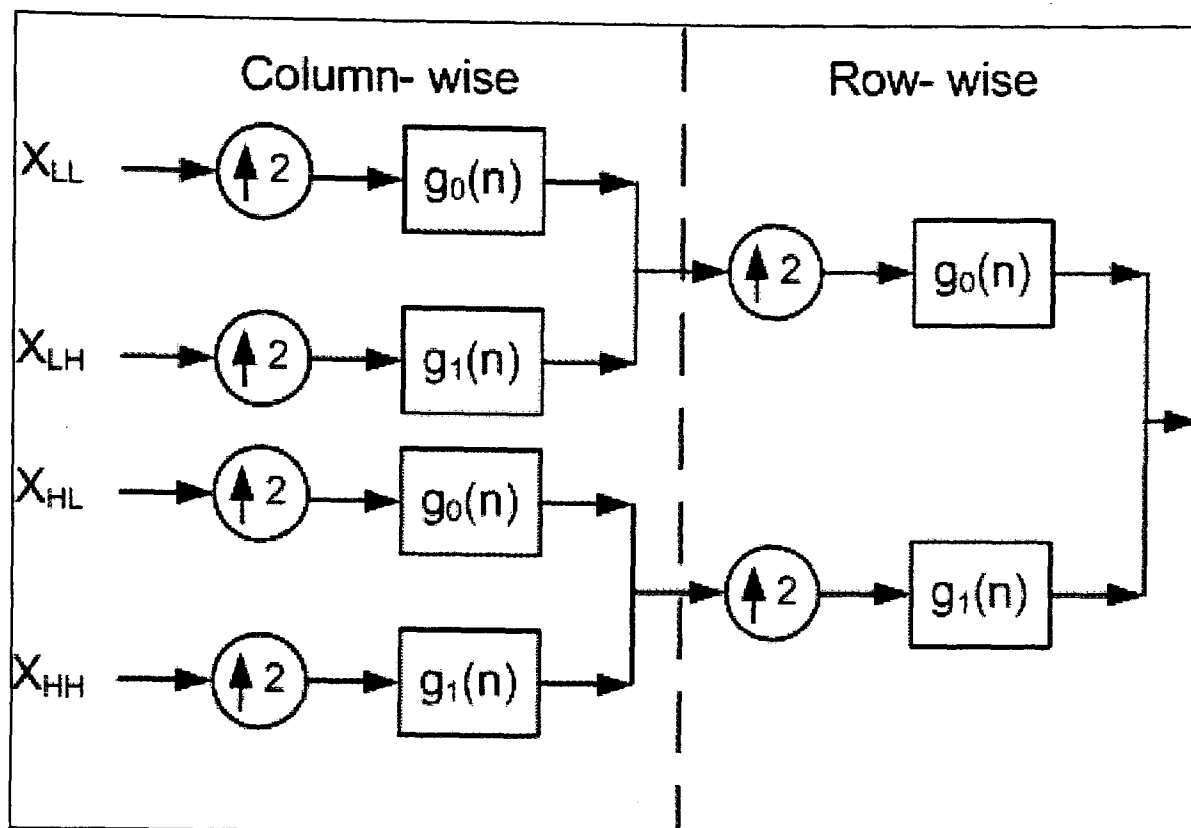
Figure 5.10 One level of inverse DWT.

5.9.1.1 DWT as Sparsifying Transform for Complex SAR Images

The compression of SAR raw data based on a low bit rate transform coding technique using DWT has been addressed in [98]. The wavelet coded quantization on magnitude and phase data separately was shown in [97]. It reported a compression of 64:1 on the magnitude data and 4:1 compression on the phase data without much degradation of the SAR image quality using the Daubechies (9,7) filter. A good compression performance with the Daubechies wavelets on SAR raw data was also shown in [22, 102]. A comparison between the complex SAR image and the detected SAR images with various wavelet transforms including Daubechies wavelet was presented in [21]. It showed that the compression performance with the detected images exceeds that with the complex raw data. The use of DWT for the compression of the complex SAR image was also studied in [22]. It showed that Daubechies wavelets have good performance on SAR complex image with compression ratio of 12:1.

We evaluated the performance of the Daubechies wavelet (D8) on both the complex SAR image and detected SAR image, shown in Figure 5.12(a). In the case of complex

116

SAR image, we first segregated it into real and imaginary images. We applied D8 wavelets on each of these images separately to produce real-valued coefficient image. Figure 5.11(a) shows the sorted wavelet coefficients of the magnitude formed by the wavelet coefficients of the real and imaginary images of the SAR image. We compare the performance of the same wavelet D8 when applied to the detected SAR image, as shown in Figure 5.11 (b). These figures show that rate of decay of the wavelet coefficients in the case of real wavelets applied to complex SAR image is inferior to that of detected SAR image. As we will see later, this poor performance of real wavelets on complex SAR images becomes a limitation for achieving good compression ratio for the SAR raw data in the compressed sensing framework with DWT as sparsifying transform.

5.9.2 Results with Discrete Wavelet Transform

The compressed sensing framework for the complex SAR raw data with DWT is shown in Figure 5.2, where the sparsifying transform is a DWT. The holographic basis, $\mathbf{K}$, in (5.3) is implemented through functions consisting of 2D FFT, *Stolt* interpolation, matched filtering, a 2D-DWT and the measurement matrix, $\mathbf{A}$, consists of random sampling points.

For the satellite data, as shown in Figure 5.12(a), we have used the 4-levels of *Daubechies-8* wavelet [103] on the complex image formed after taking the 2D IFFT, as shown in Figure 5.2. In this case the signal is compressed by a factor of 2:1. The reconstruction algorithm is based on OMP with the least square estimation performed through the conjugate gradient (CG) method for computational efficiency.

For the 256 x 256 SAR complex image, as shown in Figure 5.12 (a), the reconstruction of the image for 6000 wavelet coefficients with OMP is shown in Figure 5.12(b). This image is generated by taking the full size of the original data and then using the OMP algorithm to generate 6000 wavelet coefficients. The final image is generated by taking the inverse wavelet transform. The Figure 5.12 (c) shows the reconstruction with OMP for 6000 wavelet coefficients with 2:1 compression ratio.
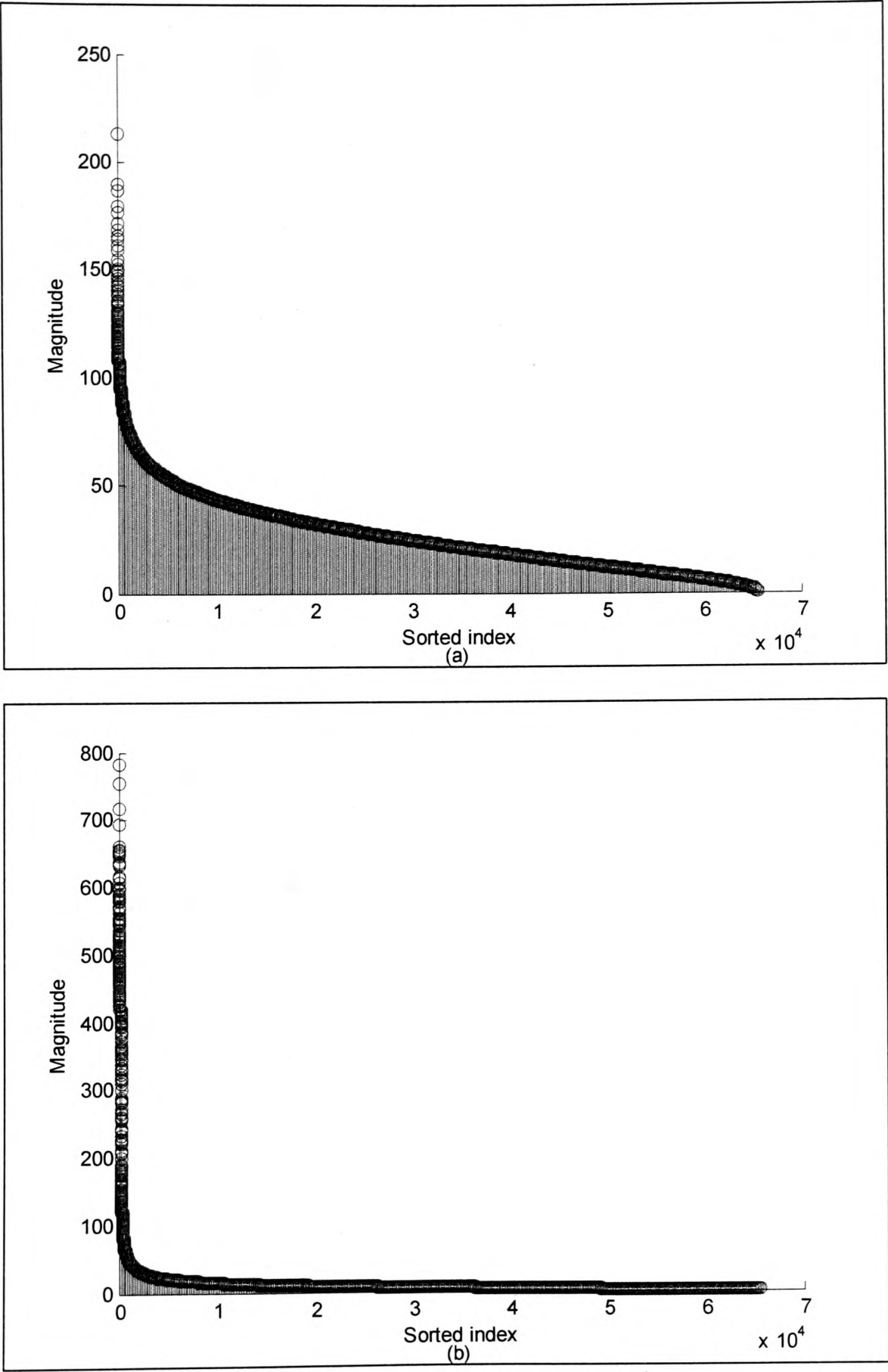
Figure 5.11(a) Sorted magnitude wavelet coefficients of real and imaginary SAR images, (b) sorted magnitude coefficients of magnitude SAR image.
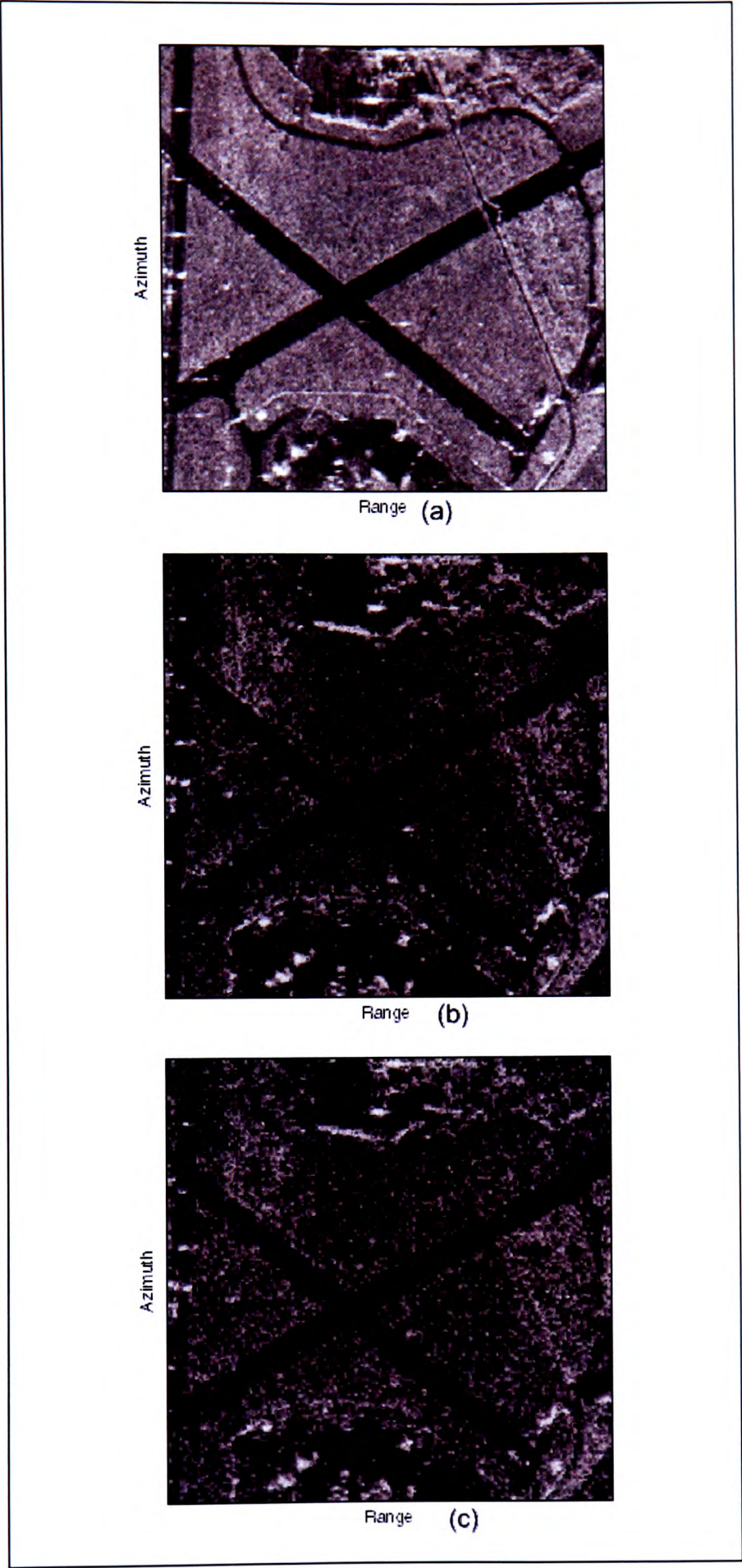
Figure 5.12(a) Original SAR image, (b) reconstructed image with 6000 DWT coefficients. (c) reconstructed image with 2:1 compression and 6000 DWT coefficients.

The reconstruction with OMP is limited to 6000 coefficients as the sparsity of the 2D-DWT is not sufficient to provide any further improvement in PSNR of the reconstructed image. The original SAR image, as shown in Figure 5.12(a), is the result of the matched filtering with the point spread function. Each pixel in the image is thus formed by the target at that location along with contribution from all adjacent targets. Whereas, the image formed through OMP, as shown in Figure 5.12(b), is proper inversion consisting of linear contributions of orthogonal bases and hence taken as a reference image. This reference image of Figure 5.12(b) consists of isolated point targets. The SAR images generated through the method of OMP are generally used to identify isolated point targets and are mainly used for detection and classification applications. The reconstructed image with 2:1 compression, as shown in Figure 5.12(c), is comparable to Figure 5.12(b). All the bright targets are clearly identifiable but some of the fine features like narrow roads are not very clear. The result shows the limitation of compressing the SAR raw data in the compressed sensing framework with DWT as sparsifying transform to get full reconstruction of SAR image. This suggests the effectiveness of this framework for detection applications without the need of full image reconstruction. The main information from these reconstructed images is the presence of strong point targets. The strong return arises due to the presence of corner shapes that are very common in man-made buildings and vehicles. The returns from such corner shaped objects are much stronger than the natural background areas.

5.10 SAR Raw Data Compression with CWT as a Sparsifying Transform

For the compression of the satellite SAR raw data, the amplitude and phase are both indispensable for many applications e.g. interferometer. Discrete Wavelet Transforms have been used for SAR intensity image compression but are not suitable to preserve the signal phase information [104]. The compression of the complex SAR image with Daubechies-8 (D8) wavelet filter, is reported in [5] and the study of the complex wavelet transform (CWT) for the SAR image compression and denoising to preserve both amplitude and phase has been reported in [22]. It showed that it is possible to compress

the SAR raw data with complex wavelets and get equivalent compression as the real discrete wavelet transforms working on the real and imaginary channels independently with a compression ratio of around 12:1.

We propose to use the dual tree complex wavelet transform (DT-CWT) [105], as a sparsifying transform with OMP algorithm to find the sparse representation of the complex SAR image. The superiority of the DT-CWT in image compression was shown in [106]. The compression of 2D image using DT-CWT despite its 4:1 redundancy through iterative projection techniques is addressed in [107] while the compression through iterative reweighted least squares algorithm is addressed in [108].

5.10.1 Complex Wavelet Transform(CWT)

The DT-CWT is an overcomplete, perfect reconstruction, separable transform. The DT-CWT comprises of two parallel wavelet filter banks that contain filters of different delays that minimises the aliasing error due to decimation to synthesis a single linear phase complex lowpass- highpass filter pair [105].

When the signal is real, its Fourier transform (FT) coefficients are symmetric about the origin i.e. *Hermitian* symmetry and no information is lost by considering only their positive frequency parts. However, in case of complex-valued SAR signal the FT coefficients are no longer symmetric and both the negative and positive frequency parts of the spectrum should be considered independently. DT-CWT has been generally applied to the real signals where the spectral decomposition takes place only for the positive part of the spectrum, as shown in Figure 5.13. It is to be noted that the plots are the frequency responses of the filters viewed at the highest sampling rate.
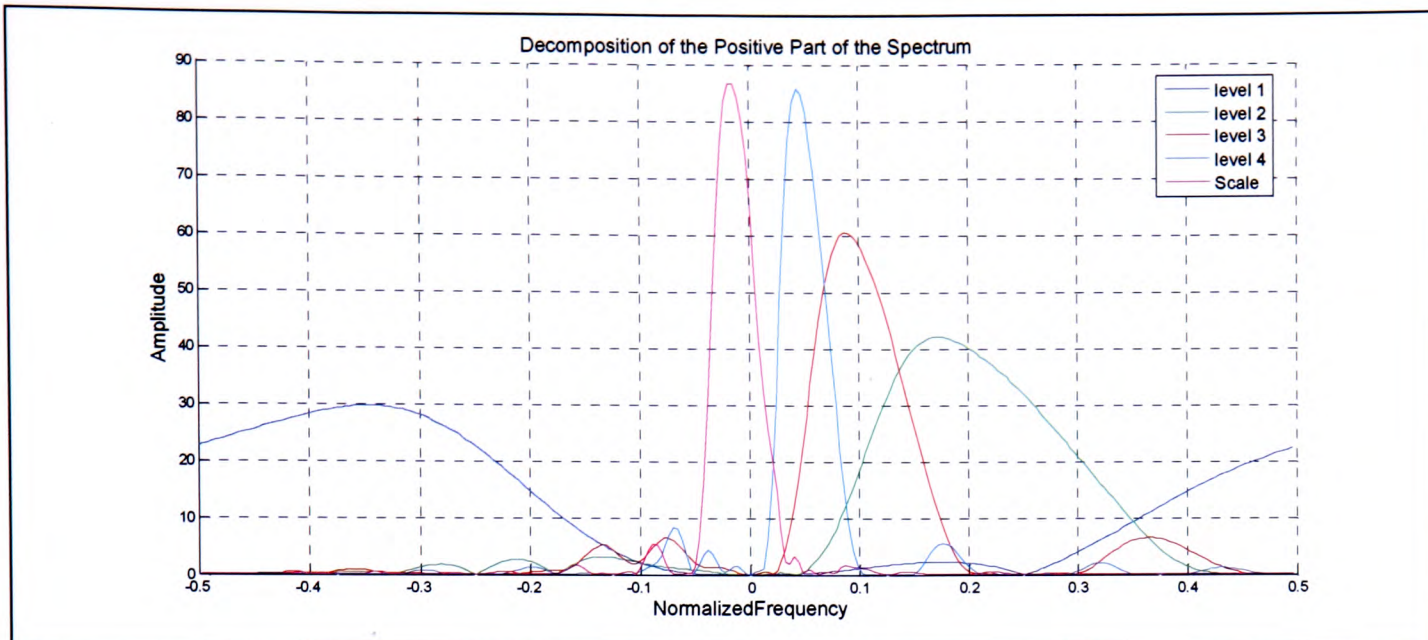
Figure 5.13 Decomposition of the positive part of the spectrum.

For the quadrature SAR image, the spectral decompositions for both negative and positive part of the spectrum are essential. This is achieved by applying the DT-CWT to the real, ξ_r, and imaginary part, ξ_i, of the complex SAR image separately and then combining the complex output as

$$\xi_+ = \xi_r + i\xi_i$$
$$\xi_- = \xi_r - i\xi_i$$

(5.5)

where ξ_+ corresponds to the positive frequency component and ξ_- corresponds to the negative frequency component. The decomposition of the spectra for both the positive and negative part is as shown in Figure 5.14. Thus, we represent the image using a frame operator rather than a basis.
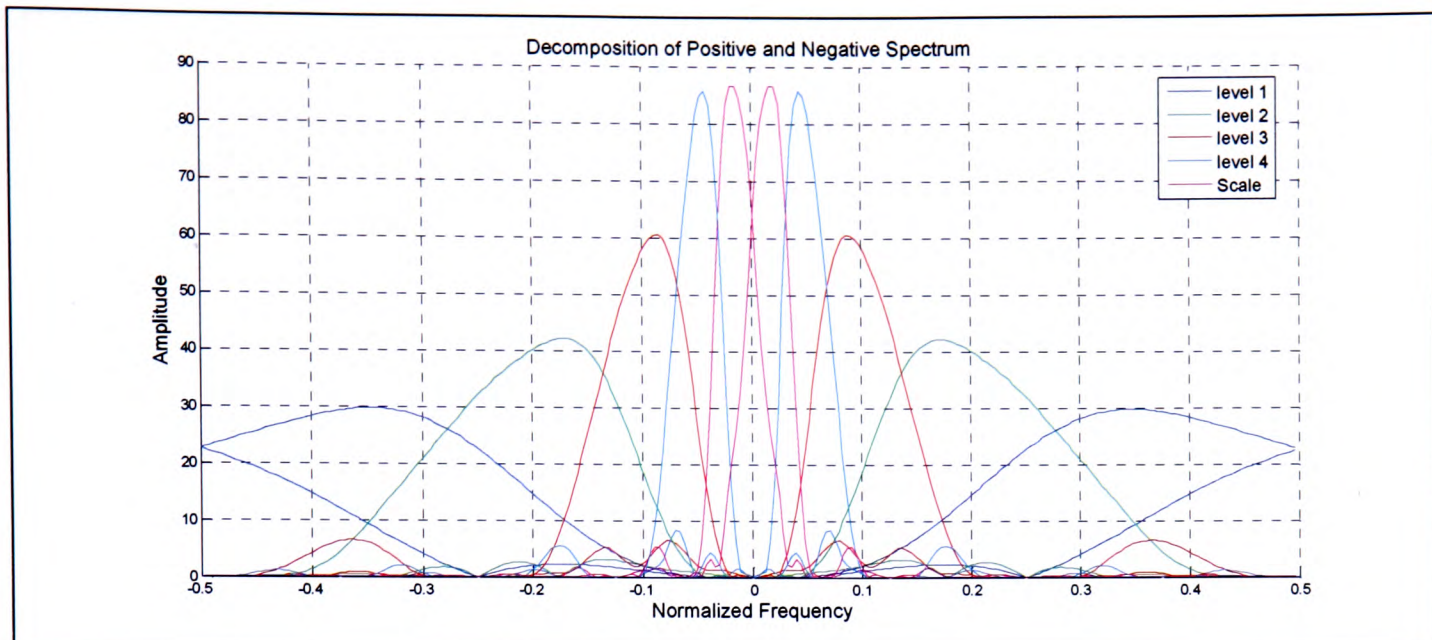
Figure 5.14 Decomposition of positive and negative part of the spectrum.

For a general N-point signal, the DT-CWT yields $2N$ complex coefficients, which implies that the DT-CWT is two times expansive (2^d for d-dimensional signals). The DT-CWT employs two real Discrete wavelet transforms (DWT); the first DWT works on the real part of the input and the second DWT works on the imaginary part of the input signal. The analysis and synthesis filterbanks that are used to implement DT-CWT and its inverse are illustrated in Figure 5.15 and Figure 5.16. The filters are themselves real and no complex arithmetic is required for the implementation of the DT-CWT. The DT-CWT achieves competitive image coding performance as compared to DWT, despite of its redundancy by a factor of four [107].
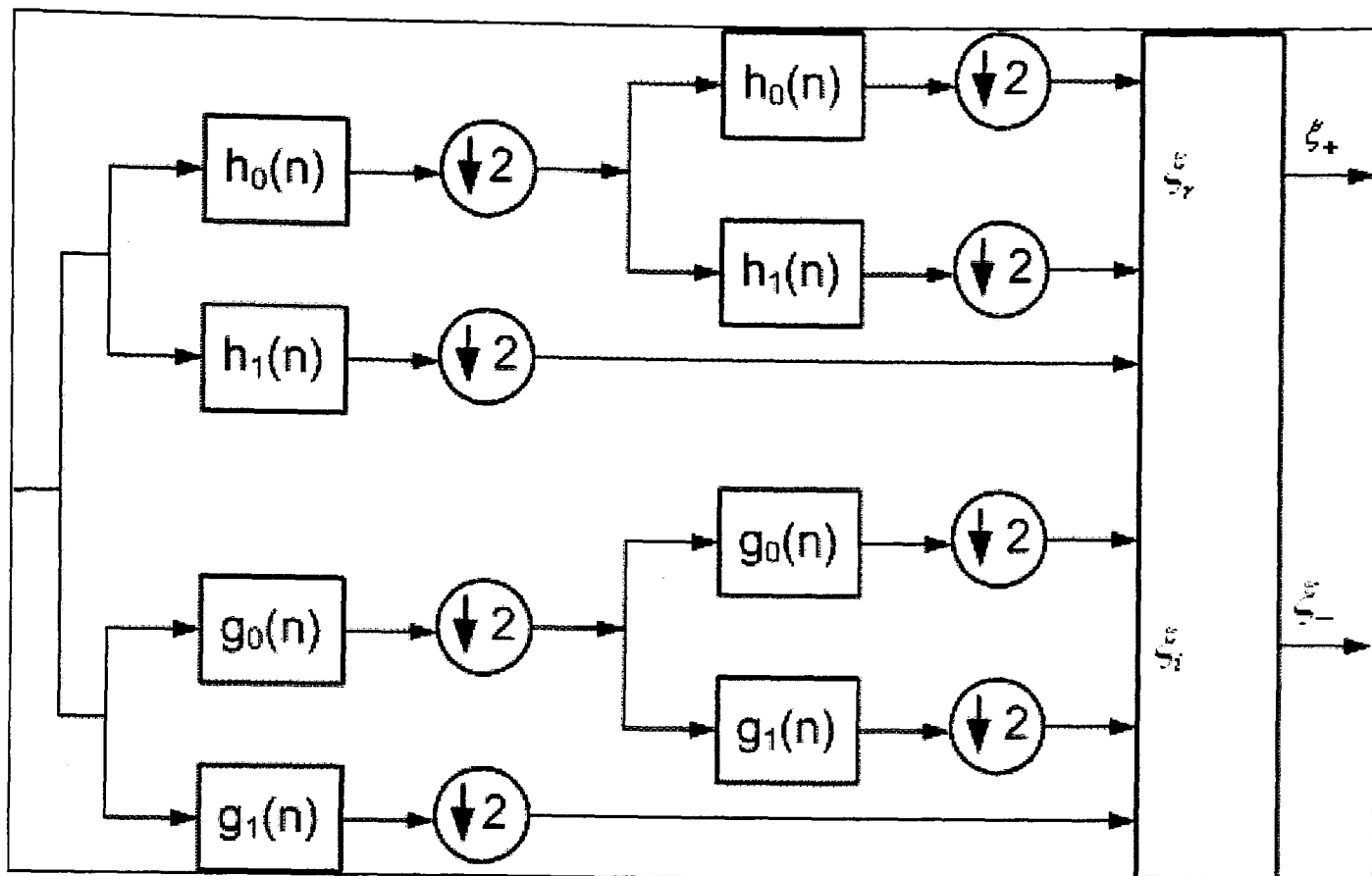
Figure 5.15 Analysis filterbanks for the DT-CWT.
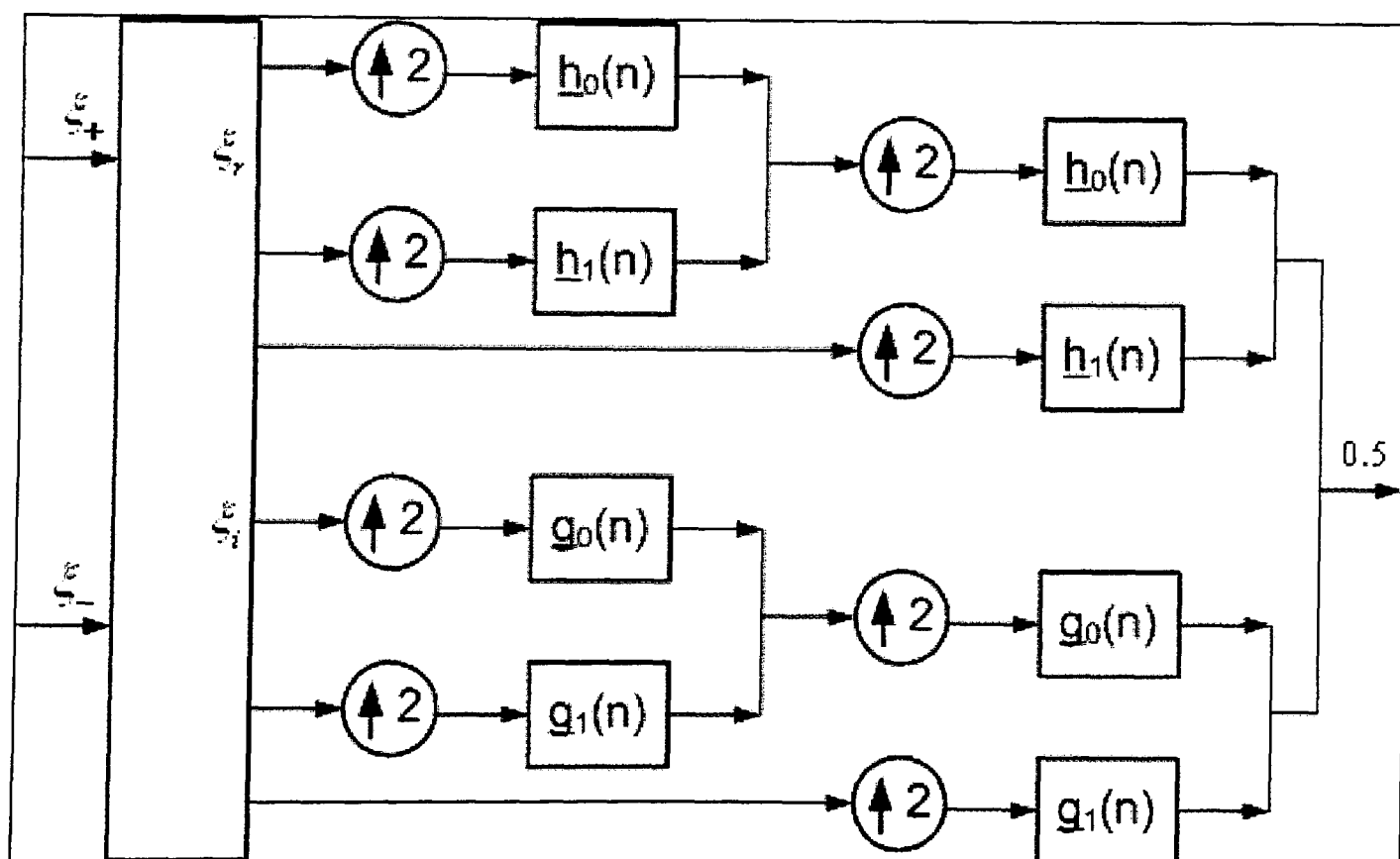
Figure 5.16 Synthesis filterbanks for the DT-CWT.

5.10.2 Results with DT-CWT

The compressed sensing framework for the complex SAR raw data with DT-CWT is shown in Figure 5.2, where the sparsifying transform is the DT-CWT. We have used the functions available at the repository [109], to perform 4-levels DT-CWT decomposition on a 2D-SAR raw data with 13,19-tap filters for level 1 and Q-shift 14-tap filters for levels ≥ 2 [62, 107]. The holographic basis, $\mathbf{K}$, in (5.3) is implemented through functions consisting of a 2D DT-CWT, a 2D FFT, *Stolt* interpolation, matched filtering and the measurement matrix, $\mathbf{A}$, consists of random sampling points. The reconstruction is similar to the one used for the point target processing.

The OMP based reconstruction for the 2:1 compression for the actual complex SAR image was carried out for 32 x 32 size image from the original image of size 256 x 256 as shown in Figure 5.17(a), to evaluate the PSNR with respect to various lengths of recovered wavelet coefficients and is tabulated in Table 5-2. The PSNR of 2:1 compressed signal degrades faster for recovery of wavelet coefficients greater than 150. This is consistent with the theory of compressed sensing to have measurement length 3 to 5 times the length of the sparse coefficients.

	50	100	150	200	250	300
Original	36.8	38.8	40.3	41.5	42.7	43.9
CS Image	36.8	38.7	39.5	39.7	39.8	39.8

Table 5-2 PSNR (dB) of 2:1 compressed signal with respect to the recovered wavelet coefficients.

For the 256 x 256 SAR complex image, as shown in Figure 5.17(a), the reconstruction of the image for 6000 wavelet coefficients with OMP is shown in Figure 5.17(b). The Figure 5.18(a) shows the reconstruction with OMP for 6000 wavelet coefficients with 2:1 compression ratio. The reconstruction with the 6000 most significant wavelet

coefficients (sorted) with DT-CWT as a frame operator is shown in Figure 5.18(b). The reconstruction with OMP is limited to 6000 coefficients as the sparsity of the complex wavelet is not sufficient to provide any substantial improvement in PSNR of the reconstructed image. The original SAR image, as shown in Figure 5.17(a), is the result of the matched filtering with the point spread function. Each pixel in the image is thus formed by the target at that location along with contribution from all adjacent targets. Whereas, the image formed through OMP, as shown in Figure 5.17(b), is proper inversion consisting of linear contributions of orthogonal bases and hence taken as a reference image. The reconstructed image with 2:1 compression, as shown in Figure 5.18(a), is comparable to Figure 5.17(b). All the bright targets and boundaries are clearly identifiable. This shows that the reconstructed image with compression in this framework is suitable for detection and classification applications.
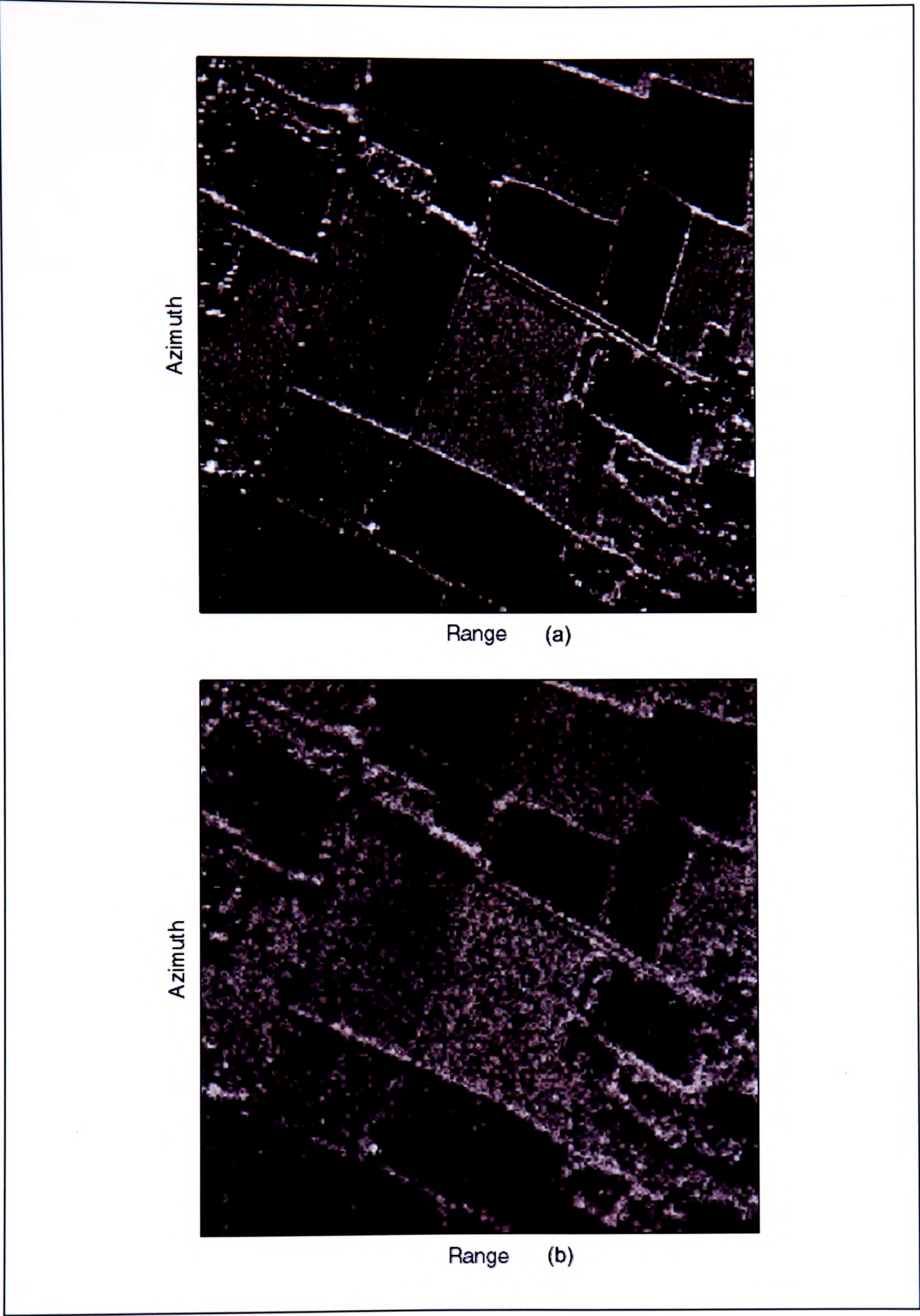
Figure 5.17(a) Original SAR Image, (b) Intensity image with OMP for 6000 CWT coefficients.
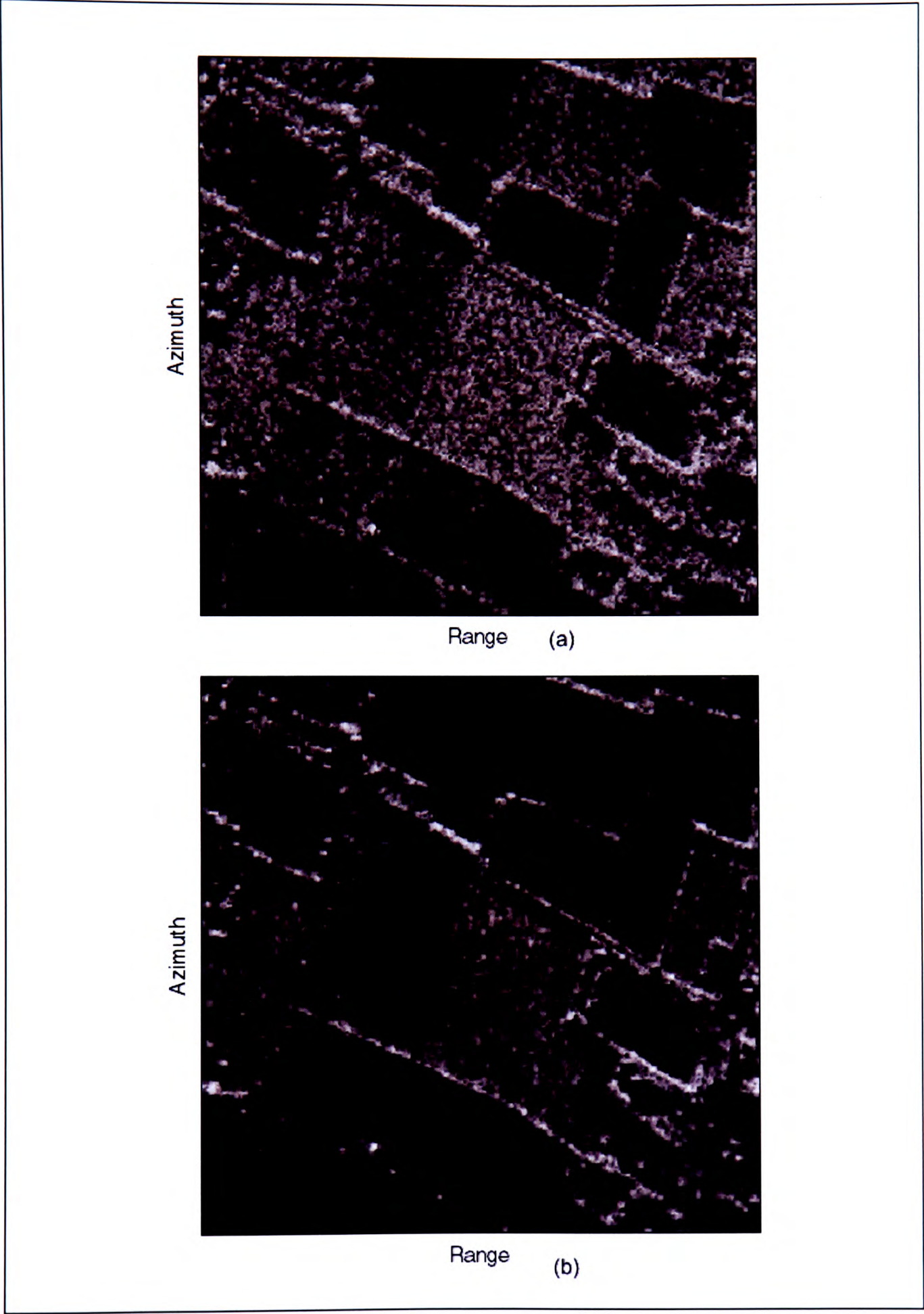
Figure 5.18(a) Intensity image for 2:1 compression with OMP for 6000 CWT coeffs. (b) Reconstructed image with 6000 sorted coeffs. (DT-CWT used as a frame operator).

5.11 Results with MSTAR Data

We now present the results on data from the moving and stationary target acquisition and recognition (MSTAR) public target data set [110]. The dataset in MSTAR repository contains focused complex image of SAR. MSTAR images are formed by taking a 2D inverse FFT of zero-padded phase history data on a rectangular grid. To get the raw data we take the 2D FFT of the 128 x 128 images. Figure 5.19 shows the mesh plot of the magnitude of the resulting 2D image of the raw data for a sample MSTAR scene.
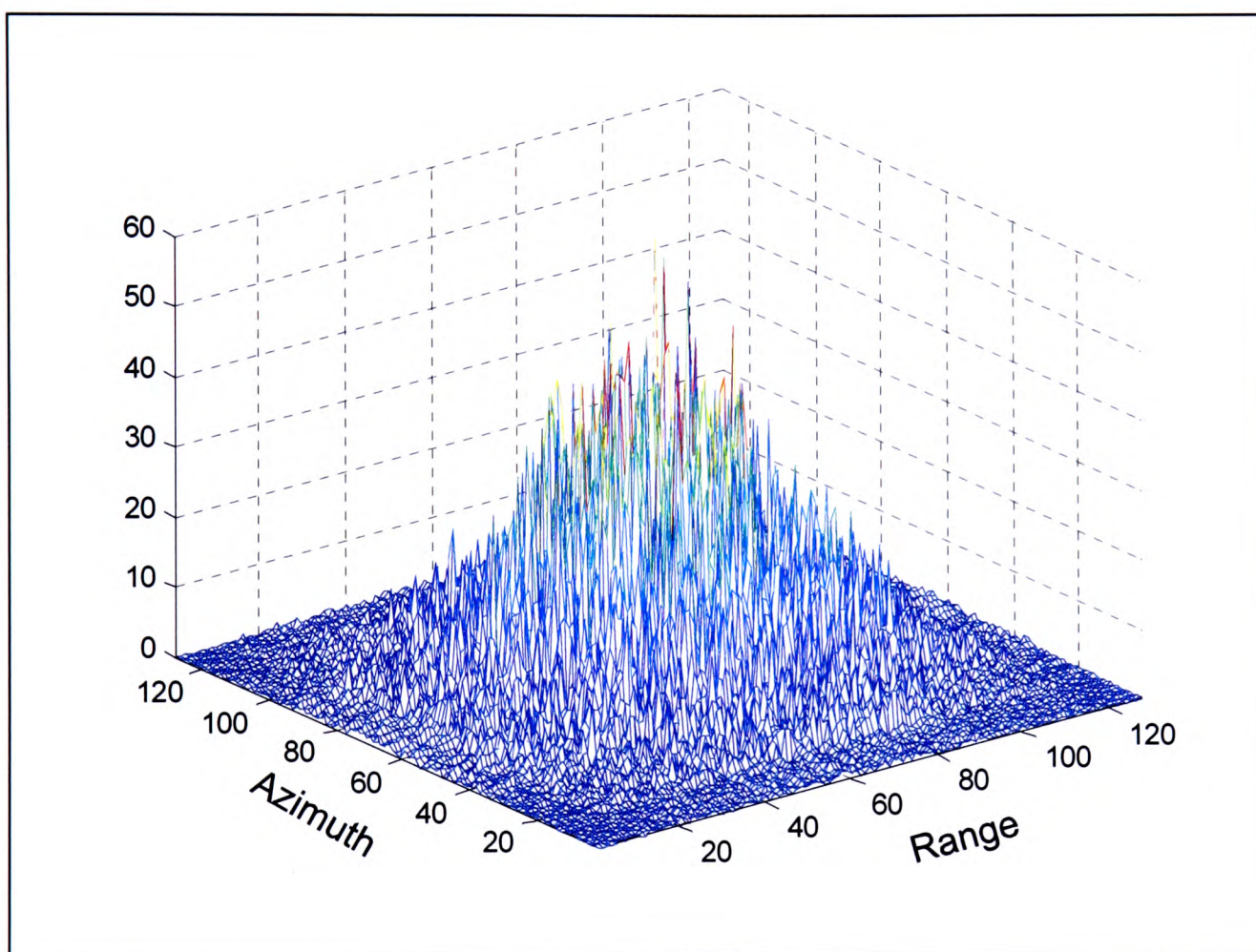
Figure 5.19 Magnitude plot of 2D FFT of MSTAR sample data.

We check the detection of 50 most significant targets in the image by using OMP and L1_Adapt algorithm as described in chapter 4. The signal is randomly sampled in the Fourier domain. The result for the 2:1 compressed signal is shown in Figure 5.20. Figure 5.20(a) shows a sample of MSTAR image used in the experiment. The 50 most

significant pixels of the image in Figure 5.20(a) are shown in Figure 5.20(b). The L1_Adapt algorithm reconstruction of 50 most significant coefficients is shown in Figure 5.20(c) whereas Figure 5.20(d) shows the reconstruction with the OMP algorithm. Similar reconstruction with 4:1 compressed data is shown in Figure 5.21. Both these cases suggest the effectiveness of this framework for detection applications without the need of full image reconstruction. The main information from these reconstructed images is the presence of strong point targets. The strong return arises due to the presence of corner shapes that are very common in man-made buildings and vehicles. The returns from such corner shaped objects are much stronger than the natural background areas.

(a)

(b)

(c)

(c)
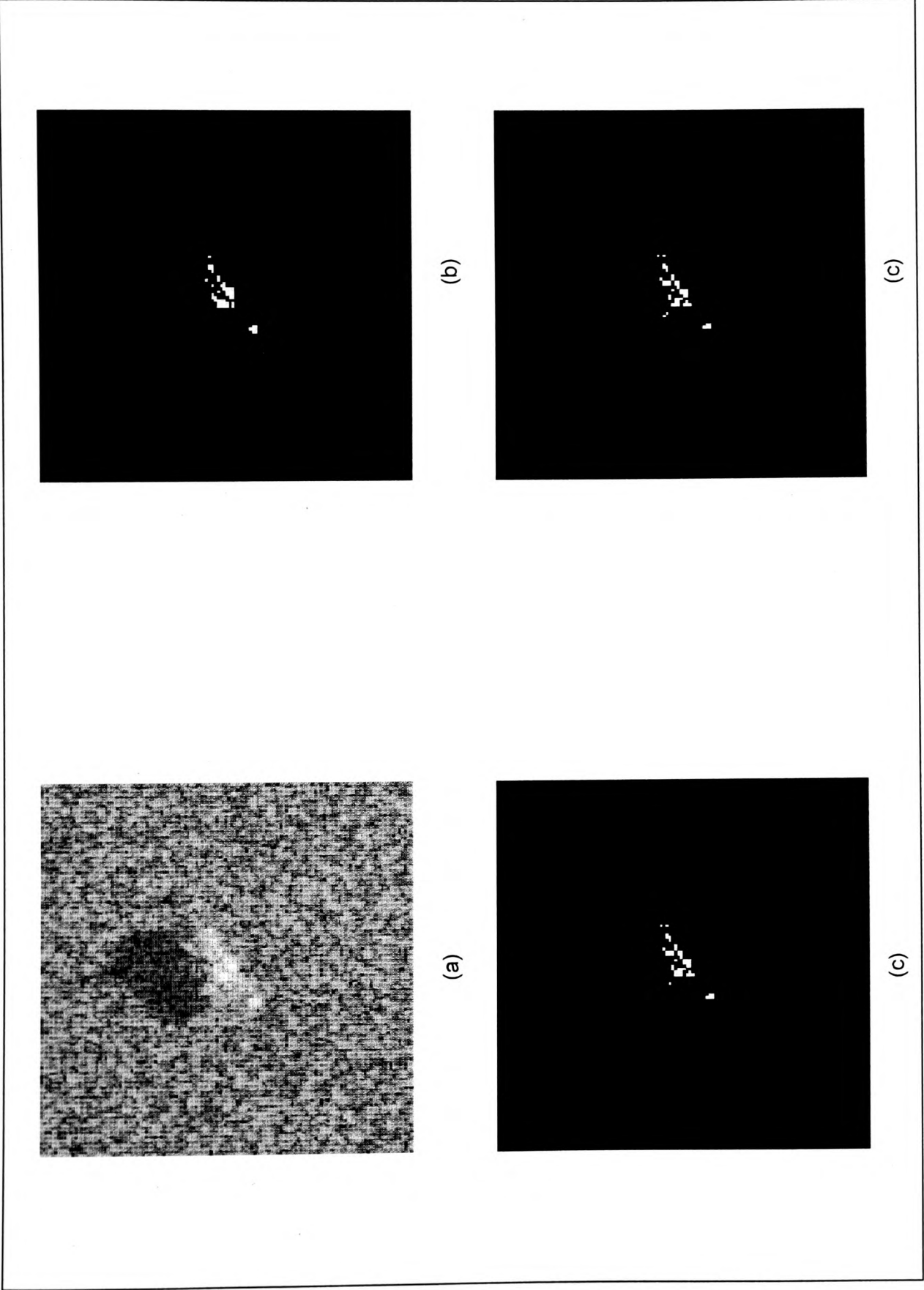
Figure 5.20(a) MSTAR sample image, (b) 50 most significant targets of (a), (c) reconstruction of L1_Adapt for 2:1 compressed data, (d) reconstruction of OMP for 2:1 compressed data.

131

(a)

(b)

(c)

(c)
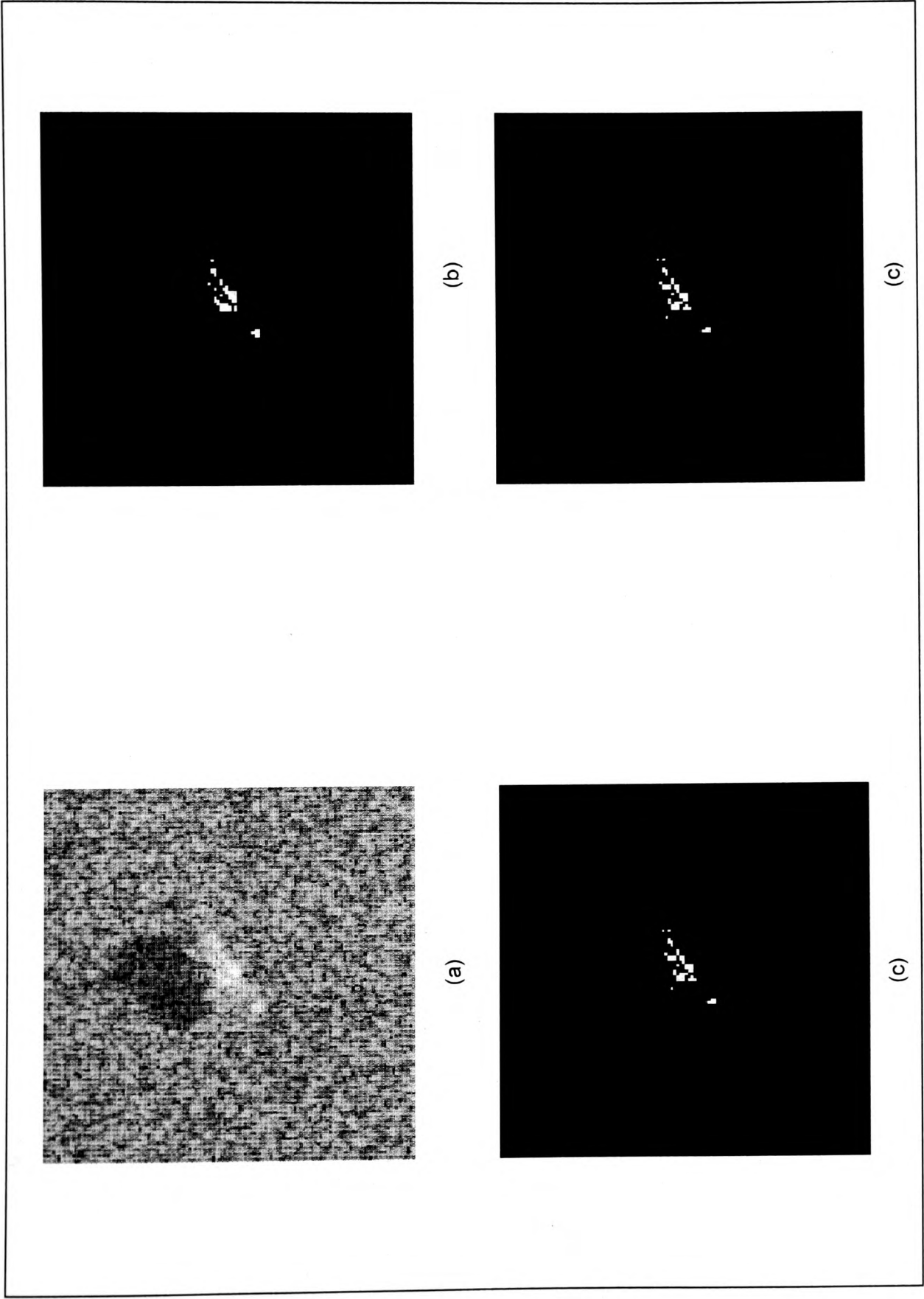
Figure 5.21(a) MSTAR sample image, (b) 50 most significant targets of (a), (c) reconstruction of L1_Adapt for 4:1 compressed data, (d) reconstruction of OMP for 4:1 compressed data.

132

5.12 Conclusions

The compression of the SAR data can be performed at three distinct points along the SAR image formation chain: (i) compression the raw SAR signals prior to or in the process of forming the complex image, (ii) compressing the complex image or (iii) compressing the detected SAR image. We have focused here on the compression of SAR raw data in the compressed sensing framework and find that its performance is related to the compressibility of the SAR complex image. The results with the point targets and the actual satellite images show that it is possible to compress the SAR raw data in the CS framework with the real and complex wavelets. No performance enhancement is seen through special sampling trajectories as the k-space samples are uniformly distributed and there is no specific concentration of high valued coefficients. The optimization based reconstruction of SAR image with small set of measurement data has an advantage that important features required for detection, classification and registration of SAR images can be recovered without reconstruction of the full image. The recovery based on CS is thus scalable depending upon various applications.

Much greater performance in terms of higher compression ratio and reconstruction qualities are expected by using transforms that could give better sparsity for the SAR complex signal as compared to the real wavelets and DT-CWT used here. Further study on the non-linear reconstruction algorithms based on the regularization of only the magnitude data in the CS framework is required to verify any additional compression gain that could be achieved by using DWT on the detected images.

Chapter 6

6. Conclusions

6.1 Summary and Conclusions

In this dissertation, we have contributed to the area of synthetic aperture radar (SAR) raw data compression and to the area of finding sparse solution to the linear inverse problems. The SAR system generates huge amount of data due to high resolution and wide swath requirements which pose severe problem for on-board storage and downlink transmission. Due to constraints of on-board power and resources, the encoder has to be simple and computationally efficient in terms of power and hardware resources. Compressed sensing (CS) has emerged as one potential framework for compressing the signal with a simple encoder at the expense of a computationally extensive decoder. We have presented here the compression of SAR complex-valued raw data in which the data is reduced by sub-sampling the Fourier domain data in the CS framework. We have seen that the reconstruction problem in compressed sensing is essentially the classical linear inverse problem with the number of variables much greater than the number of observations. The signal can be reconstructed (decoded) through a non-linear decoding scheme that uses the sparsity as *a-priori* information. A new iterative algorithm for computing the sparse solution to the inverse problems has been developed in which no prior knowledge about the regularization parameter is required and is adaptively computed at each iteration.

We have considered the stripmap mode of SAR operation in this thesis. In chapter 2, we have provided the necessary background explaining the stripmap mode of SAR operation along with the signal processing algorithm, known as *Omega-k*, to generate a SAR magnitude image from the complex-valued SAR raw data. A point targets simulator is also described to evaluate the performance of the compression. We have also

described various possible ways to generate the SAR raw data through inverse SAR processing of actual SAR complex and magnitude images. Performance metrics like peak sidelobe ratio (PSLR) and integrated sidelobe ratio (ISLR) for evaluating the performance of SAR data compression are also described.

Signal compression is carried out in the compressed sensing framework in which the encoder is simple whereas the decoder is computational expensive. The major disadvantage in conventional transform based compression of taking large samples and then rejecting most of the insignificant coefficients is taken care in the CS framework. It takes advantage of the fact that many signals are *sparse* i.e. fewer higher energy coefficients under some basis or frame. In chapter 3, we provide the necessary mathematical background to recover sparse signals from highly undersampled signals. The encoder, the sparsifying process and the decoder, which form the major components in this framework, are described in detail. The encoder which includes the measurement process consists of capturing a compressible signal through a small number of random linear projections onto a measurement basis. It is shown that the measurement matrices should satisfy certain properties like mutual coherence and restricted isometric properties for it to be non-adaptive to the input signal. It is also seen that the randomized measurement ensemble drawn from Gaussian i.i.d. or Bernoulli's distribution succeeds with high probability for most of the compressible signals. The decoder in this framework is shown to be essentially the classical linear inverse problem with the greater number of variables than the number of observations and is based on non-linear decoding scheme that uses the sparsity as *a-priori* information. Various recovery algorithms based on convex relaxation techniques and greedy algorithms are described. The robustness of the compressed sensing framework to deal with compressible signals and with the noisy measurement is also shown. The chapter concludes with examples to demonstrate the compressed sensing framework in action where the sparse/ compressible signal is captured/ measured by simply correlating with a small number of fixed waveforms that are incoherent with the sparsifying basis and also non-adaptive to the input signal.

The iterative algorithm with sparsity constraints is one of the popular methods to recover sparse coefficients from incomplete measurements, which arises in compressed sensing framework. In chapter 4, we present a new algorithm based on regularized iterations to find sparse solution for the real and complex-valued data which is based on minimization of an objective function. The objective function consists of a data fidelity term and prior information term with a regularization parameter to control the balance between these terms. In most of the iterative algorithms this regularization term is either manually set or estimated. The new iterative algorithm, L1_Adapt, developed requires no prior knowledge of the regularization parameter. The required regularization parameter is computed at each iteration step. It is shown that, this algorithm finds the sparse solution by slowly increases the l_1-norm of the successive approximations. The algorithm is based on computation of only vector operations and matrix-vector multiplications and avoids any computational expensive matrix factorizations. The various advantages of the iterative methods over the standard l_1-norm minimization algorithms and various possible extensions of the developed algorithm are also discussed. The algorithm is tested with various test signals, both real and complex, and is shown to converge to the min l_1-norm solution as that of basis pursuit (BP) algorithm. The chapter also gives an example in which the L1_Adapt finds the correct sparse solution whereas the orthogonal matching pursuit (OMP) fails. Few mechanisms to increase the speed of convergence of the algorithm are also presented. A new algorithm is used for the compression of the SAR point targets in the compressed sensing framework as described in chapter 5.

In chapter 5, our framework for the compression of complex-valued SAR raw data is established. The framework is applied to both point targets image and actual SAR data. The encoder in both the cases is simple and consists of 2D FFT with a random sampler. The reconstruction process for the point targets image involves computation of (forward and inverse) matched filtering, *Stolt* mapping and 2D FFT. The point targets image is sparse in the magnitude domain of the image itself and doesn't require any additional *sparsifying* transform. Whereas, for the actual SAR data the holographic basis

137

is implemented through functions consisting of 2D FFT, *Stolt* interpolation, matched filtering and a 2D-discrete and complex wavelet transforms. The stripmap mode SAR image is reconstructed from the sub-sampled complex valued raw data through regularization based reconstruction algorithm. The complex valued and random phase characteristics of the SAR images along with speckle noise make the regularization based reconstruction more challenging. It is seen that the compression performance in the CS framework is dependent on the effectiveness of the sparsifying transform on the SAR complex image. We have demonstrated empirically that the CS framework for compression of complex-valued SAR raw data is effective for the cases when the SAR image is sparse in the spatial domain without any degradation in the resolution, PSLR and ISLR. Thus, the optimization based reconstruction of sparse spatial points with small set of measurement data has an advantage that important features required for detection, classification and registration of SAR images can be recovered without reconstruction of the full image. The recovery based on CS is thus scalable depending upon various applications. The limitation of CS framework while dealing with actual satellite images due to lack of good sparsifying transforms for the complex-valued data is also addressed. Various options for compressibility of the actual SAR complex image in magnitude-phase domain, real-imaginary domain, shifting the spectrum to positive half through real discrete wavelets transforms (DWT) were evaluated. The compression of the magnitude-phase data through wavelet transforms made the reconstruction difficult due to the non-linear reconstruction model. The compression of the real-imaginary data through discrete wavelet transform (DWT) for the actual satellite data was not sufficient to give any appreciable compression of SAR raw data in the CS framework. In one of the experiments, we modified the complex wavelet transform (CWT) to a frame to check the compressibility of real-imaginary data. The compressibility performances of the CWT on the actual SAR satellite data were not enough to give compression ratio greater than 2:1 for the SAR raw data. It is also observed that the new algorithm L1_Adapt performed equally well as the orthogonal matching pursuit (OMP) for the point targets in terms of PLSR and ISLR and for the actual satellite data there was no substantial improvement as compared to OMP. This suggests that the performance of the

SAR raw data compression in the CS framework mainly depends upon the compressibility of the sparsifying transform.

Overall, this thesis has presented a new perspective to compression of complex-valued SAR raw data, in particular for stripmap SAR imaging mode. At the centre of new approach was the compression of the raw data by reduction of number of samples rather than the number of bits which was central to the conventional compression of SAR raw data. With this investigation, it is shown that the success of the compression of the complex-valued SAR raw data is limited to the case where the image is sparse in the spatial domain for the full image reconstruction. The other applications namely detection, classification, estimation, etc. could be performed with partial image reconstruction with the compressive measurements. The new iterative algorithm developed and its various extensions discussed in this thesis, makes it an important alternative algorithm to find sparse solution to any inverse problems.

6.2 Suggestions for Further Work

We suggest some possible directions of future research in the area of SAR raw data compression based on compressed sensing framework.

- Much greater performance in terms of higher compression ratio and reconstruction qualities are expected by using transforms that could give better sparsity for the SAR complex signal as compared to the real wavelets and DT-CWT used here. Some work in this direction is required to get better compressible performance of the complex data which is comparable to the magnitude data.

- Further study and extensions on the non-linear reconstruction algorithms based on the regularization of only the magnitude data in the CS framework is required to verify any additional compression gain that could be achieved by using DWT on

the detected images. Such half-quadratic regularization method in [99] has been successfully applied in feature-enhanced SAR imaging.

- The idea to use multiple sparsifying transforms to extract various features of the SAR image along with the regularized method of SAR image reconstruction could be explored.

- The rate distortion performance of the CS framework for the SAR raw data is required to be carried out to understand the effect of the quantization of the sub-sampled compressive measurements.

- The block adaptive quantization (BAQ) has been successfully applied to compress the SAR raw data by allocating variable number of bits to a block of data based on its computed variance [4]. It could be interesting to combine the techniques from BAQ and compressed sensing framework proposed in this thesis to get better compression performance.

- A more detailed study could be carried out to make the encoder much simpler than what is proposed here by sub-sampling the data in the time domain by using the random filtering technique suggested in [111]. The random filtering technique is based on convolution of the signal with a fixed FIR filter having random taps. This would eliminate the requirement of 2D-FFT at the encoder.

- A theoretical proof for the convergence of the iterative algorithm proposed here is to be taken up.

References

[1]   J. C. Curlander and R. N. McDonough, *Synthetic Aperture Radar: Systems and Signal Processing*. New York: Wiley, 1991.

[2]   R. Balmer and P. Hartl, "Synthetic Aperture Radar Interferometry," *Inverse Problems*, vol. 14, pp. R1-R54, 1998.

[3]   D. A. Ausherman, A. Kozma, J. L. Walker, H. M. Jones, and E. C. Poggio, "Development in Radar Imaging," *IEEE Transactions on Aerospace and Electronics Systems*, vol. AES-20, pp. 363-398, July 1984.

[4]   R. Kwok and W. T. K. Johnson, "Block adaptive quantization of Magellan SAR data," *IEEE Transactions on GeoScience and Remote Sensing*, vol. 27, pp. 375-383, July 1989.

[5]   M. Brandfass, W. Coster, U. Benz, and A. Moreira, "Wavelet based approaches for efficient compression of complex SAR image data," in *IEEE International Geoscience and Remote Sensing Symposium*, Singapore, 1997, pp. 2024-2027.

[6]   G. Poggi, L. Ragozini, and L. Verdoliva, "Compression of SAR data through range focusing and variable rate vector quantizer," *IEEE Transactions on GeoScience and Remote Sensing*, vol. 38, pp. 1282-1289, May 2000.

[7]   J. W. Owens, M. W. Marcellin, B. R. Hunt, and M. Kleine, "Compression of Synthetic Aperture Radar Phase History Data Using Trellis Coded Quantization Techniques," in *ICIP'97*, 1997, pp. 592-595.

[8]   U. Benz, K. Strodl, and A. Moreira, "A Comparison of Several Algorithms for SAR Raw Data Compression," *IEEE Transactions on GeoScience and Remote Sensing*, vol. 33, pp. 1266-1276, September 1995.

[9]   W. G. Carrara, R. S. Goodman, and R. M. Majewski, *Spotlight Synthetic Aperture Radar*. Boston: Artech House, 1995.

[10] D. C. Munson Jr., J. D. O'Brien, and W. K. Jenkins, "A tomographic formulation of spotlight-mode synthetic aperture radar," *Proceedings of the IEEE*, vol. 71, pp. 917-925, August 1983.

[11] M. Soumekh, *Synthetic Aperture Radar Signal Processing*. New York: Wiley, 1999.

[12] A. C. Fannjiang, K. Solna, and P. C. Yan, "On the Use of Start-Stop Approximation for Spaceborne SAR Imaging," *SIIMS*, vol. 2, pp. 646-669, 2009.

[13]   M. Soumekh, "Reconnaissance with Ultra Wideband UHF Synthetic Aperture Radar," *IEEE Signal Processing,* vol. 12, pp. 21-40, 1995.

[14]   D. C. Munson and R. L. Visentin, "A Signal Processing View of Strip-Mapping Synthetic Aperture Radar," *IEEE Transactions on Accoustics, Speech and Signal Processing,* vol. 37, pp. 2131-2147, December 1989.

[15]   P. T. Gough and D. W. Hawkins, "Unified framework for modern synthetic aperture imaging algorithm," *International Journal of Imaging Systems and Technology,* vol. 8, pp. 343-358, 1997.

[16]   R. Balmer, "A comparison of range-doppler and wavenumber domain SAR focusing algorithms," *IEEE Transactions on GeoScience and Remote Sensing,* vol. 30, pp. 706-713, July 1992.

[17]   J. Walker, "Range-Doppler imaging of rotating objects," *IEEE Transactions on Aerospace and Electronics Systems,* vol. AES-16, pp. 23-52, January 1980.

[18]   A. Khwaja, L. Ferro-Famil, and E. Pottier, "SAR Raw Data Generation Using Inverse SAR Image Formation Algorithms," in *IEEE International Conference on Geoscience and Remote Sensing Symposium, IGARSS 2006.* , 2006, pp. 4191-4194.

[19]   E. J. Candes, J. Romberg, and T. Tao, "Robust uncertainty principles: exact signal reconstruction from highly incomplete frequency information," *IEEE Transactions on Information Theory,* vol. 52, pp. 489-509, February 2006.

[20]   D. L. Donoho, "Compressed Sensing," *IEEE Transactions on Information Theory,* vol. 52, pp. 1289-1306, 2006.

[21]   S. A. Werness, S. C. Wei, and R. Carpinella, "Experiments with Wavelets for Compression of SAR Data," *IEEE Transactions on GeoScience and Remote Sensing,* vol. 32, pp. 197-201, 1994.

[22]   R. W. Ives, N. Magotra, and C. Kiser, "Wavelet compression of complex SAR imagery using complex- and real-valued wavelets: a comparative study," in *Thirty-Second Asilomar Conference on Signals, Systems & Computers.,* 1998, pp. 1294-1298 vol.2.

[23]   I. Daubechies, "Orthogonal bases of compactly supported wavelets," *Communciation Pure Applied Math.,* vol. 41, pp. 909-996, 1988.

[24]   M. Duarte, M. Davenport, D. Takhar, J. N. Laska, T. Sun, K. K. Kelly, and R. G. Baraniuk, "Single-pixel imaging via compressive sampling," *IEEE Signal Processing Magazine,* vol. 25, pp. 83-91, March 2008.

[25]   D. Takhar, J. N. Laska, M. Wakin, M. Duarte, D. Baron, S. Sarvotham, K. K. Kelly, and R. G. Baraniuk, "A new compressive imaging camera architecture us-

ing optical-domain compression," in *Proceedings of the Computational Imaging IV at SPIE Electronic Imaging*, San Jose, California, 2006.

[26] M. A. Sheikh, S. Sarvotham, O. Milenkovic, and R. G. Baraniuk, "DNA array denoising from nonlinear measurements by belief propagation," in *14th Workshop on IEEE Statistical Signal Processing*, Madison, 2007, pp. 26-29.

[27] R. G. Baraniuk and P. Steeghs, "Compressive radar imaging," in *IEEE Radar Conference*, 2007, pp. 128-133.

[28] J. Bobin, L. Starck, and R. Ottensamer, "Compressed sensing in astronomy," *Preprint*, 2008.

[29] M. Lustig, D. L. Donoho, and J. M. Pauly, "Sparse MRI: The application of compressed sensing for rapid MR imaging," *Magnetic Resonance in Medicine*, vol. 58, pp. 1182-1195, 2007.

[30] Y. Zhang, "When is missing data recoverable?," *Rice University's CAAM Technical Report TR06-15,* 2006.

[31] D. L. Donoho and X. Huo, "Uncertainity principles and ideal atomic decomposition," *IEEE Transactions on Information Theory*, vol. 47, pp. 2845-2862, November 2001.

[32] E. Candes and T. Tao, "Near Optimal Signal Recovery from Random Projections: Universal Encoding Strategies ?," *IEEE Transactions on Information Theory*, vol. 52, pp. 5406-5425, December 2006.

[33] J. Haupt and R. Nowak, "Signal reconstruction from noisy random projections," *IEEE Transactions on Information Theory*, vol. 52, pp. 4036-4048, September 2006.

[34] Y. Tsaig and D. Donoho, "Extensions of compressed sensing," *Signal Processing*, vol. 86, pp. 549-571, 2006.

[35] R. Coifman, F. Geshwind, and Y. Meyer, "Noiselets," *Applied and Computational Harmonic Analysis*, vol. 10, pp. 27-44, 2001.

[36] M. Elad, "Optimized Projections for Compressed Sensing," *IEEE Transactions on Signal Processing*, vol. 55, pp. 5695-5702, December 2007.

[37] E. Candes, J. Romberg, and T. Tao, "Stable Signal Recovery from Incomplete and Inaccurate Measurements," *Communications on Pure and Applied Mathematics*, vol. 59, pp. 1207-1223, August 2006.

[38] S. Chen, D. Donoho, and M. Saunders, "Atomic Decomposition by Basis Pursuit," *SIAM Review*, vol. 43, pp. 129-159, 2001.

[39] E. Candes and J. Romberg, "Quantitative robust uncertainty principles and optimally sparse decompositions " *Foundation of Computational Mathematics,* vol. 6, pp. 227-254, April 2006.

[40] S. G. Mallat and Z. Zhang, "Matching pursuits with time-frequency dictionaries," *IEEE Transactions on Signal Processing,* vol. 41, pp. 3397-3415, 1993.

[41] Y. Pati, R. Rezaiifar, and P. Krishnaprasad, "Orthogonal Matching Pursuit: Recursive Function Approximation with Applications to Wavelet Decomposition," *Proceedings of the 27th Annual Asilomar Conference on Signals, Systems and Computers,* vol. 1, pp. 40-44, November 1993.

[42] J. Tropp and A. C. Gilbert, "Signal Recovery from partial information via orthogonal matching pursuit," *IEEE Transactions on Information Theory,* vol. 53, pp. 4655-4666, 2007.

[43] E. Candes and T. Tao, "The Dantzig selector: Statistical estimation when p is much larger than n," *Annals of Statistics,* vol. 35, pp. 2313-2351, December 2007.

[44] E. J. Candes and T. Tao, "Decoding by linear programming," *IEEE Transactions on Information Theory,* vol. 51, pp. 4203-4215, 2005.

[45] E. Candes and M. Wakin, "An Introduction to Compressive Sampling," *IEEE Signal Processing Magazine,* vol. 25, pp. 21-30, March 2008.

[46] R. Tibshirani, "Regression Shrinkage and Selection via the Lasso," *Journal of the Royal Statistical Society. Series B (Methodological),* vol. 58, pp. 267-288, 1996.

[47] D. L. Donoho, "For most underdetermined systems of linear equations the minimal l1 norm solution is also the sparsest solution," *Communciation Pure Applied Math.,* vol. 59, pp. 797-829, 2006.

[48] M. Figueiredo, R. Nowak, and S. J. Wright, "Gradient projection for sparse reconstruction: Application to compressed sensing and other inverse problems," *IEEE Journal of Selected Topics in Signal Processing: Special Issue on Convex Optimization Methods for Signal Processing,* vol. 1, pp. 586-598, 2007.

[49] B. Efron, T. Hastie, I. Johnstone, and R. Tibshirani, "Least angle regression," *Annual Statistics,* vol. 32, pp. 407-499, 2004.

[50] D. Malioutov, M. Cetin, and A. Willsky, "Homotopy continuation for sparse signal representation," in *IEEE International conference on Acoustics, Speech and Signal Processing,* Philadelphia, 2005, pp. 733-736.

[51] B. Turlach, "On algorithms for solving least squares problems under an L1 penalty or an L1 constraint," in *American Statistical Association; Statistical Computing Section,* Alexandria, 2005, pp. 2572-2577.

[52] R. Chartrand, "Exact reconstruction of sparse signals via nonconvex minimization," *IEEE Signal Processing Letter*, vol. 14, pp. 707-710, 2007.

[53] R. Chartrand, "Nonconvex compressed sensing and error correction," in *International Conference on Acoustics, Speech and Signal Processing*. vol. 3 Piscataway, NJ, 2007, pp. III-889 -III-892.

[54] R. Chartrand and V. Staneva, "Restricted isometry properties and nonconvex compressive sensing," *Inverse Problems*, vol. 24, pp. 1-14, 2008.

[55] I. Daubechies, M. Defrise, and C. De Mol, "An iterative thresholding algorithm for linear inverse problems with a sparsity constraint," *Communciation Pure Applied Math.*, vol. 157, pp. 1413-1457, 2004.

[56] M. Elad, "Why simple shrinkage is still relevant for redundant representation," *IEEE Transactions on Information Theory*, vol. 52, pp. 5559-5569, 2006.

[57] E. J. Candes and J. Romberg, "Practical Signal Recovery from Random Projections," *Wavelet Applications in Signal and Image Processing XI, Proc. SPIE Conf.*, vol. 5914, 2005.

[58] K. Bredies and D. A. Lorenz, "Iterated hard shrinkage for minimization problems with sparsity constraints," *SIAM Journal on Scientific Computing*, vol. 30, pp. 657-683, 2008.

[59] S. J. Kim, K. Koh, M. Lustig, S. P. Boyd, and D. Gorinevsky, "A method for large-scale l1-regularized least-squares " *IEEE Journal of Selected Topics in Signal Processing*, vol. 1, pp. 606-617, December 2007.

[60] Bioucas, "A New TwIST: Two-Step Iterative Shrinkage/Thresholding Algorithms for Image Restoration," *Image Processing, IEEE Transactions on*, vol. 16, pp. 2992-3004, 2007.

[61] T. Blumensath and M. E. Davies, "Iterative hard thresholding for compressed sensing," *Preprint*, July 2008.

[62] N. Kingsbury, "Complex wavelets for shift invariant analysis and filtering of signals," *Applied and Computational Harmonic Analysis*, vol. 10, pp. 234-253, May 2001.

[63] K. K. Herrity, A. C. Gilbert, and J. Tropp, "Sparse approximation via iterative thresholding," in *Proceedings of the IEEE International conference on Acoustic, Speech and Signal Processing*, 2006, pp. III-14-III-19.

[64] R. Nowak and M. Figueiredo, "Fast wavelet-based image deconvolution using the EM algorithm," in *Proceedings of the 35th Asilomar conference on Signals, Systems and Computers*, Monterey, 2001, pp. 371-375.

[65]   M. Figueiredo and R. Nowak, "An EM Algorithm for Wavelet Based Image Restoration," *IEEE Transactions on Image Processing*, vol. 12, pp. 906-916, August 2003.

[66]   M. Elad, B. Matalon, J. Shtok, and M. Zibulevsky, "A wide-angle view at iterated shrinkage algorithms," *SPIE (Wavelet XII)*, vol. 6701, pp. 26-29, August 2007.

[67]   P. L. Combettes and V. R. Wajs, "Signal recovery by proximal forward-backward splitting," *SIAM Journal on Multiscale Modeling and Simulation*, vol. 4, pp. 1168-1200, November 2005.

[68]   J. A. Tropp, "Greed is good: algorithmic results for sparse approximation," *Information Theory, IEEE Transactions on*, vol. 50, pp. 2231-2242, 2004.

[69]   D. Needell and R. Vershynin, "Uniform uncertainty principle and signal recovery via regularized orthogonal matching pursuit," *Preprint*, 2008.

[70]   D. Needell and R. Vershynin, "Signal recovery from incomplete and inaccurate measurements via regularized orthogonal matching pursuit," *Preprint*, 2008.

[71]   W. Dai and O. Milenkovic, "Subspace pursuit for compressed sensing: Closing the gap between performance and complexity," *preprint*, 2008.

[72]   D. Donoho and Y. Tsaig, "Sparse solution of underdetermined linear equations by stagewise orthogonal matching pursuit," *Preprint*, 2007.

[73]   M. Duarte, M. Wakin, and R. Baraniuk, "Fast Reconstruction of Piecewise Smooth Signals from Random Projections," in *Online Proceedings of the Workshop on Signal Processing with Adaptive Sparse Structured Representations (SPARS)*, Rennes, France, 2005.

[74]   M. Andrle, L. R. Neyra, and E. Sagianos, "Flexible tree-search based orthognal matching pursuit algorithm," in *30th IEEE International Conference on Acoustics, Speech and Signal Processing*, Philadelphia, PA, 2004, pp. 673-676.

[75]   C. La and M. N. Do., "Tree-based orthogonal matching pursuit algorithm for signal reconstruction," in *13th IEEE International Conference on Image Processing*, Atlanta, GE, 2006, pp. 8-11.

[76]   D. Needell and J. Tropp, "CoSaMP: Iterative signal recovery from incomplete and inaccurate samples," *Preprint*, 2008.

[77]   M. R. Hestenes, "Iterative methods for solving linear equations," *Journal of Optimization Theory and Applications*, vol. 11, pp. 323-334, 1973.

[78]   D. L. Donoho and I. M. Johnstone, "Ideal spatial adaptation by wavelet shrinkage," *Biometrika*, vol. 81, pp. 425-455, 1994.

[79] K. Jari and S. Erkki, *Statistical and Computational Inverse Problems*, 2005.

[80] W. C. Karl, "Regularization in Image Restoration and Reconstruction," in *Handbook of Image and Video Processing*, A. Bovik, Ed.: Academic Press, 2000.

[81] C. R. Vogel and M. E. Oman, "Fast, Robust Total- Variation Based Reconstruction of Noisy, Blurred Images," *IEEE Transactions on Image Processing*, vol. 7, pp. 813-824, June 1998.

[82] E. Hale, W. Yin, and Y. Zhang, "A Fixed-Point Continuation Method for l1 - Regularized Minimization with Applications to Compressed Sensing," TR07-07, July 7 2007.

[83] A. Chambolle, R. A. DeVore, N.-Y. Lee, and B. J. Lucier, "Nonlinear wavelet image processing: variational problems, compression, and noise removal through wavelet shrinkage," *IEEE Transactions on Image Processing*, vol. 7, pp. 319-335, 1998.

[84] I. Daubechies, M. Fornasier, and I. Loris, "Accelerated Projected Gradient Method for Linear Problems with Sparsity Constraints," *Rice CAAM TR07-13*, 2007.

[85] M. Bertero and P. Boccacci, *Introduction to inverse problems in imaging*: IoP, 1998.

[86] D. Donoho, I. Drori, V. Stodden, and Y. Tsaig, "SparseLab," *http://sparselab.stanford.edu/*, 2005.

[87] G. Steidl and J. Weichert, "Relations between Soft Wavelet Shrinkage and Total Variation Denoising," *DAGM 2002 LNCS 2449*, pp. 198-205, 2002.

[88] E. Candes, "L1-Magic: Recovery of Sparse Signals," *http://www.acm.caltech.edu/l1magic/*.

[89] E. J. Candes, M. B. Wakin, and S. P. Boyd, "Enhancing Sparsity by Reweighted L1 Minimization," *Journal of Fourier Analysis and Applications; special issue on sparsity*, 2007 To appear.

[90] W. M. Brown and R. J. Fredericks, "Range-Doppler Imaging with Motion through Resolution Cells," *IEEE Transactions on Aerospace and Electronics Systems*, vol. AES-5, pp. 98-102, January 1969.

[91] A. S. Milman, "SAR Imaging by w-k Migration," *International Journal of Remote Sensing*, vol. 14, pp. 1965-1979, 1993.

[92] M. Soumekh, "A System Model and Inversion of Synthetic Aperture Radar," *IEEE Transactions on Image Processing*, vol. 1, pp. 64-76, January 1992.

[93] H. Runge and R. Bamler, "A Novel High Precision SAR Focusing Algorithm based on Chirp Scaling," in *IEEE International Geoscience and Remote Sensing Symposium*, May 1992, pp. 372-375.

[94] M. D. Desai and W. K. Jenkins, "Convolution backprojection image reconstruction for spotlight mode synthetic aperture radar," *IEEE Transactions on Image Processing*, vol. 1, pp. 505-517, October 1992.

[95] M. Lustig, J. H. Lee, D. L. Donoho, and J. M. Pauly, "Faster imaging with randomly pertubated, undersampled spirals and 11 reconstruction," in *Proceedings of the 13th Annual Meeting of ISMRM*, Miami Beach, 2005, p. 685.

[96] T. C. Chang, L. He, and T. Fang, "MRI Image reconstruction from sparse radial samples using Bregman iteration," in *Proceedings of the 13th Annual Meeting of ISMRM*, Seattle, 2006, p. 696.

[97] J. M. Heermans, R. Rouse, C. Chung-Fu, and R. Bonneau, "Wavelet/trellis coded quantization of complex SAR imagery," in *Applied Imagery Pattern Recognition Workshop, 2000. Proceedings. 29th*, 2000, pp. 121-128.

[98] V. Pascazio, G. Schirinzi, and I. D. Buttarello, "Low Bit Rate Transform Coding for SAR Raw Data Compression," *IEEE Radar Conference*, pp. 233-236, 1999.

[99] M. Cetin, "Feature-Enhanced Synthetic Aperture Radar Imaging," in *Boston University*. vol. Ph.D, 2001.

[100] L. Marple, Jr., "Computing the discrete-time analytic signal via FFT," *IEEE Transactions on Signal Processing*, vol. 47, pp. 2600-2603, 1999.

[101] M. Antonini, M. Barland, P. Mathieu, and I. Daubechies, "Image coding using wavelet transform," *IEEE Transactions on Image Processing*, vol. 1, pp. 205-220, April 1992.

[102] A. E. Boustani, A. Turiel, E. Huot, K. Brunham, and W. Kinsner, "Wavelet Transform Based Compression Techniques for Raw SAR Data," in *IEEE Canadian Conference on Electrical & Computer Engineering*, 2002, pp. 857-862.

[103] I. Daubechies, *Ten Lectures on Wavelets*: SIAM, 1992.

[104] J. E. Odegard, H. Guo, M. Lang, C. S. Burrus, R. O. Wiells, L. M. Novak, and M. Hiett, "Wavelet based SAR speckle reduction and image compression," *SPIE*, pp. 259-271, 1995.

[105] I. W. Selesnick, R. G. Baraniuk, and N. C. Kingsbury, "The dual-tree complex wavelet transform," *IEEE Signal Processing Magazine*, vol. 22, pp. 123-151, 2005.

[106] I. Voicu and M. Borda, "Image Compression Using Complex Wavelet Transform," in *The International Conference on EUROCON*, 2005, pp. 919-922.

[107] N. Kingsbury and T. Reeves, "Redundant representation with complex wavelets: How to achieve sparsity?," in *Proc. of 10th IEEE International Conference on Image Processing*, Barcelona, Spain, September 2003, pp. 45-48.

[108] T. Adeyemi and M. Davies, "Sparse representations of images using overcomplete complex wavelets," in *IEEE/SP 13th Workshop on Statistical Signal Processing*, 2005, pp. 865-870.

[109] N. Kingsbury, "Web-page," *http://www-sigproc.eng.cam.ac.uk/~ngk*.

[110] "Model Based Vision Laboratory, Sensor Data Management System (MSTAR) web page:," in *http://www.mbvlab.wpafb.af.mil/public/sdms/datasets/mstar:* Air Force Research Laboratory.

[111] J. A. Tropp, M. B. Wakin, M. Duarte, D. Baron, and R. G. Baraniuk, "Random Filters for Compressive Sampling and Reconstruction," in *ICASSP 2006*, Toulouse, 2006, pp. 14-19.

Appendix

Publications

This appendix contains re-prints of the papers published externally and submitted during the course of this research.

1. Sujit Bhattacharya, Thomas Blumensath, Bernard Mulgrew and Mike Davies, "Fast Encoding of Synthetic Aperture Radar Raw Data Using Compressed Sensing", in *Proceedings of IEEE/SP 14th Workshop on Statistical Signal Processing, (SSP '07)*, (Madison, USA), pp. 448-452, 26-29 August, 2007.

2. Sujit Bhattacharya, Thomas Blumensath, Bernard Mulgrew and Mike Davies, "Synthetic Aperture Radar Raw Data Encoding Using Compressed Sensing", in *Proceedings of IEEE Radar Conference (RADAR '08)*, (Rome, Italy), pp. 1-5, 26-30 May, 2008.

3. Sujit Bhattacharya and Bernard Mulgrew, "An Iterative Algorithm for Computing Sparse Solutions to Linear Inverse Problems", submitted to ICASSP 2010.

FAST ENCODING OF SYNTHETIC APERTURE RADAR RAW DATA USING COMPRESSED SENSING

Sujit Bhattacharya, Thomas Blumensath, Bernard Mulgrew, Mike Davies

S.Bhattacharya@ed.ac.uk

Institute of Digital Communication
Joint Research Institute for Signal and Image Processing
Edinburgh University, EH9 3JL.

ABSTRACT

Synthetic Aperture Radar (SAR) is active and coherent microwave high resolution imaging system, which has the capability to image in all weather and day-night conditions. SAR transmits *chirp* signals and the received echoes are sampled into In-phase (I) and Quadrature (Q) components, generally referred to as raw SAR data. The various modes of SAR coupled with the high resolution and wide swath requirements result in a huge amount of data, which will easily exceed the on-board storage and downlink bandwidth of a satellite. This paper addresses the compression of the raw SAR data by sampling the signal below *Nyquist* rate using ideas from *Compressed Sensing* (CS). Due to the low computational resources available onboard satellite, the idea is to use a simple encoder, with a 2D FFT and a random sampler. Decoding is then based on convex optimization or uses greedy algorithms such as Orthogonal Matching Pursuit (OMP).

Index Terms— SAR, Compressed Sensing, Encoding

1. INTRODUCTION

Synthetic Aperture Radar (SAR) is active and coherent microwave radar, which produces high spatial resolution images from a moving platform – an airplane or a satellite. The radar produces 2D (range and azimuth) terrain reflectivity images by emitting a sequence of closely spaced radio frequency pulses and by sampling the echoes scattered from the ground targets. The received echoes are sampled into In-phase (I) and Quadrature (Q) components referred to as raw SAR data. In satellite systems, raw data is directly transmitted to the ground segment via a dedicated transmission link when in view with the ground segment or is stored onboard for later transmission to the ground.

The compression of raw SAR data poses several challenges due to its noise like characteristics [1]. The noise like characteristics arises because signals from several scatters are added incoherently with unknown phase and amplitude. Typically its adjacent samples are uncorrelated in both range and azimuth directions.

The SAR processed images have compression factor of 50:1, which is much higher than the existing raw data compression factor of 4:1 [2]. Most of the traditional compression systems exploit the redundancy inherent in the *Nyquist* rate sampled signal to achieve compact representation and efficient transmission of the information. This technique of sampling at a higher rate and then eliminating redundancy by processing a large amount of data has poor efficiency in terms of both sampling rate and computational complexity.

A new framework that recovers signals from incomplete measurements is *Compressed Sensing* (CS), introduced in [3] and [4]. It was shown that a signal having a sparse representation can be captured (encoded) from a small number of random linear projections onto a measurement basis. The measurement process is *non-adaptive*. The original signal can be reconstructed (decoded) through a non-linear decoding scheme that uses the sparsity as *a priori* information for solving the linear inverse problem.

2. SAR SYSTEM AND PROCESSING

In the *Stripmap* mode the radar maps the surface with the antenna pointing downward such that the boresight (centre) of the mainlobe of the real aperture radiation pattern is perpendicular of the flight path as shown in Figure 1 [1]. The simplified model for the SAR *Stripmap* model is to

consider the stationary imaging surface to consist of several point reflectors with reflectivity σ_n and located at the location (x_n, y_n). The radar located at (o, u_n) in the spatial domain transmits wide bandwidth signal $p(t)$ of period T_p at regular interval T_{PRI}.

The processing of SAR raw data is shown in Figure 2, which involves computation of 2D FFT, matched filtering with the scene centre reference function, converting the polar format data to the rectangular format through *Stolt mapping* and finally 2D IFFT [5].

3. COMPRESSED SENSING THEORY

Let us consider signal $f \in \mathbb{R}^N$, which has a sparse representations over a fixed orthogonal transform, $\Psi \in \mathbb{R}^{N \times N}$, having columns ψ_i, $i = 1, ..., N$. Thus, we can describe the signal as $f = \Psi x$ with $\|x\|_0 \leq L \ll N$, where $\|x\|_0 = |(i : x_i \neq 0)|$. Such a signal is known as an $L - Sparse$ signal w.r.t. the dictionary Ψ.

In the CS framework, to measure (encode) f we compute the measurement vector $y \in \mathbb{R}^K$ using a linear projector $M \in \mathbb{R}^{K \times N}$, *with* $L < K \ll N$ via $y = Mf$. Since $K \ll N$, we have fewer measurements than degrees of freedom for the signal f. We refer to M as the measurement matrix whose rows are the measurement vectors and denote its columns by $\varphi_1, ..., \varphi_N$.

The measurement signal $y \in \mathbb{R}^K$ is written is terms of $x \in \mathbb{R}^N$ as

$$y = Mf = M\Psi^* x$$
$$= H x \qquad (1.1)$$

where $H = M\Psi^*$ is also known as the holographic basis.

The original signal f can be reconstructed from y by exploiting the sparsity of its representation i.e. by searching for all possible $\hat{x}$ satisfying $y = H\hat{x}$ that is the sparsest. If this representation coincides with x we get a perfect reconstruction of the signal via (1.1). Mathematically, $\hat{x}$ can be found by solving the linear inverse problem through l_0 optimization $\hat{x} = \arg \min \|x\|_0$ subject to $y = H\hat{x}$. The objective function enforces the sparsity whereas the constraint enforces data consistency. The l_0 optimisation is a combinatorial problem and is NP-hard to solve. The two most common approaches are therefore to replace the l_0 approximation problem with convex optimisation methods or greedy methods [6, 7].

4. RAW SAR DATA COMPRESSION THROUGH CS

To study the feasibility of using CS for SAR raw data compression, we used five point targets simulated through the SAR simulator as shown in Figure 3(a) with ideal point target response in Figure 3(b). The 2D FFT of the complex raw data was performed, as shown in Figure 3(c), after which the data was sampled randomly. The size of the measurement data is 4200 for the image size of 256 x 256, to recover 200 samples of the sparse image representation of five targets. The reconstruction algorithm is based on OMP with the least square estimation performed through the Conjugate Gradient (CG) method. The reconstruction process involves computation of (forward and inverse) matched filtering, *Stolt* mapping and 2D FFT. The reconstructed image for the point target simulation is shown in Figure 3(d) and was evaluated in terms of the Peak Side Lobe Ratio (PSLR) and Integrated Side Lobe Ratio (ISLR). The PSLR is defined as the ratio of the peak intensity of the most prominent sidelobe to the peak intensity of the mainlobe. The ISLR is the ratio of the power in the mainlobe to the total power in all the sidelobes. The PSLR and the ISLR of the point targets simulation for 256 x 256 size complex SAR processed image and the image generated with 4200 measurement samples and 200 wavelet coefficients are tabulated in Table 1.

	PSLR (dB)	ISLR (dB)
Original Image	-11.21	-1.75
CS Image	-10.97	-4.96

Table 1. PSLR and ISLR of the original and reconstructed CS image.

There is no degradation in PSLR and the improvement in the ISLR is due to the recovery of only 200 wavelet coefficients which resulted in the reduction of the sidelobes power.

For the compression of the satellite SAR raw data, the amplitude and phase are both indispensable for many applications e.g. interferometer. Discrete Wavelet Transforms have been used for SAR intensity image compression but are not suitable to preserve the signal phase information. The compression of the complex SAR image is reported in [8] and the study of the Complex Wavelet Transform (CWT) for the SAR image compression and denoising to preserve both amplitude and phase has been reported in [9]. We propose to use the Dual Tree CWT (DT-CWT) [10], as a sparsifying transform with OMP to find the sparse representation of the complex SAR image. The DT-CWT comprises of two parallel wavelet filter banks that contain filters of different delays that minimises the aliasing error due to decimation [10]. DT-CWT has been generally applied to the real signals where the spectral decomposition

449

takes place only for the positive part of the spectrum. For the quadrature SAR image, the spectral decompositions for both negative and positive part of the spectrum are required. This is achieved by applying the DT-CWT to the real, ξ_r, and imaginary part, ξ_i, of the complex SAR image separately and then combining the complex output as

$$\xi_+ = \xi_r + i\xi_i \ ,$$
$$\xi_- = \xi_r - i\xi_i \tag{1.2}$$

where ξ_+ corresponds to the positive frequency component and ξ_- corresponds to the negative frequency component. Thus, we represent the image using a frame operator rather than a basis.

The Compressed Sensing framework for the complex SAR raw data is shown in Figure 2. The holographic basis, $\mathbf{H}$, in (1.1) is implemented through functions consisting of 2D-DT-CWT, 2D FFT, Stolt interpolation, matched filtering and the measurement matrix, $\mathbf{M}$, consists of random sampling points. The reconstruction is similar to the one used for the point target processing.

The OMP based reconstruction for the 2:1 compression for the actual complex SAR image was carried out for 32 x 32 size image to evaluate the PSNR with respect to various lengths of recovered wavelet coefficients and is tabulated in Table 2. The PSNR of 2:1 compressed signal degrades faster for recovery of wavelet coefficients greater than 150. This is consistent with the theory of compressed sensing to have measurement length 3 to 5 times the length of the sparse coefficients.

	50	100	150	200	250	300
Original	36.8	38.8	40.3	41.5	42.7	43.9
CS Image	36.8	38.7	39.5	39.7	39.8	39.8

Table 2. PSNR (dB) of 2:1 compressed signal with respect to the recovered wavelet coefficients.

For the 256 x 256 SAR complex image, as shown in figure 4(a), the reconstruction of the image for 6000 wavelet coefficients with OMP is shown in figure 4(b). The figure 4(c) shows the reconstruction with OMP for 6000 wavelet coefficients with 2:1 compression ratio. The reconstruction with the 6000 most significant wavelet coefficients (sorted) with DT-CWT as a frame operator is shown in figure 4(d). The reconstruction with OMP is limited to 6000 coefficients as the sparsity of the complex wavelet is not sufficient to provide any substantial improvement in PSNR of the reconstructed image. The reconstructed images with and without compression do not show much perceptual difference.

The optimization based reconstruction of SAR image with small set of measurement data has an advantage that important features required for detection, classification and registration of SAR images can be recovered without reconstruction of the full image. The recovery based on CS is thus scalable depending upon various applications.

5. CONCLUSIONS

This paper proposes the use of the CS framework for fast compression of SAR raw data to ease the computational requirements of satellite onboard processing. Much greater performance in terms of higher compression ratio and reconstruction qualities are expected by using transforms that could give better sparsity for the SAR complex signal as compared to the DT-CWT used here.

6. REFERENCES

[1] A J.C. Curlander and R.N. McDonough, Synthetic Aperture Radar: Systems and Signal Processing, New York, Wiley, 1991.

[2] U. Benz, K. Strodl, and A. Moreira, "A Comparison of Several Algorithms for SAR Raw Data Compression," IEEE Trans. on Geo. and Remote Sensing, vol. 33, No. 5, pp. 1266 – 1276, Sep 1995.

[3] E. Candes, J. Romberg, and T. Tao, "Robust Uncertainty Principles: Exact Signal Reconstruction from Highly Incomplete Frequency Information," IEEE Trans. Inf. Theory, vol. 52, 2006.

[4] D. L. Donoho, "Compressed Sensing," IEEE Trans. Inf. Theory, vol. 52, pp. 1289-1306, 2006.

[5] M. Soumekh, Synthetic Aperture Radar Signal Processing, New York, Wiley, 1999.

[6] E. Candes and T. Tao, "Near Optimal Signal Recovery from Random Projections: Universal Encoding Strategies?," Tech. Rep. 04-70, UCLA Group in Comp. and Applied Math., Dec. 2004.

[7] J. Tropp and A. Gilbert, "Signal Recovery from Partial information via Orthogonal Matching Pursuit," http://www.dsp.ece.rice.edu/CS/tropp.pdf, 2005.

[8] M. Brandfaß, W. Cöster, U. Benz, and A. Moreira, "Wavelet Based Approaches for Efficient Compression of Complex SAR Image Data," in Proc. IEEE '97: IEEE, Piscataway, N.J./USA, 1997.

[9] R. W. Ives, N. Magotra, and C. Kiser, "Wavelet compression of complex SAR imagery using complex- and real-valued wavelets: a comparative study," 1998.

[10] I. W. Selesnick, R. G. Baraniuk, and N. C. Kingsbury, "The dual-tree complex wavelet transform," Signal Processing Magazine, IEEE, vol. 22, pp. 123-151, 2005.

450

Figure 1. Geometry of Stripmap SAR.

Figure 2. The Omega-K Processing of SAR data.

(a)

(b)

(c)

(d)

Figure 3 (a) Simulated Signal, (b) Point targets, (c) k-space Signal (d) Reconstructed Image (200 pts)

451
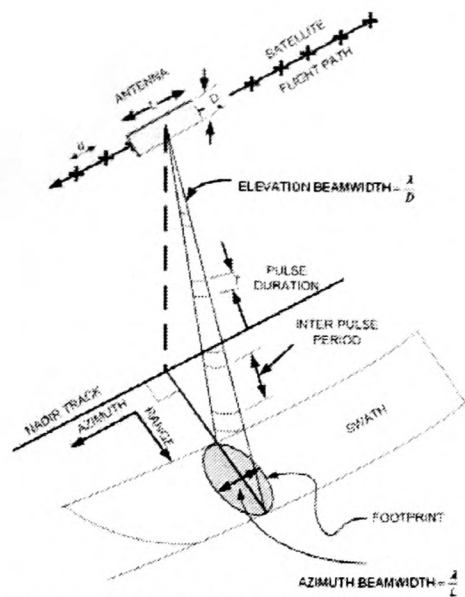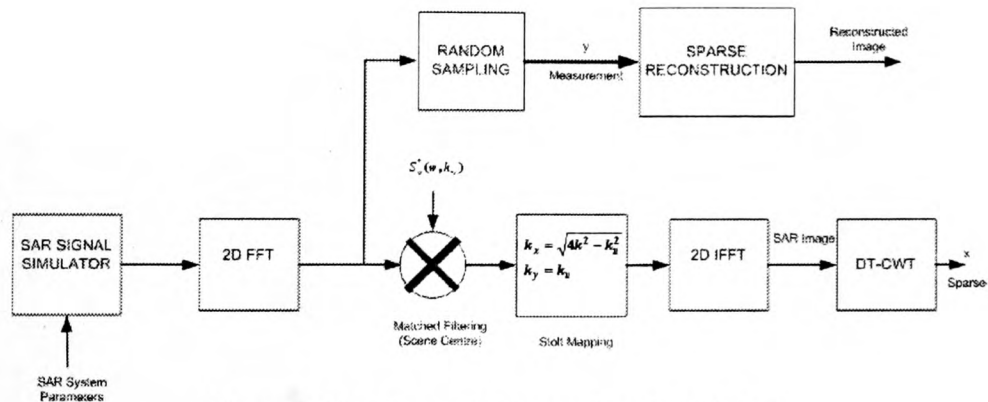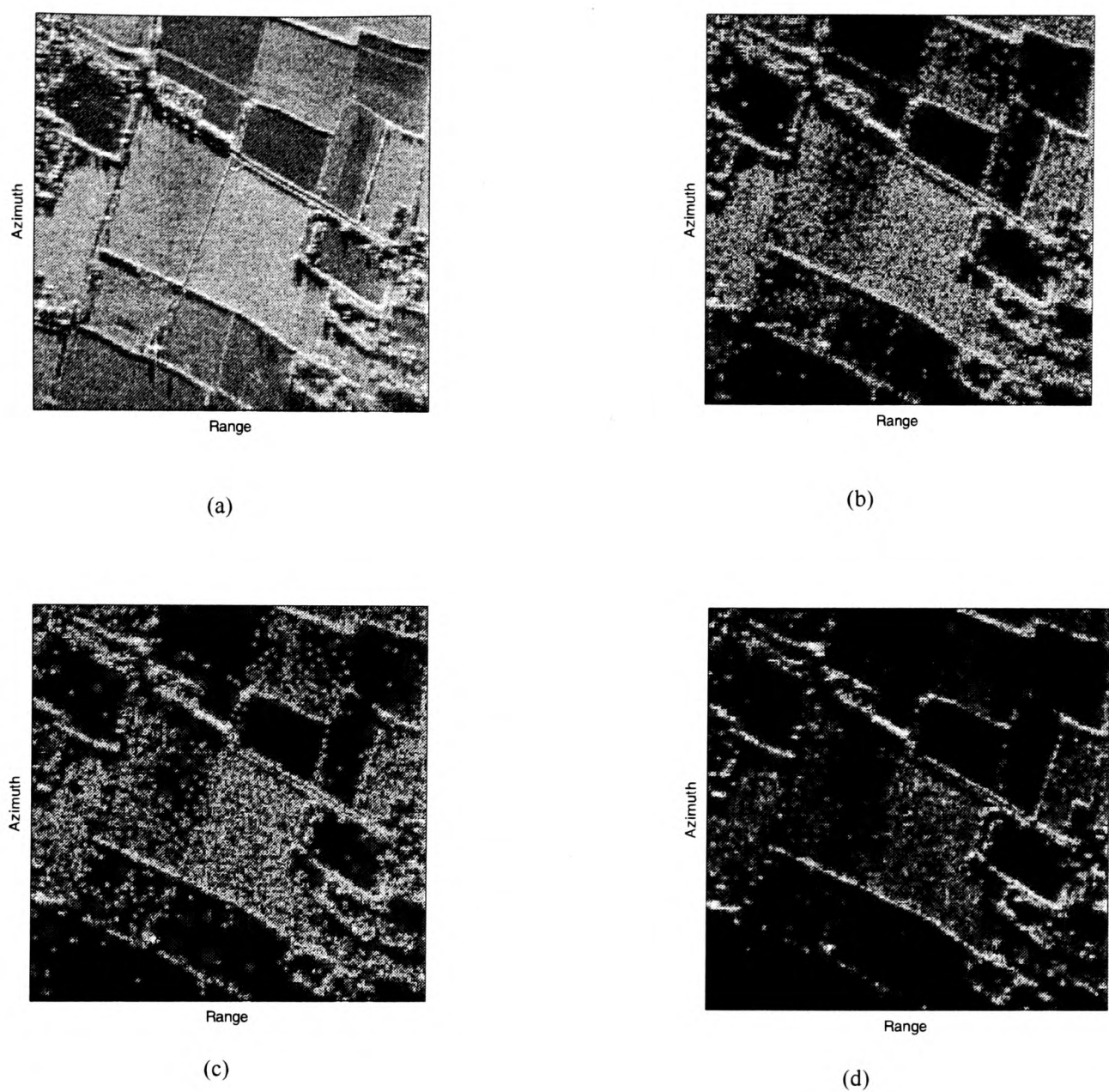
Figure 4. (a) Original SAR Image, (b) Intensity image with OMP reconstruction for 6000 coefficients, (c) Intensity image for 2:1 compression with OMP reconstruction for 6000 coefficients (d) Reconstructed Image with 6000 sorted coefficients (DT-CWT used as a frame operator).

SYNTHETIC APERTURE RADAR RAW DATA ENCODING USING COMPRESSED SENSING

Sujit Bhattacharya, Thomas Blumensath, Bernard Mulgrew, Mike Davies

Institute of Digital Communication, Joint Research Institute for Signal and Image Processing
Edinburgh University, Edinburgh, EH9 3JL, United Kingdom
Phone: + (44)131 6505659, Fax: + (44)131 650 6554, Email: S.Bhattacharya@ed.ac.uk
Web: www.see.ed.ac.uk

ABSTRACT

Synthetic Aperture Radar (SAR) is active and coherent microwave high resolution imaging system, which has the capability to image in all weather and day-night conditions. SAR transmits chirp signals and the received echoes are sampled into In-phase (I) and Quadrature (Q) components, generally referred to as raw SAR data. Raw data compression is an essential future requirement for high resolution space borne SAR sensor in order to reduce the volume of data that is stored onboard and later transmitted to ground station. Due to the low computational resources available onboard satellite a simple encoding algorithm based on Compressed Sensing framework to compress SAR raw data with real wavelets is proposed in this paper. The decoding of the data on ground is then based on convex optimization through Projections on Convex Sets (POC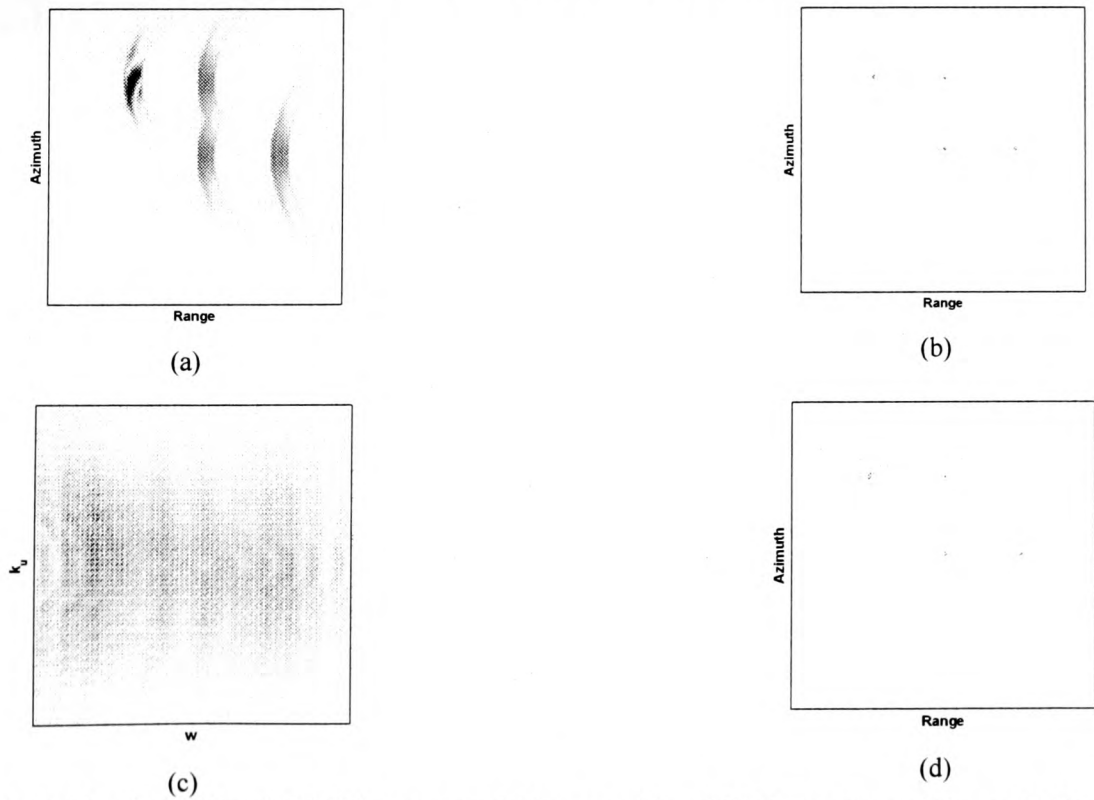S) or uses greedy algorithms such as Orthogonal Matching Pursuit (OMP). The option of converting the complex SAR signal to real data by shifting the frequency spectrum by half bandwidth and then using real wavelets as a sparsifying transform to compress the SAR signal is studied and compared with using the wavelets with the complex signal in the CS framework.

1. INTRODUCTION

Synthetic Aperture Radar (SAR) has been the sensor of choice for numerous applications due to its all weather and day-night imaging capabilities. It is active and coherent microwave radar, which uses the motion of a satellite to synthesis a much larger antenna aperture than the actual antenna aperture to generate high spatial resolution images. The radar produces 2D (range and azimuth) terrain reflectivity images by emitting a sequence of closely spaced radio frequency pulses and by sampling the echoes scattered from the ground targets. The received echoes are sampled into In-phase (I) and Quadrature (Q) components referred to as raw SAR data by the onboard electronics. The onboard satellite electronics essentially consists of transmitter, receiver and Analog-to-Digital converter, followed by a real time downlink or storage memory for later transmission to the ground.

The ever increasing demand for high resolution and large swath have resulted in a high data rate which poses major constraints in the operation of SAR to transmit the data to ground, or to store them onboard. An efficient compression algorithm has thus become important for advanced SAR systems. The compression of raw SAR data poses several challenges due to high entropy and its noise like characteristics [1]. The noise like characteristics arises because signals from several scatters are added coherently with unknown phase and amplitude. Typically its adjacent samples are uncorrelated in both range and azimuth directions.

The techniques for compression of raw SAR signal based on scalar quantizer, vector quantizer and transform domain are reviewed in [2]. All these techniques exploit the redundancy inherent in the *Nyquist* rate sampled signal to achieve compact representation and efficient transmission of the information. This technique of sampling at a higher rate and then eliminating redundancy by processing a large amount of data has poor efficiency in terms of both sampling rate and computational complexity.

A new framework that recovers signals from incomplete measurements i.e. sampling below the *Nyquist* rate is *Compressed Sensing* (CS), introduced in [3] and [4]. It was shown that a signal having a sparse representation can be captured (encoded) from a small number of random linear projections onto a measurement basis. The measurement process is *non-adaptive*. The original signal can be reconstructed (decoded) through a non-linear decoding scheme that uses the sparsity as *a priori* information for solving the linear inverse problem.

The compression of the SAR raw data in the CS framework through Complex Wavelet Transform (CWT) as a sparsifying transform was presented in [5]. The CWT did not provide enough sparsity of the SAR complex signal to give a high compression ratio. This paper proposes to use the real wavelets in the CS framework to compress the SAR raw data. The problem of converting the complex SAR signal to real data format by shifting the frequency spectrum by half the bandwidth is discussed. The results

with real wavelets for point targets and actual satellite data is presented in this paper.

2. SAR SYSTEM AND PROCESSING

The *Stripmap* mode of SAR is capable of producing a high resolution terrain image over a wide swath by a relatively small antenna. In the *Stripmap* mode, the radar maps the surface with the antenna pointing downward such that the boresight (centre) of the mainlobe of the real aperture radiation pattern is perpendicular of the flight path as shown in Figure 1 [1]. The simplified model for the SAR Stripmap model is to consider the stationary imaging surface to consist of several point reflectors with reflectivity σ_n and located at (x_n, y_n). The radar located at (o, u_n) in the spatial domain transmits wide bandwidth signal $p(t)$ of period T_p at regular interval T_{PRI}. The SAR image is reconstructed from a finite set of *projections* resulting from the interaction between the various scatters on ground and the transmitted signal.

The processing of SAR raw data is shown in Figure 2, which involves computation of 2D FFT, matched filtering with the scene centre reference function, converting the polar format data to the rectangular format through *Stolt mapping* and finally 2D IFFT [6].

3. COMPRESSED SENSING THEORY

Let us consider signal $f \in \mathbb{R}^N$, which has a sparse representations over a fixed orthogonal transform, $\Psi \in \mathbb{R}^{N \times N}$, having columns ψ_i, $i = 1, ..., N$. Thus, we can describe the signal as $f = \Psi x$ with $\|x\|_0 \leq L \ll N$, where $\|x\|_0 = |(i : x_i \neq 0)|$. Such a signal is known as an $L - Sparse$ signal w.r.t. the dictionary Ψ.

In the CS framework, to measure (encode) f we compute the measurement vector $y \in \mathbb{R}^K$ using a linear projector $M \in \mathbb{R}^{K \times N}$, *with* $L < K \ll N$ via $y = Mf$. Since $K \ll N$, we have fewer measurements than degrees of freedom for the signal f. We refer to M as the measurement matrix whose rows are the measurement vectors and denote its columns by $\varphi_1, ..., \varphi_N$.

The measurement signal $y \in \mathbb{R}^K$ is written is terms of $x \in \mathbb{R}^N$ as

$$y = Mf = M\Psi^* x$$
$$= Hx$$
(1.1)

where $H = M\Psi^*$ is also known as the holographic basis.

The original signal f can be reconstructed from y by exploiting the sparsity of its representation i.e. by searching for all possible $\hat{x}$ satisfying $y = H\hat{x}$ that is the

sparsest. If this representation coincides with x we get a perfect reconstruction of the signal via (1.1). Mathematically, $\hat{x}$ can be found by solving the linear inverse problem through l_0 optimization as:

$$\hat{x} = \arg\min \|x\|_0 \text{ subject to } y = H\hat{x}$$
(1.2)

The objective function enforces the sparsity whereas the constraint enforces data consistency. The l_0 optimisation is a combinatorial problem and is NP-hard to solve. The two most common approaches are therefore to replace the l_0 approximation problem with convex optimisation methods or greedy methods [7, 8]. The most popular greedy algorithm is the Orthogonal Matching Pursuit (OMP) [8].

The problem can also be solved through the method of alternate projections onto convex sets (POCS) algorithm [9] that requires a small amount of *a priori* information about the signal we are to recover [10]. Since, $\hat{x}$ is the unique solution to (1.2), the l_1 ball $B = \left\{ x : \|x\|_1 \leq \|\hat{x}\|_1 \right\}$ and the hyperplane $G = \{x : Hx = y\}$ meet at exactly one point; $B \cap G = \{\hat{x}\}$. The projection onto G is computed as:

$$\hat{x} = x + H^* \left(HH^*\right)^{-1} (y - Hx)$$
$$= x + H^\dagger (y - Hx)$$
(1.3)

where $H^* = \text{adj}(H)$ and $H^\dagger$ is the *pseudo-inverse* of H. The projection onto G is computed as:

$$\hat{x} = \text{sgn}(x)(|x| - \delta)_+$$
(1.4)

To determine the threshold δ such that $\|\hat{x}\|_1 \leq \tau$, $\tau \in \mathbb{R}^+$, we sort the coefficients by magnitude and perform a linear search. The value of τ is computed by $\tau = \sum_Q |\hat{x}|$, where the index set Q is expanded or contracted based on increase or decrease of previous estimate of τ in each iteration.

4. RAW SAR DATA COMPRESSION THROUGH COMPRESSED SENSING

For the compression of the satellite SAR raw data, the amplitude and phase are both indispensable for many applications e.g. interferometer. The study of the Discrete Time Complex Wavelet Transform (DT-CWT) for the SAR image compression and denoising to preserve both amplitude and phase has been reported in [11]. The DT-CWT comprises of two parallel wavelet filter banks that contain filters of different delays that minimises the aliasing error due to decimation [12]. The compression of the SAR raw data in the CS framework through DT-CWT as a sparsifying transform was presented in [5] where DT-CWT is used as a frame operator rather that a basis.

A good reconstruction of the measured signal in the CS framework is possible only if the *sparsifying* transform provides a sparse representation of the original signal. The CWT did not provide enough sparsity of the SAR complex signal for it to give a high compression ratio. The compression of the complex SAR data by using real wavelets was reported in [13] where the complex image data is converted to a real data format using Fourier Transform. The signal is converted to discrete "analytic" signal by shifting the frequency spectrum by the half bandwidth to positive frequencies [14]. The Inverse Fourier Transform of this analytic signal can now be represented by its real part without loss of any information, since the real and imaginary part of the signal are mutual Hilbert transforms. But in many practical scenarios, the acquired data does not satisfy the *Hermitian* assumptions required to form the analytic signal and one must instead handle the data in its complex form. For such cases, we propose to use the real wavelets on the complex signal. The particular advantage of these techniques is that several wavelet bases used in conventional image compression could be used as a *sparsifying* transform rather than a limited choice of Complex Wavelet basis.

The Compressed Sensing framework for the complex SAR raw data using the real wavelet as a sparsifying transform is shown in Figure 2. The holographic basis, **H** , in (1.1) is implemented through functions consisting of 2D-WT, 2D FFT, *Stolt* mapping, matched filtering and the measurement matrix, **M** , consists of random sampling points.

To study the feasibility of using CS for SAR raw data compression, we used five point targets simulated through the SAR simulator as shown in Figure 3(a) with ideal point target response in Figure 3(b). The 2D FFT of the complex raw data was performed after which the data was sampled randomly, as shown in Figure 3(c). The size of the measurement data was kept at 4200 for the image size of 256 x 256, to recover the sparse image representation of five targets. The real image is formed by shifting the frequency by half bandwidth before the 2D IFFT is performed. The wavelet used is the *Daubecies-8* (D8). The reconstruction algorithm is through the POCS method, as described above. The reconstructed image for the point target simulation as shown in Figure 3(d) and is evaluated in terms of the Peak Side Lobe Ratio (PSLR) and Integrated Side Lobe Ratio (ISLR). The PSLR is defined as the ratio of the peak intensity of the most prominent sidelobe to the peak intensity of the mainlobe. The ISLR is the ratio of the power in the mainlobe to the total power in all the sidelobes. The PSLR and the ISLR of the point targets simulation for 256 x 256 size complex SAR processed image and the image generated with 4200 measurement samples and 200 wavelet coefficients are tabulated in Table 1.

	PSLR (dB)	ISLR (dB)
Original Image	-11.21	-1.75
CS Image	-10.48	-3.57

Table 1. PSLR and ISLR of the original and reconstructed CS image.

There is no degradation in PSLR and the improvement in the ISLR is due to the recovery of only 200 wavelet coefficients which resulted in the reduction of the sidelobes power.

For the satellite data, as shown in Figure 4(a), we have used the *Daubecies-8* wavelet on the complex image formed after taking the 2D IFFT, as shown in Figure 2. In this case the signal was compressed by a factor of 2:1. The reconstruction algorithm in this case is based on OMP with the least square estimation performed through conjugate gradient (CG) method for computational efficiency.

For the 256 x 256 SAR complex image, as shown in figure 4(a), the reconstruction of the image for 6000 wavelet coefficients with OMP is shown in figure 4(b). The figure 4(c) shows the reconstruction with OMP for 6000 wavelet coefficients with 2:1 compression ratio. The reconstruction with OMP is limited to 6000 coefficients as the sparsity of the 2D-WT is not sufficient to provide any further improvement in PSNR of the reconstructed image. The reconstructed images with and without compression do not show much perceptual difference.

5. CONCLUSIONS

This paper proposes the use of real wavelet transform as a *sparsifying* transform in the CS framework for the SAR raw data compression. The option of converting the complex SAR images to real data by shifting the frequency spectrum by half bandwidth and its associated problem of using it in actual satellite data is presented. The results with the point targets and the actual satellite images show that it is possible to compress the SAR raw data in the CS framework with the real wavelets. Further studies on using other wavelet basis to get sparser representation of complex SAR data and hence more compression ratio is undertaken.

REFERENCES

[1] A. J. C. Curlander and R. N. McDonough, *Synthetic Aperture Radar: Systems and Signal Processing*. New York: Wiley, 1991.
[2] A. El Boustani, K. Brunham, and W. Kinsner, "A review of current raw SAR data compression techniques," in *Canadian Conference on Electrical and Computer Engineering*, 2001, pp. 925-930.
[3] E. Candes, J. Romberg, and T. Tao, "Robust Uncertainty Principles: Exact Signal Reconstruction from Highly

Incomplete Frequency Information," *IEEE Trans. Inform. Theory*, 2004.

[4] D. L. Donoho, "Compressed Sensing," *Information Theory, IEEE Transactions on*, vol. 52, pp. 1289-1306, 2006.

[5] S. Bhattacharya, T. Blumensath, B. Mulgrew, and M. Davies, "Fast Encoding of Synthetic Aperture Radar Raw Data Using Compressed Sensing," in *IEEE Statistical Signal Processing Workshop 2007*, Madison, WI, 2007.

[6] M. Soumekh, *Synthetic Aperture Radar Signal Processing*. New York: Wiley, 1999.

[7] E. Candes and T. Tao, "Near Optimal Signal Recovery from Random Projections: Universal Encoding Strategies ?," *Tech. Rep. 04-70, UCLA Group in Comp. and Applied Math*, December 2004.

[8] J. Tropp and A. Gilbert, "Signal Recovery from partial information via orthogonal matching pursuit," *Tech. Rep. 04-70, UCLA Group in Comp. and Applied Math.*, Dec 2004.

[9] P. A. Jansson, *Deconvolution of Images and Spectra*. San Diego: Academic Press Inc., 1997.

[10] E. J. Candĺs and J. Romberg, "Practical Signal Recovery from Random Projections," *Wavelet Applications in Signal and Image Processing XI, Proc. SPIE Conf.*, vol. 5914, 2005.

[11] R. W. Ives, N. Magotra, and C. Kiser, "Wavelet compression of complex SAR imagery using complex- and real-valued wavelets: a comparative study," in *Signals, Systems & Computers, 1998. Conference Record of the Thirty-Second Asilomar Conference on*, 1998, pp. 1294-1298 vol.2.

[12] I. W. Selesnick, R. G. Baraniuk, and N. C. Kingsbury, "The dual-tree complex wavelet transform," *Signal Processing Magazine, IEEE*, vol. 22, pp. 123-151, 2005.

[13] M. Brandfaß, W. Cöster, U. Benz, and A. Moreira, "Wavelet Based Approaches for Efficient Compression of Complex SAR Image Data," in *Proc. IEEE '97*: IEEE, Piscataway, N.J./USA, 1997.

[14] L. Marple, Jr., "Computing the discrete-time analytic signal via FFT," *IEEE Transactions on Signal Processing*, vol. 47, pp. 2600-2603, 1999.
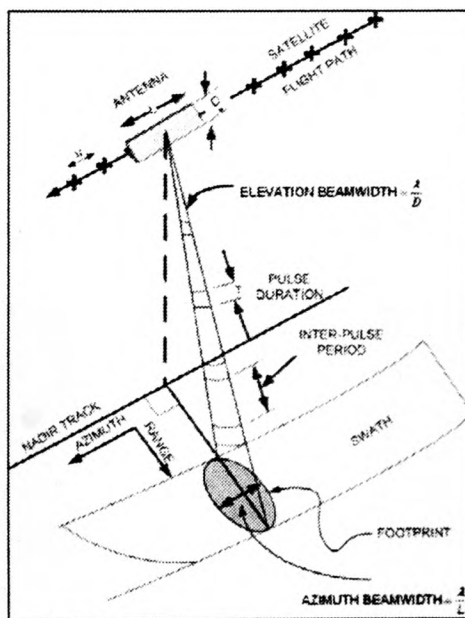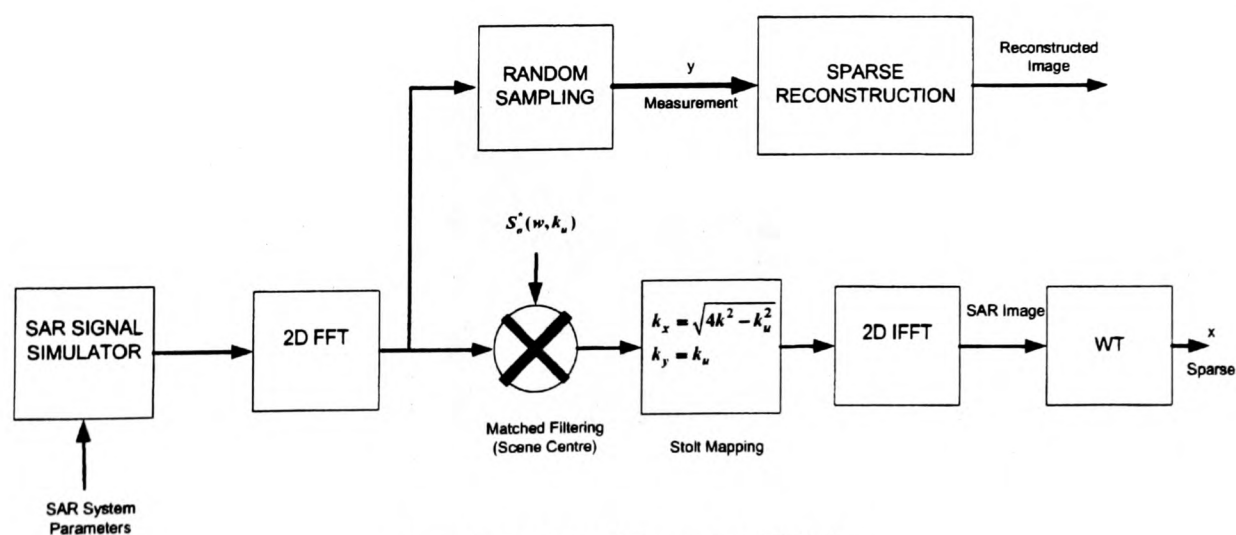
Figure 1. Geometry of Stripmap SAR.

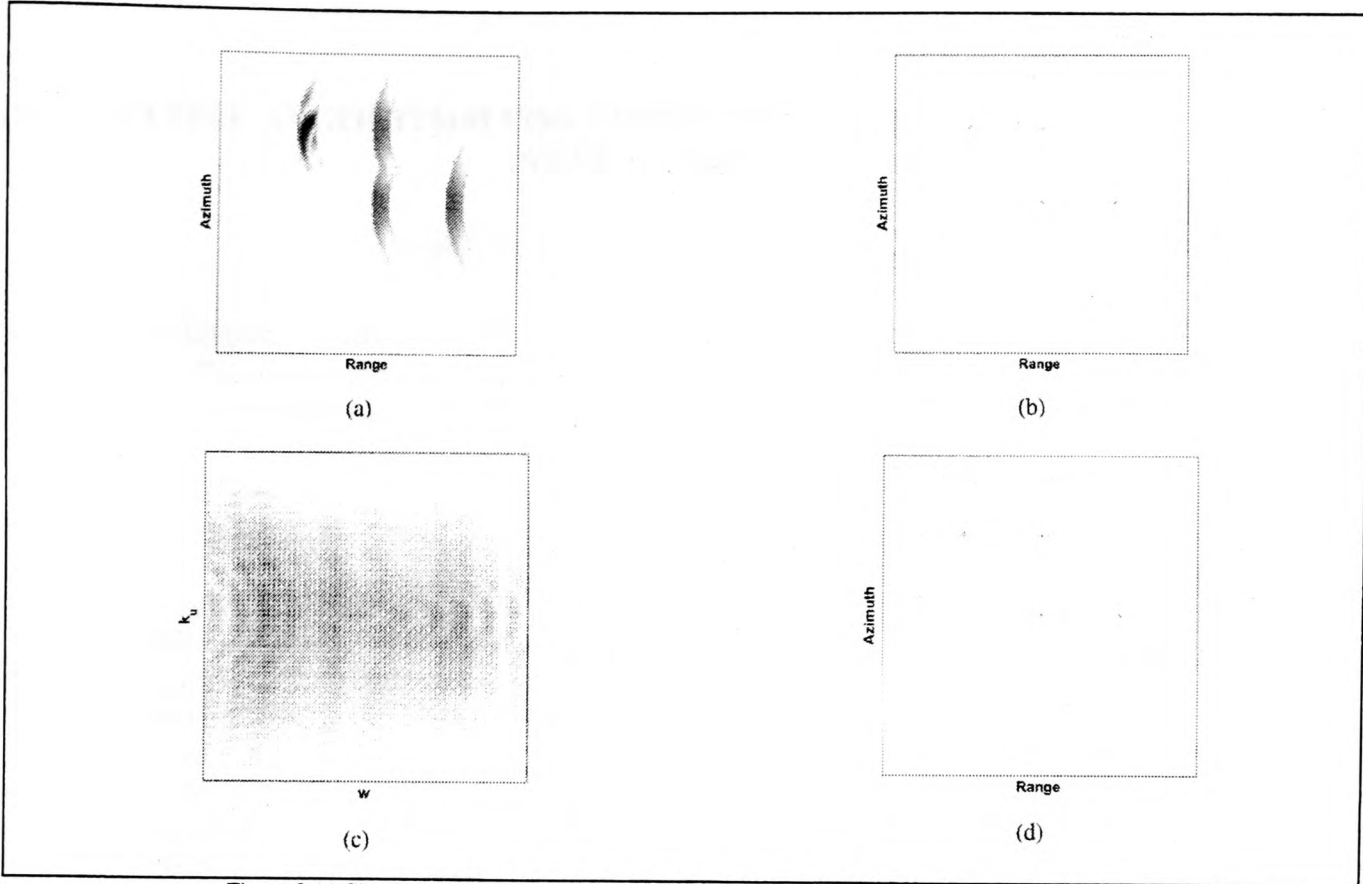Figure 2. The Omega-K Processing of SAR data.

Figure 3 (a) Simulated Signal, (b) Point targets, (c) k-space Signal (d) Reconstructed Image
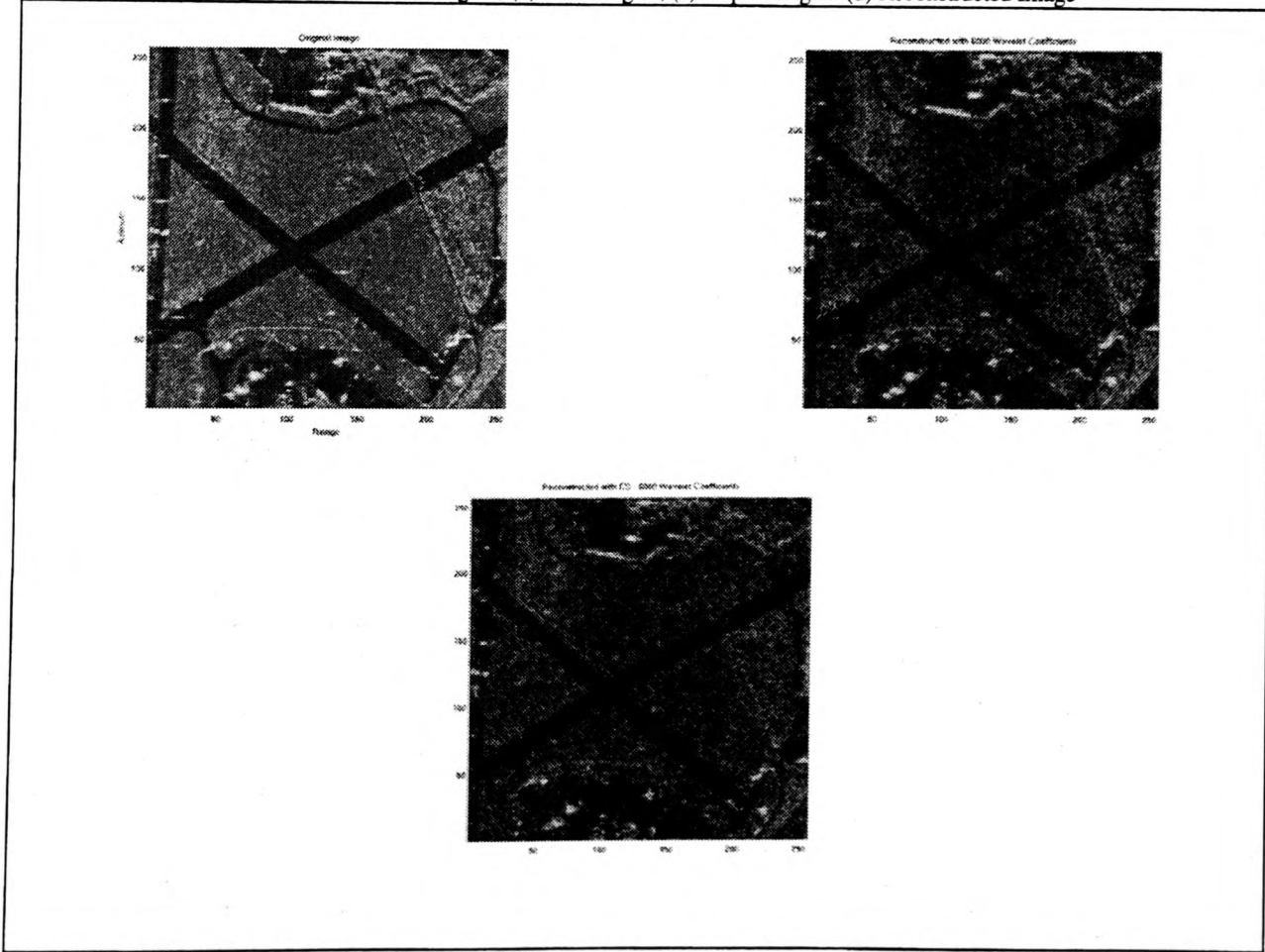

Figure 4 (a) Original SAR image, (b) reconstructed image with 6000 wavelet coeff. (c) reconstructed image with 2:1 compression and 6000 wavelet coeff.

AN ITERATIVE ALGORITHM FOR COMPUTING SPARSE SOLUTIONS TO LINEAR INVERSE PROBLEMS

Sujit Bhattacharya and Bernard Mulgrew

Institute of Digital Communication, Joint Research Institute for Signal and Image Processing
The University of Edinburgh, Edinburgh, EH9 3JL, United Kingdom
Phone: + (44)131 6505659, Fax: + (44)131 650 6554,
Email: S.Bhattacharya@.ed.ac.uk

ABSTRACT

In this paper, we propose a fast and unsupervised iterative algorithm for computing sparse solutions to linear inverse problems. Often, it has been proposed to use regularization of ill-posed linear inverse problems via l_1-penalization when the solution is sparse. The choice of the regularization parameter is important and it is either manually set or estimated. In the proposed algorithm, which is based on iterative soft-thresholding, the regularization parameter is adaptively estimated at each iteration. It is also shown here that this algorithm could be accelerated by using steepest descent method. The algorithm, *L1_Adapt*, is tested with several real and complex data and it is compared with standard algorithms like Basis Pursuit (*BP*) and Orthogonal Matching Pursuit (*OMP*).

Index Terms— Inverse problems, sparse solution, iterative algorithm, compressed sensing.

1. INTRODUCTION

One of the most important problems in signal processing has been the recovery or the restoration of the signal from its degraded version. Such problems are described as inverse problems, where one makes indirect observations of a quantity of interest. Examples of inverse problems includes (i) deconvolution i.e. recovery of the input to a linear time-invariant system from its output, (ii) restoration of signal from its projection, (iii) recovery of inputs from a time variant system, (iv) recovery of signal from incomplete measurements (*Compressed Sensing*), (v) overcomplete representation of signals and (vi) extrapolation of data from a given length of data. In all such cases, an appropriate mathematical representation is the *Fredholm equation of first kind*,

$$y = Ax + e \qquad (1.1)$$

where x is the unknown input signal, y is the known measurement, A is the known distortion operator or transformation and e is unknown noise.

In this paper, we consider the problem of estimating the vector $x \in \mathbb{R}^N$ given $y \in \mathbb{R}^M$ and matrix $A \in \mathbb{R}^{M \times N}$, where $M < N$. The solution to such underdetermined problem is not unique [1]. The non-uniqueness of the underdetermined system is commonly addressed by using some prior knowledge about x, to select from among the (many) possible representations. One such important *a-prior* is the *sparsity* of the solution which implies that the solution being sought must have a small number of large coefficients. The sparsity promoting feature of the solution to the underdetermined system of equations has been explored extensively in various signal processing applications including image, audio, video compression and recently in the framework of Compressed Sensing (CS) [2, 3].

2. SPARSE RECOVERY VIA l_1 REGULARIZATION

In the case of noiseless measurement i.e., when $y = Ax$, the problem of finding the sparsest solution can be formulated as

$$\hat{x} = \arg\min \|x\|_0 \quad \text{s.t. } y = Ax \qquad (1.2)$$

where $\|x\|_0 = \#\{i : x_i \neq 0\}$ is the l_0 semi-norm which counts the number of non-zero entries in the vector x. A vector is called R-sparse if there are R number of non-zero entries. An exact solution of this problem is computationally intractable except for small problems [4].

Basis pursuit (BP) [5], replaces the l_0 with its l_1 norm, to obtain the convex problem

$$\hat{x} = \arg\min \|x\|_1 \quad \text{s.t. } y = Ax \qquad (1.3)$$

where $\|x\|_1 = \sum_{i=1}^{N} |x_i|$. This problem can be reformulated as a linear program and so is tractable. .

However, if there is noise in the measurement y, as given by (1.1), the sparse solution is obtained through the Basis Pursuit Denoising (BPDN) problem [5]

$$\hat{\mathbf{x}} = \arg\min\left\{\frac{1}{2}\|\mathbf{A}\mathbf{x} - \mathbf{y}\|^2 + \tau\|\mathbf{x}\|_1\right\} \qquad (1.4)$$

where the variable $\tau \in \mathbb{R}^+$ is the regularization parameter.

Iterative soft-threshold algorithms to approximate the sparse solution $\hat{\mathbf{x}}$ for (1.4) have been proposed by several authors [6, 7] . It is shown in [7] that $\hat{\mathbf{x}}$ is the limit of sequences $\mathbf{x}^{(n)}$ defined recursively by

$$\mathbf{x}^{(n+1)} = \mathbf{S}_\tau\left[\mathbf{x}^{(n)} + \mathbf{A}^*\left(\mathbf{y} - \mathbf{A}\mathbf{x}^{(n)}\right)\right] \qquad (1.5)$$

starting from an arbitrary $\mathbf{x}^{(0)}$, where $\mathbf{A}^*$ is the conjugate transpose of $\mathbf{A}$ and $\mathbf{S}_\tau$ is the soft-thresholding operation defined by component-wise shrinkage as

$$\mathbf{S}_\tau(x_i) = \operatorname{sign}(x_i)(|x_i| - \tau)_+ = \begin{cases} x_i - \tau & x_i > \tau \\ 0 & |x_i| \le \tau \\ x_i + \tau & x_i < -\tau \end{cases} \qquad (1.6)$$

where $(\cdot)_+$ denotes the positive part operator defined as $(g)_+ = \max(g, 0)$, and $\operatorname{sign}(\cdot)$ is the sign function defined as $\operatorname{sign}(g) = 1$ if $g > 0$, and $\operatorname{sign}(g) = -1$ if $g < 0$. The convergence of this algorithm is proved in [7]. The above iteration is often called as the *iterative soft-thresholding* algorithm or the *thresholded Landweber iteration* [7]. The soft thresholding for the complex signal is defined in terms of its magnitude r and phase θ as $\mathbf{S}_\tau(re^{i\theta}) = \mathbf{S}_\tau(r)e^{i\theta}$ [7].

It is shown in [7] that this non-linear thresholding of the *Landweber iteration* $\mathbf{x}^{(n+1)} = \mathbf{x}^{(n)} + \mathbf{A}^*\left(\mathbf{y} - \mathbf{A}\mathbf{x}^{(n)}\right)$, which is a gradient descend algorithm with a fixed step size, converges quite slowly. This algorithm would converge faster, if the solution in each iteration is restricted to the l_1- ball $\mathbf{B}_R := \{\mathbf{x} \mid \|\mathbf{x}\|_1 \le \alpha\}$, with $\alpha := \|\mathbf{x}'\|_1$ where $\mathbf{x}' = \lim_{n\to\infty} \mathbf{x}^{(n)}$. The size of l_1-ball, α, depends on the regularization parameter τ in (1.5).

The success of the above method relies on the fact that the l_1-norm of the true solution, α, is known beforehand. Also, in many algorithms which solves the unconstrained problem of the form (1.4) requires the determination of the regularization parameter, τ, which could be quite challenging and this parameter is often either assigned manually or determined iteratively.

The proposed algorithm, as discussed in the next section, solves the problem (1.3) with the condition $\mathbf{y} = \mathbf{A}\mathbf{x}$ replaced by $\|\mathbf{y} - \mathbf{A}\mathbf{x}\|^2 \le \varepsilon_2$, by projecting the solutions of the iterative algorithm (1.5) onto an adaptive convex set of increasing l_1-norm.

3. PROPOSED ALGORITHM

We propose a fast and unsupervised algorithm to solve the so called Basis-Pursuit Denoising problems for both real and complex data. The proposed algorithm is based on the iterative soft-thresholding algorithm as given in (1.5). The novelty of the proposed algorithm is that the value of l_1 norm $\alpha^{(n)}$ for determining the threshold τ in equation (1.5) is gradually increased in each iteration.

The pseudo-code of the proposed algorithm, *L1_Adapt*, is shown in Table 1.

Initialise

$L = 1, \mathbf{x}^{(1)} = 0, \varepsilon_1 = 1e^{-5}, \varepsilon_2 = 1e^{-6}, \alpha^{(0)} = 0, n = 1$

1. $\beta = \mathbf{x}^{(n)} + \mathbf{A}^*\left(\mathbf{y} - \mathbf{A}\mathbf{x}^{(n)}\right)$

2. $a = sort(|\beta|)$ such that $a_i > a_{i+1}, \forall i$

3. $\alpha^{(n)} = \sum_{j=1}^{L} a_j$

4. If $\alpha^{(n)} - \alpha^{(n-1)} < \varepsilon_1$, then $L = L + 1$

5. $k = \arg \min_{\substack{j \in \{1,2,...N\}: \\ \|\mathbf{S}_{a_j}(\beta)\|_1 < \alpha^{(n)}}} a_j$

6. $v = \left(\alpha^{(n)} - \|\mathbf{S}_{a_k}(a)\|_1\right)/k, \quad \tau = a_k + v$

7. $\mathbf{x}^{(n+1)} = \mathbf{S}_\tau(\beta)$

8. If $\|\mathbf{y} - \mathbf{A}\mathbf{x}^{(n+1)}\|^2 > \varepsilon_2, \ n = n + 1$, go to step 1

Table 1. Pseudo-code of *L1_Adapt*.

The description of the algorithm *L1_Adapt* is as follows:

1. **Initialisation**: The algorithm begins with the initialization of the iteration no. n, the index L for computation of l_1-norm, the initial guess $\mathbf{x}^{(1)} = 0$, the convergence factor ε_1 for incrementing the index L and the convergence factor ε_2 for the algorithm to terminate.

2. **Gradient Descent Step**: This step computes the gradient of the function and finds a new value by moving in the opposite direction of the computed gradient as $\beta = \mathbf{x}^{(n)} + \mathbf{A}^*\left(\mathbf{y} - \mathbf{A}\mathbf{x}^{(n)}\right)$.

3. **Computation of l_1-norm**: The value of the l_1-norm to which the inner iteration has to converge is computed by first sorting the coefficients in the descending order and then computing the l_1-norm as $\alpha^{(n)} = \sum_{j=1}^{L} a_j$. The index, L, for estimating the $\alpha^{(n)}$ value in step 3. of the pseudo-code is increased stepwise whenever the solution has converged to the previous reference of l_1-norm.

It is to be noted that because of the shrinkage, the number of terms, k, used to form a norm of size $\alpha^{(n)}$ after thresholding will always be greater than or equal to the number L before thresholding.

4. Computation of Soft-thresholding value: The step 5 and 6 computes the value τ, which is used for soft-thresholding. A search is performed to find the index k such that $k = \arg\min_{\substack{j \in \{1,2,...N\}: \\ \left|s_{a_j}(\beta)\right|_1 < \alpha^{(n)}}} a_j$. Then we set $v = \left(\alpha^{(n)} - \left\|s_{a_k}(a)\right\|_1\right)/k$ and compute $\tau = a_k + v$.

5. Projection onto l_1-ball: The projection onto the l_1-ball is computed via the soft-thresholding as $x^{(n+1)} = S_\tau(\beta)$ as per (1.6) with the value τ as computed in the earlier step.

The algorithm iterates till the l_2-norm of the residue $y - Ax^{(n)}$ is below the threshold ε_2. Generally, ε_2 is the estimated noise level.

The convergence of L1_Adapt is accelerated by introducing a standard descent step in (1.5) as

$$x^{(n+1)} = S_\tau\left[x^{(n)} + \delta^{(n)}A^*\left(y - Ax^{(n)}\right)\right] \qquad (1.7)$$

where $\delta^{(n)} = \|r\|^2 / \|A^*r\|^2$, with $r = y - Ax^{(n)}$ and δ^n the standard descent step as calculated in Steepest Descent algorithm. The convergence of such algorithm with the step size $\delta^n \geq 1$ is proved in [8]. It is also shown in [1] that the convergence of (1.7) is assured, if and only if $0 < \delta^{(n)} < 2/\sigma_1^2$ where σ_1 is the largest singular value and $\sigma_1^2 = \|A^*A\|$.

The proposed algorithms, L1_Adapt and its faster variant, work for both real and complex vectors and are more flexible as compared to the BP algorithm solved through interior-point methods. These algorithms are also tailored for the matrices that are formed by rows taken from orthonormal matrices corresponding to fast transforms so that Ax and A^*x can be computed by fast transforms. Iterative algorithms offer interesting advantages like the possibility of developing adaptive procedures, easier ways to include constraints e.g. positivity, monitoring of the solution process and also the parameters determining the solution can be updated as the iteration progresses.

4. RESULTS

The L1_Adapt algorithm is tested with four 1D examples with $N = 1024$ from *Donoho-Johnstone* collection of synthetic test signals namely, '*Cusp*', '*Heavisine*' and '*Doppler*' [9]. The other two test cases are '*Piecewise Polynomial*' and '*Piecewise Regular*'. The measurement matrix A is obtained by sampling a matrix with i.i.d. Gaussian entries which are then orthonormalized. The sparsifying transform used here is *Daubechies-8* (D8) wavelet. The results for several values of M (the size of measurement vector) in comparison with *SolveBP* [10] for 100 runs of each experiment and are shown in Table 2. The

mean and standard deviation of SNR and l_1-norm are tabulated as Std_SNR and Std_L1 respectively in Table 2. Extensive numerical results suggest that the *L1_Adapt* algorithm converges to the minimum l_1-norm as the *SolveBP* converges to. The advantages of using the *L1_Adapt* algorithm over *SolveBP* are highlighted in the previous section.

The algorithm was also tested with Complex Wavelet Transform (CWT) [11] as frame where the signal is sparse. The sparse signal of length $M = 256$ was synthetically created. The frame size is 512. The *SolveBP* is not used in this case as A and A^* are not matrices but functions and also $y \in \mathbb{C}^M, x \in \mathbb{C}^N$. Instead, the *L1_Adapt* algorithm is compared with *OMP* method and results are shown in Figure 1. The SNR of the signal reconstructed with *L1_Adapt* (81.46 dB) far exceeds than that with *OMP* (10.18 dB). This shows that *L1_Adapt* works well for some cases where the *OMP* fails to get the sparse solution or the minimum l_1 norm solution.

10. CONCLUSIONS

An iterative algorithm for the computing sparse solutions to linear inverse problems is presented, in which no prior knowledge about the regularization parameter is required. The required regularization parameter is computed at each iteration step. The various advantages of the iterative methods over the standard l_1-norm minimization algorithms are discussed. The algorithm is tested with various test signals both real and complex and is shown to converge to the min l_1-norm solution. Future work will involve applying the algorithm and its variant to more practical cases like encoding the raw data from radar, MRI, etc.

11. REFERENCES

[1] M. Bertero and P. Boccacci, *Introduction to inverse problems in imaging*: IoP, 1998.

[2] E. J. Candes, J. Romberg, and T. Tao, "Robust uncertainty principles: exact signal reconstruction from highly incomplete frequency information," *IEEE Transactions on Information Theory*, vol. 52, pp. 489-509, February 2006.

[3] D. L. Donoho, "Compressed Sensing," *IEEE Transactions on Information Theory*, vol. 52, pp. 1289-1306, 2006.

[4] B. K. Natarajan, "Sparse approximation solutions to linear systems," *SIAM Journal on Computers*, vol. 24, pp. 227-234, April 1995.

[5] S. Chen, D. Donoho, and M. Saunders, "Atomic Decomposition by Basis Pursuit," *SIAM Review*, vol. 43, pp. 129-159, 2001.

[6] E. Hale, W. Yin, and Y. Zhang, "A Fixed-Point Continuation Method for l1 -Regularized Minimization with Applications to Compressed Sensing," TR07-07, July 7 2007.

[7] I. Daubechies, M. Fornasier, and I. Loris, "Accelerated Projected Gradient Method for Linear Problems with Sparsity Constraints," *J. Fourier Anal. Appl.*, vol. 14, pp. 764-792, 2008.

[8] E. Candes, J. Romberg, and T. Tao, "Stable Signal Recovery from Incomplete and Inaccurate Measurements," *Communciations on Pure and Applied Mathematics,* vol. 59, pp. 1207-1223, August 2006.

[9] D. L. Donoho and I. M. Johnstone, "Ideal spatial adaptation by wavelet shrinkage," *Biometrika,* vol. 81, pp. 425-455, 1994.

[10] D. Donoho, I. Drori, V. Stodden, and Y. Tsaig, "SparseLab," *http://sparselab.stanford.edu/,* 2005.

[11] I. W. Selesnick, R. G. Baraniuk, and N. C. Kingsbury, "The dual-tree complex wavelet transform," *IEEE Signal Processing Magazine,* vol. 22, pp. 123-151, 2005.
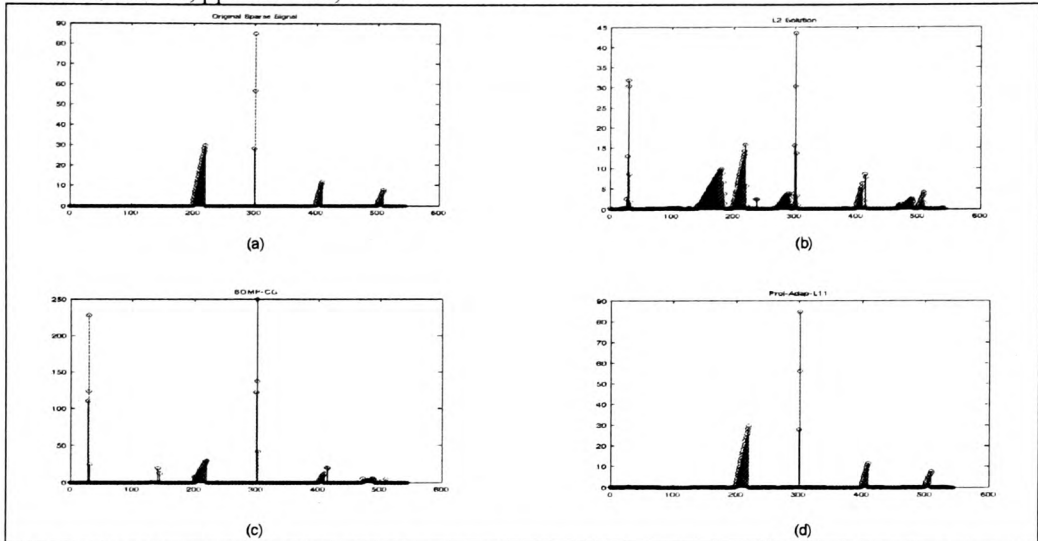
Figure 1. Results with CWT (a) Original Sparse Signal,(b) l_2-norm solution, (c) OMP solution (d) L1_Adapt solution

Measurement Length $M = 100$

	Cusp		Heavisine		Doppler		Piece-Poly		Piece_Regular	
	L1Adapt	BP	L1Adapt	BP	L1Adapt	BP	L1Adapt	BP	L1Adapt	BP
SNR	24.52	24.57	16.92	16.84	4.77	4.86	3.55	3.65	4.48	4.60
L1	35.18	35.19	308.21	308.35	36.41	36.45	6431	6439	2238	2240
Std_SNR	2.93		3.47		1.84		1.60		2.04	
Std_L1	0.09		1.43		0.49		88.62		30.17	

Measurement Length $M = 200$

	Cusp		Heavisine		Doppler		Piece-Poly		Piece_Regular	
	L1Adapt	BP	L1Adapt	BP	L1Adapt	BP	L1Adapt	BP	L1Adapt	BP
SNR	42.52	42.31	31.67	31.63	12.72	12.81	9.28	9.36	11.32	11.38
L1	36.48	36.49	327.81	327.82	46.58	46.59	8518	8522	2874	2875
Std_SNR	4.31		2.81		1.83		1.34		1.31	
Std_L1	0.01		0.20		0.15		35.97		10.06	

Measurement Length $M = 300$

	Cusp		Heavisine		Doppler		Piece-Poly		Piece_Regular	
	L1Adapt	BP	L1Adapt	BP	L1Adapt	BP	L1Adapt	BP	L1Adapt	BP
SNR	79.80	78.35	58.74	58.60	22.16	22.22	15.20	15.27	19.11	19.18
L1	36.58	36.58	330.33	330.33	49.69	49.69	9550	9551	3144	3145
Std_SNR	18.16		3.47		1.58		1.17		1.46	
Std_L1	0.00		0.01		0.04		15.45		3.31	

Table 2: Results of *L1_Adapt* and *SolveBP* for various measurement length M